University of Trento
Department of Physics

Linear and nonlinear edge dynamics and quasiparticle excitations in fractional quantum Hall systems

---

Alberto Nardin

June 2023

Supervised by Dr. Iacopo Carusotto

Submitted in partial fulfilment of the requirements for the degree of
Dottore di Ricerca in Fisica of the University of Trento
Dottorato di Ricerca XXXV Ciclo

Abstract

We reserve the first part of this thesis to a brief (and by far incomplete, but hopefully self-contained) introduction to the vast subject of quantum Hall physics. We dedicate the first chapter to a discursive broad introduction. The second one is instead used to introduce the integer and fractional quantum Hall effects, with an eye to the synthetic quantum matter platforms for their realization. In the third chapter we present famous Laughlin's wavefunction and discuss its basic features, such as the gapless edge modes and the gapped quasiparticle excitations in the bulk. We close this introductory part with a fourth chapter which presents a brief overview on the chiral Luttinger liquid theory.

In the second part of this thesis we instead proceed to present our original results. In the fifth chapter we numerically study the linear and non-linear dynamics of the chiral gapless edge modes of fractional quantum Hall Laughlin droplets – both fermionic and bosonic – when confined by anharmonic trapping potentials with model short range interactions; anharmonic traps allow us to study the physics beyond Wen's low-energy/long-wavelength chiral Luttinger liquid paradigm in a regime which we believe is important for synthetic quantum matter systems; indeed, even though very successful, corrections to Wen's theory are expected to occur at higher excitation energies/shorter wavelengths. Theoretical works pointed to a modified hydrodynamic description of the edge modes, with a quadratic correction to Wen's linear dispersion $\omega_k = vk$ of linear waves; even though further works based on conformal field theory techniques casted some doubt on the validity of the theoretical description, the consequences of the modified dispersion are very intriguing. For example, in conjunction with non-linearities in the dynamics, it allowed for the presence of fractionally quantized solitons propagating ballistically along the edge.
The strongly correlated nature of fractional quantum Hall liquids poses technical challenges to the theoretical description of its dynamics beyond the chiral Luttinger liquid model; for this reason we developed a numerical approach which allowed us to follow the dynamics of macroscopic fractional quantum Hall clouds, focusing on the neutral edge modes that are excited by applying an external weak time-dependent potential to an incompressible fractional quantum Hall cloud prepared in a Laughlin ground state. By analysing the dynamic structure factor of the edge modes and the semi-classical dynamics we show that the edge density evolves according to a Korteweg-de Vries equation; building on this insight, we quantize the model obtaining an effective chiral Luttinger liquid-like Hamiltonian, with two additional terms, which we believe captures the essential low-energy physics of the edge beyond Wen's highly successful theory. We then move forward by studying – even though only partially – some of the physics of this effective model and analyse some of its consequences.

In the sixth chapter we look at the spin properties of bulk abelian fractional quantum Hall quasiparticles, which are closely related to their anyonic statistics due to a generalized spin-statistics relation - which we prove on a planar geometry exploiting the fact that when the gauge-invariant generator of rotations is projected onto a Landau level, it fractionalizes among the quasiparticles and the edge. We then show

that the spin of Jain's composite fermion quasielectron satisfies the spin-statistics relation and is in agreement with the theory of anyons, so that it is a good anti-anyon for the Laughlin's quasihole. On the other hand, even though we find that the Laughlin's quasielectron satisfies the spin-statistics relation, it carries the wrong spin to be the anti-anyon of Laughlin's quasihole. Leveraging on this observation, we show how Laughlin's quasielectron is a non-local object which affects the system's edge and thus affecting the fractionalization of the spin.

Finally, in the seventh chapter we draw our conclusions.

Detailed outline

Part I

In the initial part we partially review the most important concepts which are required to understand the results reported in the second half of this work.

Chapter 1: we make a discursive overview of the quantum Hall physics.

Chapter 2: we begin with a review of the most basic aspects of the integer and fractional quantum Hall effects.

Chapter 3: After that, we present the wave function for the most paradigmatic quantum Hall fraction, namely the Laughlin state. We describe the gapless edge excitations and bulk gapped ones.

Chapter 4: We then recap the basic aspects of Luttinger liquids, focusing in particular on Wen's chiral Luttinger liquid model.

Part II

In this second part, we discuss the original results we have obtained for the edge and quasiparticle excitations

Chapter 5: we make use of Monte Carlo calculations to characterize the low-energy/long-wavelength behaviour of the edge excitations of Laughlin liquid droplets, confined by means of some non-harmonic potential which has the effect of producing small yet important deviations from the paradigmatic Wen's chiral Luttinger liquid behaviour. By inspecting the linear and non-linear dynamics, we write down an effective chiral Luttinger liquid-like Hamiltonian which captures the observed features, even in some regimes of hard-wall confinement. By refermionizing the model, we finally study some of its properties.

Chapter 6: we study the fractional-spin properties of bulk quasiparticles emerging in abelian fractional quantum Hall states, and how this spin quantum number is closely related to their anyonic statistics by writing down a generalized spin-statistics relation on the plane, which is ultimately due to the fact that the lowest Landau level projected gauge-invariant generator of rotations fractionalizes among the quasiparticles and the edge. We then inspect two famous quasielectron trial wavefunctions, namely Jain's – based on his composite fermion picture – and Laughlin's – which he wrote based on an analogy with his successful quasihole wavefunction. While Jain's quasielectron satisfies the spin-statistics relation and configures itself as a good anti-anyon for

the Laughlin's quasihole, Laughlin's quasielectron satisfies the spin-statistics relation but carries the wrong spin to be the anti-anyon of Laughlin's quasihole. We further explore the issues of Laughlin's quasielectron by rewriting it as a composite fermion wavefunction which uncovers its non-local nature. In particular we show how the presence of a Laughlin's quasielectron can affect the properties of the system's edge, leading to the loss of the topological robustness of its spin.

Chapter 7: we draw the conclusions by summarizing our work, briefly discuss the questions which are still opened and consider the prospects of our research.

Acknowledgements

First of all, I would like to express my deepest gratitude to my supervisor Iacopo Carusotto for his support, guidance and unconditional patience throughout these years. Without him, this whole project would have not been possible. I am also grateful for all the morning-long insightful discussions we had, and for him organizing our weekly "group meetings". I am also deeply indebted to Leonardo Mazza, for his support, help and all the countless discussions. I am also very grateful to Daniele De Bernardis and Zeno Bacciconi, for all the discussions we had. I then would like to thank all the other students and researchers in Trento I shared my time with. I am especially grateful to the persons in my office, for the great time and for being patient with my laptop's noisy fan: Francesco Piccioli, whom I also have to thank for his delicious "peposo", Daniele Contessi and Anna Berti. I also would like to give a special thank to Lennart Fernandes, for all the "notti brave". I would finally like to thank my girlfriend Elena, my friends and my family.
Thank you all for dedicating me some of your time.

CONTENTS

CHAPTER 1

INTRODUCTION

In the late 18th century, Edwin Hall discovered that a voltage difference is produced across a conductor in which some current is flowing orthogonally to an externally applied magnetic field. The effect was soon understood as a consequence of the Lorentz force acting on charges moving in the conductor, for it bends their trajectories giving rise to a transverse electric field, $V_H/I = -B/(n_{2D}q)$ where V_H is the Hall voltage, I the current flowing in the conductor, B the magnetic field, n_{2D} the number of charge carriers per unit area orthogonal to the magnetic field, and q their charge. The discovery of the effect was theoretically very important, for it allowed to test the validity of newly proposed Maxwell's ideas and to differentiate between positive or negative charges moving inside a conductor, establishing that in most metals it is electrons that carry the current; the experimental impact was not minor in any sense: still today the classical Hall effect is used to characterize electrical properties for example in semiconductor materials, and has a huge variety of applications in state-of-the-art high-precision sensing.

Almost a century later, Klaus von Klitzing was performing Hall conduction measurements with metal-oxide-semiconductor field-effect transistor (MOSFET) samples, which were effectively realizing a two-dimensional electron gas, cooled down to liquid helium temperatures and subjected to strong orthogonal magnetic fields. The remarkable discovery he made, for which he was awarded the Nobel prize, is that when the magnetic field is changed the Hall conductance does not change continuously as in the classical effect $\propto 1/B$, but in integer, discrete steps of e^2/h, with a striking accuracy. The effect is clearly quantum in its essence and was therefore

named "*integer quantum* Hall effect". Von Klitzing proposed this quantization as a new way of measuring the fine-structure constant with great accuracy, and for the very same reason the von Klitzing constant $h/e^2 \simeq 25.8\text{k}\Omega$ was used within the Internation System of Units as the standard of electrical resistance up to 2018. A satisfactory explanation for the effect came only after its discovery. The physics at the hearth of von Klitzing quantization can in its essence be understood as a single particle effect, and boils down to the single particle kinetic energy spectrum splitting into macroscopically degenerate Landau levels: whenever an integer number of Landau levels are completely occupied, the conductance is quantized precisely at the von Klitzing's value. Laughlin showed that the quantization is a result of gauge invariance whenever an energy gap for the lowest lying bulk excitations is present. The remarkable feature is that disorder and edge effects do not influence the accuracy of the quantization; on the other hand, they conspire to the make the quantized conductivity plateaus appear and become extended over a large interval of the magnetic field piercing the material. It was soon realized that robust Hall conductance quantization is also intimately related to topology; in particular it was shown how the conductance could be written as a topological invariant, the Chern number, which is an integer-valued quantity associated to the geometry of the quantum state and as such can not change continuously when the system is weakly deformed in a continuous way. An important consequence of non-trivial topology is the appearance of edge states, localized at the boundary of the system, through the so called bulk-boundary correspondence. In the quantum Hall effect, these edge modes are chiral, meaning that they can only propagate in one direction. Because of the unidirectionality of these modes, the edge currents are robust against backscattering; and this is again deeply related to the conductance quantization.

It came with great surprise when – a few years after the discovery of the integer effect – Störmer and Tsui realized that Hall conductance plateaus not only appear at integer multiples of e^2/h, but also fractional ones, corresponding to fractionally filled Landau levels. The ground state of such a state would be macroscopically degenerate, owing to the extensive degeneracy of the Landau levels, but strong interactions among the particles lift this degeneracy; at certain specific filling fractions these lead to the appearance of an energy gap for the lowest lying excitations on top of the ground state, explaining once again the quantized Hall conductivity. The emerging liquid-like macroscopic collective ground state is strongly correlated, and has been identified as a realization of new phases of matter – *topological orders* – which cannot be classified by means of broken symmetries and their associated local order parameter according to the standard paradigm of Landau theory of phase transi-

tions; rather, they are classified/characterized by new means, such the robust ground state degeneracy, the topological entanglement entropy, the presence of gapless edge excitations and, last but not least, the presence of localized quasiparticle excitations with emergent fractional charge and statistics. Indeed, the fact that particles can be categorized as being either bosons or fermions is true in three spatial dimensions, but does not stand critical scrutiny in two, where new objects – called anyons – can pop-up as emergent quasiparticles breaking the boson/fermion dichotomy. Those emerging in the "simplest" fractional quantum Hall states are abelian anyons, meaning that they pick up a $U(1)$ phase when they are exchanged, but more exotic possibilities, namely the non-abelian ones, are theorized to describe the localized bulk excitations of some particular fractional quantum Hall states whose ground state in the presence of quasiparticles is degenerate. Under such a condition an adiabatic exchange of the quasiparticle positions can cause non-trivial mixing within the ground state subspace leading to matrix-valued "exchange-phases". For this reason, these kind of anyons have attracted lots of attention when Kitaev proposed to use them to perform topologically protected fault-tolerant quantum computations.

Another key feature of quantum Hall states is the presence of robust gapless, chiral modes localized close to the system's boundary; they are usually described within the framework of the chiral Luttinger liquid theory: the basic idea behind it is simple: the system's bulk is incompressible, therefore its lowest lying modes are deformations of the liquid surface. Chirality on the other hand is caused by the presence of the strong magnetic field. Despite its simplicity, the theory is highly predictive. Most notably, the power-law (non-ohmic) behaviours in the current-voltage characteristics $I \propto V^{\alpha}$ at fractional quantum Hall constrictions (I being the current flowing through it and V the bias voltage) have been a striking prediction of Wen's theory and measurable manifestations of the strong-correlations of the system's bulk. Robust chiral edge modes are not only interesting in their own, but they have very interesting potential applications. Due to their high coherence they have been used as interferometers, a technique which was used to observe the anyonic nature of bulk excitations. Other interesting applications have been devised in the realm of topological quantum computation, most notably as a qubit readout method.

Even though mainly studied in two-dimensional electronic systems, in more recent years the possibility of exploring the physics of charged particles in a magnetic field with two-dimensional systems of neutral particles subject to some strong synthetic gauge field, both in the context of gases of ultracold atoms under synthetic magnetic fields and fluids of strongly interacting photons in nonlinear topological photonics

devices, has attracted lots of attention, to the point that many of the features of the integer quantum Hall effect have already been recovered in atomic systems as well as photonic ones. This kind of systems typically offer a wider variety of experimental tools as compared to the transport and optical probes of electronic systems, offering at the same time a clean environment in which disorder effects can be engineered rather than being intrinsic. In recent years effects of strong correlations leading to the realization of few particle Laughlin states have been observed both in atomic and photonic setups; even if still far from the thermodynamic limit of solid state devices, we believe the stage is ready for bosonic fractional quantum Hall states, as huge steps forward in the experimental preparation are constantly being made.

This strong experimental attention in conjunction with the fascinating topic of strong interparticle correlations are among the reasons that guided our theoretical interest towards the investigation of the fascinating subject of fractional quantum Hall fluids. In particular, we have directed our attention towards two crucial aspects: the linear and nonlinear dynamics of the edge excitations of fractional quantum Hall liquids, which will be the central focus of this thesis, as well as the exploration of the peculiar properties of their bulk quasiparticle excitations.

Part I
Quantum Hall Effects

CHAPTER 2

THE QUANTUM HALL EFFECT

The quantum Hall effect is probably one of the most surprising and spectacular effects in condensed-matter physics: when one confines electrons to move in a two-dimensional plane subject to a strong orthogonal magnetic field, the Hall resistivity does not vary linearly with the magnetic field – as one could expect on classical grounds – but displays a series of quantized plateaus in units of the von Klitzing constant $h/e^2 \simeq 25.8k\Omega$, regardless of sample details such as disorder or electron-electron interactions

$$R_H = \left(\frac{h}{e^2}\right) \frac{1}{\nu}.$$

In the first experiments performed by Klaus von Klitzing [1], ν was found to be an integer number with extraordinary precision, to the point that the effect was proposed as an independent way of measuring the fine structure constant. Due to the striking precision of the quantization, the effect is now known as the "integer" quantum Hall effect. A couple of years after this discovery, Daniel Tsui and collaborators [2] pointed out that resistivity plateaus not only show up when ν is an integer, but also at certain specific rational values, hence the name "fractional" quantum Hall for the effect.

Still today, more than 40 years after the discovery of these effects, strong theoretical and experimental attention is devoted to the study of these kind of systems, which inspired different research fields. For example, it was shown that the robustness of the quantization of the Hall conductance can be related to a topological invariant [3, 4] which does not change under small perturbations of the system's Hamiltonian which do not close the energy gap; these insights laid the foundations of the now-flourishing field of topological insulators [5]. The discovery of the strongly correlated

fractional quantum Hall effect led physicists to realize that symmetry alone is not enough to characterize different fractional quantum Hall states, as Landau's theory of phase transitions would suggest; rather, new forms of orders, called *topological orders*, were introduced [6, 7].

We begin this chapter by discussing the physics of the single particle electron states in a magnetic field, the so-called Landau levels, before reviewing the basic features of integer and fractional quantum Hall states. We end the chapter by discussing the new platforms in which, through the interplay of strong synthetic magnetic fields and interparticle interactions, physicists are looking for strongly correlated quantum Hall state analogues in atomic or photonic platforms.

2.1 Landau levels

In this section we briefly review the quantum mechanics of charged particles moving in a two-dimensional plane, pierced by a strong orthogonal magnetic field, a problem first solved by Landau [8]; indeed, in order to understand the physics of quantum Hall systems, one starts by building an understanding of the single particle physics.

2.1.1 Kinetic momenta

For simplicity, in the following we consider a positively charged particle carrying charge q and with some given mass m, and for simplicity neglect its spin by assuming it is polarized by the presence of the strong magnetic field. The Hamiltonian reads [9, 10]

$$H = \frac{1}{2m}(\boldsymbol{p} - q\boldsymbol{A})^2 \tag{2.1}$$

where $\boldsymbol{A}$ is the vector potential describing a uniform magnetic field $\boldsymbol{\nabla} \times \boldsymbol{A} = B\,\hat{\boldsymbol{z}}$ orthogonal to the $x-y$ plane in which the particle moves. Under a gauge transformation $\boldsymbol{A}' = \boldsymbol{A} + \boldsymbol{\nabla}\chi$, the canonical momentum transforms as $\boldsymbol{p}' = \boldsymbol{p} + q\boldsymbol{\nabla}\chi$, so it is not a gauge-invariant quantity. We can however introduce the so-called kinetic momentum $\boldsymbol{\pi} = \boldsymbol{p} - q\boldsymbol{A}$, which is a gauge invariant quantity. Its component however fail to commute due to the presence of the magnetic field

$$[\pi_x, \pi_y] = i\hbar qB = i\,\frac{\hbar^2}{l_B^2}, \tag{2.2}$$

where $l_B^2 = \hbar/qB$ is the so-called magnetic length, setting the typical length-scale of the problem. The non-commutativity (2.2) is at the heart of the quantum Hall physics; at this point one can recognize the commutation relations of Eq. (2.2) as

those of a quantum harmonic oscillator: it is indeed convenient to introduce a set of creation and annihilation operators

$$\begin{cases} a = \frac{1}{\hbar/l_B} \frac{\pi_x + i\pi_y}{\sqrt{2}} \\ a^\dagger = \frac{1}{\hbar/l_B} \frac{\pi_x - i\pi_y}{\sqrt{2}} \end{cases} \tag{2.3}$$

which satisfy the standard harmonic oscillator commutation relations $[a, a^\dagger] = 1$; the quadratic Hamiltonian (2.1) of a charged particle in a magnetic field is therefore equivalent to the one of a 1D harmonic oscillator

$$H = \hbar\omega_c \left(a^\dagger a + \frac{1}{2} \right) \tag{2.4}$$

where we introduced the cyclotron frequency $\omega_c = qB/m$ which sets the typical energy scale of the problem. The energy levels can therefore be labelled by a quantum number $n \in \mathbb{N}$,

$$E_n = \hbar\omega_c \left(n + \frac{1}{2} \right), \tag{2.5}$$

and are equally spaced by an energy gap set by the cyclotron frequency $\hbar\omega_c \propto B$. The kinetic energy in the presence of a strong magnetic field is very different from the one of a free particle, and this quantization lies at the core of the quantum Hall physics. Notice that, even though we started with a two-dimensional problem, the spectrum depends on a single quantum number: there are indeed degeneracies. These degenerate energy levels are known as Landau levels.

2.1.2 Guiding centres

To understand the degeneracies, we introduce a second pair of gauge-invariant operators, the so-called guiding centres [10, 11], which classically correspond to the centres of the cyclotron orbits

$$R_i = r_i + \frac{l_B^2}{\hbar} \epsilon_{ij} \pi_j \tag{2.6}$$

where $i = x, y$ and ϵ is the Levi-Civita tensor. Since $[\pi_i, r_j] = -i\hbar\delta_{ij}$, it is easy to show that these operators commute with the kinetic momenta

$$[R_i, \pi_j] = 0 \tag{2.7}$$

but fail to commute with each other

$$[R_x, R_y] = -il_B^2 \tag{2.8}$$

so that they define a new harmonic oscillator space orthogonal to the one defined by the kinetic momenta. Even though the guiding centres commute with the Hamiltonian Eq. (2.1), they do not commute among each other: there is therefore an Heisenberg uncertainty on the position of a quantum-mechanical guiding centre

$$\sigma_{R_x}\sigma_{R_y} \geq \frac{1}{2}\, l_B^2 \tag{2.9}$$

which can be interpreted as being the minimal surface area over which a guiding centre can be localized. Therefore one can expect that the number of states N_ϕ in a given Landau level living over a given surface area A – the Landau level degeneracy – will be of order

$$N_\phi \propto \frac{A}{l_B^2} \propto \frac{\Phi}{\phi_0} \tag{2.10}$$

where $\Phi = AB$ the magnetic flux which passes through the area A, and $\phi_0 = h/e$ the quantum of magnetic flux: the degeneracy of any given Landau level is set by the number of flux quanta threading the sample, and is therefore a macroscopic number.

Building on the commutation relations between guiding centre operators Eq. (2.8) one can introduce harmonic oscillator creation and annihilation operators

$$\begin{cases} b = \frac{1}{l_B}\frac{R_x - iR_y}{\sqrt{2}} \\ b^\dagger = \frac{1}{l_B}\frac{R_x + iR_y}{\sqrt{2}} \end{cases} \tag{2.11}$$

which satisfy the usual commutation relations $[b, b^\dagger] = 1$, while commuting with the a, $a^\dagger$ of Eq. (2.3). These operators can therefore be used to construct the eigenstates of the system as

$$|n, m\rangle = \frac{\left(b^\dagger\right)^m}{\sqrt{m!}} \frac{\left(a^\dagger\right)^n}{\sqrt{n!}} \, |0\rangle \, . \tag{2.12}$$

Finally, notice that in general a potential $V(\boldsymbol{r})$ will lift the degeneracy of the Landau levels. If V varies slowly on a length-scale set by the magnetic length and provided it does not generate significant Landau level mixing $|\boldsymbol{\nabla} V| \ll \hbar\omega_c / l_B$, one can approximate $V(\boldsymbol{r}) \approx V(\boldsymbol{R})$ and therefore the Heisenberg equations of motion

for the guiding centres become

$$i\hbar \frac{\partial R_i}{\partial t} = \frac{\partial V}{\partial R_j}[R_i, R_j] = -il_B^2 \, \epsilon_{ij} \frac{\partial V}{\partial R_j} \tag{2.13}$$

which shows that the guiding centre motion is orthogonal to the potential gradient $\boldsymbol{\nabla} V$, i.e. it occurs along equipotential lines (*Hall drift*).

2.1.3 Gauge invariant angular momentum

We conclude this section by introducing the operator $L = \mathcal{L}_R + \mathcal{L}_\pi$, where

$$\begin{cases} \mathcal{L}_\pi = -\frac{l_B^2}{2\hbar} \, \boldsymbol{\pi}^2 \\ \mathcal{L}_R = \frac{\hbar}{2l_B^2} \, \boldsymbol{R}^2. \end{cases} \tag{2.14}$$

The spectrum of L is quantized in units of $\hbar$, $\ell_{n,m} = \hbar(m-n)$ where $m, n \in \mathbb{N}$. Such a operator obeys the following set of commutation relations

$$\begin{cases} [L, \pi_i] = i\hbar \, \epsilon_{ij} \, \pi_j \\ [L, R_i] = i\hbar \, \epsilon_{ij} \, R_j. \end{cases} \tag{2.15}$$

One can therefore interpret L as the gauge-invariant generator of rotations. This definition leaves room to an ambiguity though: one could indeed add a constant to L without altering its physical meaning. Indeed any $L_c/\hbar = L/\hbar + c$, $c \in \mathbb{Z}$ has the correct commutation relations, and a spectrum which is quantized in units of $\hbar$. This is a peculiarity of $O(2)$ rotations in two-dimensional physics; $O(3)$ rotations do not leave room for such ambiguity.

2.2 Integer quantum Hall effect

In the following section we will briefly describe the integer quantum Hall effect, discovered in 1980 by Klaus von Klitzing [1] when piercing with a strong magnetic field a two-dimensional electron gas realized with metal-oxide-semiconductor field-effect transistor (MOSFET) samples developed by Michael Pepper and Gerhard Dorda. The remarkable discovery he made, for which he was awarded the Nobel prize in 1985, is that the Hall resistance of the sample does not grow linearly with the magnetic field piercing the sample, as in the classical counterpart of the effect. It instead exhibits plateaus as the magnetic field is varied, whose values are quantized

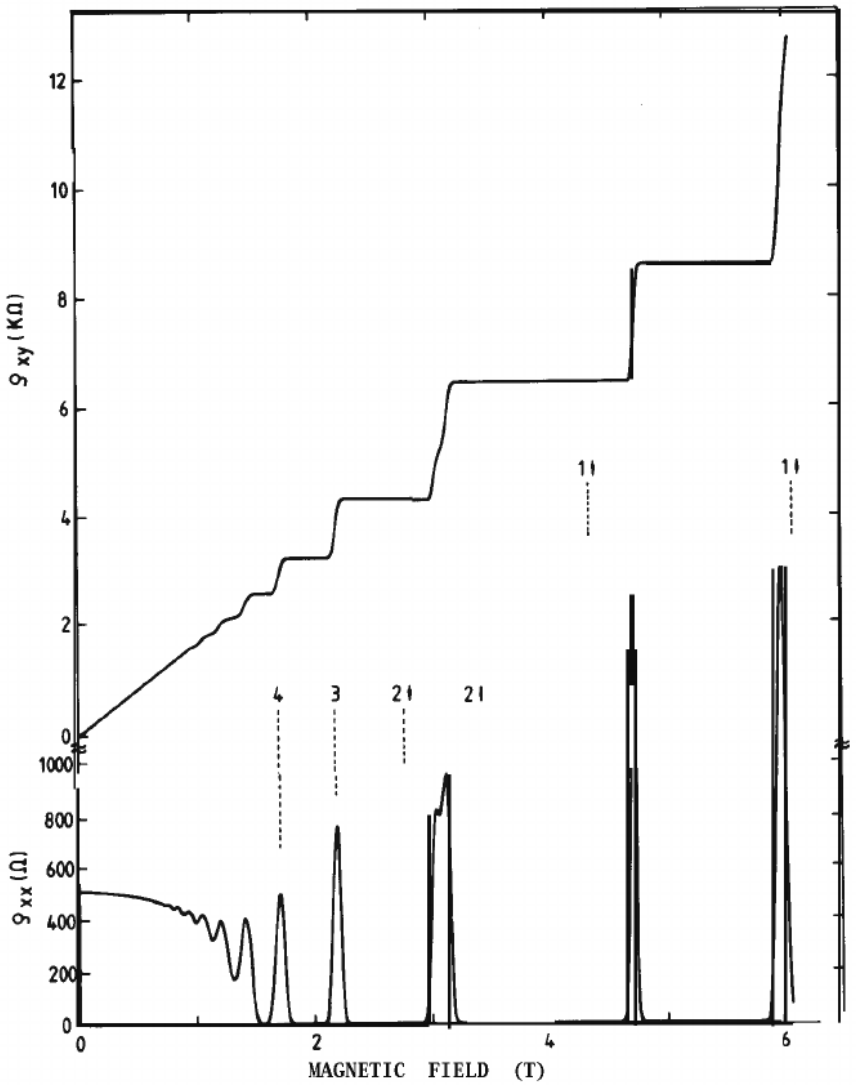

Figure 2.1: Experimental curves for the Hall resistance and longitudinal resistivity as a function of the applied magnetic field. From [12].

[Fig. 2.1] to a striking accuracy to

$$R_H = \left(\frac{h}{e^2}\right)\frac{1}{\nu} \tag{2.16}$$

in units of fundamental constants alone, regardless of the solid state system details (such as geometry, disorder, interactions...) with a strikingly small uncertainty of $\sim$ 1 part in 10^9 [13, 14]. Here ν is an integer number, hence the name of "*integer* quantum Hall effect", whose meaning we will discuss in a moment. An equally important feature of the integer quantum Hall effect is that at magnetic fields corresponding to the quantized plateaus of the transverse Hall resistance, the

longitudinal resistance becomes vanishingly small, as depicted in Fig. 2.1, exhibiting an Arrhenius behaviour $\sim \exp(-\Delta/2K_BT)$.

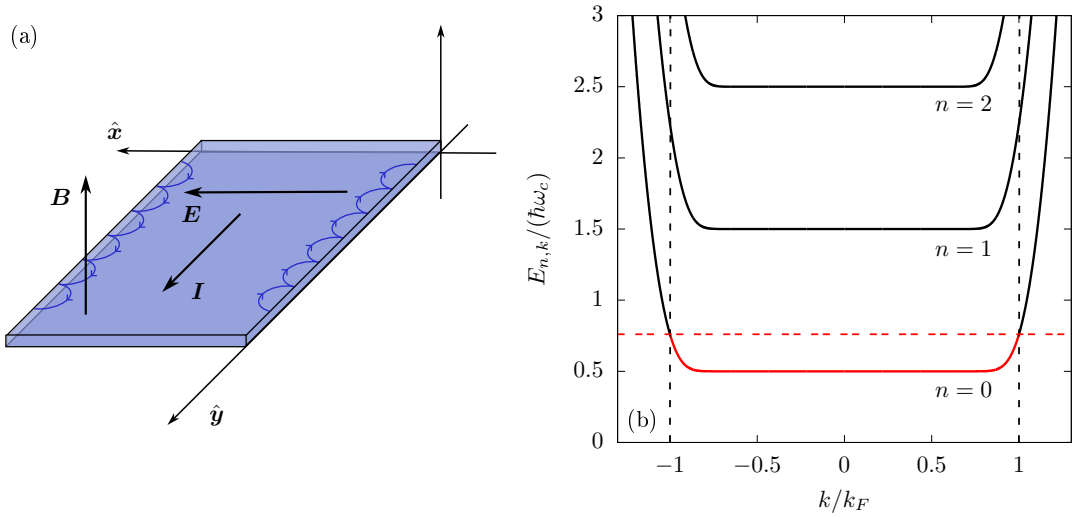

Figure 2.2: (a) Hall bar geometry: the system is confined in the transverse direction, $\hat{\boldsymbol{x}}$ and considered infinite in the longitudinal direction $\hat{\boldsymbol{y}}$. Skipping orbits are sketched (blue lines) along the system's boundary. (b) The three lowest Landau levels of Eq. (2.18) as a function of the wavevector k. An example of the lowest-Landau-level ground-state is sketched by colouring in red the occupied states below the Fermi energy (red dashed line) in the case of non-interacting particles. The corresponding Fermi points are highlighted by vertical black-dashed lines.

2.2.1 The Landau gauge

We begin this short discussion by introducing a vector potential gauge which is suited for dealing with a Hall bar geometry [Fig. 2.2(a)] which we consider to be free of any defects, infinite along the $\hat{\boldsymbol{y}}$ direction and confined along $\hat{\boldsymbol{x}}$ by some translationally-invariant confinement potential $V(x)$ which we consider to be vanishingly small in the bulk. An obvious choice is a gauge preserving translational invariance along the $\hat{\boldsymbol{y}}$ direction

$$\boldsymbol{A} = Bx\,\hat{\boldsymbol{y}} \tag{2.17}$$

called the Landau gauge. Due to translational invariance along $\hat{\boldsymbol{y}}$ the eigenstates are separable $\psi \propto \Phi_{n,k}(x)e^{iky}$. If using periodic boundary conditions along y, k is quantized in units of $2\pi/L_y$. Plugging this ansatz into the single electron Schrödinger equation gives

$$H_k\Phi_{n,k} = \left(\frac{p_x^2}{2m} + \frac{(\hbar k - qBx)^2}{2m} + V(x)\right)\Phi_{n,k} = E_n\Phi_{n,k} \tag{2.18}$$

which, in the bulk region, is a shifted harmonic one-dimensional oscillator Hamiltonian reproducing the expected spectrum Eq. (2.5) and the eigenstates are strongly localized in a stripe at $x/l_B \simeq k l_B$

$$\Phi_{n,k}(x) \propto H_n(x/l_B - k\, l_B) \exp\left[-\frac{(x/l_B - k\, l_B)^2}{2}\right]. \tag{2.19}$$

Close to the boundary, the strong confinement energy lifts the Landau level degeneracy, as can be seen in Fig. 2.2(b), effectively mixing the Landau levels.

2.2.2 A simple explanation of the effect

The very basic physics of the integer quantum Hall effect can be understood by considering completely filled Landau levels of non-interacting fermions in the strip geometry just described (see Fig. 2.2(a,b)), additionally subjected to a transverse electric field $E\hat{\boldsymbol{x}}$ which contributes the Hamiltonian of Eq. (2.18) a term $-qEx$ that will induce a purely transverse Hall current in the system [9, 11]

$$I_y = \frac{1}{L_y}\frac{q}{m}\sum_{\alpha} \langle \pi_y \rangle_{\alpha} \tag{2.20}$$

where L_y is the length of the sample along which the current is flowing, while α is an index that runs over all the occupied system eigenstates in the presence of the electric field, and occupied according to Pauli exclusion principle. On an eigenstate the expectation value of the kinetic momentum along the $\hat{\boldsymbol{y}}$ direction can be written as

$$\langle \pi_y \rangle_{n,k} = \frac{m}{\hbar}\, \langle \partial_k H_k \rangle_{n,k} = \frac{m}{\hbar}\, \frac{\partial E_{n,k}}{\partial k} \tag{2.21}$$

and therefore the current [Eq. (2.20)]

$$I_y = \frac{1}{L_y}\, \frac{q}{\hbar} \sum_n \int \frac{L_y\, dk}{2\pi}\, \frac{\partial E_{n,k}}{\partial k} = \frac{q}{h} \sum_n \left(E_{n,k_{\max}} - E_{n,k_{\min}}\right) \tag{2.22}$$

depends on the chemical potential difference between the two edges $E_{n,k_{\max}} - E_{n,k_{\min}} = q\Delta V$, which can be identified with the Hall voltage measured between the lower and upper edge. As a consequence, the Hall conductance

$$\sigma_H = \frac{I_y}{\Delta V} = \frac{q^2}{h}\, \nu \tag{2.23}$$

is quantized in units of q^2/h, where $\nu = N/N_\phi$ is the number of completely filled Landau levels.

Since the Landau levels are completely filled, in order to create bulk excitations which can contribute to transport one needs to overcome an energy gap of the order of the cyclotron splitting $\sim \hbar\omega_c$. Therefore, the longitudinal resistance will be exponentially suppressed at low energies, explaining the observed Arrhennius behaviour. This also means that the bulk is incompressible whenever an integer number of Landau levels is completely filled, meaning that all the excitations which change the density are gapped. Taking into account the vanishing longitudinal resistance one sees that the conductance result Eq. (2.23) is in agreement with the Hall resistance measurements performed by von Klitzing Eq. (2.16).

Two crucial aspects are still missing, though. Edge states and disorder.

2.2.3 Edge states

A crucial aspect for the explanation of the integer quantum Hall effect are its edge states. In a "clean" bulk the electrons undergo (classically) closed cyclotron orbits with no net transport. Close to the edge however something different can happen due to the interplay of the cyclotron motion and elastic reflection from the sharp confinement. The competition between the two results in the particles performing so called *skipping-orbit* trajectories [Fig. 2.2(a)]. The effect is that electrons can propagate in a chiral way along all the one-dimensional boundary without being back-reflected [9, 10]. The same kind of physics occurs when the the confining potential is smooth; close to the system's edge this potential induces according to Eq. (2.13) a motion of the guiding centres with a velocity which is proportional to the gradient of the confinement

$$v = \frac{E}{B}, \tag{2.24}$$

so that electrons on opposite sides of the samples move in opposite directions, but modes at each side are separately chiral; moreover, the direction (or chirality) is the same for every occupied Landau level. These features imply the robustness of the edge modes: in order to backscatter an electron, it needs to cross the entire sample; since the sample width is macroscopically large, much larger than the magnetic wavelength, such a scattering event is exponentially suppressed.

Finally, notice that in a non-interacting integer quantum Hall system all single-particle states below the chemical potential are occupied so all bulk excitations are gapped with a gap set by the cyclotron energy. However, as can be seen in Fig.2.2(b) and Fig.2.3, low-energy particle-hole excitations are strongly localized at the system's boundary, and are gapless with an approximatively linear dispersion relation with a velocity set by Eq.(2.24). They form a chiral one-dimensional Fermi

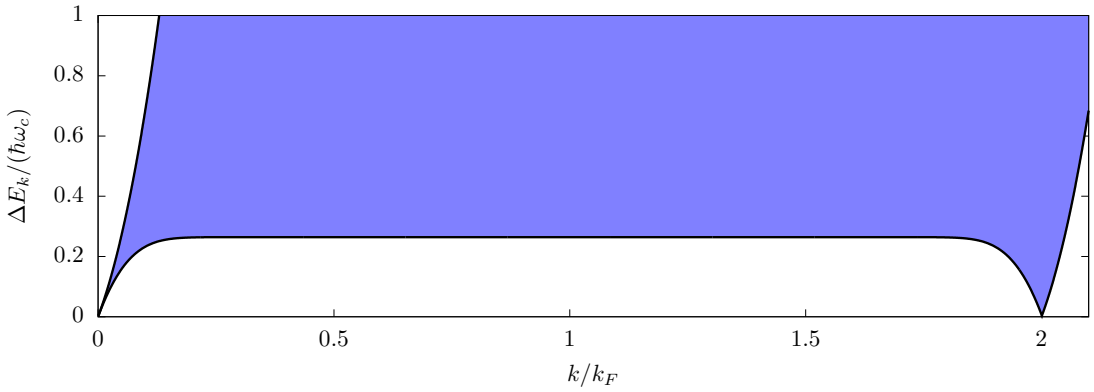

Figure 2.3: Spectrum of the positive-k single particle-hole excitations on top of the ground-state sketched in Fig. 2.2(a).

liquid, as we will more extensively discuss in Chapter 4. The important thing we wish to point out at this stage is that integer quantum Hall systems constitute a rather unusual electron liquid, with an insulating bulk and a perfectly conducting metallic edge; these same features are observed in the fractional quantum Hall case, even though more interesting things occur in this latter case.

2.2.4 The role of disorder

In the previous discussion, inherent disorder of solid state devices has been neglected. It however turns out that it plays a very important role in making the quantum Hall plateaus of Fig.2.1 extended over a wide range of magnetic fields [11, 9, 10].

This fact can qualitatively be understood on semi-classical grounds. From Eq. (2.13), since the cyclotron orbit guiding centre follows an equipotential line, it can be seen that disorder can turn many of the extended system eigenstates [Eq. (2.19)] into localized ones. These localized states can then act as a reservoir of states and, even as the magnetic field is changed and the filling fraction deviates from the ideal value N/N_ϕ, the Hall conductance does not because localized states do not contribute to transport properties. Why however the Hall conductance retains its universal value Eq. (2.23) is not obvious at all, since all the states which have localized in the presence of the disorder do not contribute to the current. It remarkably turns out that the current carried by the extended states increases by the correct amount so as to compensate for the decreased number of extended states. This was shown by a beautiful argument due to Laughlin [15] and then generalized by Halperin [16] to the presence of modest disorder in the bulk region, relying solely on gauge-invariance and on the presence of an energy gap for bulk excitations.

An alternative approach relying on the Landauer-Büttiker formalism [17] shows that the integer quantum Hall effect is the result of a complete suppression of the backscattering of the edge modes, owing to their spatial separation [10, 18]. For example, a recent experiment [19] following the theoretical proposal [20] showed that intra-edge scattering induced by cavity-enhanced vacuum-fluctuations leads to a breakdown of the protection of the Hall conductivity robust quantization.

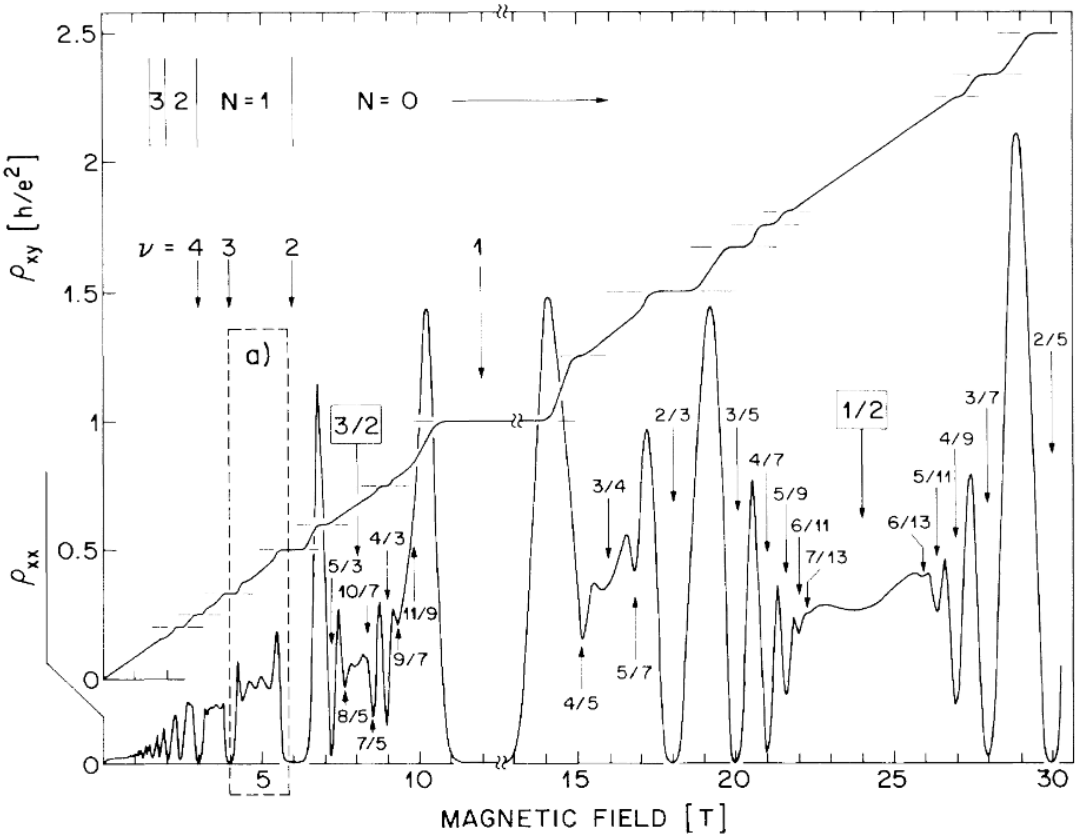

Figure 2.4: Experimental curves for the Hall resistance and longitudinal resistivity as a function of the applied magnetic field. From [21].

2.3 Fractional quantum Hall effect

A couple of years after the discovery of the integer quantum Hall effect, Daniel Tsui, Horst Störmer and Arthur Gossard were performing transport studies at low temperatures in new high-mobility two-dimensional electron gases in GaAs-AlGaAs heterojunctions subject to very strong orthogonal magnetic field, to the extent that only a fraction of the levels in the spin-polarized lowest Landau level was occupied. They discovered [2] the same phenomenology of the integer quantum Hall effect

(see Fig. 2.4) at $\nu = 1/3$ (hence the name *fractional*), namely a perfectly quantized transverse resistance plateau at

$$R_H = \left(\frac{h}{e^2}\right)\frac{1}{\nu} \tag{2.25}$$

extended over a region of magnetic fields, and an exponentially suppressed longitudinal resistance. After the discovery, for which Tsui and Stormer were awarded together with Robert Laughlin the Nobel prize in 1998, many more plateaus at fractional fillings have been observed [22, 21].

It is easy to understand that interactions among the electrons must be playing a crucial role in the appearance of plateaus at rational filling ν. As we discussed in the previous sections Sec. 2.2, in the integer quantum Hall effect there is a unique gapped Fermi-liquid-like ground state when ν Landau levels are completely filled. On the other hand, in the case of partially filled Landau levels the situation is completely different [9], for each Landau level has a macroscopic degeneracy $N_\phi = \Phi/\phi_0$. Suppose $\nu < 1$ for simplicity. Then, the number of ways $N = \nu N_\phi$ electrons can fill the N_ϕ degenerate levels making up an ideal Landau level is $\binom{N_\phi}{\nu N_\phi}$, a number exponentially large in the size of the system.

Strong enough inter-particle interactions will in general lift the degeneracy; in particular, if for some reason at some peculiar filling fraction ν they were to lead to a gapped system, then weak disorder would produce a plateau in the transverse resistance as the one observed [Eq. (2.25)] via the same mechanisms at play in the integer quantum Hall effect, and an Arrhennius-like behaviour of the longitudinal one. For this discussion to make sense, a hierarchy between the cyclotron, interaction and disorder energy-scales must emerge

$$\hbar\omega_c \gg V_{\text{interactions}} \gg V_{\text{disorder}} \tag{2.26}$$

which, at least qualitatively, explains why the fractional quantum Hall plateaus are observed only in high mobility samples, but the effect is otherwise insensitive to the microscopic fabrication details.

Under such an assumption, the kinetic energy is completely determined by the Landau level filling; the role of interaction is to break the degeneracy of the partially filled Landau level. The striking consequence is that fractional quantum Hall states are *strongly* correlated quantum-liquid-like states of matter whose essential features are solely determined by the exchange statistics and quantum fluctuations that minimize the repulsion between particles. It is thus intuitive to understand that

any perturbative treatment is doomed to fail. A well-educated guess for the ground state wavefunction [23] has indeed been what lead to a deeper understanding of the effect, as we will briefly review in the next chapter.

To conclude, we would like to mention that fractional quantum Hall liquids at different filling fractions ν turn out to be examples of a whole new class of phases of matter, so-called *topological orders* [24, 7, 6], which cannot be characterized by the breaking of any symmetry and therefore cannot be described by Landau's theory of phase transitions [25]. Rather, they are characterized by new quantum numbers such as the robust ground state degeneracy [26, 27] which depends solely on the topology of space over which the correlated quantum state is defined, the presence of one-dimensional gapless chiral edge excitations [28, 26, 29, 30, 31, 32], the long-range entanglement leading to the topological entanglement entropy[33, 34], and, last but not least, the presence of localized bulk excitations carrying a fractional charge [23] and exhibiting fractional exchange statistics, both Abelian [35] and, even more interestingly, non-Abelian [36, 37], which make fractional quantum Hall states a promising platform in which to perform topologically-protected quantum computations [38, 39].

2.4 Quantum Hall states of atoms and photons

As we already mentioned, quantum Hall states have first been discovered in two-dimensional systems of electrons subjected to strong magnetic fields; Even today, the study of quantum Hall physics through solid-state devices remains a highly active and productive field of research which in recent years achieved important milestone results; just to name a few, thermal conductance measurements [40] among which even the one of the non-abelian $\nu = 5/2$ edge [41]; the anyon-like braiding statistics of the quasiparticles of a $\nu = 1/3$ fractional quantum Hall states both through edge interferometry [42] and anyon collisions [43], which very recently have been used to the study of Abelian $\nu = 2/5$ states [44, 45]; and the space-time imaging of $\nu = 1/3$ edge modes [46].

The possibility of realizing analogous states using synthetic quantum matter systems, such as gases of ultracold neutral atoms [47, 48] and fluids of strongly interacting photons in non-linear topological photonics devices [49, 50, 51] – which hold the potential for exploiting their internal degrees of freedoms as new effective "synthetic" dimensions [52] – would however offer novel ways to explore quantum Hall physics. Even though synthetic matter platforms are technically challenging to setup, especially if the goal is to reach the strongly correlated regime, strong

experimental as well as theoretical attention is currently devoted to the simulation of quantum matter [53] using these new systems, as they hold the great potential of exploring different and/or new aspects of the relevant physics due to the high flexibility and control of the underlying Hamiltonian (both the confinement and interactions), the long coherence times and the great variety of diagnostic tools which complement the standard transport and optical probes traditionally used in solid state devices. For example, while directly accessing the Hall conductance through standard transport measurements would be extremely challenging in synthetic matter setups, alternative probing schemes for detecting topological phases have been proposed. Viable information can indeed be gained by means of an arsenal of different methods, such as the detection of edge excitations [54, 55, 56, 57, 58, 59, 60], by means of spectroscopic probes [61, 62, 63, 64, 65], the characterization of the centre-of-mass response [66, 67], density-density correlations [68] or the observation of the flat-density profiles characteristic of incompressible states [69, 70, 71], the analysis of the semiclassical dynamics of wavepackets [72], or by probing the anyonic nature of gapped bulk excitations [73, 74, 75], as well as studying how they get bound to mobile impurities [76, 77, 78, 79] and a plethora of different other techniques.

An immediate question comes however to mind: the key ingredients for fractional quantum Hall physics are the strong magnetic field, leading to Landau levels, and strong inter-particle interaction. While the latter are, at least conceptually, simple and in the atomic context can be made strong by means of Feshbach resonances [80], a neutral particle is not affected by a standard magnetic field in the way a charged one is. How can one engineer a "magnetic field for neutral particles"? It was realized that the effect of a magnetic field on the lines of Eq. (2.1) can be mimicked in a variety of different ways by the introduction of so-called synthetic gauge fields [81, 82, 83, 84, 85]. In the following, we will briefly discuss some of the most prominent examples in atomic and photonic platforms.

2.4.1 Ultracold atoms in rapid rotation and optical lattices

One of the first strategies to be developed [81, 82] was based on the mathematical similarity between the Coriolis force felt by a particle of mass m moving at velocity $\boldsymbol{v}$ in a frame rotating at angular velocity Ω, $\boldsymbol{F} = 2m\boldsymbol{v} \times \boldsymbol{\Omega}$, and the Lorentz force felt by a moving charge q in a magnetic field $\boldsymbol{B}$, $\boldsymbol{F} = q\boldsymbol{v} \times \boldsymbol{B}$; this leads to the identification $q\boldsymbol{B} = 2m\boldsymbol{\Omega}$. More formally, in the rotating frame the Hamiltonian for

a single particle in a harmonic trap of frequency ω becomes

$$H_\Omega = H - \boldsymbol{\Omega}\cdot\boldsymbol{L} = \frac{(\boldsymbol{p} - m\boldsymbol{\Omega}\times\boldsymbol{r})^2}{2m} + \frac{1}{2}m\left(\omega^2 - \Omega^2\right)\boldsymbol{r}^2 \tag{2.27}$$

where $\boldsymbol{\Omega} = \Omega\hat{\boldsymbol{z}}$ is the rotation frequency and $\boldsymbol{r}$, $\boldsymbol{p}$ are canonically conjugated variables in the plane orthogonal to the rotation axis $\hat{\boldsymbol{z}}$; the effect of the Coriolis force is formally equivalent to that of the Lorentz force appearing in Eq. (2.1), and can thus be seen as an effective uniform magnetic field $q\boldsymbol{A} = m\boldsymbol{\Omega}\times\boldsymbol{r}$, in agreement with the qualitative discussion above; a centrifugal potential term $\propto -\Omega^2\boldsymbol{r}^2$ is however seen to appear, which has the effect of weakening the harmonic confinement. Close enough to the centrifugal limit $\Omega \simeq \omega$, the residual confinement becomes irrelevant and we are left with the physics of almost degenerate Landau levels.

Over the years, rotation has been heavily investigated in atomic Bose-Einstein condensates, where it led to pioneering advances; at low rotation frequencies, vortices start to appear [86] owing to their superfluid nature; as the rotation rate increases, a triangular vortex lattice which breaks the rotational invariance of the underlying Hamiltonian is formed [87] which, in the rapid rotation regime, starts occupying the lowest Landau level [88, 89]; in recent years, Bose-Einstein condensation entirely within the lowest Landau level has been reported [90, 91]. For even large values of Ω, the Hamiltonian Eq. (2.27) becomes formally equivalent to the one of a charged particle in a magnetic field. Interesting things are expected to occur in such a regime, which is equivalent to the number of vortices N_v becoming of the order of the number of particles N [81, 82]. There, the superfluid vortex lattice is expected to "melt" due to quantum fluctuations of the vortex lines [92, 81] giving space, through a quantum phase transition, to rotationally-symmetric incompressible strongly correlated "vortex liquids" which realize bosonic analogues of the fractional quantum Hall phases, which do not have Bose-Einstein condensation or superfluidity. Supported by the fact that the exact two-dimensional ground state for bosons at the centrifugal limit has a correlated form [93], numerical studies found compelling numerical evidence for a quantum phase transition from a vortex lattice to a strongly correlated phase [94] and for the presence of many bosonic analogues of well-studied fractional quantum Hall states in the fast rotation regime of the Bose gas, both Abelian and non-Abelian [95, 96, 97, 98, 99].

Early experiments [100] following adiabatic preparation with rotating microtraps [101] reported hints of correlated fractional quantum Hall dynamics, even though the very small sizes of the atomic samples did not allow to completely and unambiguously characterize the Laughlin nature of the claimed state. At present, there is a strong

theoretical effort to develop realistic experimental protocols that can yield to the realization of strongly correlated phases [102, 103, 104].

We would then like to mention that synthetic magnetic fields can be generated in continuous spatial geometries by coherently dressing the atoms with suitably designed electric and magnetic fields [83, 84], effectively reproducing geometric phases for neutral particles; these techniques have been successfully used for example to nucleate vortices [105], to measure transverse Hall-like response [106] and observe spin Hall effect [107]; The related concept of optical flux lattices [108, 109] has been shown numerically to have the potential of hosting exotic fractional quantum Hall states [110]. However, even though these approaches eliminate some of the difficulties encountered in the fast-rotation regime of an atomic cloud, one has to face spurious heating of the atomic cloud by spontaneous emission.

Finally, we want to briefly discuss the quantum Hall physics in lattice geometries and how synthetic magnetic fields can be engineered in these setups. After the discovery of the integer quantum Hall effect, physicists started to investigate the interplay between lattice and magnetic field physics; when the magnetic length is much larger than the underlying lattice spacing the underlying lattice structure can be safely neglected, leading to the already discussed physics; the interplay between the two length-scales however leads to interesting consequences. It was shown that the energy spectrum becomes an intricate fractal structure, the so-called Hofstadter butterfly [111], and the Hall conductance is, whenever the chemical potential lies in a gap of the spectrum, related to a topological invariant associated with the filled bands, the (first) Chern number, which does not change under smooth deformations of the system's Hamiltonian unless the energy gap is closed [3].

Owing to the high-degree of their tunability, atomic platforms have proved themselves to be a valuable platform in which to observe the effects of the interplay between the lattice and a magnetic field [112, 113, 114], which can be generated by making a particle that loops around a lattice-plaquette acquire a non-trivial Berry phase [115] analogous to the Aharonov-Bohm phase [116] a charged particle acquires when moving in a magnetic field. Such a phase can be engineered by introducing non-trivial complex hopping phases, for example by means of laser-assisted-tunneling [117, 118, 119, 120], by lattice-shaking protocols [121, 122] or by lattice rotation [123, 124, 125]. These methods have been first implemented to realize an atomic Harper-Hofstadter model [119, 126], but numerous theoretical and numerical studies have shown that they hold great promise towards the realization of strongly correlated phases as well [122, 127, 61, 128, 129, 66] which can be reached through suitable protocols [130, 131, 132, 133]; recently experimental ad-

vances led to the observation of correlated two-particle dynamics [134] and to the claim of the first realization of a fractional quantum Hall state with ultracold atoms in an optical lattice [135]. Effects of strong interactions in a synthetic two-leg ladder whose plaquettes are threaded by synthetic magnetic flux have also been recently reported [136].

A final important point we would like to stress is that a magnetic field is not strictly necessary to exhibit integer quantized Hall conductance; Haldane [137] exhibited a non-interacting model for an honeycomb lattice with complex hoppings breaking time-reversal symmetry but with zero average magnetic field in which the bands have non-zero Chern number and thus can show quantized Hall response whenever a topological band is completely filled. Haldane's model has been realized with neutral atoms in a shaken optical lattice [138]. Physicists started to look for strongly correlated liquid phases as well, occurring when a topological Chern band is partially filled; it turns out that such a possibility exists [139, 140, 141, 142] provided the interaction is strong enough when compared to the bandwidth (so that the ground state is not dominated by kinetic-energy effects), but smaller than the band-gap (so that the band topology is safely preserved); luckily, the bandwidth can, at least theoretically, be reduced by introducing next-nearest-neighbour hopping [143]. Compelling numerical evidence [144] demonstrated that the these states are indeed the "Haldane" lattice analogue of fractional quantum Hall states, hence named fractional Chern insulators.

2.4.2 Optical systems

Optical setups constitute a different prominent platform for performing quantum simulations [49, 50, 51]. Even though massless and to any practical extent non-interacting in vacuum, photons can be given an effective mass through suitable spatial confinement and can be endowed with non-negligible interactions by mediating them through suitable $\chi^{(3)}$ non-linear materials.

Synthetic gauge fields for photons can be, analogously to the atomic counterpart, generated in a variety of ways. The first theoretical proposal [145, 146] built on the idea of breaking time-reversal symmetry by means of suitably engineered metamaterials; the idea was soon implemented in the laboratory [147] leading to the observation of robust, chirally propagating edge modes analogous to the ones which are present in the integer quantum Hall effect. Many other proposals for the realization of synthetic gauge fields in lattice geometries however popped up in the following years, among which one can list coupled helical waveguides in propagating

geometries [148], or the very-promising cavity- and circuit-QED systems [149, 150]. On the other hand, synthetic magnetic fields in continuous geometries have been proposed based on the analogy between the Lorentz and Coriolis forces, for example in a cavity with spherical mirrors [151, 152] and then in twisted optical ring resonators, where they have been successfully implemented, leading to the first experimental realization of synthetic photonic Landau levels [153] on an effective conical geometry. This shows the potential of these new platforms, as it can lead to new physics which can hardly be explored in solid state devices.

Physicists soon started to look for the possibility of realizing strong photon-photon interactions in order to achieve strongly correlated phases such as the Mott insulator state in the Bose-Hubbard model [154, 155], Tonks-Girardeau gases [156] and fractional quantum Hall states of light [157, 158, 159, 160, 161, 162]. A particularly effective way of realizing strong interactions is based on the photon-blockade mechanism, which can for example be realized by exploiting the hybridization of light with strongly interacting Rydberg atoms; the effect has been realized experimentally in a non-planar cavity [163] and subsequently successfully combined with a synthetic magnetic field [153] to realize the first two-photon Laughlin state [164]. Strong correlations have been reported in circuit-QED systems as well [165, 166], which could in the near future lead to realize strongly correlated fractional quantum Hall states in these devices.

In conclusion, several experimental platforms have been proposed and examined to simulate strongly correlated phases of matter, especially fractional quantum Hall physics with neutral particles. In recent years, numerous promising experimental findings have been reported in this exciting area and we believe that many more fascinating results will emerge in the coming years.

CHAPTER 3

THE LAUGHLIN STATE

In Chapter 2 we mentioned that fractional quantum Hall liquids are peculiar strongly correlated two-dimensional matter systems; perturbative analysis are doomed to failure: since the kinetic energy is completely determined by the Landau level filling, inter-particle interaction is the most important energy scale. Numerical simulations are also hard, because of the macroscopically large Hilbert space dimension: in principle, one needs to consider all the many-particle degenerate ground states of a partially filled Landau level over which the interaction energy needs then to be diagonalized.

Despite all these difficulties, Laughlin's insight [23] was to simply guess the correct wavefunction for the incompressible fractional quantum Hall liquid at filling $\nu = 1/m$, where m is an odd integer due to the fermionic nature of the constituent particles. Starting with his seminal work, theorists have managed to describe the properties of many fractional quantum Hall states by well-educated guesses of the system's wavefunction [36, 37, 167, 168, 10]. For his insight, Laughlin was awarded the Nobel prize in 1998.

In the following chapter we briefly review the main properties of the Laughlin state, including those of its edge and quasihole/quasielectron excitations.

3.1 The Laughlin state

Even though the Laughlin state has been written in the Landau gauge [169] as well with periodic boundary conditions [170] or on a sphere [171], the simplest by far is the symmetric (also called circular) gauge, suitable for a droplet geometry [23]. We

therefore begin by briefly reviewing the circular gauge; after that, we discuss the Laughlin state and its edge and bulk charged excitations.

3.1.1 Circular gauge

In the symmetric gauge the vector potential is written as

$$\boldsymbol{A} = \frac{1}{2}\,\boldsymbol{B} \times \boldsymbol{r}. \tag{3.1}$$

Such a convention apparently breaks translational symmetry in both the $\hat{\boldsymbol{x}}$ and the $\hat{\boldsymbol{y}}$ directions, but preserves rotational symmetry with respect to the chosen origin. The wave functions obtained in this gauge represent, because of their simplicity, a key ingredient to describe the fractional quantum Hall effect. In particular we focus our attention on the lowest Landau level wave functions, which satisfy $a\,|0,m\rangle = 0$. This relation can be conveniently rewritten as a differential equation using Eq. (2.3)

$$-\,i\,\frac{l_B\,(\partial_x + i\partial_y) + \frac{1}{2l_B}(x+iy)}{\sqrt{2}}\,\phi_{n=0,m} = -i\,\sqrt{2}\,\left(l_B\partial_{z^*} + \frac{z}{4l_B}\right)\phi_{n=0,m} = 0 \tag{3.2}$$

where the complex coordinates $z = x + iy$ and $z^* = x - iy$ have been introduced; the derivative operators with respect to z and z^* read $\partial_z = \frac{1}{2}\,(\partial_x - i\partial_y)$ and $\partial_{z^*} = \frac{1}{2}\,(\partial_x + i\partial_y)$. The general solution to this equation reads

$$\phi_{n=0,m}(z,z^*) = f_m(z)\,\exp\left(-\frac{zz^*}{4l_B^2}\right), \tag{3.3}$$

namely it is given by an arbitrary function $f_m(z)$ which depends only on the holomorphic coordinate z and not on the anti-holomorphic one, z^*, times a circularly symmetric Gaussian factor.

In this particular gauge, the guiding centre creation and annihilation operators read

$$\begin{cases} b = \sqrt{2}\left(-l_B\partial_z - \frac{z^*}{4l_B}\right) \\ b^\dagger = \sqrt{2}\left(l_B\partial_{z^*} - \frac{z}{4l_B}\right). \end{cases} \tag{3.4}$$

Requiring that $|0,0\rangle$ is annihilated not only by a but by b as well, and that such a state is normalized, one obtains that $f_{m=0} = 1/\sqrt{2\pi\,l_B^2}$; the generic $|0,m\rangle$ state is then built by iteratively applying $b^\dagger$. The result, apart for an irrelevant phase factor, is

$$\phi_{n=0,m} = \frac{1}{\sqrt{2\pi\,l_B^2 m!}}\left(\frac{z}{\sqrt{2}l_B}\right)^m \exp\left(-\frac{zz^*}{4l_B^2}\right). \tag{3.5}$$

These wavefunctions as expected are cylindrically symmetric and are peaked at a ring of radius $r_0 = \sqrt{2m} l_B$, making them, as anticipated, the most natural choice for dealing with droplets of quantum Hall liquid. Notice that the flux through the area enclosed by this ring is $(\pi r_0^2)B = m\phi_0$: it contains exactly m magnetic flux quanta.

Finally, notice that these eigenfunctions are also eigenfunctions of the gauge invariant angular momentum operator $L = \mathcal{L}_R + \mathcal{L}_\pi$; in particular, since $n = 0$ (lowest Landau level) $\mathcal{L}_\pi |0, m\rangle = -\hbar/2$, while $\mathcal{L}_R |0, m\rangle = \hbar(m + 1/2)$ so

$$L |0, m\rangle = \hbar m |0, m\rangle . \tag{3.6}$$

The quantum number m can thus be interpreted as an angular momentum eigenvalue. More explicitly, the angular momentum operator can be written as

$$L = \hbar(z \partial_z - z^* \partial_{z^*}) \tag{3.7}$$

and it is easy to check that the wavefunctions Eq. (3.5) indeed satisfy Eq. (3.6).

3.1.2 Laughlin's ansatz

When the particles are restricted to the lowest Landau level, the kinetic energy becomes an inessential constant. The simplest Hamiltonian capturing all the essential physics of fractional quantum Hall liquids can therefore be written as

$$H = P_{LLL} \left(\sum_{i<j} V(\mathbf{r}_i - \mathbf{r}_j) \right) P_{LLL} \tag{3.8}$$

where P_{LLL} is a lowest Landau level projector [10] which reminds us that the otherwise classical interaction-only problem [Eq. (3.8)] needs to be solved with a lowest Landau level restriction, which turns it into a genuinely highly non-trivial quantum mechanical problem, where interaction is not just a small perturbation.

Laughlin's brilliant contribution [23] was – instead of attacking the problem trying to diagonalize Eq. (3.8) – to write down the answer, a wavefunction, based on few physical observations.

- Since one considers only a partially filled lowest Landau level, the single particle states which comprise the many-body state are of the form of Eq. (3.5).

The system ground state wavefunction will thus have the following structure

$$\Psi(\boldsymbol{r}_1, \ldots, \boldsymbol{r}_N) = F(z_1, \ldots, z_N) \exp\left(-\sum_i \frac{|z_i|^2}{4l_B^2}\right), \tag{3.9}$$

namely it must be constructed out of an holomorphic polynomial function $F(z_1, \ldots, z_N)$ times a Gaussian factor for each particle.

- Fractional quantum Hall states are incompressible; the ground state wavefunction must not break any continuous spatial symmetry and have an energy gap; if a continuous spatial symmetry was indeed broken (e.g. in a Wigner crystal) long-wavelength gapless Goldstone modes (acoustic phonon modes of the crystal) would appear in the spectrum, making the system compressible.
- Since the Hamiltonian is rotationally invariant, we expect the ground state wavefunction to be itself rotationally invariant and thus be an eigenstate of the angular momentum operator. Since such operator Eq. (3.7) counts the powers of z, the polynomial part of the wavefunction must be of homogeneous degree.
- The number of fluxes piercing the system's area should equal $N_\phi = N/\nu$. Since the radius of the quantum Hall droplet is set by the highest occupied single particle state $m_{\max}$, which encloses exactly $m_{\max}$ flux quanta, the largest power of any coordinate z_k appearing in the polynomial $F(z_1, \ldots, z_N)$ should be (in the thermodynamic limit) $m_{\max} = N/\nu$.
- The wavefunction should be fully (anti/)symmetric for (Fermi/)Bose statistics of the constituent particles.

The (un-normalized) variational wavefunction Laughlin proposed satisfies all the previous requirements

$$\Psi(\boldsymbol{r}_1, \ldots, \boldsymbol{r}_N) = \prod_{i<j} (z_i - z_j)^m \exp\left(-\sum_i \frac{|z_i|^2}{4l_B^2}\right) \tag{3.10}$$

provided m is an (odd/)even integer to satisfy the constraints of (Fermi/)Bose statistics.

The maximum power of any given coordinate z_k is $N_\phi = m(N-1)$, and thus yields the filling fractions

$$\nu = N/N_\phi \to \frac{1}{m}. \tag{3.11}$$

It is worth noting that when $m = 1$ the Laughlin wavefunction corresponds to a non-interacting Fermi-liquid-like ground state; namely, the Laughlin wavefunction

coincides with a single Slater determinant (a so-called Vandermonde determinant) with all the orbitals from $m = 0$ up to $m = N_\phi = N - 1$ completely occupied

$$\Psi(\boldsymbol{r}_1, \ldots, \boldsymbol{r}_N) = \det \begin{pmatrix} 1 & 1 & \ldots & 1 \\ z_1 & z_2 & \ldots & z_N \\ \vdots & \vdots & & \vdots \\ z_1^{N-1} & z_2^{N-1} & \ldots & z_N^{N-1} \end{pmatrix} = \prod_{i<j} (z_i - z_j), \tag{3.12}$$

where the exponential factors have been omitted.

To wrap things up, let us emphasize that Laughlin's wavefunction is not based on a mathematical derivation, and does not describe the exact ground state for standard fractional quantum Hall states observed in two-dimensional electronic systems; nonetheless, it turns out to be a particularly good wavefunction even for realistic systems – with overlaps greater than 99%. This occurs because as two particles approach each other the wavefunction vanishes as m powers, and therefore the probability of having two particles close to each other is extremely low. As a consequence, also the interaction (and its details) are to some extent irrelevant. Even though the overlap is extremely large for small system sizes, it is likely that it would drop to zero in the thermodynamic limit [9]; however, it has been shown that the Laughlin wavefunction reproduces the correct long-distance features of the true ground state [172], and indeed one should think of the Laughlin's wavefunctions as states representative of "universality classes" of fractional quantum Hall ground states, meaning that the true ground states shares the same topological order.

Finally, we would like to mention the fact that many toy model Hamiltonians with short-range interactions have been built for which Laughlin's ansatz is indeed exact [171, 173, 174, 175] and which generalize to more exotic fractional quantum Hall states [176]. For example, the Laughlin wavefunction is the exact ground state for bosonic particles interacting through contact interaction[93], which makes these states particularly appealing in the atomic or photonic context.

3.1.3 Plasma analogy

For general values of m, Laughlin's state can not be written as a single Slater determinant out of single particle orbitals, as in the integer quantum Hall $m = 1$ case [Eq. (3.12)]. Computing the expectation values of observables is therefore a difficult task. To unravel the features of the state he proposed, Laughlin [23] noticed

that the norm of his wavefunction Eq. (3.10)

$$\begin{aligned} Z &= \int \prod_{i<j} |z_i - z_j|^{2m} e^{-\sum_i \frac{|z_i|^2}{2l_B^2}} \, d^2z_1 \dots d^2z_N \\ &= \int \exp\left(\sum_{i<j} 2m \log(|z_i - z_j|/l_B) - \sum_i \frac{|z_i|^2}{2l_B^2} \right) d^2z_1 \dots d^2z_N \\ &= \int e^{-\beta U(z_1,\dots,z_N)} \, d^2z_1 \dots d^2z_N \end{aligned} \tag{3.13}$$

can be identified as the canonical partition function of a classical one-component two-dimensional plasma of N identical charges of charge $Q = -m$ at temperature $\beta^{-1} = m/2$ and interacting via two-dimensional Coulomb potential $V(r) = -Q \log(r/l_B)$

$$U(z_1, \dots, z_N) = \sum_{i<j} -Q^2 \log(|z_i - z_j|/l_B) - \sum_i \frac{Q|z_i|^2}{4l_B^2}. \tag{3.14}$$

The last term can be interpreted as describing a uniform neutralizing background with charge density $1/2\pi l_B^2$.

The problem of a classical one-component plasma [Eq. (3.13)] is a well-studied one in classical statistical mechanics. In particular, Monte Carlo calculations [177] indicated that the plasma is a screening fluid when $m \lesssim 70$ (and freezes to a solid otherwise). Therefore, the equilibrium state must be uniform and electrically neutral, implying that, in order to minimise this energy, the plasma will arrange itself so as to neutralize the background charge density, or

$$\rho_0 = \frac{\nu}{2\pi l_B^2}. \tag{3.15}$$

This is indeed the expected density of an incompressible state at filling ν.

The usefulness of the plasma analogy does not stop here though, since it allows to obtain analytical results through the intuitive understanding of screening physics. For example, the presence of charged impurities in the plasma will cause it to rearrange in such a way that the impurities are exponentially screened-out at distances larger than the plasma's correlation length. This fact, which allows for analytical considerations regarding the nature of bulk quasiparticles [9], will be extensively used in Chapter 6.

We finally would like to point out that, due to their usefulness and the intuitive understanding they provide, plasma analogies for different fractional quantum Hall states have been developed, for example for multicomponent Halperin systems [178]

or the non-abelian Moore-Read fractional quantum Hall state [179].

3.2 Edge modes

As we mentioned already a couple of times, the edge modes of quantum Hall systems display peculiar behaviour in that they behave as a one-dimensional chiral quantum liquid [32] in which transport occurs in a single direction without backscattering, hence robust to disorder and general small deformations of the Hamiltonian. The properties of this one-dimensional quantum liquid have been shown to serve as a probe for the topological order characterizing different fractional quantum Hall states [180, 30, 181, 182].

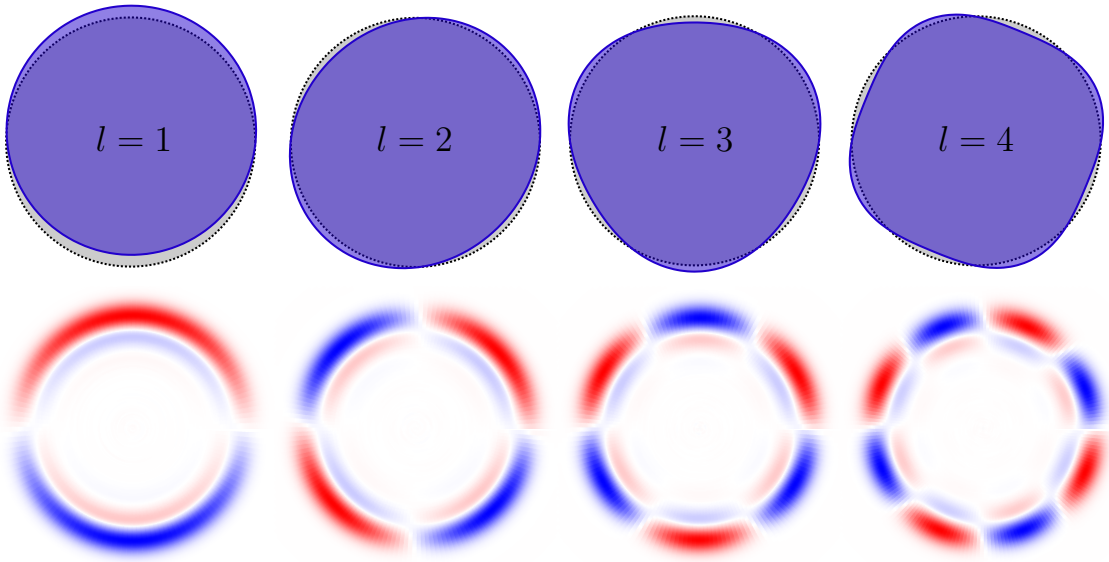

Figure 3.1: Top row: sketch of the edge deformation (blue cloud) when the system's state is a coherent superposition of the Laughlin's ground state [Eq. (3.10)] and an edge excitation [Eq. (3.16)] carrying definite angular momentum [Eq. (3.18)]. The Laughlin's ground state density is also sketched (black cloud). Bottom row: density variation, with respect to the system's Laughlin's ground state, of a coherent superposition between a $N = 25$, $\nu = 1/2$ Laughlin's ground state and the lowest lying excited state at angular momentum l, when the system is confined by means of a weak quartic $V \propto r^4$ trap (see Chapter 5).

The study of fractional quantum Hall edge modes has been the subject of intense investigation since the Wen's milestone works [26, 28, 29, 180], where it has been shown that the long-wavelength/low-energy physics of the one-dimensional edge modes in the thermodynamic limit is given by an effective simple model, the so-called chiral Luttinger liquid theory, which will be briefly reviewed in the following

Chapter. Here, we will limit ourselves to a microscopic discussion of the edge modes of the $\nu = 1/m$ circularly symmetric Laughlin state Eq. (3.10).

One can expect that, when a not-too-strong confinement is present, the ground state will still have the structure of a Laughlin state Eq. (3.10), for it is the densest state (lowest degree) which minimizes the interaction energy at fixed filling fraction. Being the densest state, one expects that it will also have the minimal possible confinement energy. To look for low energy excitations, we need to slightly alter the degree of the ground state wavefunction, without modifying the favourable interparticle correlations which are already built-in in Laughlin's ansatz. The degree of edge excitations cannot thus be smaller than the one of the Laughlin's wavefunction; on the other hand, increasing its degree is easily realized by multiplying the Laughlin wavefunction by polynomials symmetric in the particle variables z_k [31, 176], in such a way that the proper bosonic/fermionic statistics of the wavefunction is preserved; the chiral nature is apparent, as with these rules one can only increase the angular momentum of the state. For model interactions, these states have zero interaction energy, analogously to the Laughlin state; however, being of slightly higher degree, the droplet's radius will be slighly larger and thus the state will have higher confinement energy. With these considerations in mind, we can write down the generic edge excitations

$$\Psi_{EE}(\boldsymbol{r}_1, \ldots, \boldsymbol{r}_N) = P(z_1, \ldots, z_N) \prod_{i<j} (z_i - z_j)^m \exp\left(- \sum_i \frac{|z_i|^2}{4l_B^2} \right). \tag{3.16}$$

If the state has to be rotationally symmetric, the polynomial P needs to be of homogeneous degree; if its degree is l, Ψ_{EE} will carry angular momentum $L = L_0 + l$, where $L_0 = mN(N-1)/2$ is the angular momentum of the Laughlin state. For uncorrelated electrons at $\nu = 1$, these edge excitations exactly recover particle-hole excitations on top of the Fermi surface [183].

It is now easy to determine the dimension of the Hilbert space associated with the edge excitations Eq. (3.16), at fixed l. A convenient (non-orthogonal) basis for such a space can be easily written in terms of so-called power sum symmetric polynomials

$$p_l = \sum_i z_i^l. \tag{3.17}$$

Indeed, by multiplying some of the p_l together we can obtain a polynomial of degree l in different ways, the number of which will be given by the integer partitions $p(l)$ of l, namely the number of ways in which l can be written as a sum of positive

integers $\mathcal{L}_\alpha = \{l_1, l_2, \ldots\}$

$$P_{l,\alpha} = \prod_{l \in \mathcal{L}_\alpha} p_l = \prod_l p_l^{n_l}. \tag{3.18}$$

Here n_l is the multiplicity of a given l in $\mathcal{L}_\alpha$. Some examples are reported in Table 3.1. Notice that in general these states are linearly independent only if the excitation angular momentum does not exceed the number of particles in the system, $N \geq l$; furthermore, their interpretation as being edge excitations is valid as long as their wavelength is larger than the magnetic length, $l \lesssim \sqrt{2mN}$. In such a regime, the edge excitations can be interpreted as area-preserving deformations of the incompressible droplet [58], as depicted in Fig. 3.1.

Degree l	Partition $\mathcal{L}$	Polynomial	Energy
1	$\{1\}$	p_1	e_0
2	$\{2\}$	p_2	$2e_0$
	$\{1,1\}$	p_1^2	
3	$\{3\}$	p_3	$3e_0$
	$\{2,1\}$	$p_2 p_1$	
	$\{1,1,1\}$	p_1^3	
4	$\{4\}$	p_4	$4e_0$
	$\{3,1\}$	$p_3 p_1$	
	$\{2,2\}$	p_2^2	
	$\{2,1,1\}$	$p_2 p_1^2$	
	$\{1,1,1,1\}$	p_1^4	

Table 3.1: List of the lowest degree symmetric polynomials, generating Laughlin edge excitations through Eq. (3.16).

Now we consider a confining potential proportional to the angular momentum operator L; this is actually the case when the confinement potential is harmonic in the lowest Landau level since $\langle \frac{1}{2} e_0 \, r^2 \rangle = e_0(N + L)$, but gives correct long-wavelength low-energy behaviour for generic smooth potentials. In such a case, all the $p(l)$ states with given angular momentum l have the same excitation energy with respect to the Laughlin ground state

$$E_l - E_{GS} = e_0 \, l \tag{3.19}$$

and are equally spaced, so we can interpret the excitation spectrum as arising from an effective theory of harmonic oscillators, the so-called chiral Luttinger liquid theory.

3.3 Charged bulk excitations

After having briefly discussed the Laughlin wavefunction and its gapless chiral edge excitations, we will now review its gapped bulk excitations, focusing on the charged ones - namely the quasihole and quasielectron excitations, which are emergent particles having fractional charge and displaying fractional statistics.

We will just briefly mention that there is a different category of gapped collective bulk excitations, which are charge-neutral ripples in the density of the incompressible fluid. The dispersion of these excitations has a minimum (called the magnetoroton [184], in analogy to the roton minimum of superfluid Helium) at a non-zero value of the wavevector, indicating the tendency to form a Wigner crystal at small filling fractions $\nu \lesssim 1/7$ (much like the roton minimum in superfluid Helium indicates the tendency to solidification [47]). In the last years, neutral modes have attracted lots of attention, their long-wavelength behaviour being interpreted as a spin-2 excitation [185, 186] (the "graviton"), the quanta of motion of an intrinsic geometric degree of freedom [187] of fractional quantum Hall fluids which can potentially be probed when the background geometry is non-static [188, 189, 190].

In the following we will only briefly review charged elementary excitations.

3.3.1 Quasihole excitations

Laughlin noticed [23] that an elementary excitation can be created by piercing at some position η the quantum Hall fluid by an infinitely thin solenoid through which a flux quantum $\phi_0 = h/e$ is inserted adiabatically. By Laughlin's charge-pump argument [15], each single-particle state flows as $(z-\eta)^m \to (z-\eta)^{m+1}$, yielding Laughlin's famous quasihole wavefunction

$$\Psi_{QH}(\boldsymbol{r}_1, \ldots, \boldsymbol{r}_N) = \prod_i (z_i - \eta) \prod_{i<j} (z_i - z_j)^m \exp\left(-\sum_i \frac{|z_i|^2}{4l_B^2}\right) \tag{3.20}$$

which is easily generalized to the presence of many quasiholes at positions η_α by successive flux-insertions, each of which introduces a $\prod(z_i - \eta_\alpha)$ in the wavefunction. The physical interpretation is straightforward, as each prefactor makes the fluid's density vanish at η_α, creating thus a hole. Notice that this wavefunction has the same form as those of Eq. (3.16), therefore for the specific ultra-short-range interaction for which the Laughlin ground state is an exact zero-energy eigenstate, the quasihole state is an exact zero-energy eigenstate as well. This is not the case for longer ranged interactions, but it turns out to be an extremely good ansatz even for more realistic

scenarios.

The charge of the quasihole, associated to the density depletion of the fractional quantum Hall fluid close to η, can be obtained by means of the plasma analogy we briefly reviewed in subsection 3.1.3. Because the plasma is in its screening phase, one can expect the quasihole to be exponentially localised at the position η. The quasihole at η contributes to the plasma free energy [Eq. (3.14)] a term $\sum_i Q \log(|z_i - \eta|/l_B)$ which can be interpreted as the interaction energy between the plasma and an impurity with unit charge. The particles of the plasma will screen the impurity out; since each has charge $Q = -m$, one needs $1/m$ plasma particles to screen the impurity unitary charge. The quasihole charge must therefore be

$$q^* = -\frac{q}{m}, \tag{3.21}$$

which shows that fractional quantum Hall effect bulk charged excitations are remarkable in that they carry *fractional* charge [23, 35]. This is not only a coincidence of studying the Laughlin variational wavefunction, but rather a footprint of the underlying topological order [7]. Their presence has indeed been first experimentally confirmed in shot-noise experiments in a $\nu = 1/3$ fractional quantum Hall state [191].

Since fractional quantum Hall quasiparticles are exponentially localized objects which carry a well defined fractional charge, it is natural to ask what their statistical properties are. The answer to this question turns out to be remarkable [192, 35] and with far reaching consequences: the quasiparticles manage to escape the boson/fermion dichotomy, configuring themselves as *anyons*, an exotic possibility allowed in a two-dimensional world [193, 194, 195, 39]: the exchange phase can be any real-number interpolating between bosons and fermions. In particular, when two quasiholes are adiabatically exchanged, the ground-state wavefunction picks up a Berry phase [115] which comprises the Aharonov-Bohm [116] and an additional term which is interpreted as the "statistical phase" due to the localized excitations getting exchanged

$$\phi_{st} = \nu\,\pi. \tag{3.22}$$

When $\nu = 1$ (integer quantum Hall case), the holes behave as standard fermions, giving $\phi_{st} = \pi$ so that the ground-state wavefunction changes sign when the two holes are adiabatically exchanged; however at rational filling the quasiparticles have exotic (Abelian) anyonic statistics, recently observed in interferometric experiments [42, 43].

3.3.2 Quasielectron excitations

Laughlin pointed out that his fractional quantum Hall state [23] can host yet another kind of charged excitation – the quasielectron – which, contrary to the quasihole excitation Eq. (3.20), is associated with a lowering of the number of magnetic flux quanta piercing the system, for adiabatic removal of a quantum of flux will create a "lump" of charge at some point. It is however easy to understand that quasihole and quasielectrons are not "symmetric" [10]: while the quasihole is a zero-energy eigenstate of specific short-range Hamiltonians, the quasielectron must be separated from the ground state by an energy gap (the so-called many-body or Laughlin gap), because the Laughlin state is the highest-density zero-energy eigenstate: if we want to increase the electron density inside the fractional quantum Hall fluid, we need to decrease the relative angular momentum of some pair of particles, which will cost some interaction energy.

In analogy with the quasihole wavefunction Eq. (3.20), Laughlin proposed to lower the degree of Eq. (3.10) by multiplying it by a factor $\prod_i (z_i^* - \eta^*)$, which however involves the anti-holomorphic variables z^* and thus makes the resulting state have non-zero unwanted components in excited Landau levels. One thus needs to explicitly project the wavefunction back to the lowest Landau level

$$\Psi_{QE}(\boldsymbol{r}_1, \ldots, \boldsymbol{r}_N) = P_{LLL} \prod_i (z_i^* - \eta^*) \prod_{i<j} (z_i - z_j)^m \exp\left(-\sum_i \frac{|z_i|^2}{4l_B^2}\right). \quad (3.23)$$

Several inequivalent ways of explicitly doing the projection have been devised [10], which result in wavefunctions which have different short-range behaviours, but the expectation/hope is that the topological properties of the state are not affected by such a choice. The most natural scheme [196] is to "normal order" the z_k^* to the left of the z_k and then replace the anti-holomorphic coordinates by holomorphic derivatives $z_k^* \to 2\frac{\partial}{\partial z_k}$, with the convention that the derivatives do not act on the exponential factors. This yields the following variational wavefunction for the quasielectron excitation

$$\Psi_{QE}(\boldsymbol{r}_1, \ldots, \boldsymbol{r}_N) = \prod_i \left(2\frac{\partial}{\partial z_i} - \eta^*\right) \prod_{i<j} (z_i - z_j)^m \exp\left(-\sum_i \frac{|z_i|^2}{4l_B^2}\right). \quad (3.24)$$

In close analogy with the quasiholes, also quasielectron excitations carry fractional charge [23, 197, 198] and behave as emergent anyons with the same statistical parameter as the one of the quasiholes [Eq. (3.22)], but contrary to the quasihole case [Eq. (3.21)] they carry a fractional charge with the same sign of the one of the

particles forming the Laughlin state

$$q^* = +\frac{q}{m}. \tag{3.25}$$

It is finally worth mentioning that, contrary to the quasihole state, the Laughlin quasielectron state is not an eigenstate of some model Hamiltonian, and different quasielectron wavefunction have also been proposed [199] based on Jain's composite fermion approach to the quantum Hall effect [168], which has a better variational energy as compared to the Laughlin quasielectron [200]. Recently, a different proposal for the quasielectron wavefunction has been advanced [201].

In this chapter, we introduced the Laughlin's state starting from the motivations that lead Laughlin to his famous variational wavefunction, which is highly successful in the description of the main fractional quantum Hall sequence at filling $\nu = 1/m$. We then briefly described some basic features of such a state, namely the gapless edge excitations at the boundary and the bulk quasiparticles. The edge modes, being among the central topics of this thesis, will be further reviewed in the following Chapter 4. There, we briefly summarize the instructive bosonization of one-dimensional chiral fermions and Wen's hydrodynamic description of fractional quantum Hall edges.

CHAPTER 4

CHIRAL LUTTINGER LIQUID THEORY

In the previous chapters, we qualitatively discussed the edge modes of integer and fractional quantum Hall states, and discussed their microscopic wavefunctions starting from the Laughlin state. The aim of this chapter is to briefly review the basic ideas at the core of the effective low-energy description of these chiral boundary modes.

4.1 Bosonization of chiral 1D fermions

In this section we briefly sketch the bosonization procedure for one-dimensional chiral spinless fermions, mainly for two reasons. Firstly, even though simpler, they provide the key ideas and insight to the bosonization of non-chiral fermions moving in one-dimension, leading to the well known Luttinger liquid [202, 203]. Secondly, while the inclusion of inter-edge interactions slightly modifies the discussion [204, 205] making the low-energy effective theory analogous to the one originally developed for one-dimensional fermions [202], each edge of an integer quantum Hall state at unit filling map exactly to this model, as one could have guessed by comparing the low-energy, low-momentum excitations of an integer quantum Hall system (Fig. 2.2(b) and Fig. 2.3) to those of 1D chiral fermions [Fig.4.1].

For more rigorous and comprehensive descriptions, the interested reader may refer to [206, 207, 32, 208].

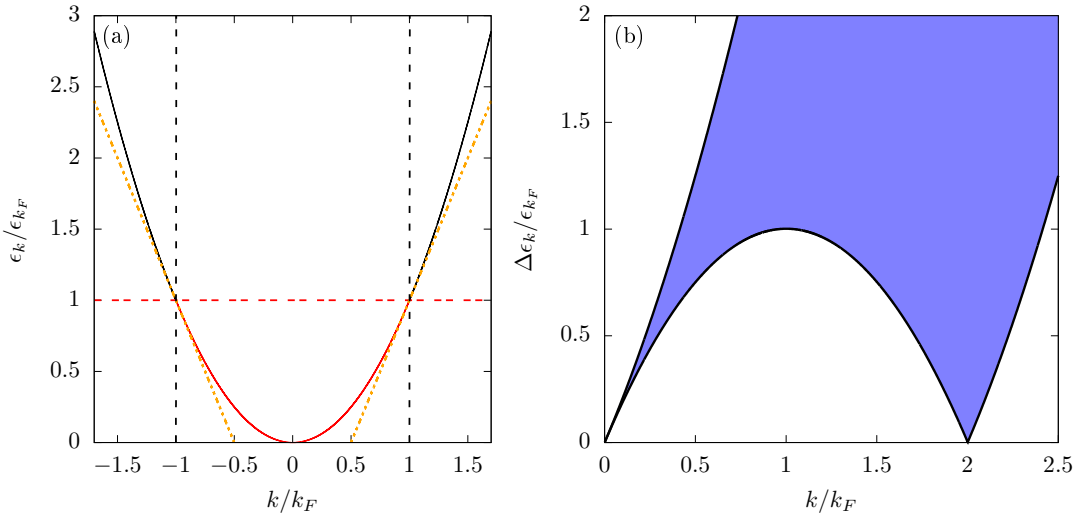

Figure 4.1: (a) Quadratic dispersion $\epsilon(k)$ for one-dimensional fermions. An example of the ground-state is sketched by colouring in red the occupied states below the Fermi energy (red dashed line) in the case of non-interacting particles. The corresponding Fermi points are highlighted by vertical black-dashed lines. Orange-dashed lines are linear approximations of the free-fermion dispersion $\epsilon(k)$ at the Fermi points. (b) Spectrum of the positive-k single particle-hole excitations on top of the ground-state sketched in panel (a).

4.1.1 Tomonaga-Luttinger model

The simplest model of interacting spinless fermions moving in one-dimension in a (periodic) wire of length L

$$H_{TL} = \sum_k \epsilon(k)\, C_k^\dagger C_k + \frac{1}{2}\sum_{k,k',q} V_q\, C_k^\dagger C_{k-q} C_{k'}^\dagger C_{k'+q} \tag{4.1}$$

is too complicated to be solved exactly for a general single-particle energy spectrum $\epsilon(k)$. The key observation though is to notice that particle-hole excitations $C_{k+q}^\dagger C_k$ carry well defined momentum and, at low-energies and long-wavelength, well defined energy due to a kinematic constraint existing in one-dimension; as can be seen in Fig. 4.1(b), differently from what happens in higher dimensions, there are no low-energy particle-hole excitations except at $k \sim 0$ and $k \sim 2k_F$. Therefore, low-momentum particle-hole excitations are long-lived elementary excitations of the one-dimensional Fermi system, and indeed they play a crucial role in the solution of the problem.

By replacing $\epsilon(k)$ with a single linear branch $v(k - k_F)$ – corresponding to chiral fermions – and considering an infinite filled Fermi sea below the Fermi point k_F, the

single particle-hole excitations at fixed momentum have the same energy. The idea is that such a model will capture the low-energy physics of the original one. One therefore introduces bosonic density fluctuations

$$\rho_q^\dagger = \sum_k C_{k-q}^\dagger C_k \tag{4.2}$$

which are the Fourier transform of the density operator

$$\rho(x) = \sum_k \frac{e^{ikx}}{L} \rho_k \tag{4.3}$$

where $\rho(x) = \psi^\dagger(x)\psi(x)$ and $\psi(x) = \sum_k \frac{e^{ikx}}{\sqrt{L}} C_k$. Since the density is real, $\rho_q^\dagger = \rho_{-q}$.

The density-fluctuation operators crucially fail to commute among each other[1] [203]

$$[\rho_q, \rho_p^\dagger] = \frac{Lp}{2\pi}\delta_{q,p} \tag{4.4}$$

which are nothing but the commutation relations of a set of independent harmonic oscillators which are used as a new basis in which to re-express the problem. Within a constant fermion-number subspace, the kinetic energy term can indeed be rewritten as a bilinear of the density operators yielding a quadratic Hamiltonian in the bosonic basis

$$H_{TL} = \frac{\pi v}{L} \sum_{k>0} \rho_k^\dagger \rho_k + \frac{1}{2L} \sum_k V_k \, \rho_k^\dagger \rho_k \tag{4.5}$$

which is easily solved. The mapping can be made rigorous by the introduction of so-called "Klein factors", to account for excitations which change the number of fermions [206]; this allows to explicitly construct the fermion operators in terms of the boson ones [210] $\psi(x) \propto \exp\left(2\pi i \int^x \rho(y)dy\right)$, and to show that the two formulations, bosonic and fermionic, are indeed equivalent [202]. Bosonization thus provides a remarkably simple way of solving the problem, and allows for the computation of many relevant quantities, such as the single-particle Green function

$$G(x,t) \propto \frac{1}{x - vt}. \tag{4.6}$$

In the context of quantum Hall physics this shows that along the one-dimensional edge of the system the Green's function decays as a power law, to be contrasted with the behaviour which is found within the gapped bulk, where one finds it to

[1] It can be shown that that such a commutation relation is a low-energy feature of one-dimensional systems in the thermodynamic limit [209], rather than the result of a non-trivial cancellations between infinities as originally shown in [203].

decay exponentially fast over a length-scale set by the magnetic length.

Secondly, the Green function has an inverse-power-law behaviour with unit exponent. Upon Fourier transform, this shows that chiral one-dimensional electrons have a behaviour similar to those of free electrons in a metal; this leads to ohmic linear current-voltage (I-V) characteristics in tunneling experiments with integer quantum Hall edges.

Finally, we want to stress that this behaviour is famously modified in the case of spinless fermions moving in one dimension, where interactions between the left and right moving fermions leads to interaction-dependent Green function exponents and to non-Fermi liquid behaviour [206]. Along similar lines, as we will discuss more extensively in the next section, the situation is drastically different for the fractional quantum Hall effect, due to the strong interparticle correlations in the bulk extending all the way through the edge.

4.2 Wen's chiral Luttinger liquid

In a series of seminal papers, Wen showed that along the one-dimensional boundary of incompressible fractional quantum Hall systems there exist gapless chirally-propagating excitations [26, 28, 29, 180] which do not form a chiral Fermi liquid, contrary to the integer quantum Hall case, but rather constitute a strongly-correlated one dimensional liquid which was named chiral Luttinger liquid, due to the similarities with Luttinger liquids and to its chiral nature. Even though the presence and nature of the edge modes can be shown to be a consequence of gauge symmetry and bulk incompressibility [29], we here review the chiral Luttinger liquid theory by taking a simple but physically insightful hydrodynamical approach [30, 31], which exploits the fact that the fractional quantum Hall states are incompressible and irrotational liquids with an energy gap for excitations in the bulk; therefore the only low-lying excitations are deformations of the cloud boundary but not of its area, with a chirality which is imposed by the external magnetic field.

Even though the hydrodynamic picture can be provided for hierarchical states as well, we here limit the discussion to the simple Laughlin fractions.

4.2.1 Hydrodynamic formulation

Consider a straight edge separating a fractional quantum Hall state at filling fraction ν from the vacuum, as sketched in Fig. 4.2. The fractional quantum Hall liquid is approximated as an incompressible homogeneous fluid with density $\rho_0 = \frac{\nu}{2\pi l_B^2}$,

confined in the half-plane $y \leq 0$ by an electric field $\boldsymbol{E} = -E\hat{\boldsymbol{y}}$. The system density can be described by means of a one-dimensional field $h(x)$ describing the edge displacement as $\rho(x, y) = \rho_0\,\Theta(y - h(x))$, Θ being the Heaviside step function. A one-dimensional density variation with respect to the ground state can henceforth be defined as $\rho(x) = \int \rho(x, y)dy - \int \rho_{GS}(x, y) = \rho_0 h(x)$. At the classical level, the particles will drift along equipotential lines of the electric field at a velocity set by Eq. (2.24), independent of their position along $\hat{\boldsymbol{y}}$. Therefore, edge waves will propagate rigidly at constant velocity v, in a chiral way, meaning that no waves can propagate in the opposite direction because of the presence of the magnetic field. The continuity equation implies that the displacement field obeys a simple wave equation

$$\partial_t \rho = -v\partial_x \rho \tag{4.7}$$

whose solutions are rigidly propagating waves $\rho(x - vt)$.

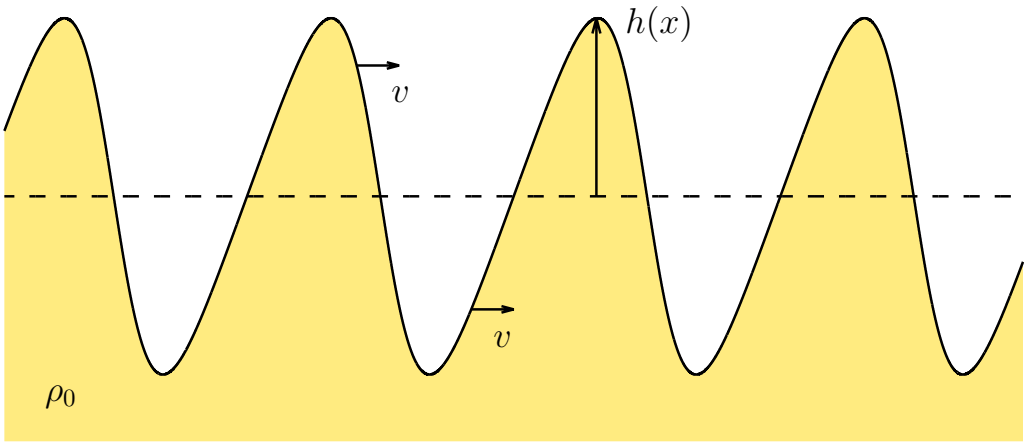

Figure 4.2: Sketch of the hydrodynamic picture of the edge modes: a density ripple on top of the unperturbed ground state (dashed line) is described as being constant "below" $h(x)$ and (yellow filling) equal to ρ_0. The perturbation propagates at constant velocity v [Eq. (2.24)].

Wen then writes down an energy function in order to quantise the theory. The electrostatic energy of the configuration is $\int V dq = \int (Ey) q\,\rho(x, y)dx\,dy$; its variation with respect to the ground state, due to a deformation of the edge, reads

$$H = \pi\,\hbar\,\frac{v}{\nu}\int \rho^2(x)dx \tag{4.8}$$

which is quadratic in the one-dimensional density $\rho(x)$. In momentum space $\rho(x) = \sum_{k\neq 0} \frac{e^{ikx}}{L}\rho_k$, where L is the length of the one-dimensional boundary, the Hamiltonian Eq. (4.8) and the chiral equation of motion Eq. (4.7) read

$$\begin{cases} H = \frac{2\pi}{L}\,\hbar\,\frac{v}{\nu}\sum_{k>0}\rho_k\rho_{-k} \\ \partial_t\rho_k = -ivk\rho_k. \end{cases} \tag{4.9}$$

By comparing these relations with Hamilton's equations of classical mechanics, one can identify "coordinates" and their corresponding canonical momenta as ($k > 0$)

$$\begin{cases} q_k = \rho_k \\ p_k = i\hbar\,\frac{2\pi}{Lk\nu}\,\rho_{-k} \end{cases} \tag{4.10}$$

The theory is quantized by the standard canonical quantization recipe of replacing the Poisson brackets $\{q_k, p_{k'}\} = \delta_{k,k'}$ with the quantum commutator $\frac{1}{i\hbar}[q_k, p_{k'}] = \delta_{k,k'}$. Equivalently

$$[\rho_k, \rho_{-k'}] = [\rho_k, \rho^\dagger_{k'}] = \frac{Lk}{2\pi}\,\nu\,\delta_{k,k'}, \tag{4.11}$$

which shows that the charge-neutral edge excitations are described by a single $U(1)$ Kac-Moody algebra [28, 26], remarkably similar to the charge-neutral edge excitations of the Tomonaga-Luttinger model (with single branch of fermions) Eq. (4.4). In coordinate space, the previous commutator reads

$$[\rho(x), \rho(y)] = -i\frac{\nu}{2\pi}\partial_x\delta(x-y). \tag{4.12}$$

The dynamics of the low-lying boundary excitations is set by

$$[H, \rho_k] = -\hbar v k \rho_k. \tag{4.13}$$

The previous relations show that the edge theory is a equivalent to a collection of uncoupled harmonic oscillators.

We shall now parallel the discussion we made about the microscopic description of the edge-excitations of the Laughlin's state in Sec. 3.2. In the case of a circularly symmetric geometry (a fractional quantum Hall droplet), the x dimension is periodic; this requires the momenta to be quantized in units of $2\pi/L$, $k_n = \frac{2\pi}{L}\,n$. The generic edge state carrying a well defined momentum k_M is therefore constructed by repeated application of $\rho^\dagger_k$ to the vacuum of edge excitations $|0\rangle$. It is not difficult then to realize that the number of such states is given by the number of integer partitions $p(M)$ of M: if $\mathcal{M}_\alpha$ is an integer partition of M, then we can write the

(unnormalized) edge state as

$$|M,\alpha\rangle \propto \prod_{m\in\mathcal{M}_\alpha} \rho^\dagger_{k_m} \, |0\rangle \tag{4.14}$$

which carries momentum $k_M = \sum_{m\in\mathcal{M}_\alpha} k_m = \frac{2\pi}{L} M$ and energy $E_{\mathcal{M}_\alpha} = \hbar v \sum_{m\in\mathcal{M}_\alpha} k_m = \hbar v \frac{2\pi}{L} M$. As anticipated, we see that the effective theory exactly matches the state counting, the degeneracies and the energy spectrum one obtains in the Laughlin state case 3.2.

4.2.2 The electron operator

Charged excitations correspond to the addition (or subtraction) of electrons at the edge. Analogously to the Tomonaga-Luttinger model [210], the underlying particle creation/annihilation operators are built by exponentiating bosonic operators

$$\psi \propto e^{-i\phi/\nu}. \tag{4.15}$$

Here, the phase field ϕ is related to the edge density through $\rho(x) = -\frac{1}{2\pi}\partial_x\phi(x)$.

It is not difficult to show that these operators indeed create a localized charge on the edge

$$[\rho(x), \psi^\dagger(x')] = \delta(x-x')\psi^\dagger(x'), \tag{4.16}$$

however, in order to be valid particle creation/annihilation operators, they should commute(/anticommute) when the particles making up the quantum Hall state are bosons(/fermions). Making use of the Baker-Campbell-Hausdorff identity one can obtain

$$\psi(x)\psi(x') = (-1)^{1/\nu}\psi(x')\psi(x), \tag{4.17}$$

which shows that one needs $1/\nu$ to be an even(/odd) integer in order for the ψ to commute/(anticommute) at different positions. With such a constraint, Wen's effective edge theory is seen to be the correct low-energy description of the boundary of a Laughlin state, but not of a generic fractional quantum Hall state. In these latter cases, this simple formulation of Wen's theory is indeed not self-consistent because it does not contain the electron operator. Leveraging on this observation, Wen concluded that states with $\nu \neq 1/m$ must contain more than a branch of edge excitations.

As a final comment, we wish to to parallel the discussion we did for the Green function at the end of Sec. 4.1. Using Eq. (4.15) one can compute the electron

propagator

$$G(x,t) \propto \frac{1}{(x-vt)^{1/\nu}} \tag{4.18}$$

which, when $\nu = 1$, reduces to Eq. (4.6), in agreement with the fact that the Laughlin state at $\nu = 1/m = 1$ is actually a non-interacting state described by a Slater determinant [Eq. (3.12)], whose boundary excitations map to a chiral Tomonaga-Luttinger model, as we mentioned in Sec. 4.1. However when $\nu \neq 1$, due to the strong correlations of the bulk liquid, the single-particle Green function acquires an anomalous exponent, showing non-Fermi-liquid behaviour in a way that is reminiscent of what happens in the Tomonaga-Luttinger model with both right- and left-moving interacting fermions [206]. While in this latter system however the anomalous exponent is set by the interactions, here it is completely determined by the bulk filling fraction ν and is thus expected to be robust against microscopic details, a central prediction of Wen's chiral Luttinger liquid theory. The anomalous exponent shows up in striking non-linear behaviour of current-voltage I-V characteristics in tunneling experiments [32], and owing to its universality can be used to characterize topological orders in fractional quantum Hall liquids [7].

Ingenious I-V characteristics experiments [211, 212] for electrons tunneling from a three-dimensional Fermi liquid into the fractional quantum Hall edge confirmed this remarkable non-ohmic behaviour, even though the measured exponent exhibits deviations from the predicted value: this discrepancy generated a large number of theoretical works trying to address the non-universality of the exponent, which has been argued to arise from edge reconstruction [213, 214], Landau level mixing due to long-range Coulomb interaction [215, 216, 217] or physics beyond the chiral Luttinger liquid [218].

4.2.3 Beyond chiral Luttinger liquid

Even though the chiral Luttinger liquid theory is expected, because of renormalization group arguments, to be the correct low-energy and long-wavelength limiting behaviour of the Laughlin state edge physics, this cannot be the case at higher-energies/shorter wavelengths; in such a regime additional contributions, irrelevant in the renormalization group scheme, will start to matter and as we are going to discuss they are crucial to understand the edge-dynamics beyond the chiral Luttinger liquid model, both at the linear and non-linear level.

Non-linear Luttinger liquids have attracted lots of attention in the context of one-dimensional fermionic matter [219], and have recently started to attract the attention in the quantum Hall field as well [220, 221, 222, 223, 224, 225, 226, 227, 228]. For

example, in recent years additional long-range "Benjamin-Ono" terms giving rise to fractionally quantized solitons moving along the one-dimensional boundary of the quantum Hall sample have been predicted to arise as a general feature of fractional quantum Hall liquids [225, 226, 227]. More recently, the presence of these long-range terms has been critically scrutinized and constrained by means of conformal field theory methods and analysis of symmetries [228], which have shown that as long as the inter-particle interactions are short ranged, so must be the effective low-energy edge Hamiltonian.

This is where our journey begins. In the rest of this thesis we will be presenting our results. More specifically, in the upcoming Chapter 5, we are going to discuss our results in this field of research. Leveraging on in-depth numerical analysis of anharmonically confined fractional quantum Hall clouds with short-range interactions, we show how the semi-classical dynamics of the edge is in our case effectively captured by a Korteweg-de Vries equation rather than by a Benjamin-Ono one. We then quantize this semiclassical dynamics and show how this leads to a highly predictive model generalizing Wen's chiral Luttinger liquid description.
In chapter 6 we instead change a bit the topic, and instead of focusing on the edge excitation we look at the bulk ones. In particular, we study how fractional quantum Hall quasiparticles not only are characterized by fractional charge and fractional statistics, but also by a fractional spin.

Part II

Results

CHAPTER 5

NONLINEAR DYNAMICS AT THE EDGE

In this chapter we study the nonlinear physics of the edge modes of fractional quantum Hall systems, beyond the regime of validity of Wen's chiral Luttinger liquid theory described in Chapter 4. As compared to our previous investigations of the non-linear features in conceptually-simpler non-interacting integer quantum Hall fluids [229] – for which exact diagonalization methods are readily implemented and yield valuable information and insight into the basic features of these systems – the strongly correlated nature of fractional quantum Hall liquids poses enormous technical challenges to their theoretical and numerical description. Given the great success of Monte Carlo methods for the study of these states, especially the simpler Laughlin's fractions, we develop a numerical approach to follow the dynamics of the edge modes of large fractional quantum Hall clouds. This allowed us to gain insight into the physics of such these strongly correlated systems, which we accompany with an in-depth study of the associated response functions.

In particular, in this chapter we are going to study the effects a weak anharmonic confinement has on the linear and nonlinear dynamics of the edge modes of macroscopic fractional quantum Hall fluids with short-ranged interactions. We characterize for such a system the first corrections to Wen's low-energy and long-wavelength chiral Luttinger liquid theory. We find that the dispersion relation of linear waves gets a cubic correction due to a combination of velocity gradients at the system's edge (induced by the anharmonic confinement) and strong bulk correlations extending all the way through the bulk. At the same time, we find sizable nonlinear effects in the dynamics, which have the potential to lead to intriguing wavebreaking dynamics.

The numerically observed features are quantitatively captured by a nonlinear chiral Luttinger liquid quantum Hamiltonian: the nonlinear behaviour found in the dynamics is mapped onto interactions between the bosons, while the modified linear-waves dispersion is accounted for by an additional quadratic term. The one-dimensional edge-density time evolution reduces to a driven Korteweg-de Vries equation in the semiclassical limit.

Making use of refermionization techniques we then show that the charge-zero sector of the theory can be exactly mapped onto a one-dimensional model of massive and interacting chiral fermions; this gives physical insight on the edge dynamical structure factor, explaining both its broadening and interestingly showing that it exhibits a universal power-law behaviour at its thresholds which depends on the filling fraction alone and not on the details of the anharmonic trap.

The contents of this chapter have been adapted from [230, 231], with some more results that will be wrapped up in an upcoming paper.

5.1 System and methods

In the following subsections, we are going to describe the system we considered and the numerical method we used to study it.

5.1.1 The system

We consider a two-dimensional system of N quantum particles of mass M, interacting through suitable short-range repulsive interactions and subject to a strong, uniform synthetic magnetic field [83, 84] B orthogonal to the plane; the system's model Hamiltonian reads

$$H_0 = \sum_i \frac{\boldsymbol{\pi}_i^2}{2M} + \sum_{i<j} V_{\text{int}}(\boldsymbol{r}_i - \boldsymbol{r}_j), \tag{5.1}$$

where $\boldsymbol{\pi}_i$ is the kinetic momentum of the i-th particle $V_{int}(\boldsymbol{r}_i - \boldsymbol{r}_j)$ the short-ranged interaction potential between the i-th and j-th particles.

As we extensively discussed in Section 2.1, in this continuous-space geometry with no underlying periodic lattice, the single-particle states in a uniform magnetic field B organize in highly degenerate and uniformly separated Landau levels: in what follows, energies are measured in units of the cyclotron splitting between Landau levels and lengths in units of the magnetic length. Moreover, we will work in the

symmetric gauge we reviewed in Sec. 3.1.1, therefore sticking with the usual complex-valued shorthand $z = x + iy$.

Two-body interactions lift the degeneracy and can lead – as we discussed in Sec. 3.1.2 – to the formation of highly-correlated incompressible ground states. The simplest examples are the celebrated Laughlin states [23]

$$\Psi_L(z_1, \ldots, z_N) = \prod_{i<j} (z_i - z_j)^{1/\nu} \exp\left(- \sum_i |z_i|^2 /4 \right), \tag{5.2}$$

entirely sitting within the lowest Landau level. The Laughlin state at filling $\nu = 1/2$ is the exact ground state for contact-interacting bosons [93], and thus could be realized in atomic [48, 82] or photonic [49, 50] systems; on the other hand, the $\nu \neq 1/2$ Laughlin states are the exact ground states of certain bosonic or fermionic toy model Hamiltonians [171, 173, 174, 175] and an excellent approximation in more realistic cases as shown by countless numerical evidence.

We focus our attention on the gapless edge-excitations – whose basic physics we reviewed in Sec. 3.2 – on top of a circularly-symmetric droplet of Laughlin fractional quantum Hall liquid, which correspond to chirally-propagating surface deformations of the incompressible cloud and, in the low-energy and long-wavelength limit, are accurately described by the chiral Luttinger liquid (χLL) model we reviewed in the previous Chapter 4. Our goal is to understand the basic features of the dynamics beyond the χLL description, when the cloud is confined by a generic non-harmonic (circularly symmetric) trap potential

$$V_{\text{conf}}(r) = \lambda r^{\delta}, \tag{5.3}$$

and the applied time-dependent excitation strength is large enough to exit the linear regime so that it provides sensible non-linear effects. We consider integer values of the exponent, $\delta \geq 2$. The limiting $\delta = 2$ case is somewhat trivial though, for when the confinement is harmonic the edge excitations disperse linearly [176] (see Fig. 5.1(b)) and the resulting edge theory reduces to the paradigmatic chiral Luttinger liquid of Wen; the anharmonic $\delta > 2$ case will be therefore the focus of the chapter.

To keep the calculation manageable, we will assume that the trap is shallow enough and the external time-dependent excitation is not too strong, so as to avoid coupling to states above the many-body energy gap Δ [96, 97, 81]. In this way the ground state remains a Laughlin state and the dynamics of the system edge is confined

to the subspace of many-body wavefunctions obtained by multiplying the Laughlin wavefunction by the holomorphic symmetric polynomials $P_\alpha(\{z_i\})$ in the particle coordinates [183, 58, 31, 176] we described in Chapter 3 (see Fig. 5.1(c)).

When is the Laughlin state the ground state?

In order to make these qualitative considerations more precise and quantitative, we can note that the Laughlin state [Eq. (3.10)] remains (approximatively) the ground state in the presence of the confinement potential as long as the energy cost of adding a particle at the system edge is smaller than the one required for inserting the extra particle into the bulk of the system, proportional to the many-body gap. Under this assumption, the ground state is a Laughlin state everywhere and its edge states are well captured by our theory [1]. If the aforementioned condition is not strictly met, a shell structure of locally homogeneous incompressible liquids has been predicted to appear [69], separated by sudden jumps (which will get regularized on the magnetic-length-scale) at the transition points between different strongly correlated liquids at different filling fractions. In spite of this additional complication, we expect that our theory will still provide an accurate description at least of the external edge between the outer Laughlin shell and the external vacuum, provided the outer shell is thicker than the characteristic correlation length of the gapped bulk, of the order of the magnetic length.

While we expect that our results can be generally applied to a variety of systems in different geometries, it is interesting to have a closer look at the relevant energy scales for the promising case of rotating clouds of bosonic atoms [81, 100, 90, 91], which we briefly discussed in Sec. 2.4.1: atoms are confined to move along a two-dimensional plane by a tight confinement along $\hat{\boldsymbol{z}}$ and are laterally trapped by a harmonic $V_2 = \frac{1}{2}M\omega^2 r^2$ potential supplemented by a anharmonic $V_{\text{conf}} = \lambda r^\delta$ one. In the fast rotation regime at $\Omega_r = \omega$, the centrifugal potential in the rotating frame is completely compensated by the harmonic part of the confinement and one is left with the anharmonic trapping only. Given the tight confinement along $\hat{\boldsymbol{z}}$, the effective two-body interaction potential is a contact one, $V_{\text{int}} = 2\hbar\Omega_r g\delta^{(2)}(\mathbf{r}/l_B^2)$, with an interaction strength g proportional to the ratio a_S/a_z between the s-wave scattering length and the harmonic oscillator length a_z. As usual, $l_B = \sqrt{\hbar/(2M\Omega_r)}$ is the effective magnetic length and $2\hbar\Omega_r$ the effective cyclotron gap.

The characteristic energy scale of the interactions between the bosons is thus $V_{\text{int}} = 2\hbar\Omega_r g(n_{2D}l_B^2)$, where n_{2D} is the two-dimensional density of the gas: for a

[1] This of course holds unless the edge is reconstructed[213, 214, 232, 233], which however does not typically happen for local interactions.

Laughlin state at half filling $n_{2D} = 1/(4\pi\, l_B^2)$, so the interaction energy scale is of order $V_{\rm int}/2\hbar\Omega_r = g/4\pi$. While the quantum correlations between particles make the Laughlin state and its edge excitations exact zero-energy eigenstates of the Hamiltonian, the typical energy of quasi-particle excited states is set by $V_{\rm int}$. In particular, numerical calculations [81] have shown that the many-body energy gap in these systems is of the order of $\Delta \approx 0.1\, g\, \hbar\Omega_r$. While the dimensionless parameter g could be tuned to relatively large values by means of Feshbach resonances [80], in our case it is beneficial to keep it moderate $g/(4\pi) \lesssim 1$ so as to suppress Landau level mixing. As a result, one can expect optimal values of the many-body gap to be on the order of a fraction of $\hbar\Omega_r$, which visibly points in the direction of using strong in-plane harmonic potentials.

To conclude, let us clearly state the requirements for avoiding closing the many-body gap in a quartic $\delta = 4$ anharmonic confinement potential and thus favour "wedding-cake" structures [69]. This requires that at the position of the edge ($r \sim \sqrt{2N/\nu}\, l_B$) the anharmonic part is much smaller than the harmonic one, $V_{\rm conf}/V_2 \sim 10^{-3}$. For a system of $N = 25$ particles, for which as we will show in what follows the physics already approaches the thermodynamic limit, this condition sets the magnitude of the anharmonic potential to be roughly $V_{\rm conf}(R_{\rm cl})/2\hbar\Omega_r \approx 0.01$, which imposes $\hbar\lambda/M^2\Omega_r^3 \approx 10^{-5}$. Under these conditions the ground state of the system will be the bosonic Laughlin state at half filling. Scaling up the size of the system will in principle require precise control on the trap parameters; however, as will discuss later in this chapter, we see the same physics emerging even for the extreme case of an hard-wall confining potential in real space, under suitable conditions.

5.1.2 The numerical method

Before we start with the discussion of the physics, we would like to give a brief description of the numerical method we envisioned to perform all the numerical simulations of this chapter.

Since we are assuming a clean separation of scales

$$\hbar\omega_c \gg V_{\rm int} \gg V_{conf} \tag{5.4}$$

the system's ground-state will be a Laughlin state and its edge excitations will be described by many-body wavefunctions of the form of Eq. (3.16), which we expand using the power-sum symmetric polynomials [Eq. (3.17)] as a basis in which to

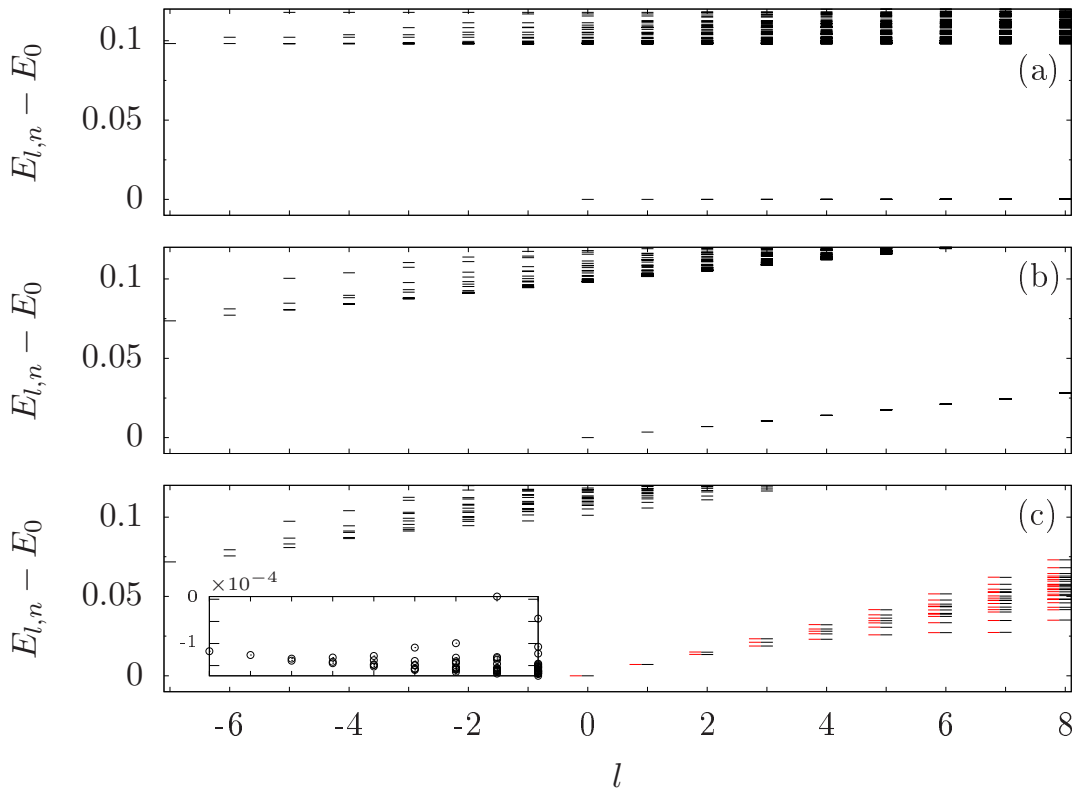

Figure 5.1: We plot the exact-diagonalization spectrum (restricted to the lowest Landau level) for a system of $N = 7$ bosons, interacting through a short range potential $g\,\delta^{(2)}(r)$, as horizontal black lines against the conserved angular momentum l measured with respect to the Laughlin's ground state value $mN(N-1)/2$. Energies are in units of g/l_B^2, in the case of (a) no confinement ($\lambda = 0$), (b) purely harmonic ($\delta = 2$) confinement, with $\lambda = 1.76 \times 10^{-3} g/l_B^4$ and (c) purely quartic ($\delta = 4$) confinement, with $\lambda = 6.4 \times 10^{-5} g/l_B^6$. In the bottom panel (c) we compare exact diagonalization data with Monte Carlo diagonalization ones (horizontal red lines, plotted against a slightly shifted value of angular momentum). In the inset of (c), we plot $E_{l,n}^{\mathrm{ED}} - E_{l,n}^{\mathrm{MC}}$.

describe the edge-excitation $P(z_1, \ldots, z_N)$ [Eq. (3.18)]

$$\Psi(z_1, \ldots, z_N) = \sum_{l,\alpha} C_{l,\alpha} P_{l,\alpha}(z_1, \ldots, z_N)\, \Psi_L(z_1, \ldots, z_N)\,, \tag{5.5}$$

where α runs through the $p_N(l)$ states corresponding to the integer partitions of l restricted to N elements at most, which span each l sector.

The unperturbed system's Hamiltonian $H = H_0 + V_{\mathrm{conf}}(r)$ commutes with the angular momentum operator; its eigenstates and eigenvalues can therefore be labelled by the angular momentum eigenvalue l. Projecting the many-body Schrödinger

equation over these many-body basis states, we obtain a Schrödinger equation

$$E_{l,n}\,\mathbb{M}_{(l,\alpha),(l,\alpha')}C_{l,\alpha'} = \mathbb{H}_{(l,\alpha),(l,\alpha')}C_{l,\alpha'} \tag{5.6}$$

for the expansion coefficients $C_{l,\alpha}$. The kinetic energy is constant within the lowest Landau level and the two-body interaction energy is assumed to be negligible within the subspace of Laughlin-like states (it is exactly zero for the case of contact-interacting bosons, or model interactions). The Hamiltonian $\mathbb{H}$ then only includes the confinement potential $V_{\mathrm{conf}}(r)$, while the "metric" $\mathbb{M}$ accounts for the non-orthonormality of the basis wavefunctions, and makes the time-independent version of the problem a generalized eigenvalue problem. A similar approach was previously adopted to study the ground-state properties and the spectrum of edge-excitations of a fractional quantum Hall fluid of Coulomb-interacting fermions [234, 218, 235].

Here we make a step forward and apply it to the study of relevant response functions and crucially of the time-dependent dynamics of the strongly correlated fractional quantum Hall fluid, in particular to its response to an external potential U. In particular, when a time-dependent excitation potential is present, the projection of the time dependent Schrödinger equation

$$i\,\mathbb{M}_{(l,\alpha),(l',\alpha')}\dot{C}_{l',\alpha'}(t) = \mathbb{H}_{(l,\alpha),(l',\alpha')}(t)\,C_{l',\alpha'}(t) \tag{5.7}$$

couples different angular momenta. The great advantage of our approach is that it allows to tame the dimension of the many-body Hilbert space: for a given l, the dimension of the Hilbert subspace does not grow with N, as opposed to the exponentially increasing dimension of the full N-particle Hilbert space. The price to pay is the need to compute the high-dimensional integrals hidden in the matrix elements of $\mathbb{H}$ and $\mathbb{M}$; their number moreover grows quite fast[2] with the angular momentum l, which in practice limits our analysis to not-too-large values of l. In our calculations, the evaluation of the integrals is done stochastically, by means of a Monte Carlo sampling of the many-body wavefunction via the Metropolis-Hastings algorithm, which we parallelized on a GPU to obtain a significant speed-up. Specifically, the calculation of the matrices $\mathbb{M}$ and $\mathbb{H}$ appearing in Eq. (5.7) require the evaluation of matrix elements of a generic real-space observables $\mathcal{O}(z_1,\ldots,z_N)$ between two (non-necessarily normalized) many-body states $\psi_{1,2}(z_1,\ldots,z_N)$. This

[2]The number of partitions asymptotically grows as $p(l) \sim \frac{1}{4\sqrt{3}\,l}\,\exp\left(\pi\sqrt{\frac{2l}{3}}\right)$.

quantity can be rewritten as

$$\int \mathcal{D}z \, \frac{\psi_1^*(z)}{\sqrt{\|\psi_1\|^2}} \, \mathcal{O}(z) \, \frac{\psi_2(z)}{\sqrt{\|\psi_2\|^2}} = \frac{\int \mathcal{D}z \, \frac{|\psi_1(z)|^2}{\|\psi_1\|^2} \, \frac{\mathcal{O}(z)\,\psi_2(z)}{\psi_1(z)}}{\sqrt{\int \mathcal{D}z \, \frac{|\psi_1(z)|^2}{\|\psi_1\|^2} \left|\frac{\psi_2(z)}{\psi_1(z)}\right|^2}} \tag{5.8}$$

where we have introduced the short-hands $z = \{z_1 \dots z_N\}$ and $\mathcal{D}z = dz_1 \dots dz_N$ and we have defined the norm as $\|\psi_{1,2}\|^2 = \int \mathcal{D}z \, |\psi_{1,2}(z)|^2$. The integrals in both the numerator and the denominator are then performed with the Metropolis-Hastings algorithm using $\mathcal{P}(z) = |\psi_1(z)|^2/\|\psi_1\|^2$ as the target probability distribution function [236, 237, 238]. Since the $\psi_{1,2}(z)$ wavefunctions have the form given by Eq. (5.5), consisting of a Laughlin state multiplied by a suitable polynomial of moderate degree, they share most of their zeros and their weights are concentrated in similar regions of configuration space. This feature is strongly beneficial in view of the convergence of the Monte-Carlo sampling. Further details are provided in Appendix A.

Using this method we have been able to study the dynamics of systems of up to $N \sim 80$ particles. In the following we will mostly show results for up to 40 particles for which the statistical error of the Monte Carlo sampling is smaller. As we are going to see, for this particle number, the system is in fact large enough to be in the macroscopic limit where the edge properties are independent of the system size.

5.2 Numerical results

In the following subsections we are going to describe our numerical results.

5.2.1 Benchmark

A first application of the numerical Monte-Carlo method is illustrated in Fig. 5.1(c) and Fig. 5.2(b), where we compare the energies of the low-lying excited-states obtained in two independent ways, namely Monte Carlo diagonalization and exact diagonalization (always performed within the lowest Landau level).

The excited state energies successfully compare to exact diagonalization results in every angular momentum sector l tested and for all particle numbers for which exact diagonalization is easy to perform [Fig. 5.2(b)]. When the confinement is not harmonic the ground state is not exactly a Laughlin state, but even when the effect of the confinement is relatively strong [Fig. 5.1(c)] ($V_{\rm conf}(R_{cl}) \sim 0.5\Delta$, Δ being the many-body Laughlin gap) the ground state and its edge excitations are still well described by Eq. (5.2) and Eq. (5.5). Notice that the low-energy description will

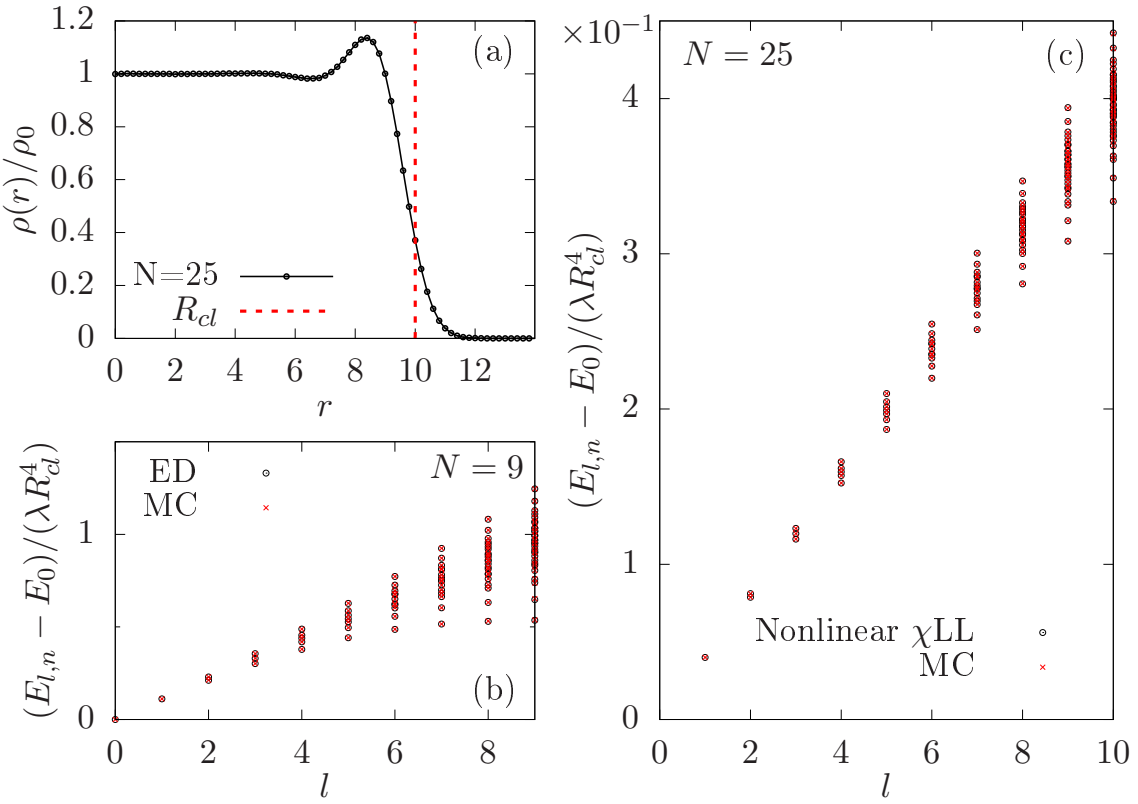

Figure 5.2: (a) Radial profile of the ground state density. (b,c) Excitation spectra for (b) $N = 9$ and (c) $N = 25$ bosons (red crosses), compared to exact diagonalization (black dots in (b)) and the nonlinear χLL theory [Eq. (5.25)] (black dots in (c)). The confinement is quartic, namely we set $\delta = 4$ in Eq. (5.3); the bulk filling factor is $\nu = 1/2$.

become more accurate as V_{conf} gets smaller.

In Fig. 5.2(a) we show a radial cut of the Laughlin's ground state density, which exhibits the typical profile of a Laughlin state: a density plateau corresponding to the incompressible bulk $\rho_0 = \nu/(2\pi)$ is well visible and separated by density oscillations close to the edge of the system in proximity of the classical radius $R_{cl} = \sqrt{2N/\nu}$, where the density transitions from the bulk to the vacuum value.

Finally, notice that the Monte Carlo diagonalization allows us to deal with larger systems [Fig. 5.2(c)]. We here just limit ourselves to observe that the same structure of the spectrum as the one showcased in Fig. 5.2(b) survives as the droplet is made larger.

5.2.2 Quantized transverse conductivity

We then investigate the dynamical evolution of the system in response to a temporally short excitation. With no loss of generality we assume for simplicity a radially

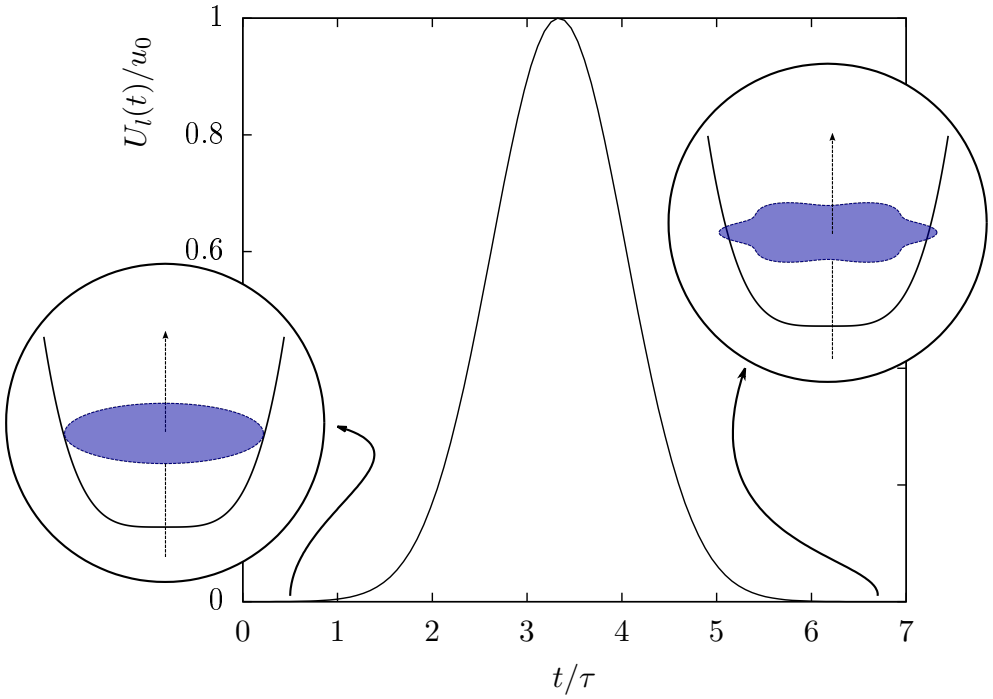

Figure 5.3: Temporal shape of the pulsed-excitation Eq. (5.9). The insets sketch the density associated to the system's state before the pulse (in its ground state) and after the excitation has been switched off (in a coherent superposition of ground- and excited- states).

flat potential which we assume to be carrying definite angular momentum l. In the (r, θ) polar coordinates, suitable for our circularly-symmetric geometry, the potential has then the simple form

$$U(r, \theta, t) = U(\theta, t) = U_l(t)\, e^{il\,\theta} + \text{c.c.}. \tag{5.9}$$

where $U_l(t)$ is the (complex-valued) time-dependent amplitude of the excitation at angular momentum l. Here, l plays the role of a proxy of the excitation wavevector: for a fixed cloud size, the higher l, the shorter the effective wavelength of the excitation along the edge. While the calculations reported in the main text refer to this r-independent potential, the general case of a r-dependent $U(r, \theta, t)$ is discussed in Appendix B and shown to bring no additional physics. From the temporal point of view, we focus on the case of a pulsed excitation with a Gaussian temporal shape $U_l(t) = u_0 \exp(-(t/\tau)^2)$. The characteristic time τ for turn-on and then switch-off is taken to be slow enough $\tau \gg \hbar/\Delta$ to avoid a significant excitation of states above the many-body gap, but fast enough compared to the edge mode frequencies so to induce a significant excitation of them. As sketched in Fig. 5.3, we start our protocol with the system in its Laughlin ground state and pulse $U_l(t)$ on a timescale τ. After

the excitation potential has been switched-off the system's state will be a coherent superposition of the Laughlin state and its edge modes.

As expected on physical grounds, the force along the azimuthal direction induced by the angular gradient of $U(\theta, t)$ generates a transverse Hall current along the radial direction (see Sec. 2.1.2 and Sec. 2.2.2) which locally changes the cloud density on the edge.

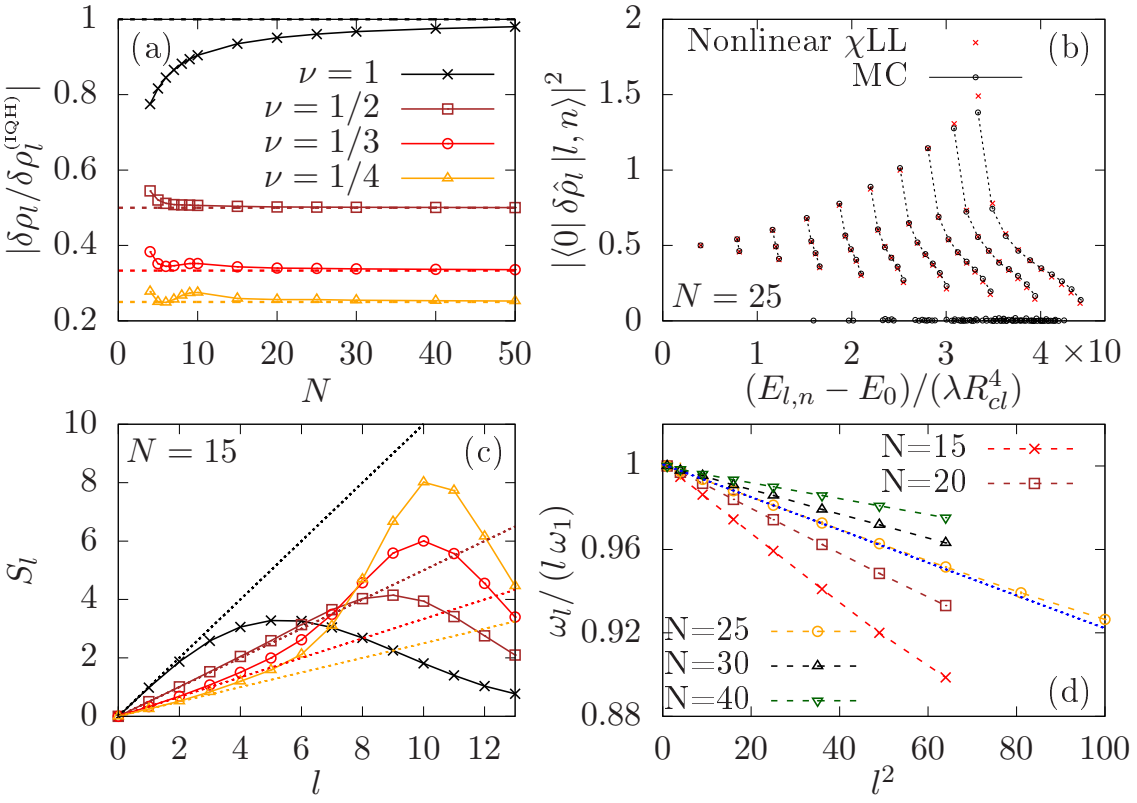

Figure 5.4: (a) Amplitude of the edge density response after the weak $l = 2$ external potential has been switched off, for different filling factors ν, normalized to the one of a large integer quantum Hall system. (b) Dynamic structure factor weights plotted against the excitation energy of each eigenstate. Within each angular momentum l sector, the dashed lines are guides to the eye. Monte Carlo diagonalization data (black dots) are compared to the nonlinear chiral Luttinger liquid model of Eq. (5.25) (red crosses). (c) Static structure factor S_l as a function of l for the same values of ν as in (a). Dashed lines indicate the χLL prediction $S_l = \nu l$. (d) Edge-mode dispersion for different N, normalized by ω_1 so that at $l = 1$ all curves start at 1. We also normalize by the excitation angular momentum l and plot the results against l^2, so as to highlight the cubic $\propto l^3$ shift. The same trap potential as in Fig.5.2 has been used. In panels (b,d) the filling factor is fixed to $\nu = 1/2$.

Numerical results for the linear-response amplitude of the radially-integrated system's density (the "built-up" charge) to a weak excitation are displayed in Fig. 5.4(a): in agreement with transverse conductivity quantization arguments, a clear propor-

tionality of the response to the fractional quantum Hall filling factor ν is found in the large-N limit. Quite remarkably, this limiting behaviour is accurately approached already for way lower particle numbers ($N \gtrsim 15$) in the fractional quantum Hall than in the $\nu = 1$ integer quantum Hall case. This conclusion is of great experimental interest as it suggests that evidence of the quantized conductivity can be observed just by probing the response to trap deformations of the edge of realistic-size rapidly-rotating clouds [83], a technique of widespread use for ultracold atomic clouds [47].

This behaviour can be understood using linear time-dependent perturbation theory to study the edge-density $\hat{\rho}(\theta)$ response when the system is excited by a perturbation which couples to the system's density, in our case the external potential $U(\theta, t)$. The system's response after the excitation U_l has been turned off reads, to linear order (See Appendix C for more details)

$$\langle \delta\hat{\rho}(\theta, t)\rangle = \frac{1}{\pi}\Im\left[\sum_l \int \widetilde{U}_l(\omega) S_l(\omega) e^{i(l\theta-\omega t)}\, d\omega\right], \tag{5.10}$$

where $\widetilde{U}_l(\omega)$ is the space-time Fourier transform of $U(\theta, t)$ and

$$S_l(\omega) = \int \frac{dt}{2\pi}\, e^{i\omega t}\, \langle e^{i\hat{H}t}\delta\hat{\rho}_l e^{-i\hat{H}t}\delta\hat{\rho}_{-l}\rangle \tag{5.11}$$

is the dynamic structure factor – restricted here to the edge-modes manifold of states – and $\delta\hat{\rho}_l$ is the angular Fourier transform of the edge-density variation $\delta\hat{\rho}(\theta)$. When the trap is quadratic, the edge is a prototypical χLL and the dynamic structure factor is a δ-peak centred at $\omega_l = \Omega\, l$, with $\Omega = 2\lambda$ the angular velocity of the edge modes.

For anharmonic traps [Fig.5.5(a)], Ω is still determined by the potential gradient at the cloud edge, analogously to Eq. (2.24) (a more extensive discussion is given in Appendix F though),

$$\Omega = r^{-1}\partial_r V_{\rm conf}(r)\big|_{R_{cl}} \propto N^{(\delta-2)/2} \tag{5.12}$$

but at the same time the dynamic structure factor broadens. Up to not-too-late times however the broadening can nevertheless be neglected and the density response can be accurately approximated as

$$\langle \delta\hat{\rho}(\theta, t)\rangle \simeq \frac{1}{\pi}\Im\left[\sum_l \widetilde{U}_l(\omega_l)\, e^{i(l\theta-\omega_l t)} S_l\right], \tag{5.13}$$

where $S_l = \int S_l(\omega)\, d\omega$ is the edge-mode static structure factor. As long as the confinement potential is not strong enough to mix with states above the many-body gap, the static structure factor keeps its chiral Luttinger liquid value $S_l = \nu l$ for $l \geq 0$ and zero otherwise up to l values where finite-N effects get important [Fig.5.4(c)] (See Appendix C for a discussion of this fact).

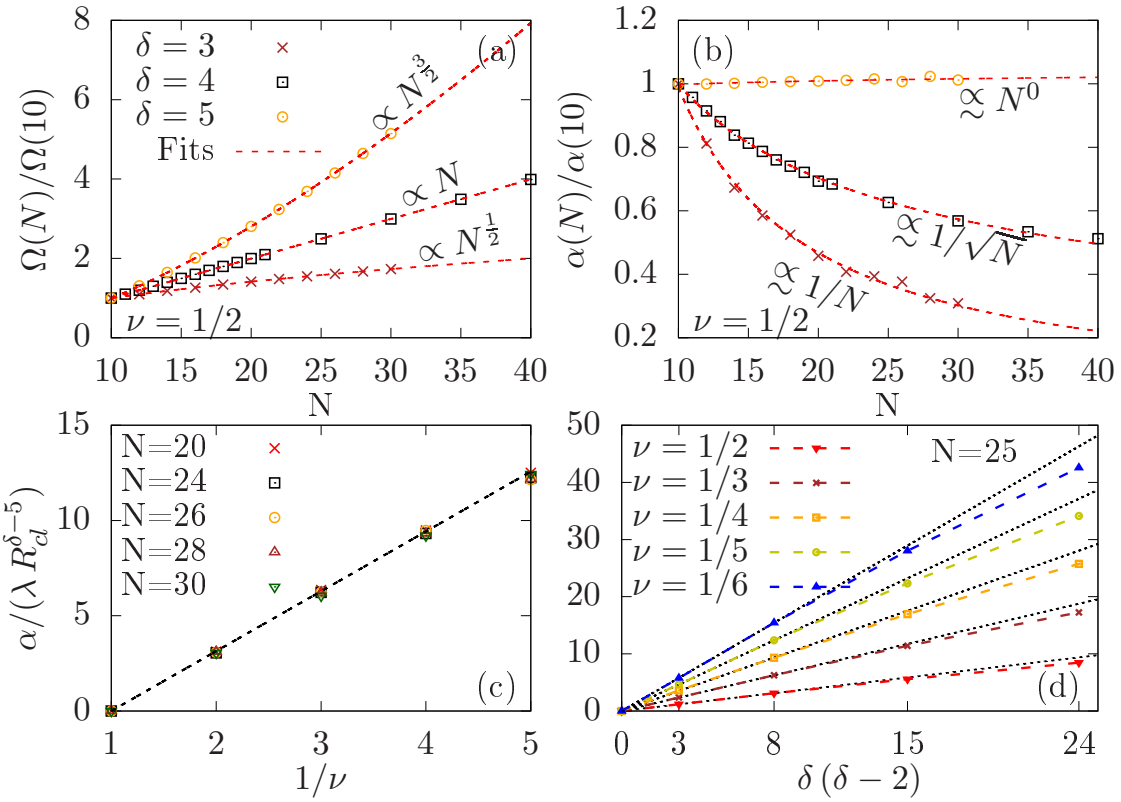

Figure 5.5: (a) Angular velocity Ω plotted against the number of particles N, and normalized to $\Omega(10)$, the angular velocity extracted from a system of $N = 10$ particles. (b) Group velocity dispersion parameter α as a function of N and normalized to the extracted $\alpha(10)$, for different trap exponents δ at a constant filling fraction $\nu = 1/2$. (c, d) Properly normalized α (c) as a function of the reciprocal of the filling, $1/\nu$, in the case of a quartic $\delta = 4$ trap and different number of particles N and (d) as a function of the trap curvature $\propto \delta(\delta - 2)$, for different filling fractions ν at given $N = 25$.
All points are extracted from low-l polynomial fits to the numerical Monte Carlo diagonalization data for ω_l as a function of l.

5.2.3 Beyond chiral Luttinger liquid effects

Our numerical framework is not restricted to study the response of the system to weak and long-wavelength excitations as captured by the standard chiral Luttinger liquid theory. The goal of this Section is to explore the physics beyond Wen's chiral

Luttinger liquid theory, namely the response of the edge to stronger and shorter wavelength excitations.

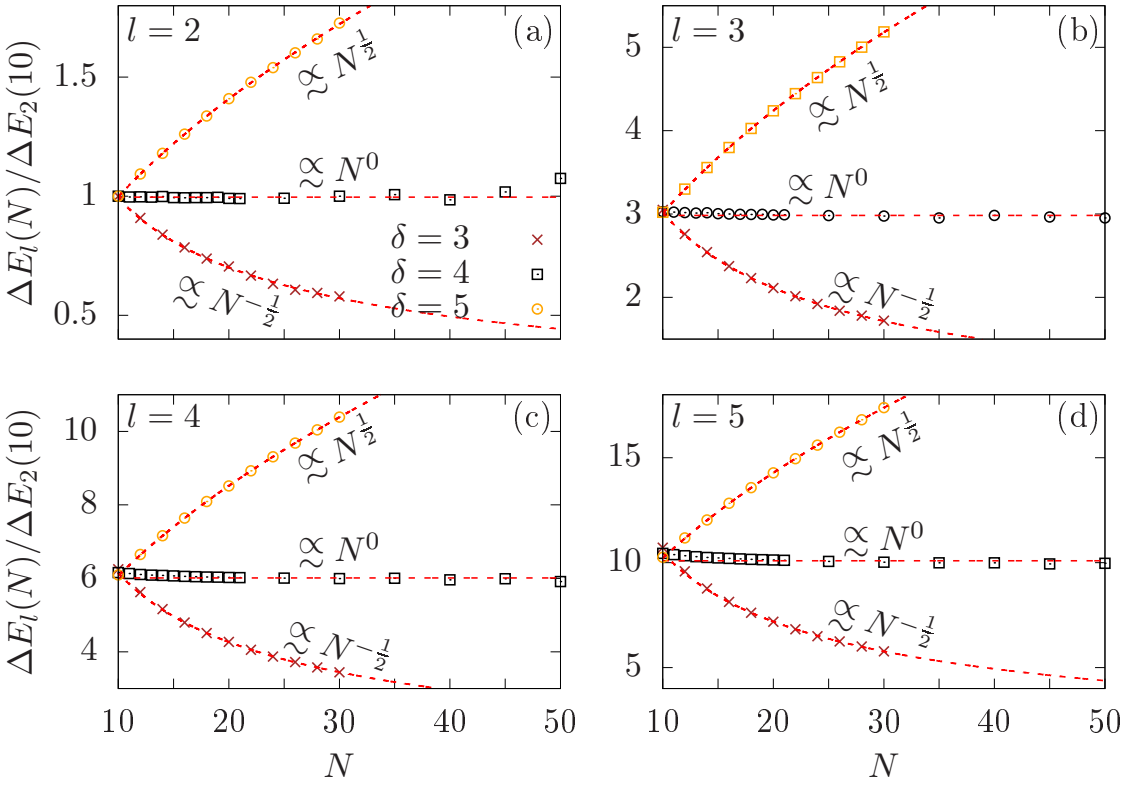

Figure 5.6: Dynamic structure factor width ΔE_l, normalized by the one at $N = 10$ and $l = 2$ in the case of a $\nu = 1/2$ fractional quantum Hall droplet as a function of the particle number N for different values of (a) $l = 2$, (b) $l = 3$, (c) $l = 4$, and (d) $l = 5$. The dashed lines are power law fits to the data and highlight the scaling with N at fixed l, for different confinements δ. The fitted exponents are in close agreement with the expected ones indicated in the legends.

Dynamical structure factor

As we have seen in the previous Section, anharmonic confinements cause the dynamic structure factor to broaden [Fig. 5.4(b) and Fig. 5.10] within a finite frequency window, whose extension (as we will more extensively discuss in Sec. 5.4.2) is proportional to l^2 and to the curvature of the trap potential at the classical radius

$$c = R_{cl}^{-1}\partial_r \left(r^{-1}\partial_r V_{\text{conf}}(r)\right)\big|_{R_{cl}} = \lambda\,\delta(\delta-2)R_{cl}^{\delta-4}\,, \tag{5.14}$$

a quantity related to the second l-derivative of the lowest Landau level projection of $V_{\text{conf}}(r)$, which physically corresponds to the radial gradient of the angular velocity. Analogously to the integer quantum Hall case [229], the broadening is responsible

for the decay of the oscillations at late time that is visible in Fig. 5.8(b). However, in contrast to the integer quantum Hall case, the distribution of the dynamic structure factor weights at fixed angular momentum l is non-flat: as one can see in Fig. 5.4(b), within each l sector, the weight of the states close to the high-energy threshold is suppressed, while the one of the states close to the low-energy threshold is reinforced. This behavior is in close analogy to what was found for a fermionic Luttinger liquid beyond the linear dispersion approximation [219, 239, 240, 223, 224], and the parallelism will be further explored in Sec. 5.4.1 and Sec. 5.4.3.

We will now present numerical data that substantiates this claim regarding the broadening of the dynamic structure factor. However, a more comprehensive discussion on this matter will be presented in Sec. 5.4.2.

Broadening of the dynamical structure factor of edge modes

When the cloud is non-harmonically confined with $\delta \neq 2$, the dynamic structure factor broadens within a finite frequency window, whose width can be easily estimated by looking at the difference ΔE_l between the largest and smallest energies in a given angular momentum l sector. The corresponding states have in fact a non-vanishing weight $|\langle 0|\,\delta\hat{\rho}_l\,|l,n\rangle|^2$, and their energies thus correspond to the dynamic structure factor thresholds.

In close analogy to to the integer quantum Hall case, we expect the dynamic structure factor to broaden $\propto c\,l^2$. Here we verify this scaling. In particular, data in Fig. 5.6 suggest the following simple form

$$\Delta E_l = \mu_\nu \frac{c}{2} l(l-1). \tag{5.15}$$

The proportionality $c \propto R_{cl}^{\delta-4}$ is visible from the N dependence in each l sector. Since all data have been normalized by $\Delta E_{l=2}$ (at a fixed number of particles, $N = 10$), the proportionality to $l(l-1)/2$ can be instead read out by looking at the first point on y-axis. Notice that, apart for the ν-dependent proportionality factor, the result in Eq. (5.15) is exactly the same as in the integer quantum Hall case, where the lower (upper) threshold corresponds to a particle (/hole) created just above (/below) the Fermi surface. An interpretation of this result, as well as the μ_ν coefficient, are presented in Sec. 5.4.2.

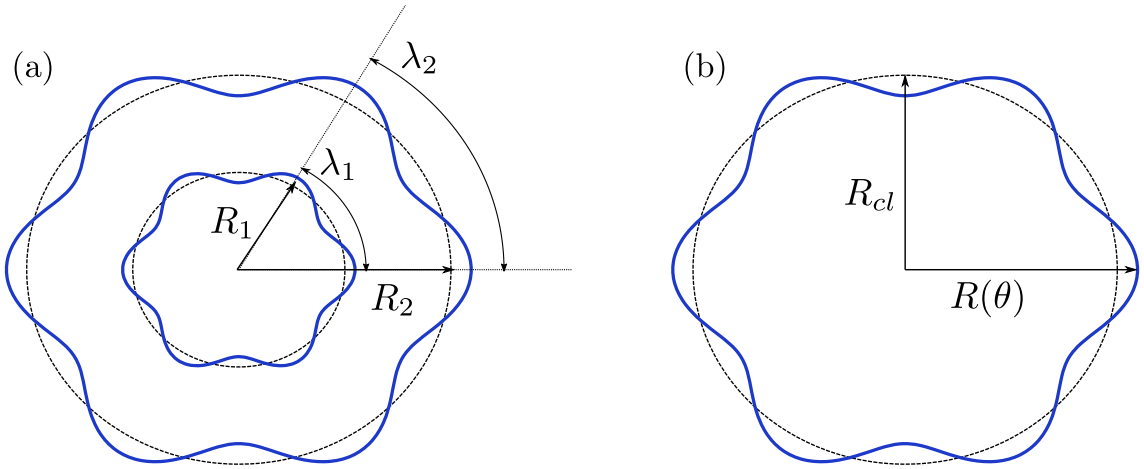

Figure 5.7: Sketches of the excited droplet. (a) Excitation wavelength λ at fixed excitation angular momentum l when the droplet is enlarged. (b) The undeformed boundary, at a distance R_{cl} from the trap centre, and the deformed one parametrized by a local radius $R(\theta)$.

Group velocity dispersion

This asymmetrical distribution of the dynamic structure factor makes its centre-of-mass frequency (its first moment, normalized to the zeroth one)

$$\omega_l = \frac{\int \omega S_l(\omega) d\omega}{\int S_l(\omega) d\omega} \tag{5.16}$$

shift from the low-energy result $\omega_l \simeq \Omega\, l$. Edge-excitations experience a wavevector-dependent frequency-shift and, thus, a finite group velocity dispersion. As shown in Fig. 5.4(d), the negative shift [3] gets stronger according to a cubic law at small l,

$$\omega_l = \Omega\, l - \alpha\, l^3\,. \tag{5.17}$$

Notice that the cubic form of the frequency shift is different from the quadratic term that appears in typical non-chiral Luttinger liquid theories describing, e.g., interacting Fermi gases, as well as from the Benjamin-Ono term introduced in the context of fractional quantum Hall fluids in [227, 226] and already critically scrutinized on the basis of conformal field theory and symmetries in [228].

Whereas the numerical results shown in Fig.5.4(d) may suggest that the shift is a finite-size effect, as the droplet size is increased the wavelength of the excitation gets larger, as sketched in Fig. 5.7(a). Indeed, a careful account of the N dependence,

[3] In Appendix F we discuss small finite size corrections to the angular velocity parameter Ω with respect to the physical expectation Eq. (5.12).

of the geometry and confinement parameters indicates that the shift persists in the macroscopic limit. To this purpose, we note that as N increases at fixed trapping parameters λ and δ, the cloud gets correspondingly larger as $R_{cl} = \sqrt{2N/\nu}$, so the effective spatial wavevector of an excitation at l decreases as $q = l/R_{cl}$. At fixed q, we expect the frequency shift to be proportional to the curvature of the confining potential in a straight-edge geometry, which in our case suggests

$$\alpha\, l^3 = \beta_\nu\, \tilde{c}\, q^3 \tag{5.18}$$

with

$$\tilde{c} = R_{cl}^2\, c = \lambda\, \delta(\delta - 2)\, R_{cl}^{\delta-2} \tag{5.19}$$

and a size-independent coefficient β_ν which in general will depend on the bulk filling fraction. This functional form is validated against the numerical results in Fig.5.5(b-d). Fig.5.5(b) shows that α is indeed proportional to $\sqrt{N}^{\delta-5}$ at fixed λ. Fig.5.5(c) and Fig. 5.5(d) illustrate the linear dependence on the filling factor and on the trap curvature parameter, respectively.

From these data, we extract the size-independent β_ν coefficient [4]

$$\beta_\nu \simeq \frac{\pi}{8}\frac{1-\nu}{\nu}. \tag{5.20}$$

Since $\beta_\nu \propto 1 - \nu$, we see that the frequency shift of Eq. (5.18) is related to the strong correlations of the quantum liquid extending all the way through the edge, for β_ν vanishes at integer filling. Work is still in progress to understand the physical origin of this term which we think could be related to the Hall viscosity[241], edge dipole moment [242] and the magneto-roton excitations in the bulk of the fractional quantum Hall fluid[243]. Interestingly, recently the oscillatory behaviour in the proximity of the Laughlin state boundary, visible in Fig. 5.2(a), has been numerically studied and the wavevector of such a oscillation was found to be related to the wavevector of the bulk magnetoroton minimum [244].

Non-linear dynamics

When the excitation strength increases, nonlinear effects start to play an important role in the edge mode evolution. Numerical results illustrating this physics are displayed in Fig.5.8; in particular, Fig.5.8(a) shows the density profile of the cloud edge after a relatively long evolution time past a sinusoidal excitation with given

[4] Note that additional, yet typically smaller and opposite in sign group velocity dispersion effects may arise from higher-order terms in the single-fermion dispersion even for $\nu = 1$ [229].

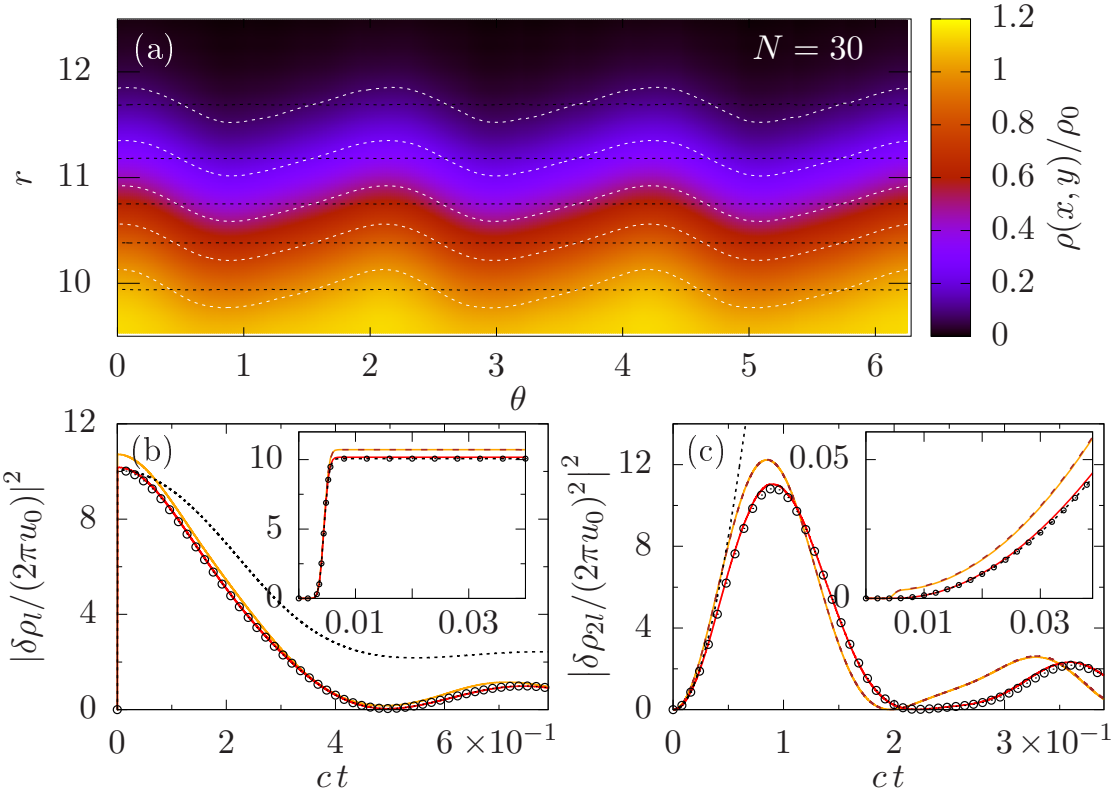

Figure 5.8: (a) Colorplot of the density near the edge at $ct \simeq 0.1$ after an excitation pulse of the form of Eq. (5.9) with an intensity large enough to induce a significant non-linear dynamics on this temporal scale. White (black) lines are iso-density contours for the excited (unexcited) system. (b,c) Time-evolution of the (modulus of the) fundamental and second harmonic spatial Fourier components of the edge density variation of $N = 30$ (red) and $N = 9$ (yellow) clouds, computed via Monte Carlo diagonalization. Exact diagonalization data for $N = 9$ are shown as brown dashed lines as a benchmark. Dotted black lines and black dots indicate respectively the solution of the semi-classical equation Eq. (5.23) and of the quantum model $\hat{H}^{NL}_{\chi LL}$ of Eq. (5.28). Insets show a magnified view of the dynamics at early times. Same trap parameters as in Fig. 5.2, filling factor $\nu = 1/2$.

l. In contrast to the weak excitation case discussed above where the density profile keeps at all times a plane-wave form proportional to $\cos(l\theta - \omega_l t)$, here a marked forward-bending of the waveform is visible, leading to a sawtooth-like profile. Upon angular Fourier transform, this asymmetry corresponds to the appearance of higher spatial harmonics.

The physical mechanism underlying the nonlinearity can be understood in analogy with the integer quantum Hall case [229]. Because of the incompressibility condition, a local variation $\delta\rho(\theta)$ of the radially-integrated angular density must correspond to a variation of the cloud radius $\delta R(\theta) \simeq \delta\rho(\theta)/(\rho_0 R_{cl})$ (see the sketch in Fig. 5.7).

This then leads to a variation of the local angular velocity

$$\bar{\Omega}(\theta) = r^{-1}\partial_r V_{\rm conf}\big|_{R(\theta)} \simeq \Omega + (2\pi c/\nu)\,\delta\rho\,. \tag{5.21}$$

This nonlinear effect can be combined with the group-velocity dispersion and the excitation potential $U(\theta,t)$ discussed above into a single semiclassical evolution equation

$$\frac{\partial\delta\rho}{\partial t} = -\left(\Omega + \frac{2\pi c}{\nu}\delta\rho\right)\frac{\partial\delta\rho}{\partial\theta} - \alpha\,\frac{\partial^3\delta\rho}{\partial\theta^3} - \frac{\nu}{2\pi}\,\frac{\partial U}{\partial\theta} \tag{5.22}$$

which we reformulate in terms of the 1D density variation along a "straightened" edge by defining $\sigma(\zeta,t) = \delta\rho(\theta,t)/R_{cl}$, where $\zeta = R_{cl}\theta$ is the physical position along the edge. The resulting evolution equation

$$\frac{\partial\sigma}{\partial t} = -\left[\tilde{v} + \frac{2\pi\tilde{c}}{\nu}\sigma\right]\frac{\partial\sigma}{\partial\zeta} - \beta_\nu\tilde{c}\,\frac{\partial^3\sigma}{\partial\zeta^3} - \frac{\nu}{2\pi}\frac{\partial U}{\partial\zeta} \tag{5.23}$$

and has the form of a driven classical Korteweg-de Vries equation [245] whose coefficients only involve macroscopic parameters such as the linear speed

$$\tilde{v} = R_{cl}\,\Omega \tag{5.24}$$

determined via Eq. (5.12) by the transverse response to the inward trapping force at the cloud edge, $\tilde{v} \sim -\,\partial_r V_{\rm conf}(r)|_{R_{cl}}$. The confinement potential curvature is defined via Eqs.(5.14) and (5.19) and is proportional to the second derivative $\tilde{c} \sim \partial_r^2 V_{\rm conf}(r)|_{R_{cl}}$, namely the gradient of the trapping force.

As one can see in the time evolution of the spatial Fourier components of the density shown in Fig.5.8(b,c) and in Fig.5.9, the semiclassical equation accurately reproduces the numerical evolution up to relatively long times, where the forward-bending due to the density dependent speed of sound is well visible. It would be interesting to study whether a suitable semiclassical limit (e.g. larger systems so that the density ripples on the edge effectively contain larger number of particles) exists in which Korteweg-de Vries solitons [246] can emerge.

On the time-scales where the semiclassical dynamics Eq. (5.23) fails, the broadening of the dynamic structure factor discussed above starts to play a dominant role, giving rise to the collapse and revival features visible in the plots; equivalently, these effects can be seen as the emergence of quantum fluctuations on top of the semiclassical dynamics, as we are now going to see.

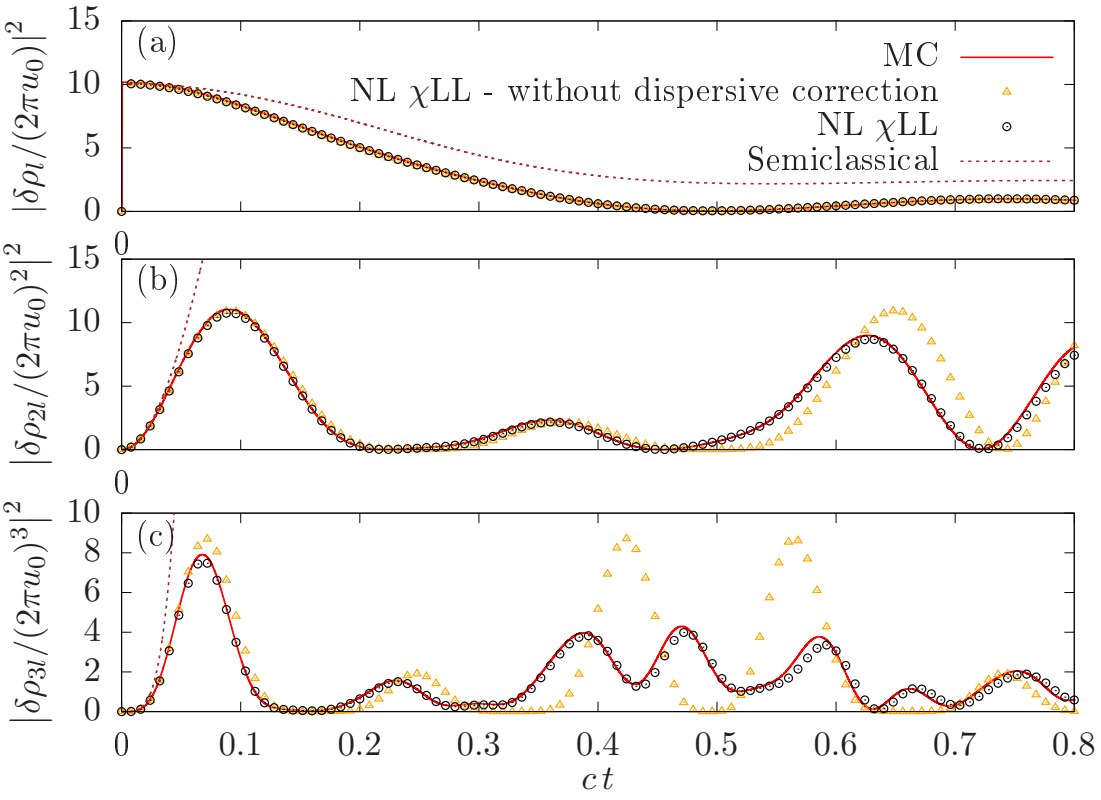

Figure 5.9: Time evolution of the fundamental (a), second (b) and third (c) harmonic of the spatial Fourier transform of the edge density variation of a $N = 30$ cloud at filling factor $\nu = 1/2$ in a $\delta = 4$ quartic trap. The results of the microscopic Monte Carlo diagonalization calculations (red lines) are compared with those of the non-linear χLL model (black circles) and of its semiclassical limit (brown dashed lines). For comparison, the result of a non-linear χLL model without the dispersive contribution is shown as yellow triangles.

5.3 Non-linear chiral Luttinger liquid theory

In order to properly capture these last features, quantum effects must be included in the theoretical description. In this perspective, the semiclassical evolution Eq. (5.23) can be seen as the classical limit of the Heisenberg equation for the density operator of a χLL supplemented with a group velocity dispersion term and a forward-scattering non-linearity.

This reasoning suggests the following form for the lowest non-universal corrections to the quantum chiral Luttinger liquid Hamiltonian for our short-ranged interacting, non-harmonically confined fractional quantum Hall fluid

$$\hat{H} = \int d\theta \left(\pi \frac{\Omega}{\nu} \hat{\rho}^2 + \frac{c}{\nu^2} \frac{2\pi^2}{3} \hat{\rho}^3 - \pi \frac{\beta_\nu}{\nu} \frac{c}{R_{cl}} (\partial_\theta \hat{\rho})^2 \right) \tag{5.25}$$

where the the density operator of the chiral edge mode obeys the usual χLL commutation rules [31],

$$[\hat{\rho}(\theta), \hat{\rho}(\theta')] = -i\frac{\nu}{2\pi}\partial_\theta \delta(\theta - \theta'). \tag{5.26}$$

or, in the straight-line geometry,

$$\hat{H}^{NL}_{\chi\mathrm{LL}} = \int d\zeta \left[\frac{\pi\,\tilde{v}}{\nu}\,\hat{\sigma}^2 - \frac{\pi\,\beta_\nu \tilde{c}}{\nu}\left(\frac{\partial\hat{\sigma}}{\partial\zeta}\right)^2 + \frac{2\pi^2\tilde{c}}{3\nu^2}\,\hat{\sigma}^3 + U(\zeta,t)\,\hat{\sigma} \right] \tag{5.27}$$

and the $U(1)$ Kac-Moody algebra Eq. (5.26) becomes $[\hat{\sigma}(\zeta), \hat{\sigma}(\zeta')] = -i\,\frac{\nu}{2\pi}\,\partial_\zeta \delta(\zeta - \zeta')$.

It is straightforward to verify that the evolution equation for $\hat{\sigma}$ that is obtained by taking the classical limit of the Heisenberg equation

$$\frac{\partial\hat{\sigma}}{\partial t} = i\left[\hat{H}^{NL}_{\chi\mathrm{LL}}, \hat{\sigma}\right] = -\tilde{v}\,\frac{\partial\hat{\sigma}}{\partial\zeta} - \frac{\pi\tilde{c}}{\nu}\,\frac{\partial\hat{\sigma}^2}{\partial\zeta} - \beta_\nu\tilde{c}\,\frac{\partial^3\hat{\sigma}}{\partial\zeta^3} - \frac{\nu}{2\pi}\frac{\partial U}{\partial\zeta} \tag{5.28}$$

indeed recovers the classical wave equation Eq. (5.23) when operators are replaced by complex numbers.

The different terms in the Hamiltonian Eq. (5.27) (or Eq. (5.25)) correspond to the different physical effects discussed in the previous Sections. The first term, proportional to $\hat{\sigma}^2$, is quadratic in the density operators $\hat{\sigma}$: it is already present in the standard chiral Luttinger liquid Hamiltonian and accounts for the increase of energy of the cloud when the edge is deformed from its equilibrium position. The second term is proportional to the second spatial derivative $(\partial_\zeta\hat{\sigma})^2$ and is still quadratic in the density bosonic operators: it arises from the cubic correction to the dispersion of weak-amplitude waves in Eq. (5.17); the additional third derivative appearing in the corresponding term in the wave equation Eq. (5.23) comes from the derivative present in the commutator Eq. (5.26). The microscopic origin of this term will be the subject of future work – here we just note that it has the suggestive form of a surface-tension energy.

The third term is proportional to $\hat{\sigma}^3$ and therefore is no longer quadratic in $\hat{\sigma}$: it stems from the intrinsic nonlinearities discussed in 5.2.3 and it describes interactions among the bosonic modes of the chiral Luttinger liquid. Finally, the last term proportional to the density operator $\hat{\sigma}$ is analogous to the coupling to the electromagnetic field in the Wen's chiral Luttinger liquid theory [28]: in our model, it describes the external driving generated by the coupling of the cloud density to the external potential $U(\theta, t)$ in Eq. (5.9).

All numerical coefficients appearing in the quantum Hamiltonian Eq. (5.27) can be straightforwardly calculated in terms of the bulk filling fraction ν and the radial

dependence of the confinement potential $V_{\text{conf}}(r)$ around the classical radius $r = R_{cl} = \sqrt{2N/\nu}$ using Eq. (5.19), Eq. (5.20), and Eq. (5.24). This confirms the physical expectation that the edge dynamics only depends on the local features of the confinement. The resulting formulas

$$\tilde{v} = \partial_r V_{\text{conf}}(r)\big|_{R_{cl}} \tag{5.29}$$

$$\tilde{c} = R_{cl}\partial_r \left(r^{-1}\partial_r V_{\text{conf}}(r)\right)\big|_{R_{cl}} \tag{5.30}$$

can be used to obtain quantitative predictions for specific physical systems.

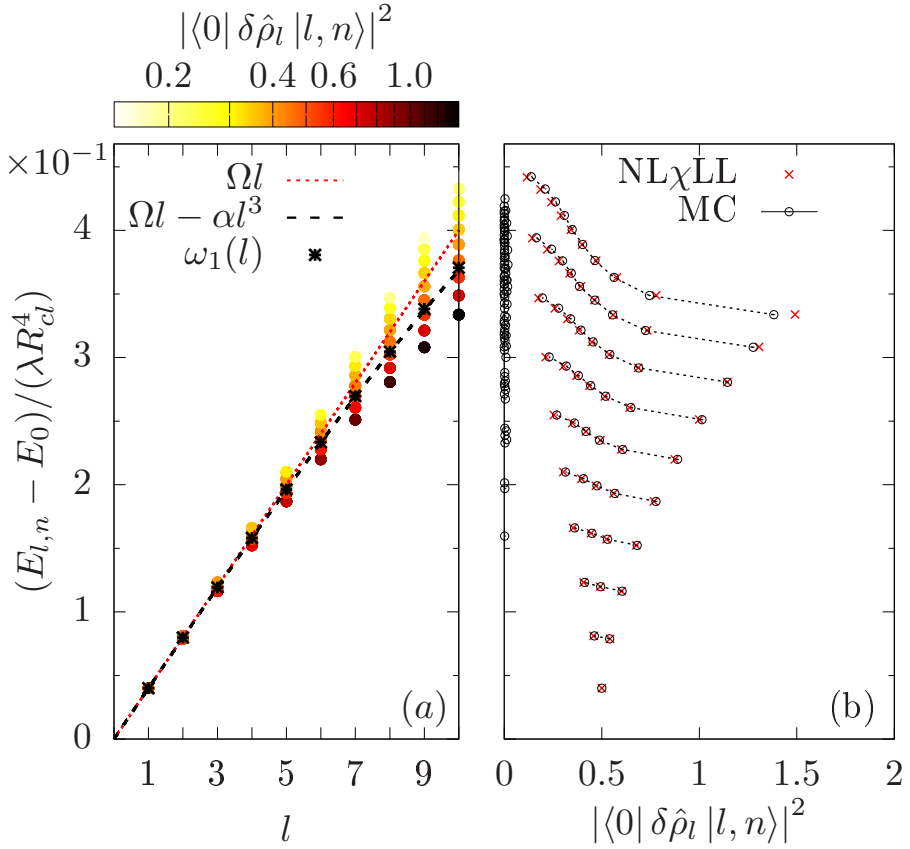

Figure 5.10: (a) Energy spectrum $E_{l,n} - E_0$ of the system confined by a quartic $U(r) = \lambda r^4$ trap, in units of the trap strength λ and coloured according to the dynamic structure factor weight $|\,|0\rangle\,\delta\hat{\rho}_l\,|l,n\rangle\,|^2$ and plotted against the angular momentum sector l. The red dotted line is Wen's linear dispersion of the edge modes, Ωl; the black line is the cubic correction $\Omega l - \alpha l^3$. Black circles with crosses are the dynamic structure factor central frequency $\omega_1(l) = \frac{\int d\omega\, \omega S_l(\omega)}{\int d\omega\, S_l(\omega)}$. (b) Dynamic structure factor weights (on the x-axis) are plotted against the excitation energies $E_{l,n} - E_0$ (on the y-axis). Black circles are Monte Carlo points, red crosses have been obtained from Eq. (5.25). The principal emerging features of the dynamic structure factor at angular momentum l have been joined with black-dashed lines as a guide for the eye. All the data are for $N = 25$ bosons at $\nu = 1/2$ filling.

We here wish to highlight the importance of the aforementioned dispersion $\propto (\partial_\zeta \hat{\sigma})^2$ and interaction $\hat{\sigma}^3$ terms in Eq. (5.27). In Fig. 5.10 we show again the energy spectrum of the system (left panel), highlighting both the dynamic structure factor weights (colorscale) and the modified linear waves dispersion Eq. (5.17). Even though for a fixed l most of the dynamic structure factor weight is concentrated in the lowest energy state, a non-zero weight is present in higher energy states as well. As a result, the dispersion of linear waves, defined as the centre-of-mass of the dynamic structure factor [Eq. (5.16)] does not coincide with the lowest energy state at $E_-(l)$. It is henceforth not possible to identify this state with a single boson excitation at the same angular momentum l, as previously done [221, 232, 247, 234, 218]. The boson-boson interaction term proportional to $\hat{\sigma}^3$ in the nonlinear chiral Luttinger liquid model is therefore playing a crucial role in spreading the dynamic structure factor over a finite range of energies. Furthermore, as it will be apparent from the discussion in Sec. 5.4.2., the fact that $\omega_1(l)$ deviates from a linear behaviour highlights the importance of the dispersive term proportional to $(\partial_\zeta \hat{\sigma})^2$.

The surprisingly good accuracy of the physical predictions of the nonlinear chiral Luttinger liquid Hamiltonian Eq. (5.27) are showcased in Fig. 5.2(d), Fig.5.4(b), Fig. 5.8(b,c) and Fig. 5.9 for the eigenenergy spectrum, the dynamic structure factor [5] and the complete time evolution, respectively. In each of these plots, the predictions of Eq. (5.27) are compared to results obtained from the full microscopic Hamiltonian, and an excellent agreement is found. In the panels of Fig. 5.9 we further compared the numerically calculated microscopic time-evolution (the modulus of the spatial Fourier transform of the edge-density variation, up to the third harmonic) with the results of the nonlinear chiral Luttinger liquid model[6], with and without the cubic correction associated to the modified phonon dispersion. Notice that the latter is essential to correctly capture the late-time dynamics, in particular of the harmonic components at $2l$ and $3l$ (yellow triangles in Fig. 5.9). Of course, the nonlinear terms are even more important [228], and they are responsible for the very appearance of a finite amplitude in the higher harmonic components. A very good agreement can be seen, which gets slightly worse at larger angular momenta l: this small deviation may be caused by a higher-order correction of the phonon dispersion (beyond the cubic term considered here) and/or by the increasing difficulty in accurately sampling the matrix elements of the excitation Hamiltonian between

[5] The slight deviations at large momenta are due to the higher-order group velocity dispersion and finite-size effects that are visible also in Fig. 5.4(c,d). When the droplet is made larger, the deviations become smaller as can be seen in Fig. 5.12(b).

[6] To this purpose, the free parameters of the model have been determined according to the scaling formulas previously discussed, without any additional fine-tuning.

higher-l subspaces which would then result is numerical error increasing over time.

All together, these results strongly support the predictive power of the nonlinear χLL model. Given the favourable scaling of its numerical complexity with particle number N as compared to the full two-dimensional calculations, the one-dimensional nonlinear χLL appears as a most promising tool to describe the dynamics of large fractional quantum Hall clouds well beyond the limitations of the full many-body description.

In the sections that follow we are going to discuss some simple consequences of such a model.

5.4 Refermionization

In the following subsections, we are first going to describe an equivalent fermionic model for the description of the bosonic edge modes. Even though equivalent, such a dual description turns out to be convenient when dealing with nonlinear Luttinger liquids. Leveraging on this picture we then describe some consequences.

5.4.1 The refermionization scheme

Starting from the nonlinear chiral Luttinger liquid Hamiltonian Eq. (5.25), we now show how the quantum dynamics of the (bosonic) edge excitations (the charge-zero sector) of the Laughlin fractional quantum Hall droplet can be exactly mapped onto an equivalent model of one-dimensional, massive, interacting and chiral fermions, where one can make use of the artillery of techniques developed in the context of non-linear Luttinger liquids [239, 219].

By rescaling the bosonic field as $\hat{\rho}' = \hat{\rho}/\sqrt{\nu}$, the Hamiltonian of Eq. (5.25) can be written as

$$\hat{H} = \int d\theta \left(\pi \, \Omega \, \hat{\rho}'^2 + \frac{c}{\sqrt{\nu}} \frac{2\pi^2}{3} \, \hat{\rho}'^3 - \pi \alpha \left(\partial_\theta \hat{\rho}' \right)^2 \right), \tag{5.31}$$

where for convenience we introduced the shorthand $\alpha = \beta_\nu c / R_{cl}$, and the commutatation relations Eq. (5.26) are correspondingly rescaled to

$$[\hat{\rho}'(\theta), \hat{\rho}'(\theta')] = -i \frac{1}{2\pi} \partial_\theta \delta(\theta - \theta'), \tag{5.32}$$

which is the standard commutation rule of bosonized density modes in a Tomonaga-Luttinger model [248, 206], as we saw in Chapter 4.

The similarity with the Tomonaga-Luttinger does not stop here, and standard

bosonization identitites [206] can be used to show [7] that the full rescaled Hamiltonian Eq. (5.31) is the bosonized version of a model of one-dimensional (chiral) fermions with Hamiltonian

$$\hat{H}' = \sum_l \epsilon_l \hat{R}_l^\dagger \hat{R}_l - \frac{\alpha}{2} \sum_l l^2 \hat{\rho}_l \hat{\rho}_{-l} \,, \tag{5.33}$$

where the free-fermion dispersion

$$\epsilon_l = \Omega l + \frac{l(l-1)}{2m^*} \tag{5.34}$$

has a quadratic contribution with an effective mass $m^* = (c/\sqrt{\nu})^{-1}$ and interactions occur via the short-range potential $V_{12}(\theta_1 - \theta_2) = -2\pi\,\alpha\,\delta''(\theta_1 - \theta_2)$. As usual, the fermionic creation (annihilation) operators $\hat{R}_l^\dagger$ ($\hat{R}_l$) obey anticommutation rules

$$\{R_l, R_{l'}^\dagger\} = \delta_{l,l'} \,, \tag{5.35}$$

and $\rho_l = \sum_{l'} \hat{R}_{l-l'}^\dagger \hat{R}_{l'}$ is the Fourier transform of the density operator $\hat{\rho}$.

It is interesting to note that the term proportional to $\hat{\rho}^3$ describing the interactions between the bosonic modes in Eq. (5.25) translates into the non-interacting mass term in the refermionized Eq. (5.34). Vice-versa, the quadratic term proportional to $(\partial_\theta \hat{\rho})^2$ describing the group velocity dispersion of the bosons translates into an interaction term in the fermionic picture.

In the regime we are investigating here the ground state $|0\rangle$ of the fermionic Hamiltonian Eq. (5.33) is a Fermi sea filling all the states below the Fermi point $l_F = 0$

$$\begin{cases} R_{l\leq 0}^\dagger |0\rangle = 0 \\ R_{l>0} |0\rangle = 0 \end{cases} \tag{5.36}$$

and is the only available state for its value of the angular momentum. Notice that in principle higher-order terms in the fermion free-particle dispersion are required to make this ground-state well defined, which we however neglect mainly for two reasons: first of all, these corrections are expected not to be relevant at the energy scales we are considering; secondly, we have not characterized these higher order terms numerically.

To conclude this Section, it is important to note that density-related observables of the physical fractional quantum Hall system directly map onto the density operator

[7] Note that the refermionization map is not complete as $\psi = e^{i\phi/\nu} \to e^{i\phi'/\sqrt{\nu}}$ is not a single fermion annihilation operator. In spite of this, the above mapping works as long as we compute density-related observables.

of the refermionized model, showing that the charge-zero sector of the fractional quantum Hall edge theory maps (at low energies) onto a chiral generalization of the non-linear Luttinger model of one-dimensional fermions [239, 219]. On the other hand, the creation/annihilation operators of the physical particles forming the fractional quantum Hall fluid cannot be mapped in a simple way to fermionic creation/annihilation operators. As we are going to see in the next Section, this mathematical fact makes the refermionization approach a useful tool for characterizing the dynamic structure factor – and similarly all density-related observables.

5.4.2 Broadening of the dynamic structure factor

As a first application of the refermionized Hamiltonian Eq. (5.33), we look at the broadening of the dynamic structure factor that is well visible in Fig. 5.10 and manifests as a progressive spreading of the energies with the angular momentum l of the droplet.

In order to get a simple picture of the underlying physics, we make the approximation of neglecting the interactions between fermions described by the last term of the Hamiltonian (5.33). This leaves us with a free fermion model of dispersion ϵ_l whose excitations consist of particle-hole pairs around the Fermi level, which is taken to be at $l_F = 0$. Within this approximation, for a given value of the angular momentum l of the excitation, the dynamic structure factor has a flat profile in between the least and the most energetic excitations, whose energies are respectively equal to

$$E_+(l) = \epsilon_l - \epsilon_0 \tag{5.37}$$

$$E_-(l) = \epsilon_1 - \epsilon_{1-l}\,. \tag{5.38}$$

Taking the difference of these energies gives an estimate for the broadening

$$\Delta E_l = E_+(l) - E_-(l) = \frac{c}{\sqrt{\nu}}\, l(l-1), \tag{5.39}$$

which is proportional to the trap curvature parameter c and grows quadratically with the excitation angular momentum l, as we observed in Section 5.2.3. Interestingly, the prefactor depends on the filling fraction of the underlying fractional quantum Hall state. Notice that the normalized first moment of the dynamic structure factor $\omega_1(l)$ Eq. (5.16) coincides in this simple case with the average

$$\omega_1(l) = \frac{E_+ + E_-}{2} = \Omega l \tag{5.40}$$

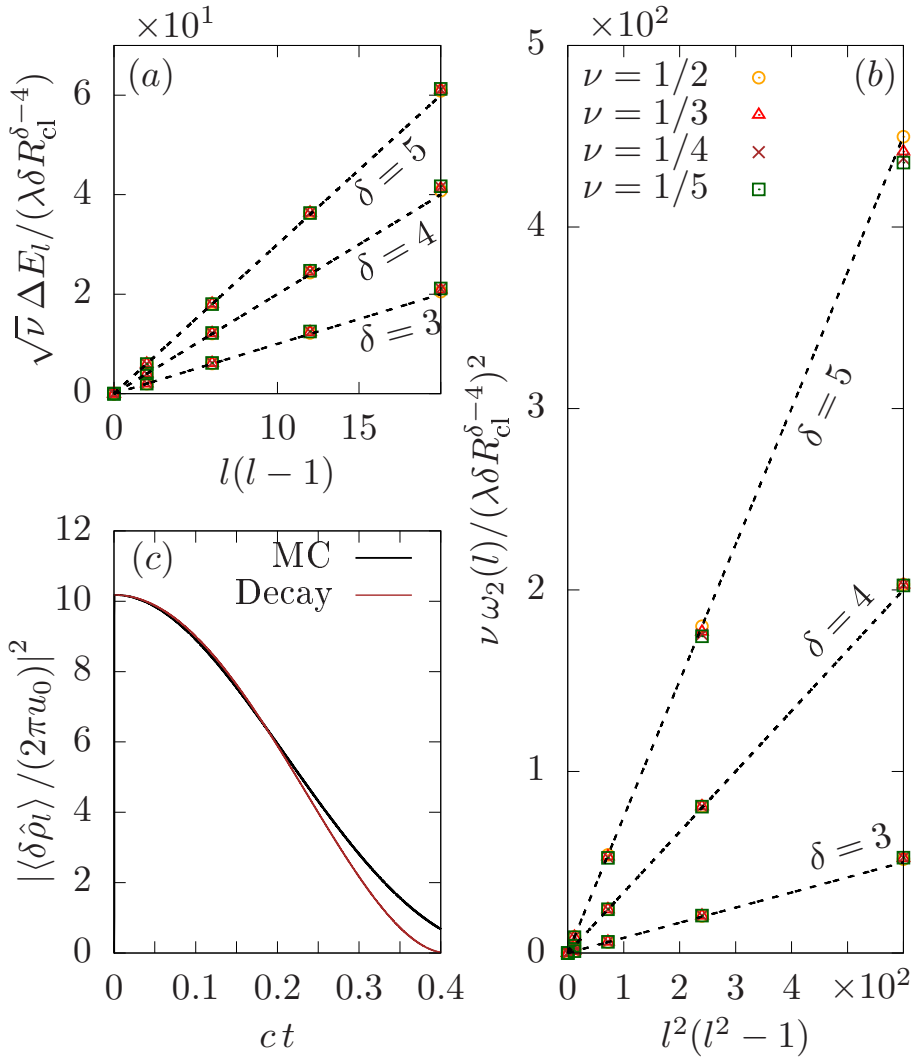

Figure 5.11: (a) Plot of the (normalized) total width $E_+(l) - E_-(l)$ defined in Eq. (5.39) as a function of the (rescaled) angular momentum $l(l-1)$. The results of full 2D numerical calculations for various values of ν and δ accurately follow the behaviour $\sqrt{\nu}\Delta E_l/(\lambda\delta R_{cl}^{\delta-4}) = (\delta-2)l(l-1)$ predicted by Eq. (5.39) together with Eq. (5.14), shown here as black-dashed lines. (b) Plot of the second moment $\omega_2(l)$ of the dynamic structure factor as a function of the (rescaled) angular momentum $l^2(l^2-1)$. The results of the full 2D numerical calculations for various values of ν and δ accurately follow the behaviour $\nu\omega_2(l)/(\lambda\delta R_{cl}^{\delta-4})^2 = (\delta-2)^2 l^2(l^2-1)/12$ predicted by Eq. (5.42) together with Eq. (5.14), shown here as black-dashed lines. (c) Time-evolution of the square modulus of the fundamental component of the edge-density response in response of a weak pulsed excitation of strength u_0 and angular momentum $l = 3$. The black curve is the result of the full 2D numerical calculation, while the brown curve is the the short-time decay prediction of Eq. (5.46). In all panels, a fractional quantum Hall cloud of $N = 25$ particles is considered.

which highlights, as we foretold in the discussion in Sec. 5.3, the importance of the

fermion interaction term, or, equivalently, of the additional bosonic dispersive term.

An alternative measure of the dynamic structure factor broadening is provided by its second (normalized) moment

$$\omega_2(l) = \frac{\int (\omega - \omega_1(l))^2 S_l(\omega)\, d\omega}{\int S_l(\omega)\, d\omega}\,, \tag{5.41}$$

which, for the flat dynamic structure factor of non-interacting fermions, is equal to

$$\omega_2(l) = \frac{c^2}{\nu}\,\frac{l^2(l^2-1)}{12}. \tag{5.42}$$

The two broadening measures Eq. (5.39) and Eq. (5.42) are compared with microscopic Monte Carlo data for different values of the confinement trap exponent δ and of the filling factor ν in Fig. 5.11(a) and Fig. 5.11(b) respectively. For both quantities, the analytical predictions appear to accurately capture the numerical data, especially for low values of the filling fraction ν and of the confinement exponent δ: this regime allows in fact to minimize effects caused by the gradient of the curvature parameter c, which is approximated as a constant in the nonlinear χLL theory. As a further evidence of our conclusions, more numerical results on the quartic $\delta = 4$ case are shown in the Appendix D.

From an experimental perspective, beside the employment of spectroscopic probes [249] the second moment [Eq. (5.42)] of the dynamic structure factor can be indirectly measured by looking at the short- and moderate-time part of the temporal decay of edge-density excitations on top of the fractional quantum Hall droplet. Consider that the droplet is excited via a time-dependent perturbation $U(\theta, t)$ whose strength at the classical radius is almost constant. Using linear perturbation theory (see Eq. (5.10) and Appendix C) we obtain that

$$\langle \delta\hat{\rho}(\theta, t)\rangle = \frac{1}{\pi}\Im\left[\sum_l e^{il\theta}\int \widetilde{U}_l(\omega)\, S_l(\omega)\, e^{-i\omega t}\, d\omega\right] \tag{5.43}$$

where $\widetilde{U}_l(\omega)$ is the Fourier transform of the excitation potential and $S_l(\omega)$ the dynamic structure factor defined in Eq. (5.11).

Assuming that the spectrum $\widetilde{U}_l(\omega)$ of the perturbation is approximately constant across the peak of $S_l(\omega)$ (this requires that the excitation pulse is sufficiently short compared to the characteristic time-scale of the edge dynamics), we can approximate

the integral appearing on the right-hand side of (5.43) as

$$\widetilde{U}_l(\omega_1(l))e^{-i\omega_1(l)t}\int S_l(\omega)\, e^{-i(\omega-\omega_1(l))t}\, d\omega. \tag{5.44}$$

Up to not-too-large times, the exponential inside this integral can be expanded to second order, which gives

$$\widetilde{U}_l(\omega_1(l))e^{-i\omega_1(l)t}\int S_l(\omega)\, \left(1-\frac{(\omega-\omega_1(l))^2t^2}{2}\right) d\omega\,. \tag{5.45}$$

Using the sum-rule $\int S_l(\omega)d\omega = l\Theta(l)\nu$ for the edge static structure factor of a fractional quantum Hall droplet in the thermodynamic limit (Θ is here the Heaviside step function), we finally get

$$\langle\delta\hat{\rho}(\theta,t)\rangle \simeq -\frac{\nu}{\pi}\sum_{l>0}\left(1-\frac{\omega_2(l)t^2}{2}\right)\frac{\partial}{\partial\theta}\,\Re\left[e^{i(l\theta-\omega_1(l)t)}\widetilde{U}_l(\omega_1(l))\right]. \tag{5.46}$$

This shows that, at short times after the excitation, the decay of density modes follows a quadratic law. Its time-scale is set by the second moment of the dynamic structure factor which, in turn, depends on the curvature parameter c and on the filling fraction of the bulk, ν according to Eq.(5.42). As a sidenote, notice that it is indeed $\omega_1(l)$ [Eq. (5.16)] which sets the propagation velocity.

The accuracy of the approximated expression Eq. (5.46) at short times is successfully validated against the exact evolution in Fig. 5.11(c) in response to an excitation carrying definite angular momentum. These results support a physical interpretation of the edge excitation decay as the result of the decoherence of the different particle-hole excitations that we originally proposed in [229] for the integer quantum Hall case.

To conclude this Section, it is interesting to highlight that the formulas Eq. (5.39) and Eq. (5.42) for the dynamic structure factor broadening, obtained neglecting interactions between fermions, remain accurate well outside the regime where interactions are irrelevant. The non-interacting fermion approximation predicts in fact the dynamic structure factor to be flat and centered at the linear χLL dispersion [Eq. (5.40)] $\omega_1(l) = \Omega l$; however, as one can see in Fig. 5.10, while $\omega_1(l)$ only slightly deviates from the linear behaviour over the values of l considered in Fig. 5.11, the dynamic structure factor rapidly starts acquiring a highly non-trivial lineshape much before the non-interacting fermion approximation for the broadening breaks down. Analogously, while the broadening ΔE_l in Eq.(5.39) compares remarkably well with the full 2D numerical calculation, the threshold energies $E_\pm$ predicted by the non

interacting model Eq. (5.37) separately do not.

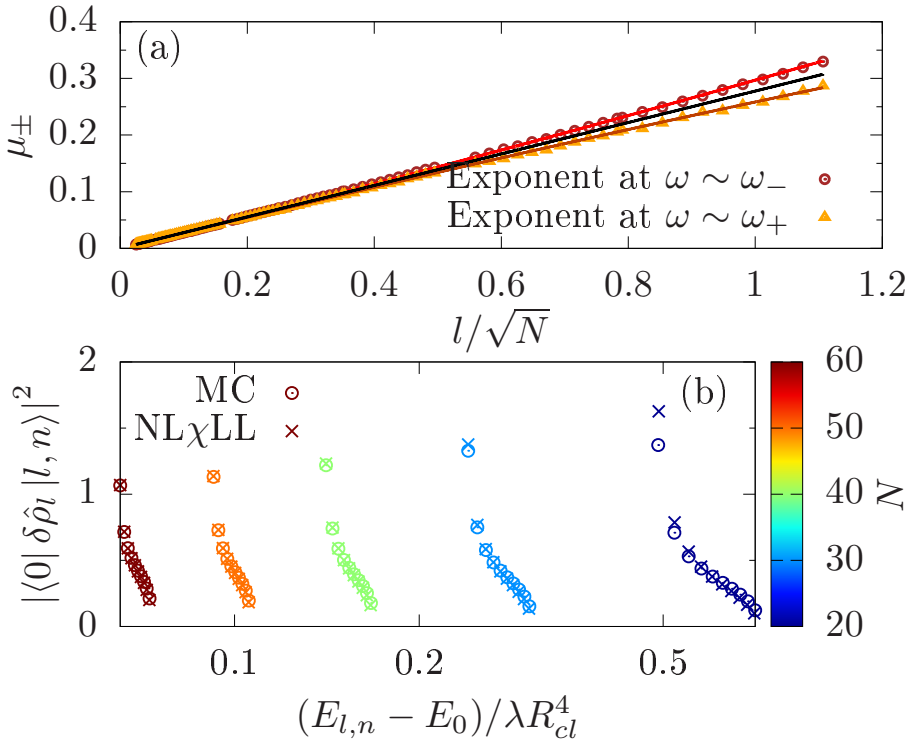

Figure 5.12: (a) Plot of the dynamic structure factor threshold exponents $\mu_\pm$ as a function of the excitation momentum $q = l/R_{cl} \propto l/\sqrt{N}$, extracted from the predictions of the nonlinear χLL model of Eq. (5.25) by means of a power-law fit to the dynamic structure factor data close to the lower and upper threshold. (b) Comparison between the microscopic dynamic structure factor weigths extracted from 2D numerical calculations (circles) and those obtained from the nonlinear χLL model Eq. (5.25) (crosses) for different number of particles N (colorscale) at fixed angular momentum $l = 10$. The dynamic structure factor weights are plotted against the excitation energies in logarithmic scale.

5.4.3 Threshold singularities of the dynamic structure factor

On top of the broadening effect discussed in the previous Subsection, the curves for the dynamic structure factor plotted in Fig. 5.10(b) for growing l clearly show the appearance of some peculiar singular behaviour close to its energy thresholds. Such features are reminiscent of those emerging from the theory of non-linear (non-chiral) Luttinger liquids [219] and will be the subject of the present Section.

The main challenge in the theoretical study of both the bosonic and fermionic models of Eq. (5.25) and Eq. (5.33) comes from the fact that both the group velocity

dispersion and the non-linearity are proportional to the same curvature parameter c. For this reason, perturbative approaches based on a hydrodynamic formulation where dispersion dominates over interactions [223, 224] do not give consistent results. On the other hand, many features of the fermionic theory Eq. (5.33), in particular the behaviour around the energy thresholds, can be be successfully studied making use of so-called "mobile-impurity" approaches.

Within a non-interacting fermion model, the lower threshold corresponds in fact to the displacement of a particle from deep below the Fermi point to right above it and, correspondingly, the upper threshold corresponds to the displacement of a particle right at the Fermi point up to high energy states. This can be seen as the creation of a deep-hole or a high-energy-particle accompanied by a slight shift of the Fermi point (sketched in the last or first row of Fig. 5.13, respectively). Once we include again interactions, if we focus on the threshold regions, the full model Eq. (5.33) can therefore be replaced by an effective two-band model, namely a (chiral) Luttinger liquid at $l \sim 0$ and a single deep-hole/high-energy-particle at l [240, 250, 219]. This latter then acts as an impurity off which particles close to the Fermi point, that is the Luttinger liquid, can scatter by small-momentum transfers. As discussed in detail in [240], this then leads to a power-law enhancement at the lower-energy threshold $\omega_-(l)$ and a power-law suppression at the high-energy one $\omega_+(l)$. In formulas, we have that

$$\begin{cases} S_l(\omega \sim \omega_-) \propto \theta(\omega - \omega_-) \left(\frac{1}{\omega - \omega_-}\right)^{\mu_-} \\ S_l(\omega \sim \omega_+) \propto \theta(\omega_+ - \omega) \left(\omega_+ - \omega\right)^{\mu_+} \end{cases} \tag{5.47}$$

where the exponents

$$\mu_+ \simeq \mu_- \simeq \frac{2\alpha l}{c/\sqrt{\nu}} = 2\beta_\nu \sqrt{\nu}\, \frac{l}{R_{cl}} \tag{5.48}$$

only depend on the excitation momentum l/R_{cl} and the bulk filling fraction ν, but not on the specific values of the non-universal trap parameters Ω and c. Even though a finite value of c is essential for the emergence of the singular power-law behaviour, the value of the exponents turn out to be universal properties of strongly correlated fractional quantum Hall fluids with short-ranged interactions, a manifestation of strong bulk correlations extending all the way through the edge. This peculiar universal behaviour emerges because the exponent is set by $2m^*\alpha$, but both the effective mass m^* and the interaction strength proportional to α emerge because of the presence of the trap causing a gradient of angular velocity at the cloud's edge. So, while α is directly proportional to c, the effective mass m^* is inversely proportional to it: the curvature parameter c therefore cancels out from the exponents $\mu_\pm$.

A direct validation of the power-law behaviour via microscopic simulations of

the fractional quantum Hall droplet is made difficult by the fast growth of the Hilbert space dimension $\mathcal{D}$ at the large angular momentum l values (sub-exponential, $\log \mathcal{D} \propto \sqrt{l}$, see the Footnote 2) that are needed to interpolate power-law behaviours at both thresholds. However, since the nonlinear χLL Hamiltonian gives results which are in quantitative agreement with microscopic Monte-Carlo diagonalization, we restrict our numerical analysis to this former theory which grants us access to the large l values that are needed to precisely extract the power law exponents. To corroborate this statement, in Fig. 5.12(b) we compare the results of the nonlinear χLL theory with microscopic results obtained from Monte Carlo diagonalization at fixed angular momentum l for increasing number of particles N: as the excitation wavevector $\sim l/R_{cl} \propto l/\sqrt{N}$ decreases the effective model becomes more accurate, so we can expect it to correctly account for the behaviour of the dynamic structure factor in the thermodynamic limit.

The numerical predictions for the exponents at the lower and higher thresholds are plotted in Fig. 5.12(a): a good agreement with the analytical prediction of Eq. (5.48) is found for small wavevectors q, with quadratic corrections at higher q phenomenologically compatible with the form

$$\mu_{\mp} = \pm \left[\left(1 \pm \frac{\alpha l}{c/\sqrt{\nu}} \right)^2 - 1 \right]. \tag{5.49}$$

These results illustrate the power of the refermionized theory in capturing the peculiar behaviour of the charge-zero sector of fractional quantum Hall edges and show that they behave as a peculiar nonlinear Luttinger liquid [219].

5.4.4 Fine structure of the dynamic structure factor

Going beyond the mesoscopic quantities investigated in the previous Subsections, it is interesting to see how the refermionized theory provides an interesting physical interpretation also for the microscopic structure of the eigenstates, in particular the values of the matrix elements $|\langle 0| \delta\hat{\rho}_l |l, n\rangle|^2$ entering the dynamic structure factor. As an example, a plot of these matrix elements is displayed in Fig. 5.14 for the $l = 10$ case.

From the fermionic model, we expect that at the level of the free fermion approximation, the $\delta\hat{\rho}_l$ operator only connects the ground state Fermi sea to the single particle-hole states on top of it (first, second, fourth and fifth rows of Fig. 5.13) and the l such transitions have the same amplitude. This simple picture is of course modified by the presence of fermionic interactions, so that non-zero matrix elements

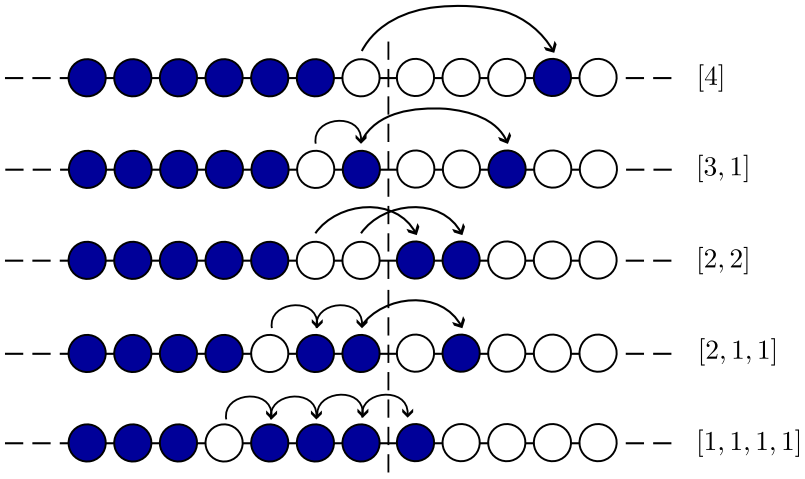

Figure 5.13: Schematic diagram of the different particle-hole excitations (black-arrows) across the Fermi point (vertical-dashed lines) at a fixed angular momentum $l = 4$. For each state, the corresponding partition of $l = 4$ are indicated on the right-hand side of the plot.

may appear also for states corresponding to several particle-hole excitations (third line of Fig. 5.13).

This expectation is fully confirmed by the numerical data shown in Fig. 5.14. As it is displayed in Fig.E.2 of Appendix E, the interacting eigenstates are found to maintain a dominant weight on the particle-hole basis of non-interacting fermions. On this basis, in Fig. 5.14 we keep labelling the states in terms of the partition η of the non-interacting particle-hole state which has the largest weight on the eigenstate. As usual, a partition $\eta = [\eta_1, \eta_2, \eta_3 \ldots]$ is defined to have $\eta_1 \geq \eta_2 \geq \eta_3 \geq \ldots$ and corresponds to a state where, starting from a filled Fermi sea, the highest energy particle is promoted by η_1 orbitals, the second-highest one by η_2 orbitals and so on: for the sake of clarity, a few examples of partitions and of the corresponding states are illustrated in Fig. 5.13.

From Fig. 5.14, it is apparent how the matrix elements tend to organize in a hierarchical way. Besides the principal sequence of highest-weight states corresponding to single particle-hole excitations discussed above, well-distinguishable secondary sequences of states are visible, carrying a much weaker dynamic structure factor weight. For all these data-points, an excellent agreement is found between the non-linear χLL model and the full two-dimensional calculation.

While this latter method gets quickly impracticable for larger values of l, the non-linear χLL model provides a manageable and reliable approach up to much larger l values. An example of such calculation is displayed in Fig.5.15: thanks to the larger

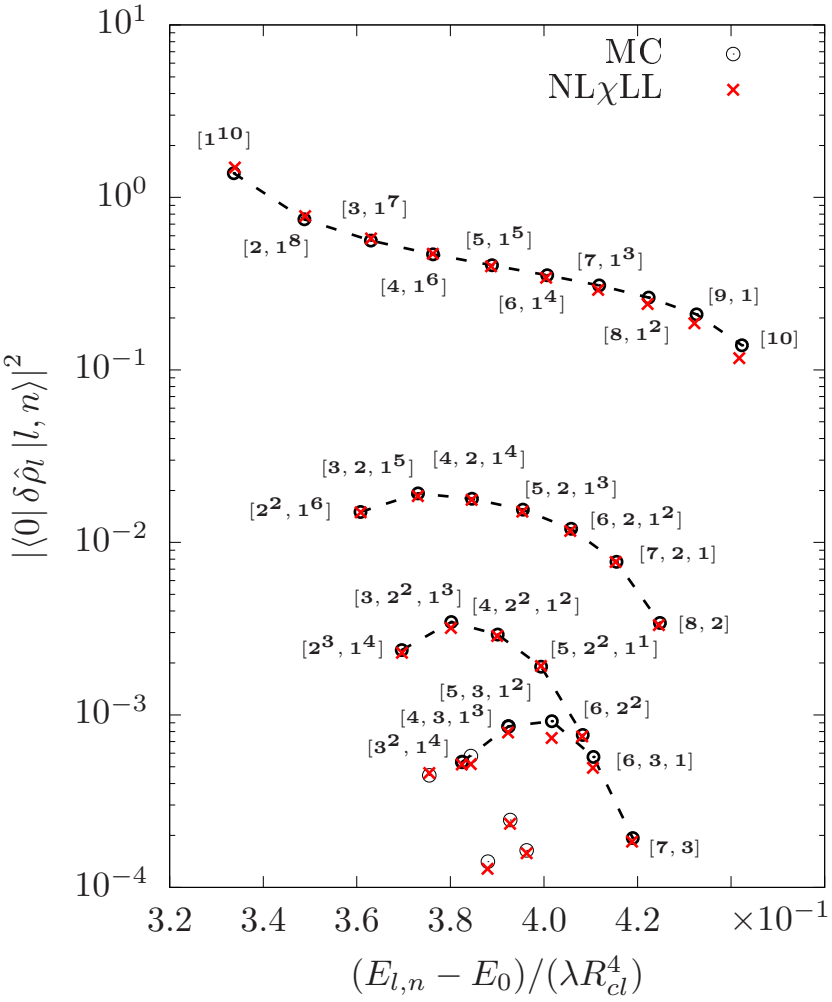

Figure 5.14: Plot of the dynamic structure factor weights $|\,\langle 0|\,\delta\hat{\rho}_l\,|l,n\rangle\,|^2$ against the excitation energy $E_{l,n} - E_0$ for a $l = 10$ excitation of a fractional quantum Hall cloud of $N = 25$ bosons at filling $\nu = 1/2$ confined by a quartic $\delta = 4$ trap. The black circles are the result of a full 2D numerical calculation and are compared to the predictions of the nonlinear χLL model [Eq. (5.25)]. Differently from Fig. 5.10(b), the weights are plotted here in logarithmic scale. All points with a sizable dynamic structure factor weight are labeled in terms of the partition η corresponding to the particle-hole excitation with the largest overlap with the eigenstate.

$l = 20$ value, a larger number of secondary structures is clearly discernible. Interestingly, these structures can be grouped together (black-dashed lines) by considering squeezing processes in which the high-energy fermion looses one unit of angular momentum by exciting one more fermion across the Fermi point that delimits the Fermi sea of filled states, e.g. $[7,3] \to [6,3,1] \to [5,3,1,1] \to \ldots [3,3,1,1,1,1]$.

As a final point, it is interesting to look at these structures from the point of view of the two-dimensional fractional quantum Hall cloud. Remarkably, we find

a large overlap ($\gtrsim$ 95% for the considered system sizes) between the eigenstates of the 2D quantum Hall system and Jack polynomial states [251, 252] labeled by the *same* partitions η. The interested reader can find a color plot of the overlap matrix in Fig.E.1 of Appendix E, together with a brief description of the numerical method used to compute them. While no complete explanation of this remarkable result is available yet, it hints at a deep relation between the Pauli principle for the fermions of the refermionized theory and the generalized Pauli principle naturally implemented by the Jacks [253]. Getting an understanding of this relation will be the subject of future work.

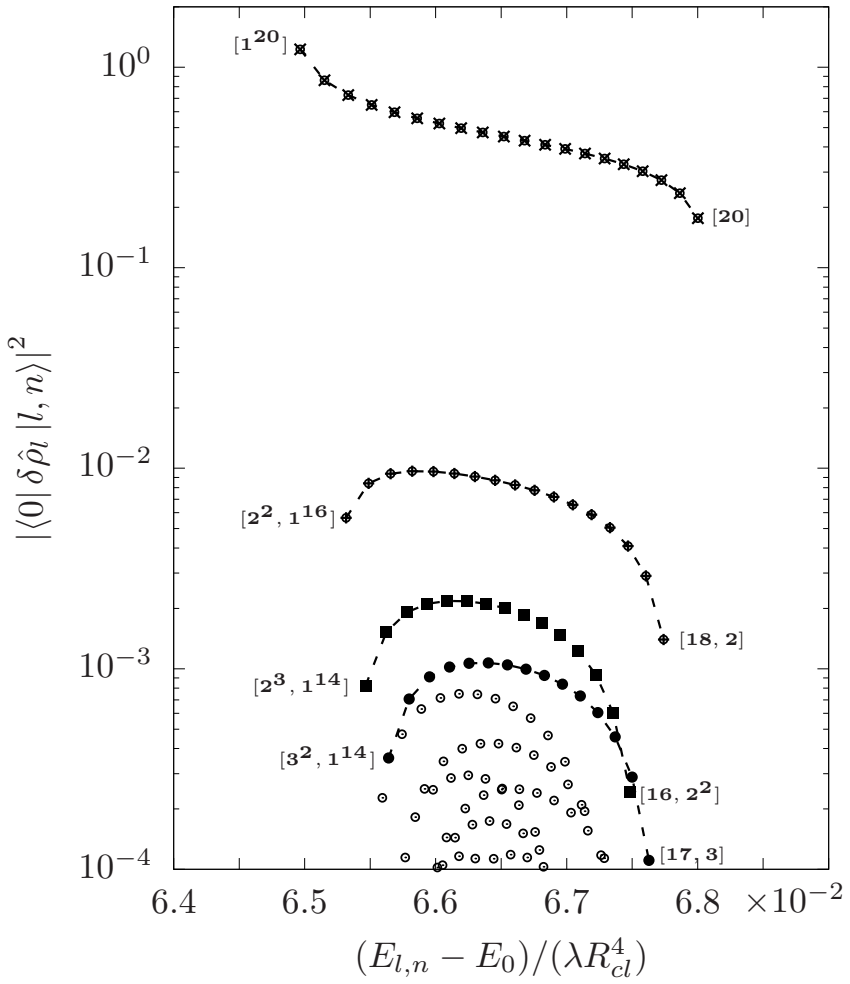

Figure 5.15: Dynamic structure factor weights $|\,\langle 0|\,\delta\hat{\rho}_l\,|l,n\rangle\,|^2$ against the excitation energy $E_{l,n} - E_0$, for a $l = 20$ excitation of a fractional quantum Hall cloud of $N = 300$ bosons at filling $\nu = 1/2$, confined by a quartic $\delta = 4$ trap. The points have been computed via the nonlinear χLL model of Eq. (5.25).

5.4.5 Spectral function

Another quantity of great interest in the study of Luttinger liquids is the spectral function, which describes the probability of removing a particle from the system at a given energy. This quantity is relevant for the study of particle tunneling into χLL and is connected to power-laws in the current-voltage characteristic of fractional quantum Hall systems [180]. Recently it was shown to contain relevant information on Haldane fractional exclusion statistics [62] and to be directly accessible to experiments in various synthetic setups [62, 159].

Focusing on the bosonic Laughlin state at $\nu = 1/2$, in this Subsection we show how the results of the full two-dimensional calculation of the spectral function are quantitatively captured by the nonlinear χLL model of Eq. (5.25) once this is supplemented with the bosonized form of the particle annihilation operator [30] we reviewed in Sec. 4.2.2

$$\hat{\psi}(\theta) = e^{-i\hat{\phi}(\theta)/\nu}, \tag{5.50}$$

which is defined in terms of a bosonic phase operator $\hat{\phi}$ related to the density through $\hat{\rho} = -\partial_\theta \hat{\phi}/2\pi$ [30, 31]. The refermionized approach is then used to shine physical light on the peculiar properties of the spectral function.

Comparison with full 2D numerical calculations

As usual, we define the spectral function as

$$A_l(\omega) = \sum_f \left| \langle f | \, \hat{a}_{(N-1)/\nu - l} \, |0\rangle \right|^2 \delta(\omega - \omega_{f,0}). \tag{5.51}$$

where the sum runs over all $N-1$ particle states $|f\rangle$ and $|0\rangle$ is the N particle Laughlin ground state. Here, $\hat{a}_{(N-1)/\nu-l}$ annihilates a particle with angular momentum $(N-1)/\nu - l = \Delta l$. The reason behind this notation for the angular momentum will be clarified shortly.

Let us first notice that, provided the anharmonic confinement does not induce mixing of the low-lying edge excitations with states above the many-body gap, the frequency-integrated $A_l = \int d\omega \, A_l(\omega)$ at fixed l is independent of the the particular confinement as the eigenstates $|f\rangle$ will be connected by a unitary transformation. The standard χLL result $A_l \propto l^{1/\nu - 1}$ (at small values of l) is therefore maintained in spite of the spectral function being broadened and having a highly non-trivial line-shape. As such, we focus here on the energy-resolved $A_l(\omega)$.

The initial N particle Laughlin state has total angular momentum $L_0^{(N)} = N(N -$

$1)/(2\nu)$. The occupied single-particle orbital of largest angular momentum has angular momentum $(N-1)/\nu$, so the angular momentum L_f of the final state after removing one particle lies in the range

$$\frac{(N-1)(N-2)}{2\nu} \leq L_f \leq \frac{N(N-1)}{2\nu}\,, \tag{5.52}$$

that is, between $L_0^{(N-1)}$ and $L_0^{(N)}$. For convenience, we will focus our attention on the removal of a particle close to the system's edge; such a particle carries a large angular momentum, $\lesssim (N-1)/\nu$. In this way, the final state can be interpreted as a low-angular-momentum edge-excitation with angular momentum l with respect to the Laughlin ground state of $N-1$ particles; therefore, the relevant matrix elements can be studied through the nonlinear χLL model of (5.25).

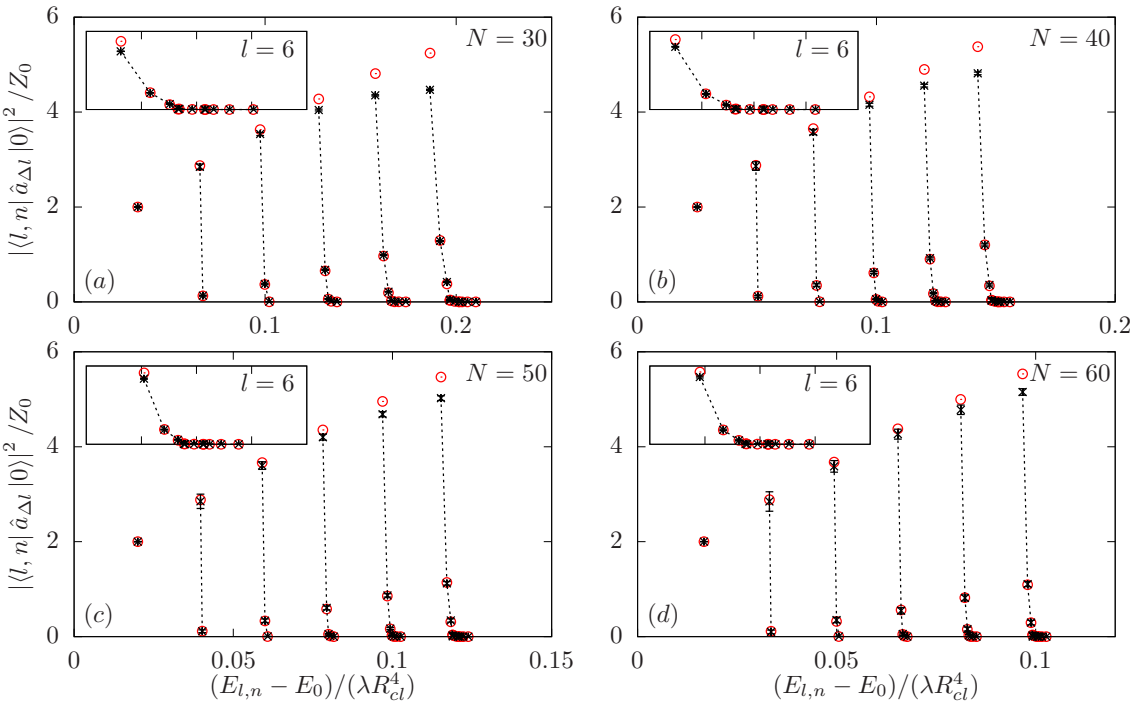

Figure 5.16: Spectral function weight $|\,\langle f|\,\hat{a}_{(N-1)/\nu-l}\,|0\rangle\,|^2$, normalized to the $l=0$ Laughlin-Laughlin matrix element $Z_0 = |\,\langle f|\,\hat{a}_{(N-1)/\nu}\,|0\rangle\,|^2$. the result of the full 2D numerical calculation for bosons at a constant filling $\nu = 1/2$ in a quartic $\delta = 4$ trap but different numbers of particles in each panel: (a) $N = 30$, (b) $N = 40$, (c) $N = 50$ and (d) $N = 60$. The red circles display the results of the nonlinear χLL model of Eq. (5.25). The insets display a magnified view of the $l = 6$ curves. Amplitudes relative to different l-sectors ($l = 1 \ldots 6$) have been joined with black dashed lines as a guide for the eye. The point corresponding to $l = 0$ is not shown as it equals 1 by definition due to the normalization factor.

Within our theoretical framework, we calculate the matrix elements appearing in

Eq. 5.51 through Monte-Carlo sampling on the full two-dimensional model, as described in Appendix A.3. The results of this microscopic calculation are shown in Fig. 5.16 and are compared to the prediction of the nonlinear χLL model. In this latter calculation, the single-particle destruction operators $\hat{a}_{\Delta l}$ of the full two-dimensional theory are interpreted within the χLL framework as

$$\hat{a}_{\Delta l} = \int d\theta \, \frac{e^{i\,\Delta l\,\theta}}{\sqrt{2\pi}} \, \hat{\psi}(\theta)\,, \tag{5.53}$$

where the bosonized form of the annihilation operator Eq.(5.50) is used. In order to remove an overall normalization factor which ambiguously depends on the cutoff length-scale of the effective edge-boson theory [254, 235, 234, 218, 206], all matrix elements have been normalized to the Laughlin-Laughlin transition matrix element $Z_0 = |\,\langle 0|\, a_{(N-1)/\nu}\,|0\rangle\,|^2$. As expected, only a limited number of states within each angular momentum $L_f = L_0^{(N-1)} + l$ sector have a significant matrix element.

A good qualitative and quantitative agreement between the two theories is clearly visible in Fig. 5.16, in particular for the low-energy states at low l. At large l, a good agreement is recovered as the system is made larger and the wavelength gets correspondingly longer. Most interestingly, these numerical results prove the correctness of the exponential expression Eq.(5.50) for the particle annihilation operator in terms of the bosonic field within our nonlinear χLL model Eq. (5.25).

Behaviour of the spectral function at the energy thresholds

Following [62] and based on the microscopic insight discussed in the previous Sec.5.4.4, we can identify the states corresponding to the energetic thresholds of $A_l(\omega)$: the lower threshold corresponds to the state labelled by the partition $[1^l]$, while the upper threshold corresponds to the state of partition $[2^{l/2}]$ if l is even or $[2^{(l-1)/2}, 1]$ if l is odd. These partitions have a simple interpretation in terms of the fermionic model: as in the dynamic structure factor case, the state at the lower threshold of the spectral function has a deep-hole at $\sim -l$ (an impurity) off which particles at the Fermi point at $l = 0$ (i.e. the Luttinger liquid) can scatter with small angular momentum exchanges. On the other hand, the state at the upper threshold displays a pair of deep holes at $\sim -l/2$ and dramatically differs from the (higher energy) state with a high-energy particle at $\sim l$ related to the upper threshold of the dynamic structure factor. Therefore, the upper threshold of the spectral function does not correspond to the highest energy eigenstate at the given angular momentum l.

For small systems, our results are in agreement with exact diagonalization results and with the counting prescription derived from Haldane's fractional exclusion

statistics principle [255, 253] as discussed in [62]. Thanks to the larger values of N accessible to our calculations, we find that this counting prescription remains accurate for odd values of l for growing N, while for even l one state ends up eventually losing all its spectral function weight. A precursor of this difference can already be appreciated for the moderate system sizes considered in [62]: a single state has a systematically smaller spectral weight for even l than for odd l values. This different behaviour can be attributed to the qualitatively different structure of the state with the smallest possible spectral function weight at a given l, that is the state closest to the upper threshold, which corresponds to the $[2^{l/2}]$ and $[2^{(l-1)/2}, 1]$ partitions for respectively even and odd values of l. This unexpected suppression of the spectral weight is even more remarkable if one thinks the state of partition $[2^{l/2}]$ as the result of removing one particle of well-defined angular momentum $(N-1)/\nu - l$ from the N particle Laughlin state partition, which is equivalent to the creation of a double quasihole at the same angular momentum. All other states with non-zero spectral weight correspond instead to the insertion of two quasiholes with distinct values of the angular momentum.

In analogy to the dynamic structure factor shown in Fig. 5.10, also the spectral function displays a marked singularity at the lower threshold within each l sector. The characterization of the functional form of the threshold behaviour however appears to be far more challenging than in the dynamic structure factor case, and no robust conclusion can yet be drawn from the available theoretical insight and numerical data.

From the theoretical side, a study of the spectral function threshold within the bosonized theory is made difficult by the exponential form Eq. (5.50) of the single-particle annihilation operator, to be contrasted to the expression Eq. (5.11) of the dynamic structure factor that directly involves the density operator $\hat{\rho}$. It is reasonable to think that the refermionized model may still be relevant for extracting information on the spectral function, especially at the lower energy threshold which, as we discussed above, corresponds to a simple situation in which a Luttinger liquid scatters from a deep-hole. However, a naive attempt to express the bosonized form of the particle annihilation operator Eq. (5.50) in terms of the fermions $e^{-i\hat{\phi}(\theta)/\nu} = e^{-i\hat{\phi}'(\theta)/\sqrt{\nu}} \sim \Psi^{1/\sqrt{\nu}}$ leads to an ill-defined operator, whose value in the characterization of the spectral function singularities using a mobile-impurity model [219] is far from obvious and calls for more sophisticated treatment.

Serious difficulties are also present from the numerical side. Testing the power-law behaviour by fitting the spectral function $A_l(\omega)$ computed with the nonlinear χLL model requires working at even larger l values than for the dynamic structure factor

case, as the number of points that are available to the fit for given l is roughly halved as compared to the dynamic structure factor case. Moving to higher l values forces to work in larger Hilbert spaces leading to an intractable numerical complexity of the calculation.

In spite of these theoretical difficulties, the spectral function remains a quantity of key experimental interest. On one hand, it can be directly probed in the single-particle spectroscopy experiments proposed for fractional quantum Hall clouds of atoms or photons in [62, 159]. Specially in the photonic case the spectral function is directly observable from the emission spectrum of the fluid, so our predictions are of direct application to the experiments. On the other hand, a complete understanding of the spectral function will be instrumental to attack the harder questions related to the non-perturbative dynamics of the edge: large density dips at the edge of the fractional quantum Hall cloud can in fact be be produced by selectively removing particles close to the edge of the cloud. It is therefore very interesting to investigate the emerging non-linear Korteweg-de Vries hydrodynamics described by Eq. (5.25), which, analogously to what occurs at the classical level, may lead to shockwaves and solitons that chirally propagate along the edge, a possibility already pointed out in [226, 227].

5.5 Hard-wall confinement

We end this chapter by investigating the edge-mode physics in the case of hard-wall confinements [251, 252], steeply-rising in real-space over a lengthscale which is short compared to the magnetic length. We specifically consider $V_{\rm conf}(r) = \lambda\Theta(r - R)$ which however, contrary to [256, 251, 252], we consider not to be steep when projected on the lowest Landau level

$$U_l = \int |\Phi_l(z)|^2 \, \lambda \, \Theta\left(|z| - R\right) \, dz = \frac{\lambda}{l!} \, \Gamma_{l+1}\left(\frac{R^2}{2}\right). \tag{5.54}$$

Indeed, provided $R_{cl} \sim R$, at the edge of the quantum Hall droplet $l \sim (N-1)/\nu$ we can expand U_l as a linear function Ωl with a small quadratic correction $cl^2/2$. In the previous equation, $\Gamma_a(z) = \int_z^\infty t^{a-1} e^{-t} dt$ is the incomplete gamma function.
In order to avoid Landau level mixing, as well as mixing with states above the many-body energy gap Δ, the wall must not be too high. Roughly speaking, we need $U_{l\sim(N-1)/\nu} \approx \lambda \lesssim \Delta$.

We here show that under these conditions essentially the same physics as the one investigated in the previous Sections emerges in this case, provided one replaces the

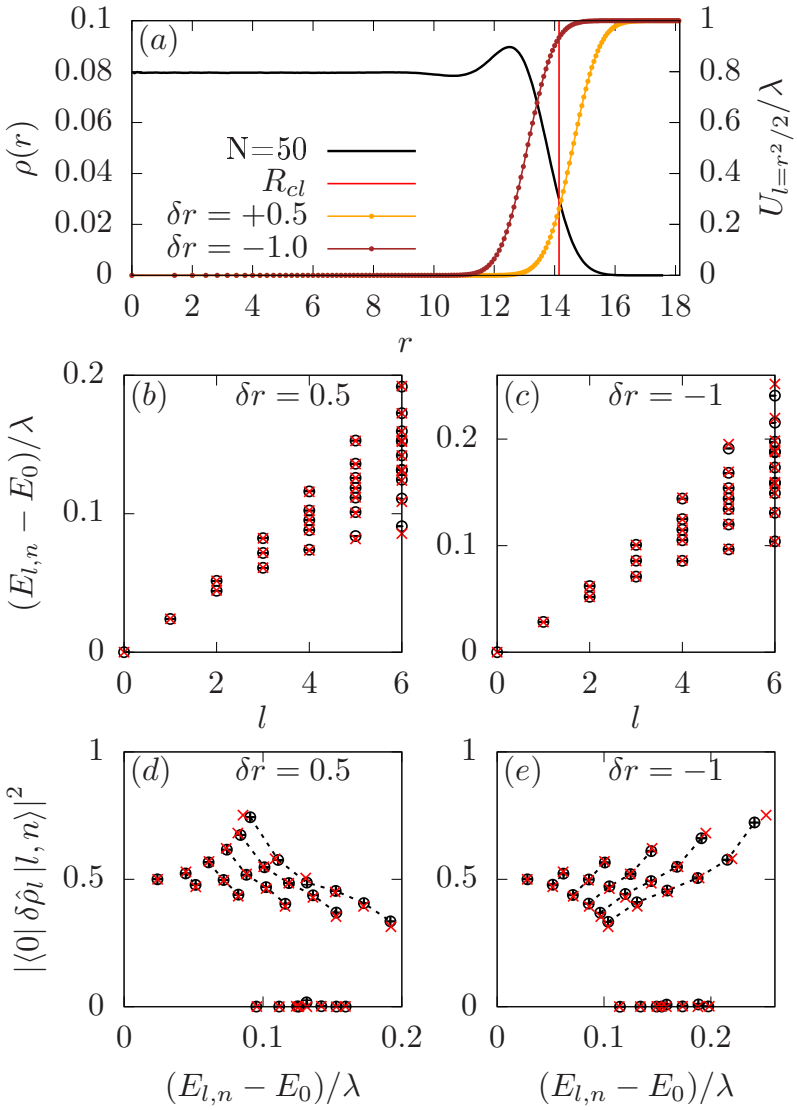

Figure 5.17: (a) Laughlin state of $N = 50$ bosons at half filling, $\nu = 1/2$ (black curve, the values are on the left-hand side y-axis). The red vertical line indicates the position of the classical radius. Orange and brown line-points denote the confinement U_l (the values are on the right-hand side y-axis), plotted in real space by identifying its l component with the average radial position of the corresponding lowest Landau level orbital $\Phi_l(z)$ in the circular gauge, $r = \sqrt{2l}$. The two curves refer to different positions of the hard-wall potential, $R = R_{cl} + \delta r$. (b-c) Excitation spectrum of the system $E_{nl} - E_0$ in units of the hard-wall confinement strength λ, for the two hard-wall potentials shown in panel (a). Black-circles are microscopic Monte Carlo data, red crosses the low-energy effective model Eq. (5.25). (d-e) Dynamic structure factor weights $|\langle 0|\,|\delta\hat{\rho}_l\,|l,n\rangle\,|^2$, for the two hard-wall potentials shown in panel (a), as a function of the excitation energies $E_{nl} - E_0$. Black-circles are microscopic Monte Carlo data, red crosses the low-energy effective model Eq. (5.25). The principal emerging features of the dynamic structure factor for a fixed angular momentum l have been joined with black-dashed lines as a guide for the eye.

radial gradients of the confinement with proper angular momentum finite-differences of the projected version, as we discuss in Appendix F.

Even though highly idealized, this hard-wall case is interesting in three respects; first of all, both positive and negative angular velocity gradients c can be obtained. In the refermionized Hamiltonian Eq. (5.33) this means that the fermion effective mass m^* can become negative. Secondly, it allows us to test the nonlinear χLL model Eq. (5.25) for fractional quantum Hall fluids confined by heavily anharmonic traps, yet still close to the Luttinger fixed point. Finally, the curvature parameter c can potentially become small as compared to higher order corrections at the potential U_l inflection point, leading to different emergent physics of the edge excitations. Indeed, we expect that in such a regime both the cubic non-linearity term $\propto \hat{\rho}^3$ and the quadratic dispersive correction $\propto (\partial_\theta \hat{\rho})^2$ term appearing in Eq. (5.25) could become small when compared to higher order corrections. In a future work we will try to address such a case, so as to understand how this can modify the emergent Kortweg-de Vries-like hydrodynamics.

In Fig. 5.17, we show two cases, one in which m^* is positive (panels (b,d)) and the other in which it is negative (c,e). For clarity, the ground state density is plotted together with the two projected hard-wall confinement potentials in panel (a). The excitation spectrum and the edge dynamic structure factor are compared with the results obtained by diagonalizing Eq. (5.25). The parameters Ω and c have been extracted from the lowest lying energy levels using Eq. (F.1) and Eq. (5.39) respectively, because they get slightly renormalized with respect to the simpler Eq. (F.18), as we discuss in Appendix F. The model captures qualitatively (and quantitatively) the underlying microscopic behaviour in a quite broad region of parameters away from the U_l inflection point or from the super-steep regime [256, 251, 252] (which is achieved when the projected potential U_l of Eq. (5.54) grows abruptly in angular momentum space), also highlighting the universality of the low-energy Korteweg-de Vries behaviour [Eq. (5.25)] emerging in the edge dynamics of trapped fractional quantum Hall fluids, at least when the interactions are short-ranged.

Notice finally that, even though the energy spectra in the two cases (panels (b) and (c)) look alike, the emergent dynamics can be pretty different, as can be seen from the qualitative differences appearing in the edge dynamic structure factor in the two cases, Fig. 5.17(d,e). Let us also recall that we expect the power-law threshold exponent $\mu_\pm$ to be the same regardless of the curvature sign, because (see Eq. (5.48)) it does not depend on the curvature parameter c; however by looking at the panels (d,e) this could seem not to be the case. This seemingly paradoxical situation can actually be easily explained by looking at the energy thresholds of the dynamic structure

factor from the point of view of the refermionized model [Eq. (5.33)]: when the mass m^* of the fermions is positive(/negative), the particle-hole excitation giving rise to the lower threshold corresponds to a deep-hole below the Fermi point(/high-energy particle above it), and vice-versa for the higher threshold. This means that, when the sign of m^* changes, the two thresholds interchange. In particular, when m^* becomes negative the power-law enhancement(/suppression) of the dynamic structure factor is found at the upper(/lower) threshold rather than at the lower(/upper) one: in this case, most of the dynamic structure factor weight is carried by high energy states rather than low energy ones (as was the case for the anharmonic potentials we considered so-far. See for example Fig. 5.10).

5.6 Discussion and outlooks

In the following subsections we are first of all going to discuss about the experimental observability of our predictions, complementing the discussion we started in Sec. 5.1.1. After that, we will draw our conclusions and discuss the prospects of our research.

5.6.1 Experimental observability

We conclude the Chapter with a brief discussion of the actual relevance of our predictions in view of experiments with synthetic quantum matter systems, in particular trapped atomic gases for which an artillery of experimental tools is already available.

As several strategies to induce synthetic magnetic fields are nowadays well established, from rotating traps [89, 88] to combinations of optical and magnetic fields [114, 84], the open challenge is to reach sufficiently low atomic filling factors and sufficiently low temperatures to penetrate the fractional quantum Hall regime [81, 83]: an intense work is being devoted to this issue from both the theoretical [101, 104] and experimental sides, and promising preliminary observations have appeared in the literature [100, 90, 135]. In this, an important challenge is to design an adiabatic protocol for reaching a Laughlin state with large fidelity. Once the desired many-body state is generated, arbitrary confinement potentials can be generated with optical techniques [89, 257] and the response to rotating potentials of the form of Eq.(5.9) can be measured via the same tools used, e.g., to study surface excitations of rotating superfluid clouds [258].

While transverse conductivity features [Fig.5.4(a)] are independent of the shape of the confinement potential, both the group velocity dispersion and the nonlinear

effects crucially depend on the trap anharmonicity that also helps stabilizing the cloud at large rotation speeds close to the centrifugal limit. A rough estimate of the maximum potential curvature $\tilde{c}$ that the fractional quantum Hall liquid can withstand before being significantly affected is set by the many-body gap over the squared magnetic length. Since both the group velocity dispersion and the nonlinearity terms in Eq. 5.27 scale proportionally to the curvature $\tilde{c}$, and the chiral dynamics factors out as a rigid translation at $\tilde{v}$, such an upper bound on $\tilde{c}$ does not impose any restriction on the observability of interesting effects due to their interplay. It only requires that the dynamics is followed on a temporal scale much longer than the inverse many-body gap, a condition which is anyway automatically enforced upon working with a correlated many-body state.

To be more specific, let us consider again the case of ultracold bosons in the fast rotation regime already mentioned at the end of Sec.5.1.1. In this case, for a $\delta = 4$ quartic anharmonic potential, the curvature parameter can be written as $c/2\Omega_r = \lambda\hbar/M^2\Omega_r^3$. Based on the constraints discussed in the aforementioned section, the timescale for the correction of linear waves Eq. (5.17) is then set by the reciprocal of $T_l = 1/(cl^3)$, which is $10^2 \div 10^3$ longer than the timescale set by the many-body energy gap Δ. In order to be able to observe the correlated many-body state one needs to maintain the system over a timescale much longer than the reciprocal of the many-body energy gap. When the droplet gets excited by a time-dependent external potential of the form Eq. (5.9), the edge density variation $\delta\sigma$ predicted by Eq.(5.28) in the linear regime of weak excitations is proportional to $lu_0\tau/R_{\rm cl}$, where τ is the duration of the (short) Gaussian excitation pulse and u_0 is its strength [8]. Given the incompressible nature of the fractional quantum Hall fluid, the edge density variation $\delta\sigma$ then results in a corresponding variation of the cloud radius $\delta R/R_{\rm cl} = \delta\sigma\,\nu/(2\pi\,R_{\rm cl}) \sim lu_0\tau\nu/N$ which can be detected either in-situ or, if needed, after a time-of-flight expansion: as one can see in Fig.5.8, the relative change in the cloud radius can be a significant fraction of its equilibrium value, which supports the experimental observability of our predictions.

A different strategy to observe strong nonlinear dynamics and highlight Korteweg-de Vries behaviour would be to induce a spatially localised density modulation by selectively removing a controlled number of particles in the vicinity of the system edge [62], as we discussed in Section 5.4.5. Importantly, the nonlinear χLL model provides also in this respect quantitative information, since it is able to capture the behaviour of the spectral function of the fractional quantum Hall fluid corresponding

[8] Of course, stronger excitations could be obtained by a careful engineering of the excitation sequence that may include resonant temporal oscillations.

to the removal of a particle from the system, as we we showed in Fig. 5.16. Since the equation of motion of the edge-density operator has a Korteweg-de Vries classical limit, and such an equation is well-known to admit solitonic solutions, it will be interesting to address the emergent dynamics of the large density depletions caused by the removal of a particle close to the edge and investigate whether shock-wave-like behaviours can lead to the formation of solitons [226, 227].

5.6.2 Conclusions and perspectives

In this chapter we extensively studied the linear and nonlinear edge dynamics of a Laughlin state fractional quantum Hall droplet of macroscopic size, trapped by some anharmonic potential. Our calculations are based on a numerical method based on the expansion of the many-body wavefunction on those many-body states which lie below the many-body gap for short-ranged interaction Hamiltonians. This expansion allows us to evaluate the relevant matrix elements by means of Monte Carlo techniques, which we then use to study the dynamics and extract relevant observables.

Our calculations highlight a number of effects of direct experimental interest, both at linear and nonlinear regime: a sizable group velocity dispersion of the edge mode related to strong bulk correlations as well as significant nonlinearities, both induced by the velocity gradients at the system's edge.

From the theoretical side, the numerical results are used to build an effective one-dimensional nonlinear chiral Luttinger liquid quantum formalism describing the dynamics of the one-dimensional edge in the form of a quantum Korteweg-de Vries equation, which is quantitatively accurate. Such a model can be conveniently reformulated in terms of an effective Hamiltonian of interacting massive chiral fermions in one-dimension, which allows to extract quantiative information on the quantum Hall edge. In particular, we characterize the dynamic structure factor broadening and its threshold singularities, which exhibit power-law behaviour with universal exponents. An intriguing question which we would like to address is whether the refermionized theory of the edge modes can say something about the threshold behaviour of the spectral function.

The natural next step would be to obtain a microscopic derivation of the filling-dependent β_ν parameter related to the group velocity dispersion of the edge modes, and to put it on solid theoretical grounds, as our studies highlight the crucial role such a parameter has in the description of the edge dynamics. Indeed, not only it directly enters the dynamic structure factor threshold exponent, but also sets the

dispersive behaviour of the edge modes, endowing them with an emergent quantum-Korteweg-de Vries collective behaviour. In this respect, since the equation of motion of the edge-density operator has a true Korteweg-de Vries form in the classical limit, and such an equation is well-known to admit solitonic solutions, a future task will be to address the emergent dynamics of the large density depletions caused for example by the removal of particles close to the edge and investigate whether shock-wave-like behaviours can lead to the formation of solitons.

Since our conclusions are based on a very generic model with short-ranged interactions, they directly apply to fractional quantum Hall fluids in atomic or photonic synthetic quantum matter. As such, they are ready to be experimentally verified with state-of-the-art technology and hold a great promise as a novel probe of the bulk topological order and its anyonic excitations. Future efforts will however be devoted to the generalization of our approach to the study of long-range interacting systems and to understand how the interplay between the confinement-induced physics studied here and the non-vanishing interaction energy in a two-dimensional electron gas in solid-state devices modifies the picture we presented.

Finally, we mention here another long-term route we would like to pursue. We believe that our numerical approach can be generalized to the more exotic (and more challenging) case of non-abelian quantum Hall states, such as the Moore-Read [36] state, which do host a more complex manifold of edge modes. It would be interesting to explore the nonlinear edge physics in such a case.

On a longer run, we believe our results will contribute paving the way towards the study of fractional quantum Hall fluids as a novel platform for nonlinear quantum optics of edge excitations with unprecedented dynamical and statistical properties.

CHAPTER 6

SPIN-STATISTICS RELATION FOR BULK QUASIPARTICLES

In the previous Chapter 5 we dealt with the nonlinear dynamics at the edge of a fractional quantum Hall system. In this Chapter we are instead going to discuss about the gapped quasiparticle excitations that the bulk of a fractional quantum Hall fluid can host, and that were briefly reviewed in Sec. 3.3. In particular, we are going to talk about how a fractional spin for these quasiparticle excitations emerges, and about its relation with their fractional braiding statistics.

The spin-statistics theorem is one of the pillars of our description of the world and classifies quantum particles into bosons and fermions according to their spin, integer or half-integer [259]. It was early noted that in two spatial dimensions this relation is modified and intermediate statistics exist, called ayonic [260, 194, 195]. These objects too satisfy a generalised spin-statistics relation, and it is common nowadays to speak of fractional spin and fractional statistics [261, 262]. This type of spin-statistics relation we consider arises in a non-relativistic, non-field-theoretic context [263].

As we discussed in Chapter 3, topologically ordered fractional quantum Hall fluids are one of the prominent setups where emergent anyons have been studied. Whereas the notion of fractional statistics has been early applied to the localised bulk quasiparticles [35, 192, 39, 264], the notion of spin has been more controversial. The existence of a fractional spin satisfying a spin-statistics relation has been established for setups defined on curved spaces thanks to the coupling to the curvature of the surface [265, 266, 267, 268, 269, 270]. The extension of this notion to planar surfaces has required more care and it is not completely settled yet [271, 272, 273].

In this chapter we discuss how a spin quantum number can be naturally defined on a flat disk in terms of the (measurable) local angular-momentum of the fractional quantum Hall quasiparticles, i.e. in terms of the gauge invariant generator of rotations.

In particular, we prove with mild assumptions that this spin obeys a spin-statistics relation, and show that the gauge-invariant generator of rotations fractionalizes among the quasiparticles and the edge, leading to spin robustness. We also show that information on the braiding phase can be read off from the fractionalized angular momentum at the edge.

We then predict the value of the spin of the composite-fermion quasielectron proposed by Jain, numerically compute the associated spins and show them to satisfy the spin-statistics relation. We also analyse the case of Laughlin's quasielectron. We show that, even though it satisfies the spin-statistics relation, it carries the wrong spin and cannot thus be identified as the anti-anyon of a Laughlin's quasihole. Building from the aforementioned considerations, we argue that Laughlin's quasielectron shows the wrong spin because it has a long-range correlation tail which alters the structure of the boundary. We show this by rewriting Laughlin's quasielectron as a composite-fermion wavefunction, and construct a class of wavefunctions which interpolates between Jain's and Laughlin's quasielectrons. We numerically show that, as long as the edge the structure of the edge is not affected by the presence of the bulk excitation the value of the quasiparticle spin is robust.

We finally briefly discuss the non-Abelian case.

The contents of this chapter have been adapted from [274] and from an article which is currently being prepared.

6.1 The system

As in the previous Chapter 5, the system we consider here is a two-dimensional one, consisting of N quantum particles with mass m and charge $q > 0$ pierced by a uniform and perpendicular magnetic field $\boldsymbol{B} = B\hat{\boldsymbol{z}}$, $B > 0$. The cyclotron frequency and the magnetic length read $\omega = qB/m$ and $\ell_B = \sqrt{\hbar/(qB)}$. As we described in Sec. 3.1.1, we adopt the standard parametrization of the plane $z_j = x_j + iy_j = |z_j|e^{i\phi_j}$, suitable for lowest Landau level physics in the symmetric gauge.

The Hamiltonian we consider reads

$$H_0 = \sum_{i=1}^{N} \left(\frac{\pi_{i,x}^2 + \pi_{i,y}^2}{2m} + v(|z_i|) \right) + \sum_{i<j} V_{\text{int}}(|z_i - z_j|) \tag{6.1}$$

where $\pi_{i,a} = p_{i,a} - qA_a(z_i)$ is the particle kinetic momentum (see Sec. 2.1.1) and $v(|z|)$ is a central confining potential, analogous to those we considered in the previous chapter. Differently from the previous chapter though we here assume no specific form for the interaction energy, but only that is rotationally invariant and can thus be written as $V_{\text{int}}(|z|)$. This is for example the case of the Coulomb interaction relevant for electrons [275] or the contact interaction relevant for cold atomic gases [96] and photonic systems [49]. We also assume that the ground state of Eq. (6.1) is not degenerate and realizes an incompressible fractional quantum Hall state characterised by screening, which we discussed in the context of the Laughlin state in Sec. 3.1.3: in the presence of perturbations which do not close the energy gap the particles will arrange in such a way that the density of the system is everywhere the same except in an exponentially localized region close to the defects; gentle modifications of the confinement potentials fall into this class of perturbations, so that the specific form of $v(|z|)$ is not important if we are only interested in the bulk, and we argue that most of our conclusions carry over to cases in which the confinement potential lacks rotational invariance.

We assume the presence of N_{qp} pinning potentials located at positions $\mathbf{s}_\alpha$; using the complex-plane parametrisation $\eta_\alpha = s_{\alpha,x} + i s_{\alpha,y} = |\eta_\alpha| e^{i\theta_\alpha}$ we write:

$$H_1(\boldsymbol{\eta}) = \sum_{\alpha=1}^{N_{qp}} \sum_{i=1}^{N} V_\alpha(|z_i - \eta_\alpha|), \tag{6.2}$$

where $\boldsymbol{\eta}$ is a shorthand for $\eta_1, \ldots, \eta_{N_{qp}}$. Since the pinning potentials might be different, we keep the subscript V_α; they are all assumed to be rotationally invariant.

We denote the ground state of the total Hamiltonian $H_{\boldsymbol{\eta}} = H_0 + H_1(\boldsymbol{\eta})$ by $|\Psi_{\boldsymbol{\eta}}\rangle$; we assume that it is unique and that it localises N_{qp} quasiparticles at η_α. By virtue of screening, the density is everywhere the same as in the absence of pinning potentials, except close to the defects and at the boundary. Since the pinning potentials can be different, the quasiparticles need not be of the same kind. The set of η_α is completely arbitrary and rotational invariance is generically broken; in our discussion, we will assume that they are always kept far from the boundary. These assumptions imply that $|\Psi_{\boldsymbol{\eta}}\rangle$ is a smooth function of $\boldsymbol{\eta}$.

6.2 Gauge fixing

We introduce the operator that is the sum of the particle angular momentum and of its quasiparticle generalisation, measured in units of $\hbar$ (we use the symmetric gauge $\mathbf{A} = \frac{1}{2}\mathbf{B} \times \mathbf{r}$),

$$\tilde{L} = L_z + L'_z \tag{6.3}$$

where

$$L_z = -i \sum_{i=1}^{N} \frac{\partial}{\partial \phi_i} \tag{6.4}$$

$$L'_z = -i \sum_{\alpha=1}^{N_{qp}} \frac{\partial}{\partial \theta_\alpha}. \tag{6.5}$$

We also define the group operator $U_\beta = e^{i\beta\tilde{L}}$ that is generated by Eq. (6.3), with $\beta \in \mathbb{R}$. Physically, U_β represents the quasiparticle self-rotations over an angle β. The physical meaning of U_β is best understood by considering its effect on a generic function $f(z, \eta)$, see Fig. 6.1. As it is well known, L_z induces the rotation of the dynamical quantum particles, and thus U_β maps $z_j \to z_j e^{i\beta}$: in the z space, the function is translated backwards along a circular path and rotated. On the other hand, the operator L'_z simply generates a translation of the quasiparticles along a circular trajectory, and thus U_β maps $\eta_\alpha \to \eta_\alpha e^{i\beta}$. Globally, U_β is the composition of the two transformations. It therefore represents the quasiparticle self-rotations over an angle β.

Since the η_α are parameters, a gauge transformation $|\Psi_{\boldsymbol{\eta}}\rangle \to e^{ig(\boldsymbol{\eta})} |\Psi_{\boldsymbol{\eta}}\rangle$ using an arbitrary smooth function of the parameters $g(\boldsymbol{\eta})$ does not change the energy of the state. Our goal is to show that it is always possible to use a gauge such that the ground-state is annihilated by $\tilde{L}$ and is thus invariant under the quasiparticle self-rotation operator U_β; this result will be essential for the proof of the spin-statistics relation.

Let us first consider for simplicity the case of a single quasiparticle, $N_{qp} = 1$, so that $L'_z = -i\partial_\theta$ (we suppress the index $\alpha = 1$ for conciseness). The Hamiltonian is explicitly invariant under the action of the group: $U_\beta H_\eta U_\beta^\dagger = H_\eta$. With a quasiparticle at η, the ground state satisfies the Schrödinger equation $H_\eta |\Psi_\eta\rangle = E_\eta |\Psi_\eta\rangle$. However, E_η can only depend on $|\eta|$, and not on θ; thus, $\partial_\theta E_\eta = 0$. We conclude that $H_\eta U_\beta |\psi_\eta\rangle = U_\beta E_\eta |\Psi_\eta\rangle = E_\eta U_\beta |\Psi_\eta\rangle$, namely that $U_\beta |\Psi_\eta\rangle$ is an eigenvector of H_η with energy E_η. If the ground state is unique, it must be an eigenvector of U_β

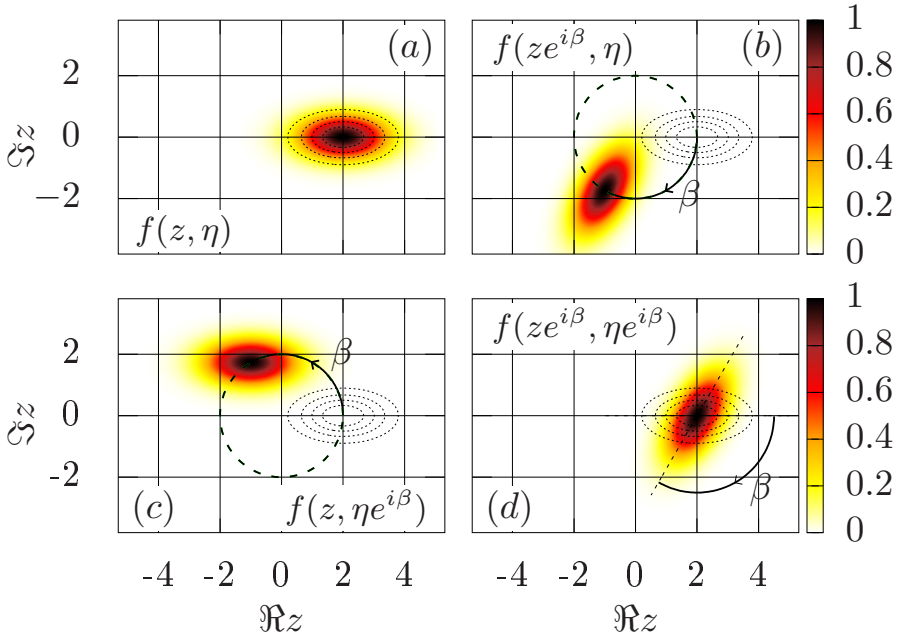

Figure 6.1: Action of $\tilde{L}$. Panel (a): contour plot in z space of the function $f(z,\eta) = \exp[-\frac{1}{2}\Re(z-\eta)^2 - 2\Im(z-\eta)^2]$ for $\eta = 2$. Panel (b): contour plot of $f(ze^{i\beta},\eta)$ for $\beta = 2\pi/3$: with respect to (a), the plot is translated and rotated. Panel (c): contour plot of $f(z,\eta e^{i\beta})$: this time, the plot is only translated. Panel (d): contour plot of $f(ze^{i\beta},\eta e^{i\beta})$: the composition of the two is just a rotation and thus $\tilde{L}$ generates the self-rotations of the quasiparticles in the z plane.

and of its generator $\tilde{L}$; we dub the eigenvalue of the latter ℓ_η

$$U_\beta \left|\Psi_\eta\right\rangle = \ell_\eta \left|\Psi_\eta\right\rangle . \tag{6.6}$$

For example, in the case of the normalised Laughlin state with a quasihole at position η

$$\mathcal{N}(|\eta|)^{-1/2} \prod_i (z_i - \eta) \prod_{j<k} (z_j - z_k)^m e^{-\sum_i |z_i|^2/4\ell_B^2} \tag{6.7}$$

the eigenvalue $\ell_\eta = \frac{m}{2}N(N-1) + N$ is the degree of the polynomial in z_i and η.

We now perform a gauge transformation that unwinds the generalised angular momentum ℓ_η moving along a trajectory at fixed $|\eta|$. Namely

$$|\tilde{\Psi}_\eta\rangle = e^{i\tilde{g}(\eta)} \left|\Psi_\eta\right\rangle \tag{6.8}$$

with

$$\tilde{g}(\eta) = -\int_0^\theta \ell_{|\eta|e^{i\theta'}} d\theta'. \tag{6.9}$$

In the aforementioned case of the Laughlin's quasihole, the Laughlin state gets

multiplied by the phase $(\eta/\eta^*)^{-\frac{m}{4}N(N-1)-\frac{N}{2}}$.

With this choice, the gauge-transformed state $|\tilde{\Psi}_\eta\rangle$ is in an eigenvector of $\tilde{L}$ with vanishing eigenvalue

$$\tilde{L}\,|\tilde{\Psi}_\eta\rangle = 0. \tag{6.10}$$

By definition, $\tilde{L}\,|\tilde{\Psi}_\eta\rangle = e^{i\tilde{g}(\eta)}\tilde{L}\,|\Psi_\eta\rangle + \left(L' e^{i\tilde{g}(\eta)}\right)|\Psi_\eta\rangle$. The first term of the sum is $\ell_\eta\,|\tilde{\Psi}_\eta\rangle$, the second term is obtained by differentiating the exponential, and equals $-\ell_\eta\,|\tilde{\Psi}_\eta\rangle$. Thus, one can find a gauge such that $\tilde{L}$ annihilates the ground state.

Note that for a state satisfying Eq. (6.10), it is also true that $U_\beta\,|\tilde{\Psi}_\eta\rangle = |\tilde{\Psi}_\eta\rangle$ for any angle β. Choosing $\beta = 2\pi$ we obtain that this state is single-valued in the η coordinate because $U_{2\pi}\,|\tilde{\Psi}_\eta\rangle$ is also equal to $|\tilde{\Psi}_{\eta e^{i2\pi}}\rangle$.

This reasoning can be easily extended to the case of several quasiparticles. We can define a reference angle θ_0 and express $\theta_\alpha = \theta_0 + \Delta\theta_\alpha$, treating the variables $\Delta\theta_\alpha = \theta_\alpha - \theta_0$ as independent from θ_0. The operator $-i\partial_{\theta_0}$ generates the group $\exp\left(i\beta(-i\partial_{\theta_0})\right)$ that modifies the quasiparticle polar angles as follows: $\theta_\alpha \to \theta_\alpha + \beta$, leaving the radial distance unchanged; thus: $\eta_\alpha \to \eta_\alpha e^{i\beta}$. This is exactly the action of L'_z, and thus we conclude that $L'_z = -i\partial_{\theta_0}$. With arguments paralleling those for one quasiparticle, one can (i) show that $\tilde{L}\,|\Psi_{\boldsymbol{\eta}}\rangle = \ell_{\boldsymbol{\eta}}\,|\Psi_{\boldsymbol{\eta}}\rangle$, (ii) by making the dependence on θ_0, $\Delta\theta_\alpha$ and the $|\eta_\alpha|$ explicit by writing $\ell_{\theta_0,\Delta\theta_\alpha,|\eta_\alpha|}$, one can define $|\tilde{\Psi}_{\boldsymbol{\eta}}\rangle = e^{ig(\boldsymbol{\eta})}\,|\Psi_{\boldsymbol{\eta}}\rangle$ with $g(\boldsymbol{\eta}) = -\int_0^{\theta_0} \ell_{\theta'_0,\Delta\theta_\alpha,|\eta_\alpha|}\,d\theta'_0$, which is in the kernel of $\tilde{L}$.

6.3 Berry phase for the translation of the quasiparticles along a circle

We now compute the Berry phase corresponding to the translation along a closed circular path of the N_{qp} quasiparticle coordinates via $\theta_0 \to \theta_0 + 2\pi$ generated by L'_z leaving all the $\Delta\theta_\alpha$ and $|\eta_\alpha|$ invariant. Using the fact that $|\tilde{\Psi}_{\boldsymbol{\eta}}\rangle$ is single-valued in $\boldsymbol{\eta}$, this Berry phase is $\gamma_{\boldsymbol{\eta}} = \int_0^{2\pi} \langle\tilde{\Psi}_{\boldsymbol{\eta}}|\, i\partial_{\theta_0}\,|\tilde{\Psi}_{\boldsymbol{\eta}}\rangle\, d\theta_0$, where only the θ_0 coordinate is changed in the state inside the integral. Employing the definitions of $\tilde{L}$ and L'_z, and using Eq. (6.10), we get

$$\gamma_{\boldsymbol{\eta}} = \int_0^{2\pi} \langle\tilde{\Psi}_{\boldsymbol{\eta}}|\, L_z\,|\tilde{\Psi}_{\boldsymbol{\eta}}\rangle\, d\theta_0 = \int_0^{2\pi} \langle\Psi_{\boldsymbol{\eta}}|\, L_z\,|\Psi_{\boldsymbol{\eta}}\rangle\, d\theta_0. \tag{6.11}$$

The matrix element in the integral is manifestly gauge-independent, as the L_z operator does not act on the $\boldsymbol{\eta}$; one can thus also use the original states. Finally, let us note that the integrand cannot be a function of θ_0, and thus we have an even

simpler expression

$$\gamma_{\boldsymbol{\eta}} = 2\pi \langle \Psi_{\boldsymbol{\eta}} | L_z | \Psi_{\boldsymbol{\eta}} \rangle . \tag{6.12}$$

Like any operator projected onto the lowest Landau level, the angular momentum L_z is a function of the guiding-center operators [11] $R_{j,x} = x_j + (\ell_B^2/\hbar)\pi_{j,y}$ and $R_{j,y} = y_j - (\ell_B^2/\hbar)\pi_{j,x}$, which, as discussed in Sec. 2.1.2, do not commute along different directions $[R_{j,x}, R_{j',y}] = -i\ell_B^2\delta_{j,j'}$. As can be easily seen from the discussion in Sec. 2.1.3, the lowest Landau level projected angular momentum operator reads $L_z = \sum_j (R_j^2/\ell_B^2 - 1)/2$. Written in this projected form, L_z is the gauge-invariant generator of rotations, and its expectation value is just a function of the density of the gas $\rho_{\boldsymbol{\eta}}(z)$, which, due to the screening property of the fractional quantum Hall fluid, can be split into a bulk contribution $\rho_b(z)$ (the state without quasiparticles), an edge contribution $\rho_e(z)$ (the difference at the edge with respect to the state without quasiparticles) and a quasiparticle contribution localised around the η_α, $\rho_{qp,\boldsymbol{\eta}}(z)$. We therefore split the integrand into three parts:

$$\langle \Psi_{\boldsymbol{\eta}} | L_z | \Psi_{\boldsymbol{\eta}} \rangle = L_b + L_e(N_{qp}) + L_{qp}(\boldsymbol{\eta}). \tag{6.13}$$

As long as the quasiparticles are far from the edge, the screening property ensures that L_e can only depend on their number, or, more precisely, on the number of quasiparticles of each species, but not on their positions; in fact, it also does not change when two of them are put close by or stacked on top of each other.

Notice that L_b is an integer, thanks to rotational invariance. Therefore its contribution to the Berry phase Eq. (6.11) can be discarded. The only relevant information is contained in the remaining pieces, which indeed depend, directly or indirectly, on the quasiparticles alone

$$\gamma_{\boldsymbol{\eta}} = 2\pi\big(L_e(N_{qp}) + L_{qp}(\boldsymbol{\eta})\big). \tag{6.14}$$

Let us consider now the case of a single quasiparticle at η; on the basis of very general arguments, γ_η should be the Aharonov-Bohm phase $qQ\pi|\eta|^2 B/\hbar$, where Q is the charge of the quasiparticle in units of the charge of the fractional quantum Hall state constituents, q. Let us compare Eq. (6.14) with this widely-accepted result. In very general terms, the angular momentum of a rotationally-invariant quasiparticle $L_{qp}(\eta) = \int d^2r\,(r^2/2\ell_B^2 - 1)\,\rho_{qp,\eta}(r)$ can be split into an orbital part $\frac{Q|\eta|^2}{2\ell_B^2}$ and an intrinsic part

$$J_{qp} \equiv L_{qp}(0) = \int d^2r \left(\frac{r^2}{2\ell_B^2} - 1\right) \rho_{qp,\eta=0}(r). \tag{6.15}$$

We can therefore write

$$\gamma_\eta = \pi Q|\eta^2|/\ell_B^2 + 2\pi(L_e(1) + J_{1qp}). \tag{6.16}$$

We recognise the Aharonov-Bohm phase, to which an apparently spurious contribution has been added; yet, we can show that it is an integer multiple of 2π, and thus inessential. To show that $L_e(1) + J_{1qp}$ is an integer, we consider a system with a quasiparticle *at its centre*. The state in this case is rotationally symmetric, so its angular momentum $L_b + J_{1qp} + L_e(1)$ is an integer; since $L_b \in \mathbb{Z}$, $J_{1qp} + L_e(1)$ is also an integer. By the same logic $J_{nqp} + L_e(n) \in \mathbb{Z}$ where J_{nqp} is the spin of the rotationally symmetric quasiparticle obtained by fusing n quasiparticles together, stacking them on top of each other.

Very generically, the gauge-invariant generator of rotations fractionalizes between the bulk quasiparticles and the edge, implying that the spin is robust to local circularly-symmetric perturbations which do not couple the quasiparticles to the edge.

6.4 Spin-statistics relation

We consider two identical quasiparticles placed at opposite positions η and $-\eta$ and far from each other and from the edge. In order to compute the statistical parameter κ, we consider a double exchange, that gives a gauge-invariant expression and avoids any discussion on the identity of the pinning potentials [35]. Accordingly, we study the difference between the Berry phase for exchanging two opposite particles and the single-particle Aharonov phases [197]:

$$\kappa_{qp} = \frac{1}{2\pi}\left(\gamma_{\eta,-\eta} - 2\gamma_\eta\right). \tag{6.17}$$

Using Eq. (6.14), we can rewrite the previous equation as $\kappa_{qp} = L_e(2) + L_{qp}(\eta, -\eta) - 2L_e(1) - 2L_{qp}(\eta)$. As long as the quasiparticles are well separated, and given that the fractional quantum Hall liquid is screening, we can separate $\rho_{qp}(\eta, -\eta) = \rho_{qp,\eta} + \rho_{qp,-\eta}$. We therefore obtain $L_{qp}(\eta, -\eta) = 2L_{qp}(\eta)$; since $L_e(n) + J_{nqp} \in \mathbb{Z}$ we obtain the spin-statistics relation:

$$\kappa_{qp} = -J_{2qp} + 2J_{1qp} \pmod 1. \tag{6.18}$$

This result allows us to identify the intrinsic angular momentum with the fractional spin associated to the fractional statistics. Interestingly, we have linked the statistics

to a local property of the quasiparticles: if we assume screening, the fine details of the boundary do not matter, and – as we argued above – one could prove Eq. (6.18) without requiring that $v(|z|)$ is a central potential.

With similar arguments, the spin-statistics relation can be extended to the situation where the two quasiparticles are different: calling J_a and J_b their spins, and J_{ab} the spin of the composite quasiparticle obtained by stacking them at the same place, we obtain the mutual statistics parameter

$$\kappa_{ab} = -J_{ab} + J_a + J_b \pmod 1. \tag{6.19}$$

Moreover, the fractionalization property allows us to read the phase κ directly at the edge; indeed, one easily obtains

$$\kappa_{qp} = L_e(2) - 2L_e(1) \tag{6.20}$$

or, more generally,

$$\kappa_{ab} = L_e(a,b) - L_e(a) - L_e(b). \tag{6.21}$$

These last equations are neat manifestations of the bulk-boundary correspondence: information on the topological properties of the bulk are encoded in system's edge properties, in this case in the form of fractionalized angular momentum.

6.4.1 The spin of the quasielectron

As a first application of the spin-statistics relation Eq. (6.18), we consider the quasielectron of the Laughlin state we described in Sec. 3.3.2, at filling $\nu = 1/m$. Numerical studies have highlighted that the composite-fermion wavefunction for the quasielectron proposed by Jain [168, 200] has the correct statistical properties when the quasielectron is braided with another one ($\kappa_{qe} = 1/m$) or with a quasihole ($\kappa_{qe-qh} = -1/m$) [198, 276, 277, 278, 279, 280]. Previous articles have already shown that lowest Landau level quasiparticles composed of p stacked quasiholes fractionalize the angular momentum

$$J_p = -\frac{p^2}{2m} + \frac{p}{2}, \tag{6.22}$$

and that these results are compatible via the spin-statistics relation Eq. (6.18) with a correct quasihole statistics $\kappa_{qh} = 1/m$ [273, 270].

On the basis of these results and of the spin-statistics relation, it is easy to predict that Jain's quasielectron fractionalizes the same spin J_p (where $p < 0$ for quasielec-

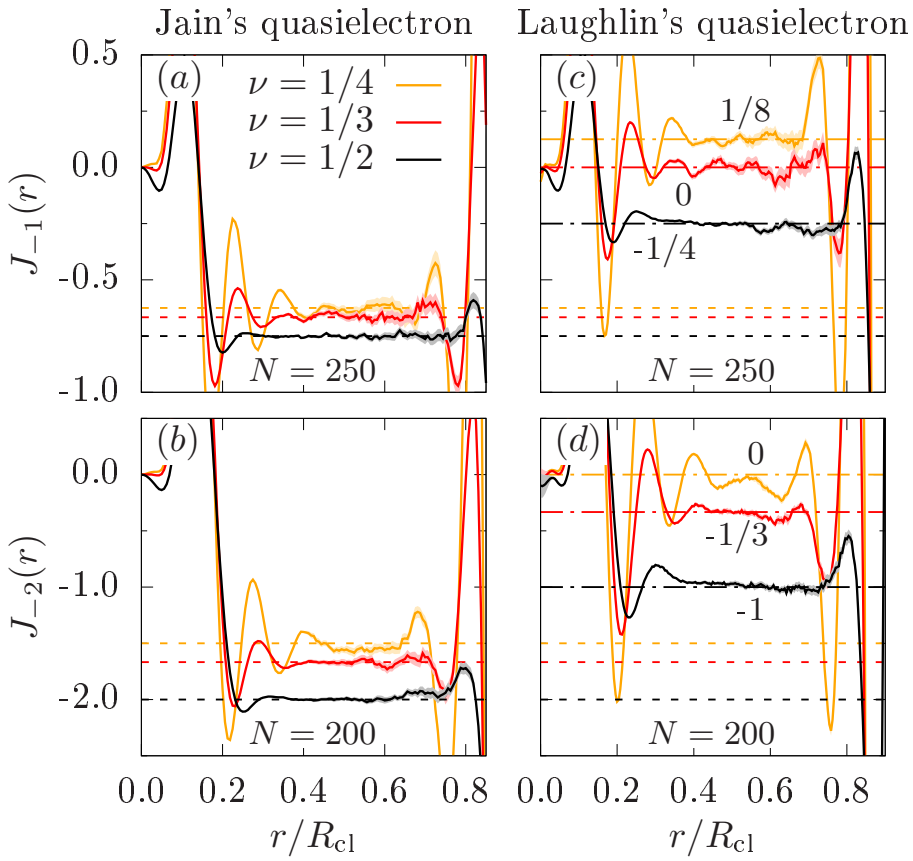

Figure 6.2: Calculation of the quasielectron spin via the integral $J(r) = \int_0^r \left(\frac{|r'|^2}{2\ell_B^2} - 1\right) \rho_{qp}(r) 2\pi r' dr'$; the spin of Eq. (6.15) coincides with the plateau appearing when r is far from the center and the boundary; $R_{\rm cl} = \sqrt{2N/\nu}$ is the classical radius of the droplet. Panel (a): the spin of a single Jain's quasielectron for $\nu = 1/2$, $1/3$ and $1/4$. Panel (b): the case of two stacked Jain's quasielectrons. Panels (c) and (d): the same for one and two Laughlin's quasielectrons, respectively. Theoretical predictions following from the spin-statistics relation in Table 6.1 are marked with dashed lines and are only compatible with the spin of Jain's quasielectron. Dashed-dotted lines in panels (c) and (d), together with their values, highlight the position of the spin plateaus in the case Laughlin's quasielectrons.

	$\nu = \frac{1}{2}$	$\nu = \frac{1}{3}$	$\nu = \frac{1}{4}$
$p = -1$	$-\frac{3}{4}$	$-\frac{2}{3}$	$-\frac{5}{8}$

	$\nu = \frac{1}{2}$	$\nu = \frac{1}{3}$	$\nu = \frac{1}{4}$
$p = -2$	-2	$-\frac{5}{3}$	$-\frac{3}{2}$

Table 6.1: The spin J_p of Jain's quasielectron at filling factor ν.

trons and $p > 0$ for quasiholes). We numerically verify this statement by performing a Monte-Carlo analysis of Jain's wavefunction with one quasielectron ($p = -1$) or two ($p = -2$). See Appendix G for additional details. Table 6.1 summarizes the expected values. The results of our simulations are in Fig. 6.2(a,b) and they agree

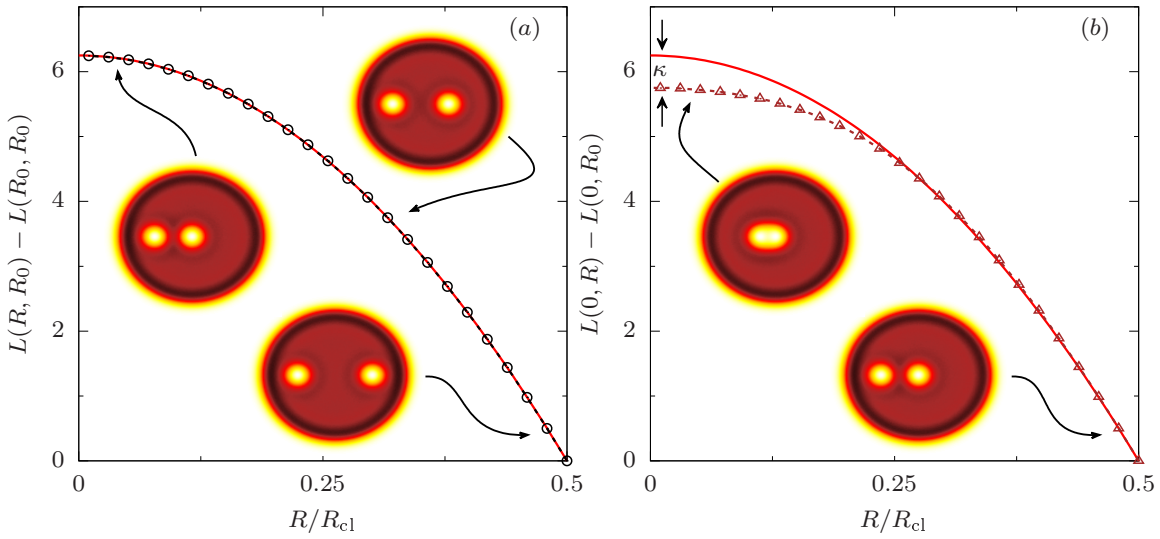

Figure 6.3: Angular momentum $L(R_1, R_2)$ of a Laughlin state ($N = 25$, $\nu = 1/2$) with two quasiholes at distances R_1 and R_2 from the center, computed with Monte Carlo techniques. Panel (a): displacement of the first quasihole; the angular momentum variation $L(R, R_0) - L(R_0, R_0)$ is plotted in black circles, and it is a quadratic function of R that agrees with the theory prediction $-\epsilon(R^2 - R_0^2)$ (red line). Panel (b): displacement of the second quasihole; the variation $L(0, R) - L(0, R_0)$ is plotted in brown triangles and it is a quadratic function of R only at large R; when the quasiholes fuse a deviation sets in that equals $-\kappa$, the statistical parameter. Here, R_0 is the quasihole initial position.

perfectly with our theory.

Notice that this way of assessing the statistics of the quasielectron does not suffer from the undesired multi-quasiparticle position shift that needs to be taken into account in order to get the correct statistical phase [276, 280].

Concerning the quasielectron wavefunction proposed in the original article by Laughlin [23], it was shown that it fractionalizes the correct charge, without making definitive statements about its braiding properties though [197, 198, 276, 277, 279]. The results of our numerical simulations are in Fig. 6.2(c,d). The plateau values can be phenomenologically described by the spin values $J'_p = -p^2/(2m) + p(2-m)/(2m)$, that gives the correct braiding phase for the Laughlin quasielectron, but also shows that it is not the anti-anyon of the Laughlin's quasihole.

6.4.2 Angular-momentum of the gas

As a further application of the spin-statistics relation, let us consider what happens when two quasiholes initially placed far apart are displaced radially towards the centre of the cloud. Let us call L_0 the angular momentum of the initial state with

both quasiparticles at the same distance R_0 from the center.

The first quasihole is then moved to the center. During this process the angular momentum increases and depends on the distance R in a parabolic fashion, as $L(R) = L_0 - \epsilon(R^2 - R_0^2)$ with $\epsilon = qQ\pi B/h$. A gain in angular momentum of ϵR_0^2 is expected at the end of the process.

The same is now done with the second quasihole. Whereas also in this case the angular momentum increases, it does not in a parabolic way. Indeed, at the end of the process it can not attain the value $L_0 + 2\epsilon R_0^2$ because when the two quasihole fuse, their total spin changes. The final value is in fact $L_0 + 2\epsilon R_0^2 - \kappa$. We verify this result with numerical simulations reported in Fig. 6.3. This provides an experimental procedure for measuring the mutual statistics of two generic quasiparticles in a controllable quantum simulator of the fractional quantum Hall effect.

6.5 Laughlin quasielectron

Leveraging on the numerical results we presented in the last section [Sec. 6.4.1], in this one we are going to explore the link between the quasielectron wavefunctions proposed by Laughlin and by Jain. We show that Laughlin's quasielectron can be understood as a non-local composite fermion state due to a long-range tail which affects the boundary properties of the fractional quantum Hall cloud and, as a consequence, the spin and braiding properties of the quasielectron itself. These facts we believe lead to the ambiguities which have been reported in many studies [197, 198, 279].

6.5.1 Laughlin's quasielectron in the light of the composite fermion theory

Our starting point is Laughlin's quasielectron [Eq. (3.24)] in its unprojected form [Eq. (3.23)]

$$\begin{aligned}\Psi_{LQE}(\{z_i\}) &\sim \left(\prod_i z_i^*\right)\prod_{i<j}(z_i - z_j)^{1/\nu} \\ &\sim \underbrace{\left(\prod_i z_i^* \prod_{i<j}(z_i - z_j)\right)}_{\Phi(\{z_i\})}\prod_{i<j}(z_i - z_j)^{1/\nu - 1}\end{aligned} \tag{6.23}$$

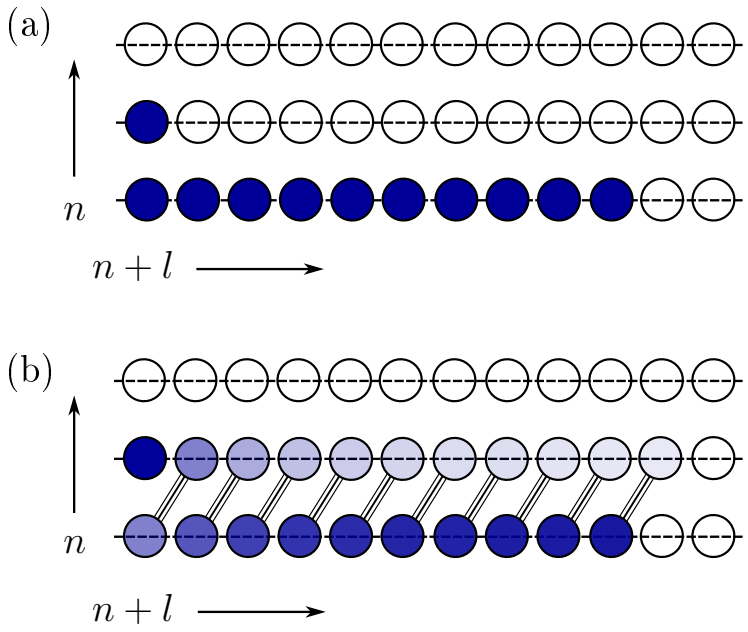

Figure 6.4: Schematic view of (a) Jain's quasielectron [Eq. (6.29)] and (b) Laughlin's quasielectron [Eq. (6.27)], in terms of their composite fermion descriptions. Composite fermion states are denoted by the circles (the fluxes are not shown for graphical convenience) and labelled by their Λ-level (index n) and angular momentum (index l). Empty circles denote free states, blue-filled ones the occupied ones. In (b) the transparency of the circles has been regulated according to the occupation probabilities Eq. (6.28). Diagonal bars serve as a reminder that each composite fermion is in a superposition state of a $n = 0$ and a $n = 1$ Λ-level state.

where, according to the standard composite fermion theory, we separated a "vortex attachment" term $\prod_{i<j}(z_i - z_j)^{1/\nu-1}$ from a non-interacting fermionic wavefunction $\Phi(\{z_i\})$ which we can conveniently write as a Slater determinant

$$\Phi(\{z_i\}) = \begin{vmatrix} z_0^* & z_1^* & z_2^* & \dots \\ z_0^* z_0 & z_1^* z_1 & z_2^* z_2 & \dots \\ z_0^* z_0^2 & z_1^* z_1^2 & z_2^* z_2^2 & \dots \\ \vdots & \vdots & \vdots & \ddots \end{vmatrix}. \tag{6.24}$$

This shows that each non-interacting electron sits in orbitals whose wavefunction is proportional to $z^* z^l$, which carries angular momentum $l - 1$. These orbitals are a coherent superposition of the two states belonging to the lowest and the first Landau

levels with the same angular momentum $l-1$

$$\begin{cases} \phi_{n=0,l-1}(z) = \frac{1}{\sqrt{2\pi(l-1)!}} \left(\frac{z}{\sqrt{2}}\right)^{l-1} \\ \phi_{n=1,l}(z) = \frac{1}{\sqrt{2\pi l!}} \left(\frac{z}{\sqrt{2}}\right)^{l-1} \left(\frac{z}{\sqrt{2}}\frac{z^*}{\sqrt{2}} - l\right). \end{cases} \tag{6.25}$$

Let us show this explicitly by introducing the single-particle orbital

$$\psi_{l-1}(z) \equiv \sqrt{\frac{1}{l+1}}\, \phi_{n=1,l}(z) + \sqrt{\frac{l}{l+1}}\, \phi_{n=0,l-1}(z). \tag{6.26}$$

Since in Eq. (6.25) we have used normalized states, the orbital in Eq. (6.26) is also normalized. Moreover, it is easy to see that $\psi_{l-1} \propto z^*\, z^l$, which are precisely the terms that appear in the non-interacting fermionic wavefunction Eq. (6.24). We rewrite Eq. (6.24) in an equivalent manner (the only difference being an overall irrelevant normalization factor) as

$$\Phi(\{z_i\}) = \begin{vmatrix} \psi_{-1}(z_0) & \psi_{-1}(z_1) & \psi_{-1}(z_2) & \dots \\ \psi_0(z_0) & \psi_0(z_1) & \psi_0(z_2) & \dots \\ \psi_1(z_0) & \psi_1(z_1) & \psi_1(z_2) & \dots \\ \vdots & \vdots & \vdots & \ddots \end{vmatrix}. \tag{6.27}$$

The probabilities for a fermion labelled by the angular momentum l to sit in the lowest or in the first excited Landau level therefore read

$$\begin{cases} P_0(l) = \frac{l+1}{l+2} \\ P_1(l) = \frac{1}{l+2}, \end{cases} \tag{6.28}$$

which manifestly shows the long-range nature of Laughlin's quasielectron: even though $\lim_{l\to\infty} P_1(l) = 0$, the decay is algebraic and very slow. Let us consider for instance a finite system with N particles. We argue that this slow algebraic decay can indeed affect the system's boundary and change the topological properties of Laughlin's quasielectron.

On the contrary, it is easy to realize that Jain's quasielectron [200, 10]

$$\Psi_{JQE}(\{z_i\}) \sim \hat{P}_{\mathrm{LLL}} \begin{vmatrix} z_0^* & z_1^* & z_2^* & \dots \\ 1 & 1 & 1 & \dots \\ z_0 & z_1 & z_2 & \dots \\ \vdots & \vdots & \vdots & \ddots \end{vmatrix} \prod_{i<j} (z_i - z_j)^{m-1} \tag{6.29}$$

has basically no such tail. In Fig. 6.4 we present a sketch comparing the two situations.

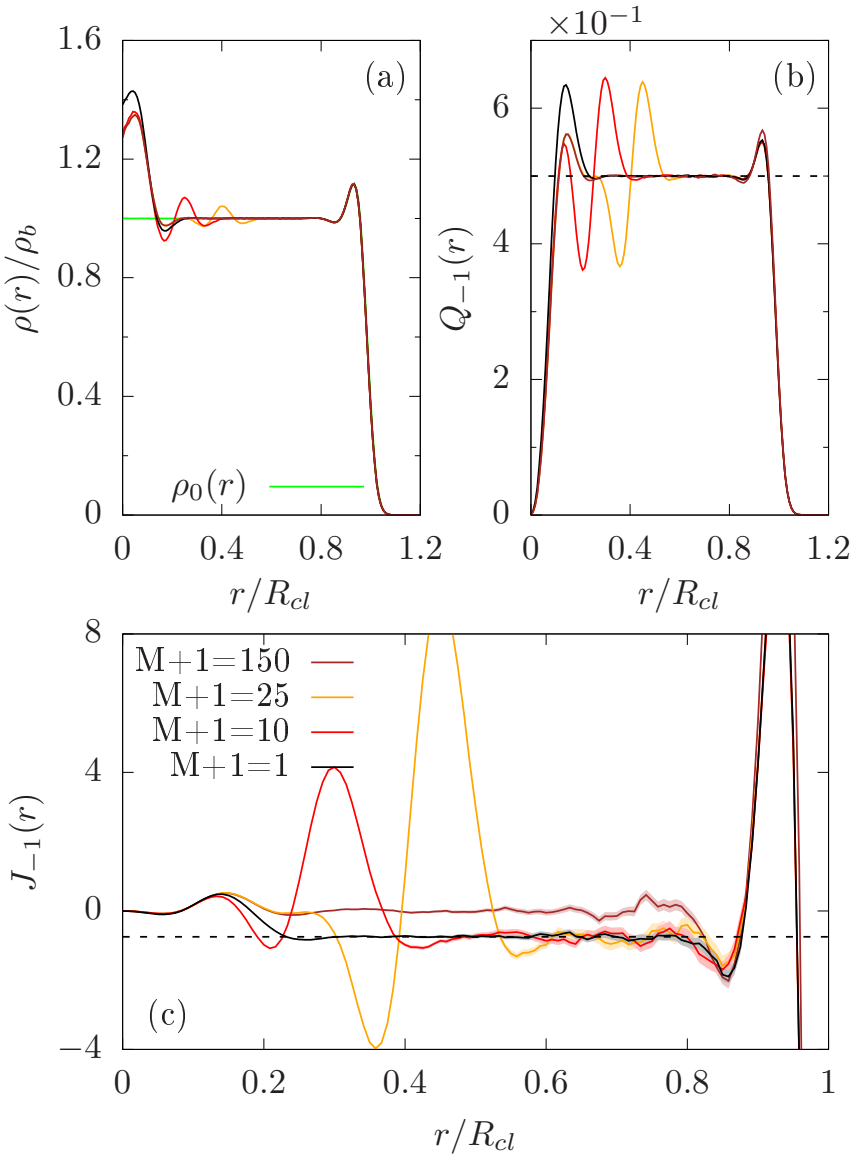

Figure 6.5: Numerical results for (a) the density profiles, (b) the quasielectron charge $Q(r) = \int_0^r (\rho(r') - \rho_0(r'))\, d^2r'$ and (c) its spin $J(r) = \int_0^r \left(r'^2/2 - 1\right)\, (\rho(r') - \rho_0(r'))\, d^2r'$ in the case of $N = 150$ bosons at filling $\nu = 1/2$. The different curves (see the legend in panel (c)) are associated to quasielectron wavefunctions Eq. (6.31) truncated at different levels M. The green-curve in panel (a) is the Laughlin's state background density $\rho_0(r)$.

6.5.2 Numerical analysis of truncated wavefunctions

In this subsection we are going to show that, provided the long-range tail is suitably truncated, one recovers the correct value of the spin [267, 269, 273] given by Eq. (6.22).

In order to do that, we introduce the "M-th level truncation" of Eq. (6.27)

$$\Phi_{[M]} = \begin{vmatrix} \psi_{-1}(z_0) & \psi_{-1}(z_1) & \psi_{-1}(z_2) & \dots \\ \vdots & \vdots & \vdots & \dots \\ \psi_{M-1}(z_0) & \psi_{M-1}(z_1) & \psi_{M-1}(z_2) & \dots \\ z_0^M & z_1^M & z_2^M & \dots \\ z_0^{M+1} & z_1^{M+1} & z_2^{M+1} & \dots \\ \vdots & \vdots & \vdots & \ddots \end{vmatrix} \tag{6.30}$$

which qualitatively corresponds to the Laughlin's quasielectron up to the M-th orbital, in the sense that the composite fermions are in the coherent superposition Eq. (6.26). From the $M+1$-th orbital, the composite fermion occupations are instead the same as those of the Laughlin's state. Something interesting can already be seen: while by construction the truncation at $M = N-1$ restores Laughlin's quasielectron [Eq. (6.23)], truncating at $M = 0$ gives exactly Jain's quasielectron [Eq. (6.29)].

A quasielectron wavefunction which interpolates between Jain's and Laughlin's quasielectrons can therefore be constructed by "attaching vortices" to the non-interacting fermions [10] as

$$\psi^{[M]} = \hat{P}_{LLL}\, \Phi_{[M]} \prod_{i<j} (z_i - z_j)^{1/\nu - 1}. \tag{6.31}$$

Notice that at $M = N - 1$, doing the "standard" Girvin-Jach lowest Landau level projection [9, 196] leads indeed to Laughlin's version of the quasielectron [Eq. (3.24)]. For a generic truncation level $M \gtrsim 1$ however such a projection scheme is intractable. Since one heuristically expects the topological features of the state to be independent of the projection scheme, we resort on the Jain-Kamilla scheme [281, 10], which in this case is easier to employ. It must be noted that in this case the quasielectron one obtains when $M = N - 1$ is not mathematically the same as Laughlin's one.

We perform standard Monte-Carlo sampling on the wavefunction Eq. (6.31) to characterize the density profile, the charge and the spin of the quasielectrons at different truncation levels M. We show our results in Fig. 6.5 and Fig. 6.6 for bulk filling fractions $\nu = 1/2$ and $1/3$ respectively.

While it can be seen in Fig. 6.5(b) and Fig. 6.6(b) that the quasielectron charge is independent of the truncation parameter M, we see in Fig. 6.5(c) and Fig. 6.6(c) that the spin is not. In particular, as long as $M \ll N$ (i.e. the edge is unaffected by the presence of the quasielectron at the centre) the correct value of the spin [Eq. (6.22)] is recovered even if [Fig. 6.5(a), Fig. 6.6(a)] the quasielectron density profiles are quite different, and therefore these quasielectron states describe "good" antianyon wavefunctions of Laughlin's quasihole.

This is not the case in the Laughlin's quasielectron limit ($M = N - 1$), where we find a value of the spin that not only is different from that of Laughlin's quasihole [Eq. (6.22)] – thus strengthening the conclusions we drew in subsection 6.4.1 – but is also different from the value we found there ($J_{LQE} = -1/4$ and $J_{LQE} = 0$ at $\nu = 1/2$ and $\nu = 1/3$ respectively) by employing the "standard" Laughlin's quasielectron of Eq. (3.24). This demonstrates that Laughlin's quasielectron spin is not "topologically robust" in the sense that its value strongly depends on the detailed short-range structure of the wavefunction and consequently on the method one employs to project out higher Landau level components, which obviously should not be the case.

6.6 The non-Abelian case

In this final section, we want to stress that our arguments carry over to non-Abelian quantum Hall states. In this latter case, fusing two quasiparticles generically can lead to more than one different outcome. This means that in the presence of several quasiparticles, the ground state is typically degenerate. When considering a state with two quasiparticles in a definite fusion channel, the ground state is however unique (we restrict ourselves to the case without fusion multiplicities). Therefore, even the non-Abelian case is covered, because the hypotheses of derivation of the spin-statistics relation are uniqueness of the ground state, screening and rotational invariance. The non-Abelian nature shows up via the possibility that fusing two quasiparticles can lead to different anyons, which leads to a different spin-statistics relation for each possibility

$$\kappa_{ab,c} = -J_c + J_a + J_b \pmod 1, \tag{6.32}$$

where c denotes the particular fusion outcome of fusing a with b. We numerically support this claim by explicitly analysing the Moore-Read [36] case and comparing them to analytical results.

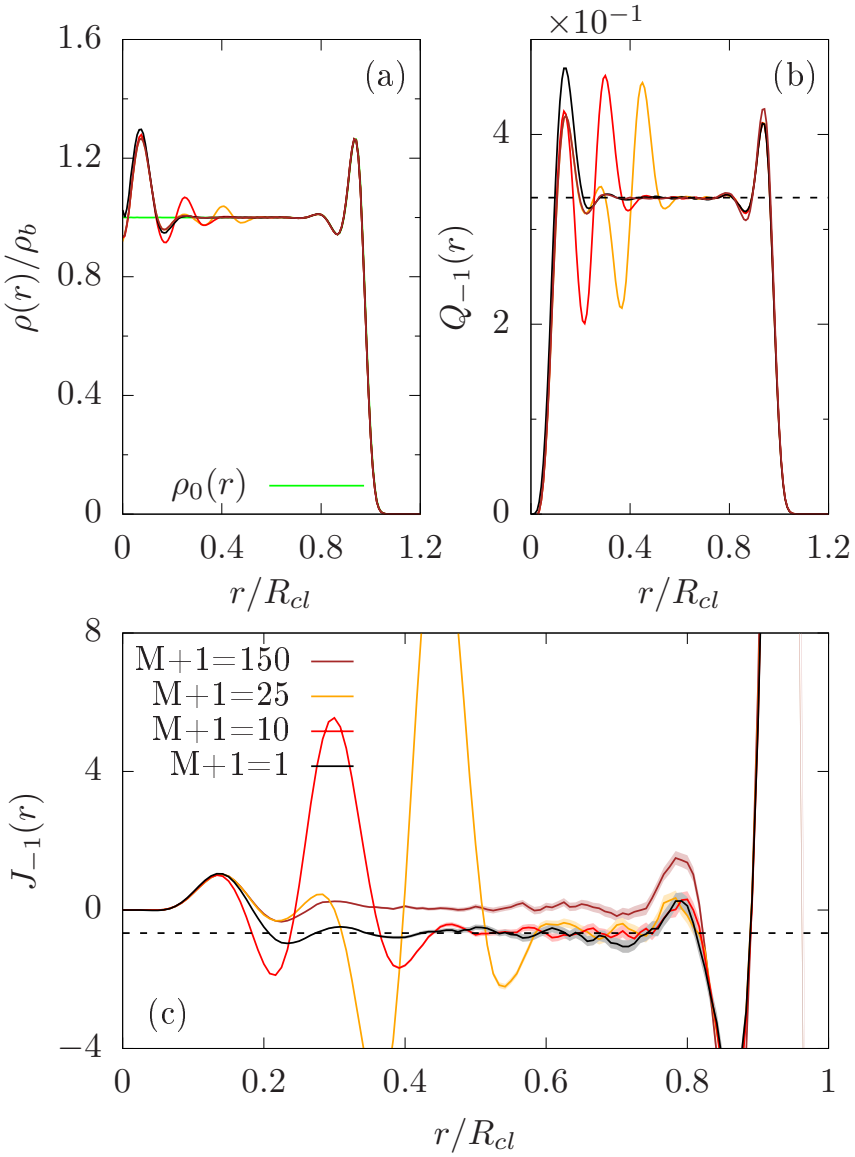

Figure 6.6: Numerical results for (a) the density profiles, (b) the quasielectron charge $Q(r)$ and (c) its spin $J(r)$ in the case of $N = 150$ fermions at filling $\nu = 1/3$. The different curves (see the legend in panel (c)) are associated to quasielectron wavefunctions Eq. (6.31) truncated at different levels M. The green-curve in panel (a) is the Laughlin's state background density.

6.6.1 The Moore-Read case

We now discuss how we obtain analytical results for the values of the spins of the Moore-Read state quasiholes.

We write the filling fraction of the state as $\nu = \frac{1}{q}$, where q is even(/odd) in the fermionic(/bosonic) case. The Moore-Read state is defined in terms of a chiral boson

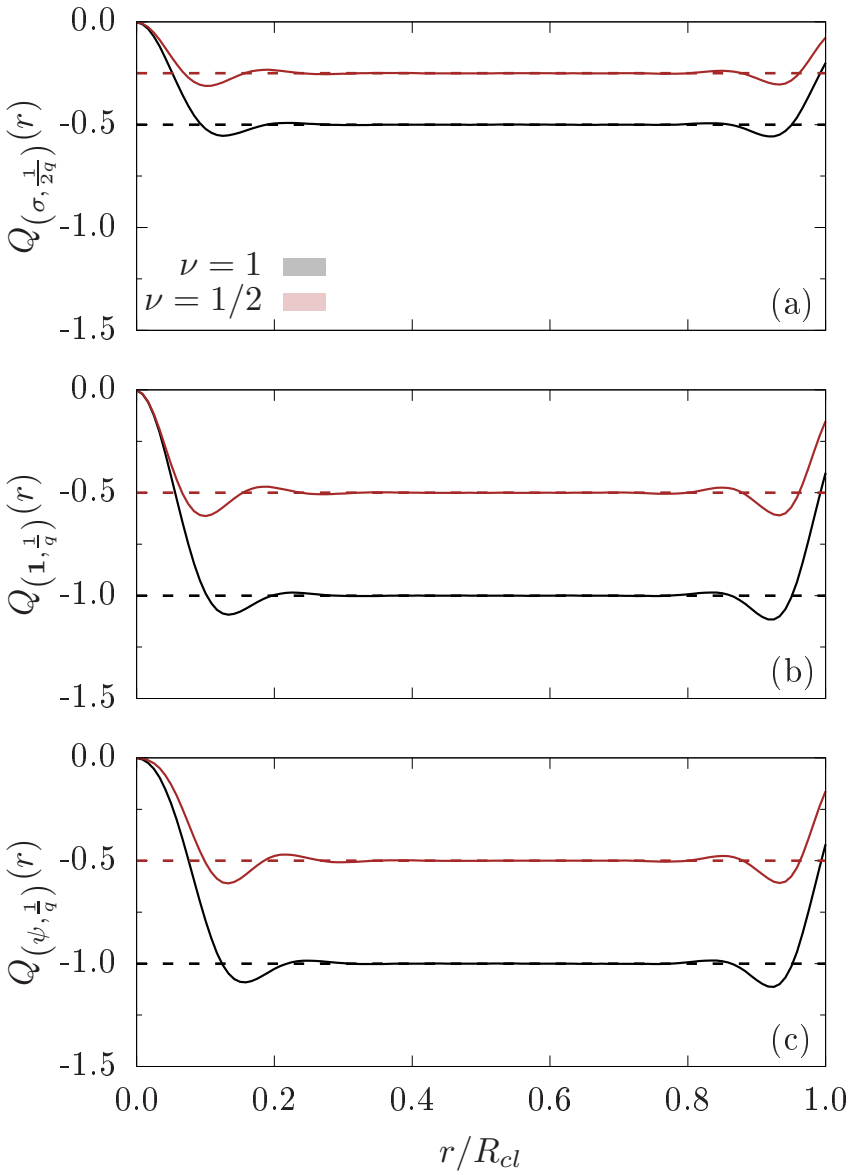

Figure 6.7: Comparison of the quasihole charges $Q(r) = \int_0^r (\rho_{qp}(r') - \rho_{MR}(r'))\, r' dr'$, where $\rho_{qp}(r)$ is the quasihole density and $\rho_{MR}(r)$ the background Moore-Read density, for the different Moore-Read quasiholes: (a) the $\left(\sigma, \frac{1}{2q}\right)$, (b) the $\left(\mathbf{1}, \frac{1}{q}\right)$ and (c) the $\left(\psi, \frac{1}{q}\right)$, for the bosonic filling $\nu = 1$ (corresponding to $q = 1$) and the fermionic $\nu = \frac{1}{2}$ ($q = 2$). $R_{\mathrm{cl}} = \sqrt{2N/\nu}$ is the classical radius of the droplet.

field φ and the fields of the Ising conformal field theory. This means that we should label the quasiholes by their Ising sector (i.e., $\mathbf{1}$, σ or ψ), and their charge. The smallest charge quasihole has the labels $\left(\sigma, \frac{1}{2q}\right)$. Because the fusion of two σ fields has two possible outcomes, $\sigma \times \sigma = 1 + \psi$, the fusion of two quasiholes also leads to two possible results. In particular, we have (the charge label is additive, as it is the

case for the Laughlin state)

$$\left(\sigma, \frac{1}{2q}\right) \times \left(\sigma, \frac{1}{2q}\right) = \left(\mathbf{1}, \frac{1}{q}\right) + \left(\psi, \frac{1}{q}\right) \ . \tag{6.33}$$

The first possible outcome $\left(\mathbf{1}, \frac{1}{q}\right)$ is the quasihole one obtains by piercing the sample with an additional flux, i.e., the "ordinary" Laughlin quasihole. The second possible outcome "contains" an additional neutral fermionic mode ψ.

The braiding phases can be read from the explicit conformal field theory construction [36] (see also [179]). In this way one obtains the statistical parameters of the double exchange of two charge $\frac{1}{2q}$ quasiholes, for both possible fusion outcomes. For clarity, we drop the charge label when referring to the braid parameter κ. In particular, one finds $\kappa_{\sigma\sigma,\mathbf{1}} = \frac{1}{4q} - \frac{1}{8}$ (when the quasiholes fuse to $\left(\mathbf{1}, \frac{1}{q}\right)$, the ordinary Laughlin quasihole). For the other fusion channel, one has $\kappa_{\sigma\sigma,\psi} = \frac{1}{4q} + \frac{3}{8}$, that is, one has $\kappa_{\sigma\sigma,\psi} = \kappa_{\sigma\sigma,\mathbf{1}} + h_\psi$, where $h_\psi = \frac{1}{2}$ is the scaling dimension of the neutral fermion.

We know, on theoretical grounds, the spin of the Laughlin's quasihole in the Moore-Read state, which we label $J_{(\mathbf{1},1/q)}$. We can then first make a prediction for the spin of an elementary quasihole, $J_{(\sigma,1/(2q))}$, using the spin-statistics relation. Finally, using $J_{(\sigma,1/(2q))}$, we can obtain the spin for the quasihole of type $\left(\psi, \frac{1}{q}\right)$, i.e. $J_{(\psi,1/q)}$. In the following, we provide numerical results that confirm the values of the spin in these three cases.

Generically, the spin of a Laughlin quasihole is given by

$$J_{(\mathbf{1},1/q)} = -\left(\frac{1}{2q}\right) + \frac{\mathcal{S}}{2q}, \tag{6.34}$$

where $\mathcal{S}$ is a number known as the "shift" of the state[31, 176]. This result can for instance be computed from the assumption of a rigid shift of the droplet's boundary [273] and by writing the total angular momentum of the state as [187] $L = \frac{N/\nu - \mathcal{S}}{2} N$. The reasons for the introduction of the shift will be clear in a moment.

In the case of the Moore-Read Pfaffian state, the shift is given by $\mathcal{S} = q + 1$, which results in

$$J_{(\mathbf{1},1/q)} = \frac{1}{2}, \tag{6.35}$$

independent of the filling fraction $1/q$.

By making use of $J_{(\mathbf{1},1/q)} = \frac{1}{2}$, $\kappa_{\sigma\sigma,\mathbf{1}} = \frac{1}{4q} - \frac{1}{8}$, and the spin-statistics relation

$J_{(\sigma,1/(2q))} = \frac{1}{2}(\kappa_{\sigma\sigma,\mathbf{1}} + J_{(\mathbf{1},1/q)})$, we find

$$J_{(\sigma,1/(2q))} = -\left(\frac{1}{8q} + \frac{1}{16}\right) + \frac{\mathcal{S}}{4q} = \frac{1}{8q} + \frac{3}{16}. \tag{6.36}$$

For $q = 1$, this results in $J_{(\sigma,1/2)} = \frac{5}{16}$, while for $q = 2$, we have $J_{(\sigma,1/4)} = \frac{1}{4}$.

With the values of $J_{(\sigma,1/(2q))} = \frac{1}{8q} + \frac{3}{16}$ and $\kappa_{\sigma\sigma,\psi} = \frac{1}{4q} + \frac{3}{8}$ at hand, we can now obtain $J_{(\psi,1/q)}$. Invoking again the spin-statistics relation $J_{(\psi,1/q)} = 2J_{(\sigma,1/(2q))} - \kappa_{\sigma\sigma,\psi}$, we obtain

$$J_{(\psi,1/q)} = -\left(\frac{1}{2q} + \frac{1}{2}\right) + \frac{\mathcal{S}}{2q} = 0. \tag{6.37}$$

Again, this value is independent of q.

Notice interestingly that the spins on the plane, as we defined them, take the same form that is found by Berry phase arguments on curved spaces, thanks to the coupling of the spin to the surface curvature [269]. Moreover, the second term $Q_{qh}\,\frac{\mathcal{S}}{2}$ is proportional to the shift quantum number $\mathcal{S}$ and linearly proportional to the quasihole charge Q_{qh} measured in units of the "elementary" Moore-Read quasihole charge $1/2q$, and can be removed by a suitable redefinition of the angular momentum operator in 2D 2.1.3. On the other hand, the first piece corresponds to the topological spin of the Moore-Read quasihole [179] - analogously to how in Eq. (6.22) the first piece, quadratic in the quasihole charge, corresponds to the topological spin of a Laughlin quasiparticle, while the second is related to the shift of the Laughlin state (in this case $Q_{qh}\,\frac{\mathcal{S}}{2} = p/2$ for p quasiholes fused together). Notice that the piece linear in the quasihole charge and proportional to the shift does not contribute to the spin-statistics relation [Eq. (6.18)], only the quadratic part does. The reasons that lead us to split the topological-spin contribution from the shift in Eq. (6.34) should now be clear. While the first piece, quadratic in the quasihole charge, is related to their anyonic nature and encodes topological properties, the second piece is instead associated to the angular momentum of the background liquid[31]. This intriguing connection will be explored in future work.

In the following sub-subsection, we numerically confirm the spin values obtained here.

6.6.2 Numerical results

We now proceed to describe how we employed a Monte-Carlo sampling of the Moore-Read wavefunction in the presence of the different quasiholes $\left(\sigma, \frac{1}{2q}\right)$, $\left(\mathbf{1}, \frac{1}{q}\right)$ and $\left(\psi, \frac{1}{q}\right)$ in order to characterize their charges and spins. We here always consider N

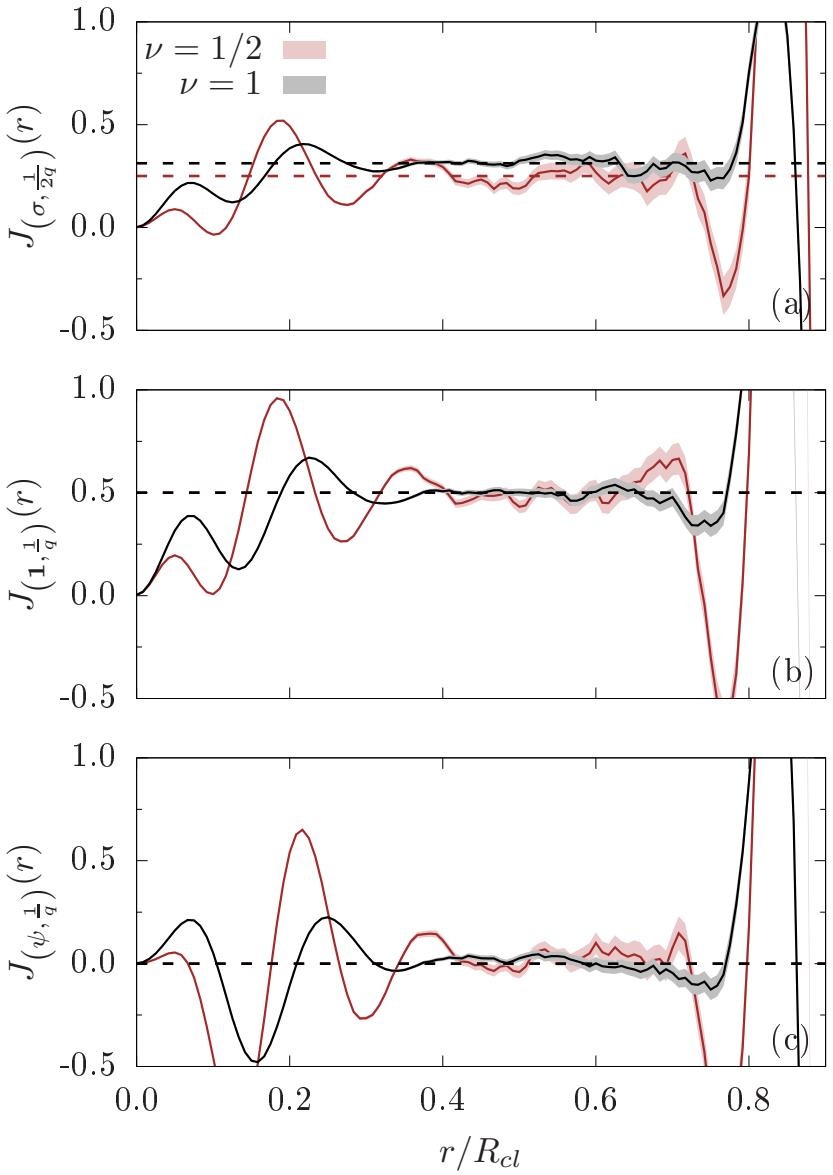

Figure 6.8: Comparison of the quasihole spins $J(r) = \int_0^r \left(r'^2/2 - 1\right)\left(\rho_{qp}(r') - \rho_{MR}(r')\right) r' dr'$, where $\rho_{qp}(r)$ is the quasihole density and $\rho_{MR}(r)$ the background Moore-Read density, for the different Moore-Read quasiholes: (a) the $\left(\sigma, \frac{1}{2q}\right)$, (b) the $\left(\mathbf{1}, \frac{1}{q}\right)$ and (c) the $\left(\psi, \frac{1}{q}\right)$, for the bosonic filling $\nu = 1$ (corresponding to $q = 1$) and the fermionic $\nu = \frac{1}{2}$ ($q = 2$). $R_{\mathrm{cl}} = \sqrt{2N/\nu}$ is the classical radius of the droplet.

to be even.

The "Laughlin" quasihole $\left(\mathbf{1}, \frac{1}{q}\right)$ can be obtained by adiabatically piercing the

system with a flux at position η, resulting in

$$\Psi_{\left(\mathbf{1},\frac{1}{q}\right)}(\eta) = \prod_i^N (z_i - \eta)\,\mathrm{Pf}\left(\frac{1}{z_i - z_j}\right)\prod_{i<j}^N (z_i - z_j)^q \exp\left(-\frac{1}{4}\sum_i |z_i|^2\right). \tag{6.38}$$

The Gaussian factors will henceforth be omitted.

The $\left(\sigma, \frac{1}{2q}\right)$ quasiholes are instead obtained by "splitting" a Laughlin quasihole making use of the properties of the Pfaffian factor

$$\Psi(\eta_1, \eta_2) = \mathrm{Pf}\left(\frac{(z_i - \eta_1)(z_j - \eta_2) + (i \rightleftarrows j)}{z_i - z_j}\right)\prod_{i<j}^N (z_i - z_j)^q. \tag{6.39}$$

From the numerical point of view, it is useful to maximize the distance between the quasiholes and the boundary of the system; the optimal solution is to place a single $\left(\sigma, \frac{1}{2q}\right)$ quasihole at $\eta = 0$ – the system's centre – and send the other at spatial infinity. This will in general modify the properties of the boundary, but not those of the quasihole at the centre of the system. We obtain

$$\Psi_{\left(\sigma,\frac{1}{2q}\right)}(\eta = 0) = \mathrm{Pf}\left(\frac{z_i + z_j}{z_i - z_j}\right)\prod_{i<j}^N (z_i - z_j)^q. \tag{6.40}$$

Finally, we introduce a quasihole $\left(\psi, \frac{1}{q}\right)$ by inspecting the four-$\left(\sigma, \frac{1}{2q}\right)$ quasiholes wavefunction. Introducing the four quasi-hole "building-block"

$$\Psi_{(ab)(cd)} = \mathrm{Pf}\left(\frac{(z_i - \eta_a)(z_i - \eta_b)(z_j - \eta_c)(z_j - \eta_d) + (i \rightleftarrows j)}{z_i - z_j}\right)\prod_{i<j}^N (z_i - z_j)^q \tag{6.41}$$

it is possible to define two degenerate four-quasihole states for suitable short-ranged Hamiltonians with pinning potentials [282]

$$\begin{cases} \Psi_0 = \prod_{\mu<\nu}^4 \eta_{\mu\nu}^{\frac{1}{4q}-\frac{1}{8}} \frac{(\eta_{13}\eta_{24})^{\frac{1}{4}}}{\sqrt{1+\sqrt{1-x}}}\left(\Psi_{(13)(24)} + \sqrt{1-x}\,\Psi_{(14)(23)}\right) \\ \Psi_1 = \prod_{\mu<\nu}^4 \eta_{\mu\nu}^{\frac{1}{4q}-\frac{1}{8}} \frac{(\eta_{13}\eta_{24})^{\frac{1}{4}}}{\sqrt{1-\sqrt{1-x}}}\left(\Psi_{(13)(24)} - \sqrt{1-x}\,\Psi_{(14)(23)}\right) \end{cases} \tag{6.42}$$

where $\eta_{\mu\nu} = \eta_\mu - \eta_\nu$ and $x = \frac{\eta_{12}\eta_{34}}{\eta_{13}\eta_{24}}$; these states are orthonormal [179].

By taking the appropriate limit of Ψ_1, we obtain

$$\Psi_{\left(\psi,\frac{1}{q}\right)}(\eta = 0) \propto \mathrm{Pf}\left(\frac{z_i^2 + z_j^2}{z_i - z_j}\right)\prod_{i<j}^N (z_i - z_j)^q. \tag{6.43}$$

In Fig. 6.7 and Fig. 6.8 we exhibit Monte Carlo results for the charge $Q(r) = \int_0^r (\rho_{qp}(r') - \rho_L(r'))\, r' dr'$ and spin Eq. (6.15) of the different Moore-Read quasiholes $\left(\sigma, \frac{1}{2q}\right)$ Eq. (6.40), $\left(\mathbf{1}, \frac{1}{q}\right)$ Eq. (6.38) and $\left(\psi, \frac{1}{q}\right)$ Eq. (6.43). The results for both the charge and spin are in excellent agreement with the predictions.

6.7 Conclusions and perspectives

In this chapter we have presented a general derivation of a spin-statistics relation for Abelian quasiparticles on planar surfaces, derived from very mild assumptions. We have shown that the quasiparticles fractionalize the gauge-invariant generator of rotations and that this quantity can be used to define a measurable spin. We showed that to the fractionalization of angular momentum at the quasiparticle position corresponds a factionalized angular momentum at the edge which encodes crucial information about the topological state of the bulk. Specifically, the braiding properties are there encoded, which we believe to be a neat manifestation of the bulk-boundary correspondence.

Our results carry over naturally to non-Abelian quantum Hall states. We explicitly analysed the quasiholes in the Moore-Read case, but a long term goal would be to try addressing the problem in more exotic states belonging to the Read-Reazayi series - even though doing numerical calculations appear to be daunting. Secondly, it would be extremely interesting to fully uncover the relation between the fractionalized rotation generator and the topological spin.

A natural follow-up study will try to address the link between the local angular momentum at the quasiparticle position, which we associate with its fractional spin, and the spin that quasiparticles exhibits when moving on curved surfaces. A possible direction could for example be studying the effective dynamics of an impurity immersed in a fractional quantum Hall bath along the lines of [79].

Finally, we explicitly showed that Laughlin's quasielectron is not the antiparticle corresponding to Laughlin's quasihole. We argue that this is an effect of Laughlin's quasielectron influencing the structure of the edge of the system. We further investigated this hypothesis by rewriting Laughlin's quasielectron in terms of a composite fermion description and showing that it has a long-range tail which affects the system's edge. By defining a truncated quasielectron wavefunction – which interpolates between those of Jain and Laughlin – we show that as long as the tail is truncated away from the edge the correct value of the spin is recovered. We argue these to be the reason behind the contradictory results reported in the literature in the last 30 years concerning the Laughlin's quasielectron wavefunction.

CHAPTER 7

CONCLUSION

In this Chapter we want to give an overall conclusion to this thesis work and briefly give our outlooks.

7.1 Summary

In Chapter 5, we tackled the problem of studying the linear and nonlinear edge dynamics of large Laughlin-like fractional quantum Hall states trapped by some anharmonic potential. We developed an efficient numerical method based on a joint use of exact diagonalization and Monte Carlo sampling of the relevant matrix elements. This allowed us to extract response functions, relevant for the linear regime, and also to study the real-time dynamics of our system. In this way we were able to uncover details of the nonlinear physics as well. In both the linear and nonlinear regimes our calculations highlighted a number of effects of direct experimental and theoretical interest, such as a sizable group velocity dispersion of the edge mode related to strong bulk correlations as well as significant amplitude-dependent effects, both induced by velocity gradients at the system's edge.
We leveraged on these numerical results to build an effective one-dimensional nonlinear chiral Luttinger liquid quantum model, which describes the dynamics of the one-dimensional edge in the form of a quantum Korteweg-de Vries equation.
We subsequently reformulated this model in terms of an effective system of interacting massive chiral fermions in one-dimension to extract quantitative information on the quantum Hall edge, such as the dynamic structure factor broadening and its threshold singularities which exhibit power-law behaviour with universal exponents.

In Chapter 6 we have presented a general derivation of a spin-statistics relation for Abelian quasiparticles on planar surfaces, derived from very mild assumptions. This naturally carries over to the non-Abelian case provided the fusion channel is well defined. We have shown that the quasiparticles fractionalize the gauge-invariant generator of rotations and that this quantity can be used to define a measurable spin. We showed how to the fractionalization of angular momentum at the quasiparticle position corresponds a factionalized angular momentum at the edge, which encodes crucial information about the topological state of the bulk.
We explicitly analysed two paradigmatic quasielectron wavefunctions, the one proposed by Laughlin based on the adiabatic extraction of flux and the one propesed by Jain based on his composite-fermion approach to the fractional quantum Hall effect. Our results suggest that Jain's quasielectron is a good quasielectron wavefunction. Laughlin's one instead satisfies the spin-statistics relation, but does not have the correct spin to be the anti-anyon of Laughlin's quasihole.
This pushed us to further investigate the structure of Laughlin's quasielectron: we showed how its presence has a long-distance effect on the system's boundary, which in turn affects the topological robustness of the spin. We argue these to be the reason behind the contradictory results reported in the literature in the last 30 years concerning Laughlin's quasielectron wavefunction.
We finally briefly discussed the non-Abelian case, showing how our conclusions are easily extended to such a case. We explicitly analysed the most simple and paradigmatic case, provided by the Moore-Read state.

7.2 Future Work

Regarding the nonlinear dynamics at the edge, many questions are still opened and currently being investigated. Among these, we would like to mention a few.
First of all, we would like to understand the physical mechanism giving rise to the modified group-velocity dispersion we numerically observed, and in this way to explain the coefficient of the cubic term in the dispersion. We believe this to be related to the Hall viscosity and to the bulk magneto-roton excitations, but work is still (slowly) in progress.
Secondly, a more detailed understanding of the spectral function at its thresholds would be desirable; is some power-law behaviour emerging even in this quantity? Can the refermionization of the edge-dynamics answer this question?
Thirdly, it would be interesting to further understand and characterize the emergent nonlinear and dispersive Korteweg-de Vries dynamics at the edge, in particular the

emergence of shock-waves and/or solitons. Furthermore, we pointed out how situations could emerge in which the gradient of the force on the fractional quantum Hall boundary can vanish. In this case, higher order terms can be expected to set the dynamics of the edge modes. How is the emergent hydrodynamics modified?
As a fourth point, we would like to extend our numerical analysis to the Moore-Read case. Even though more challenging, the non-Abelian nature of the state can potentially lead to highly interesting and non-trivial nonlinear behaviours of the edge modes.
Fifth, we would like to extend our work to lattice systems and in particular address the question of how the underlying periodic spatial structure modifies the emergent linear and nonlinear dynamics of the edge modes.
Finally, we aim to analyse the role of non-ultrashort-ranged interactions. We believe this last point to be of high relevance, given that large fractional quantum Hall systems are currently available only in electronic condensed matter systems. A deeper understanding of how the interplay of confinement and interactions sets the edge linear and nonlinear dynamics beyond the chiral Luttinger liquid model would therefore be desirable.

Many open questions are still present, also concerning the spin of fractional quantum Hall quasiparticles.
First of all, it would be extremely interesting to fully uncover the relation between the fractionalized rotation generator at the quasiparticle position, which we associate with its fractional spin, and the topological spin discussed in anyon models [283, 179]. We also would like to explicitly link the local angular momentum at the quasiparticle position and the spin that quasiparticles exhibit when moving on curved surfaces. We think that a possible direction to investigate this link would be studying the effective dynamics of an impurity immersed in a fractional quantum Hall bath [79], for it must inherit the effects of the quasiparticle spin.
Concerning the non-Abelian case, a natural follow-up question would be the extension of our analysis to the more exotic Read-Rezayi states; the numerical study via Monte Carlo techniques is however much more difficult, and it is absolutely not obvious what strategy (e.g. the use of Jack polynomials or the MPS formulation) would be more suitable in such a case.

To conclude, we believe that our results will be important towards a complete understanding the linear and nonlinear dynamics of the edge modes and of the bulk excitations in fractional quantum Hall liquids in state-of-the-art atomic or photonic synthetic quantum matter platforms.

Part III
Appendices

APPENDIX A

MONTE CARLO CALCULATIONS

In this Appendix we discuss further details of the Monte Carlo calculations we performed.

A.1 Numerical details

As we already explained in Sec. 5.1.1 and Sec. 5.1.2, provided the coupling to states above the many-body Laughlin gap can be neglected, the system eigenstates – which here we denote as $|n,l\rangle$ – can be entirely written expanding them using the many-body linearly-independent model wavefunctions $|\alpha_l,l\rangle$ spanning the edge-state space at angular momentum L_0+l

$$|n,l\rangle = \sum_{\alpha_l} C_{\alpha_l}^{[n,l]} \frac{|\alpha_l,l\rangle}{\sqrt{\langle\alpha_l,l|\alpha_l,l\rangle}} \tag{A.1}$$

where α_l runs through the $p_N(l)$ states corresponding to the integer partitions of the angular momentum l of length smaller or equal to N. Using this expansion, since the states $|\alpha_l,l\rangle$ are not orthogonal, the time-independent Schrödinger equation turns into the generalized eigenvalue problem of Eq. (5.6) for the expansion coefficients $C_{\alpha_l}^{[n,l]}$

$$\mathbb{H}_{\beta_l,\alpha_l} C_{\alpha_l}^{[n,l]} = E_{n,l}\, \mathbb{M}_{\beta_l,\alpha_l} C_{\alpha_l}^{[n,l]}\,. \tag{A.2}$$

Here, the matrix elements $\mathbb{H}$ and $\mathbb{M}$ are defined as

$$\begin{cases} \mathbb{H}_{\beta_l,\alpha_l} = \frac{\langle \beta_l, l|H|\alpha_l, l\rangle}{\sqrt{\langle \beta_l|\beta_l\rangle\langle\alpha_l|\alpha_l\rangle}} \\ \mathbb{M}_{\beta_l,\alpha_l} = \frac{\langle \beta_l, l|\alpha_l, l\rangle}{\sqrt{\langle \beta_l|\beta_l\rangle\langle\alpha_l|\alpha_l\rangle}}. \end{cases} \tag{A.3}$$

Since the kinetic energy is constant within the lowest Landau level and the two-body interaction energy is assumed to be negligible within the subspace of Laughlin-like states, the effective Hamiltonian $\mathbb{H}$ only includes the confinement potential $V_{\mathrm{conf}}(r)$, while the "metric" $\mathbb{M}$ accounts for the non-orthonormality of the basis wavefunctions. The high-dimensional integrals in Eq. (A.3) are computed by means of a standard single-component Metropolis-Monte Carlo sampling [284] which allows for efficient exploration of the configuration space at large N without the acceptance rate dropping. Notice that, since the states $|\alpha_l, l\rangle$ and $|\beta_l, l\rangle$ are polynomials of not-too-large degree with a Laughlin wavefunction Eq. (5.2) common factor, they share most of their zeros, so the sampling procedure is highly efficient. In principle the matrices $\mathbb{M}$ and $\mathbb{H}$ obtained in this way are not exactly Hermitian, so we perform a preliminary Hermitization step before proceeding with the diagonalization Eq. (A.2).

General observables are computed in an analogous way, e.g. those appearing in the dynamic structure factor (Section A.2) and in the spectral function (Section A.3). These calculations are performed by sampling the relevant observable using the power-sum symmetric polynomials basis $|\alpha_l, l\rangle$, and then rotating the results onto the system eigenstates via Eq. (A.1) which thus requires to be computed with sufficient accuracy. This typically requires much more samples than obtaining the energy eigenvalues, as it is apparent by comparing for example Fig. A.1 and Fig. A.2.

Notice finally that with the choice of gauge we made (power-sum symmetric polynomials as a basis spanning the relevant many-body subspace of the total Hilbert space), the system's wavefunction can be expanded as a linear combination of monomials in the z_i with real coefficients

$$\langle z_1, \ldots, z_N|\alpha_l, l\rangle = \sum_{m_1,\ldots,m_N} C_{m_1,\ldots,m_N}\, \phi_{m_1}(z_1)\phi_{m_2}(z_2)\ldots\phi_{m_N}(z_N) \tag{A.4}$$

where $\phi_m(z)$ are the circular gauge wavefunctions given by Eq. (3.5) and as already stated the coefficients $C_{m_1,\ldots,m_N}$ are real. The matrix-elements of local observables

in real space therefore read

$$\langle \beta_l, l | \, o(z_1) \, | \alpha_l, l \rangle = \\ = \sum_{\substack{m_1, m_1' \\ m_2, \ldots, m_N}} C'_{m_1', m_2, \ldots, m_N} C_{m_1, m_2 \ldots, m_N} \int \phi_{m_1'}(z_1) o(z_1) \phi_{m_1}(z_1) dz_1 \quad \text{(A.5)}$$

and it follows that if the single particle matrix element $\int \phi_{m_1'}(z_1) o(z_1) \phi_{m_1}(z_1) dz_1$ is real/imaginary, so will be the many-body one. Therefore, imaginary/real parts of the matrix elements can be discarded.

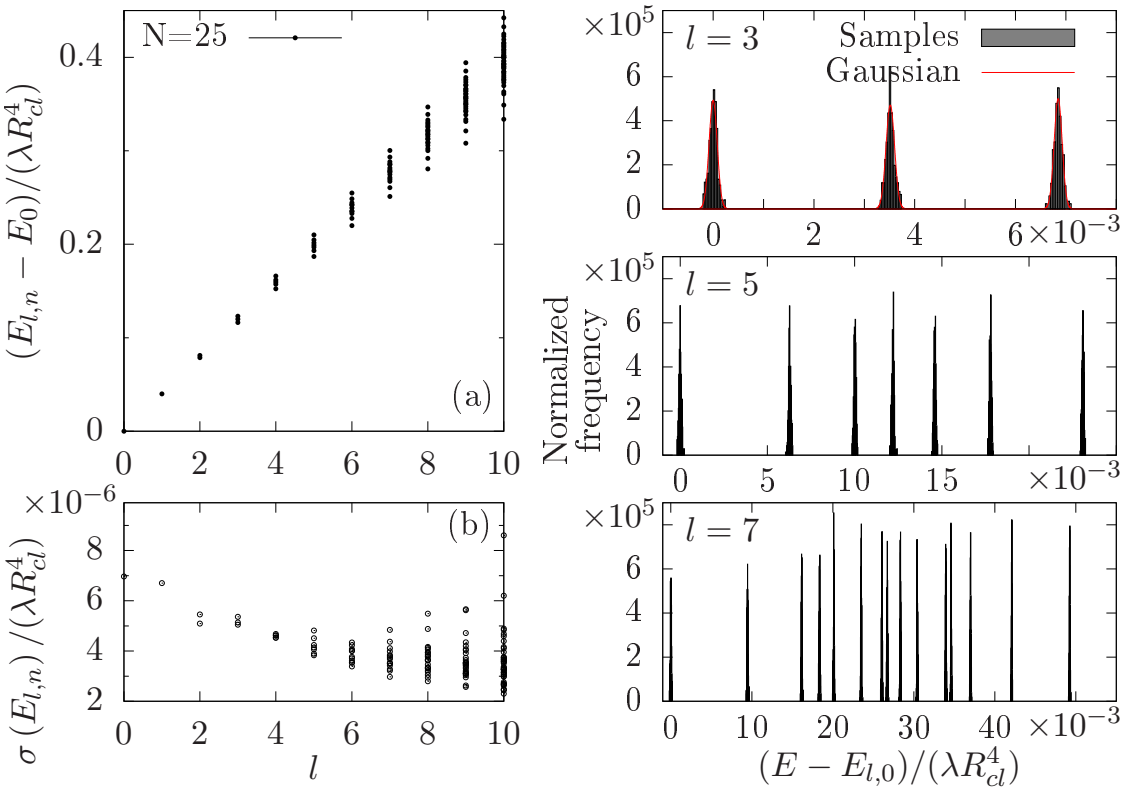

Figure A.1: (a) Eigenenergy spectrum (with errorbars) for a $N = 25$, $\nu = 1/2$ fractional quantum Hall cloud confined by a $\delta = 4$ quartic potential. (b) Magnified view on the statistical errors on the eigenenergies. The panels on the right show histograms for the $M = 250$ Monte Carlo realizations of the energy spectrum in each l-sector. Each point is obtained by an independent run.

A.2 Dynamic structure factor

We here briefly describe how we write the dynamic structure factor weights (yet to be rotated over the system's eigenstates) appearing in Eq. (C.11)

$$\frac{\langle \alpha_l, l |\, \delta\hat{\rho}_{-l}\, | 0 \rangle}{\sqrt{\langle \alpha_l, l | \alpha_l, l \rangle \, \langle 0 | 0 \rangle}}. \tag{A.6}$$

We expand the density operator as $\delta\hat{\rho}_{-l} = \int e^{il\theta}\delta\hat{\rho}(\theta)d\theta$. Here, we defined the edge-density operator as the difference between the density operator and its ground state expectation value, integrated over the radial direction $\delta\hat{\rho}(\theta) = \int_0^\infty (\hat{\rho}(\mathbf{r}) - \rho_0(\mathbf{r}))\, r\, dr$. In first quantization language then we can write, for $l \neq 0$,

$$\delta\hat{\rho}_{-l} = \int e^{il\theta} \sum_i^N \frac{\delta(r - r_i)}{r} \delta(\theta - \theta_i)\; r\, dr d\theta = \sum_i^N e^{il\theta_i} \tag{A.7}$$

which is then be sampled according to Eq. (5.8).

A.3 Spectral function

We here briefly describe how we write the matrix elements appearing in the spectral function Eq. (5.51) in a way which is amenable of Monte Carlo sampling. We expand the annihilation operators at angular momentum $\Delta l = (N-1)/\nu - l$ as

$$\hat{a}_{\Delta l} = \int dz_1 \Phi^*_{\Delta l}(z_1)\hat{\psi}(z_1), \tag{A.8}$$

where $\Phi_{\Delta l}(z_1)$ are the single-particle lowest Landau level orbitals in the circular gauge $\Phi_{\Delta l}(z_1) = \left(z_1/\sqrt{2}\right)^{\Delta l} \exp(-|z_1|^2/4)/\sqrt{2\pi \Delta l!}$. We then write the matrix elements explicitly in first quantization language as

$$\langle f |\, \hat{a}_{\Delta l}\, | 0 \rangle = \sqrt{N} \int \Phi_{\Delta l}(z_1)^* \frac{\Psi_f^{[N-1]}(z')^*}{\mathcal{N}_f} \frac{\Psi_0^{[N]}(z)}{\mathcal{N}_0}\, \mathcal{D}z \tag{A.9}$$

where z is a shorthand for the the particle coordinates $z = \{z_1, \ldots, z_N\}$ and z' a shorthand for all the particle coordinates exception made for z_1, $z' = \{z_2, \ldots, z_N\}$, and we define the normalization factors as

$$\mathcal{N}_0 = \left[\int \mathcal{D}z \left| \Psi_0^{[N]}(z) \right|^2 \right]^{1/2} \tag{A.10}$$

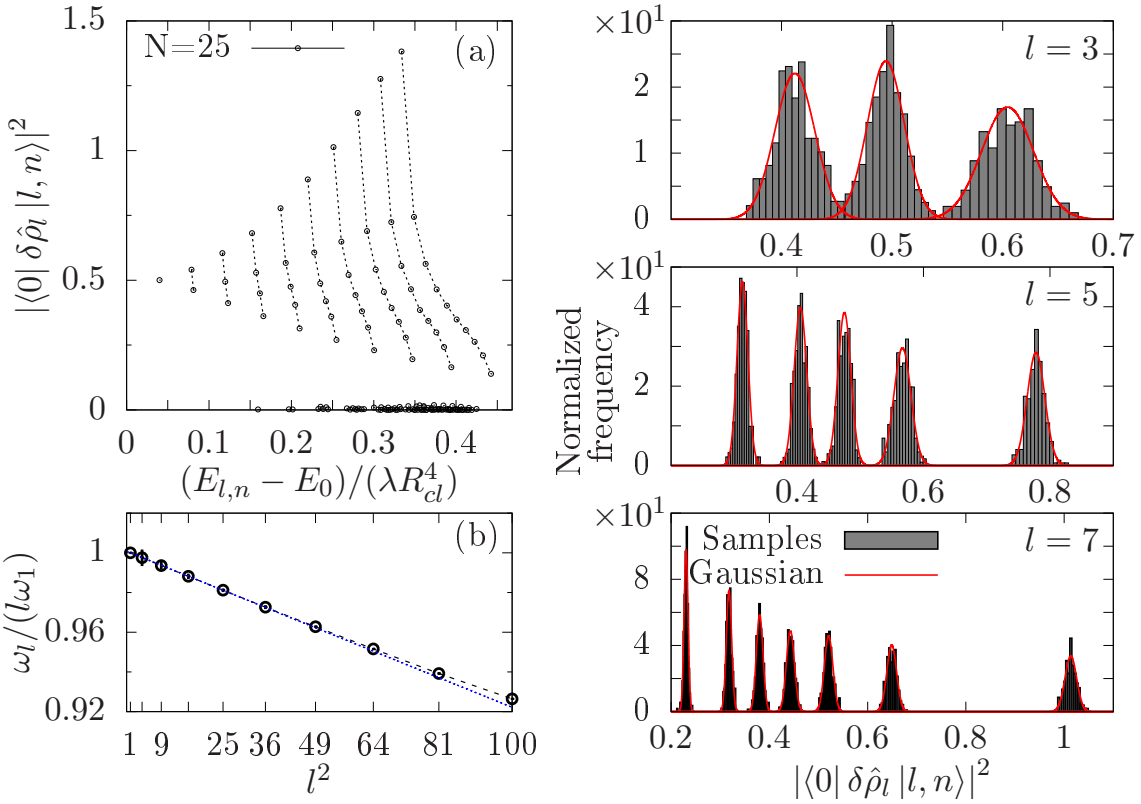

Figure A.2: (a) Dynamic structure factor weights $|\,\langle 0|\,\delta\hat{\rho}_l\,|l,n\rangle\,|^2$ (with errorbars) for a $N = 25$, $\nu = 1/2$ fractional quantum Hall cloud confined by a $\delta = 4$ quartic potential. (b) Suitably normalized first moment ω_l of the dynamic structure factor (with errorbars). The panels on the right show histograms for the $M = 250$ Monte Carlo realizations of the dynamic structure factor weights in each l-sector.

and

$$\mathcal{N}_f = \left[\int \mathcal{D}z' \left|\Psi_f^{[N-1]}(z')\right|^2\right]^{1/2}. \tag{A.11}$$

The final states Ψ_f are expanded as power-sum symmetric polynomials multiplying a $(N-1)$-particles Laughlin wavefunction $\Psi_L^{[N-1]}(z')$. We find that the Monte Carlo sampling of the integrals is strongly facilitated by introducing the probability distribution function

$$\mathcal{P}(z) = \frac{|\Psi_0^{[N]}(z_1\dots z_N)\Psi_0^{[N-1]}(z_2\dots z_N)|}{\int |\Psi_0^{[N]}(z_1\dots z_N)\Psi_0^{[N-1]}(z_2\dots z_N)|\mathcal{D}z} \tag{A.12}$$

since in this way we have zeros of the correct order at each particle's position, which makes the sampling more effective. The obvious disadvantage is that, since not all the coordinates are treated on an equal footing, the relevant matrix element which needs to be sampled [Eq. (A.9)] cannot be symmetrized over all the coordinates:

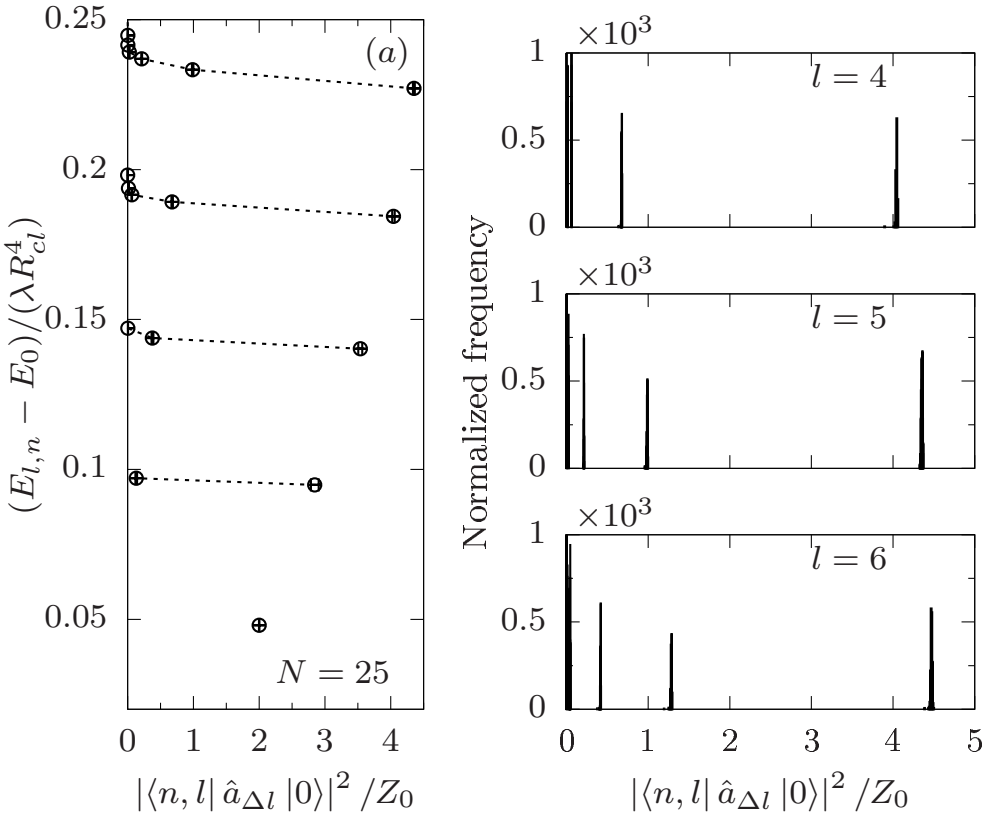

Figure A.3: (a) Spectral function weight $|\,\langle f|\,\hat{a}_{\Delta l}\,|0\rangle\,|^2$, normalized to the Laughlin-Laughlin matrix element $Z_0 = |\,\langle f|\,\hat{a}_{(N-1)/\nu}\,|0\rangle\,|^2$, obtained through Monte Carlo diagonalization for $N = 30$ bosons at half filling $\nu = 1/2$, in a quartic $\delta = 4$ trap. The panels on the right show histograms for $M = 250$ Monte Carlo realizations of the spectral function weights for some of the angular momentum l sectors considered.

we however empirically find the usage of Eq. (A.12) to be a compromise worth the additional computational price.

A.4 Statistics of the sampling

In order to estimate the statistical error of the Monte Carlo sampling, we performed some statistical analysis on the numerical data. In particular, we split the calculations of our observables into $M = 250$ groups for the same droplet configuration. The obtained results are treated as a population of which we studied the statistics. The average energies

$$E_{l,n} = \frac{1}{M}\sum_{i=1}^{M} e_{l,n}[i] \tag{A.13}$$

are shown in Fig. A.1(a) with their standard errors

$$\sigma(E_{l,n}) = \left(\frac{1}{M(M-1)} \sum_{i=1}^{M} \left(e_{l,n}[i] - E_{l,n} \right)^2 \right)^{\frac{1}{2}} . \tag{A.14}$$

Since these latter are very small and almost invisible in Fig. A.1(a), we have replotted them separetely in panel (b). Histograms of the $M = 250$ samples for the eigenstate energies at a few values of l are shown in the right panels.

The same analysis has been repeated for the dynamic structure factor and the spectral function; the results for the dynamic structure factor weights are shown in Fig. A.2(a), with the associated errorbars; histograms of the $M = 250$ samples for a few l components of the dynamic structure factor are shown in the panels on the right. Error propagation then yields small but sizeable errorbars on the central frequency ω_l, in particular at $l = 1$, as shown in Fig. A.2(b). The results for the spectral function weights are instead shown in Fig. A.3.

Notice that all the histograms are approximatively Gaussian, showing that indeed the samples are independent, and well separated.

APPENDIX B

EXCITATIONS WITH A RADIAL DEPENDENCE

In Chapter 5 we dealt with an excitation $U(\mathbf{r}, t)$ (see Eq. (5.9)) which is uniform in the radial direction $\hat{\mathbf{r}}$. In this Appendix we show that the results we obtained remain valid, under reasonable approximations, even when the externally applied excitation depends on the radial coordinate.

The external potential couples to the density (apart for a time-dependent additive constant which is anyway irrelevant for the dynamics) via

$$\hat{V}(t) = \int U(\mathbf{r}; t)\, \delta\hat{\rho}(\mathbf{r})\, d^2\mathbf{r}. \tag{B.1}$$

For edge excitations, the support of the density variation $\delta\hat{\rho}(\mathbf{r})$ is exponentially localized close to the edge, $r \simeq R_{\rm cl}$: if the excitation potential is nearly uniform in the radial direction over the width of the edge mode, we can approximate the previous excitation potential as

$$\hat{V}(t) \simeq \int U(R_{\rm cl}, \theta; t) \left(\int \delta\hat{\rho}(\mathbf{r})\, r\, dr \right) d\theta = \int U(R_{\rm cl}, \theta; t)\, \delta\hat{\rho}(\theta)\, d\theta\,, \tag{B.2}$$

which indeed yields a minimal coupling between the edge density variation and an effectively azimuthal excitation. On physical grounds one can indeed expect that as long as the radially-dependent excitation potential is almost constant over the edge width, reaching the incompressible bulk on the inner side and the vacuum on the outer one, a quantized transverse Hall current will flow during the excitation time from the bulk all the way through the edge, where it is accumulated. Then, the edge-density variation will be proportional to the macroscopic bulk transverse conductivity set by the filling fraction.

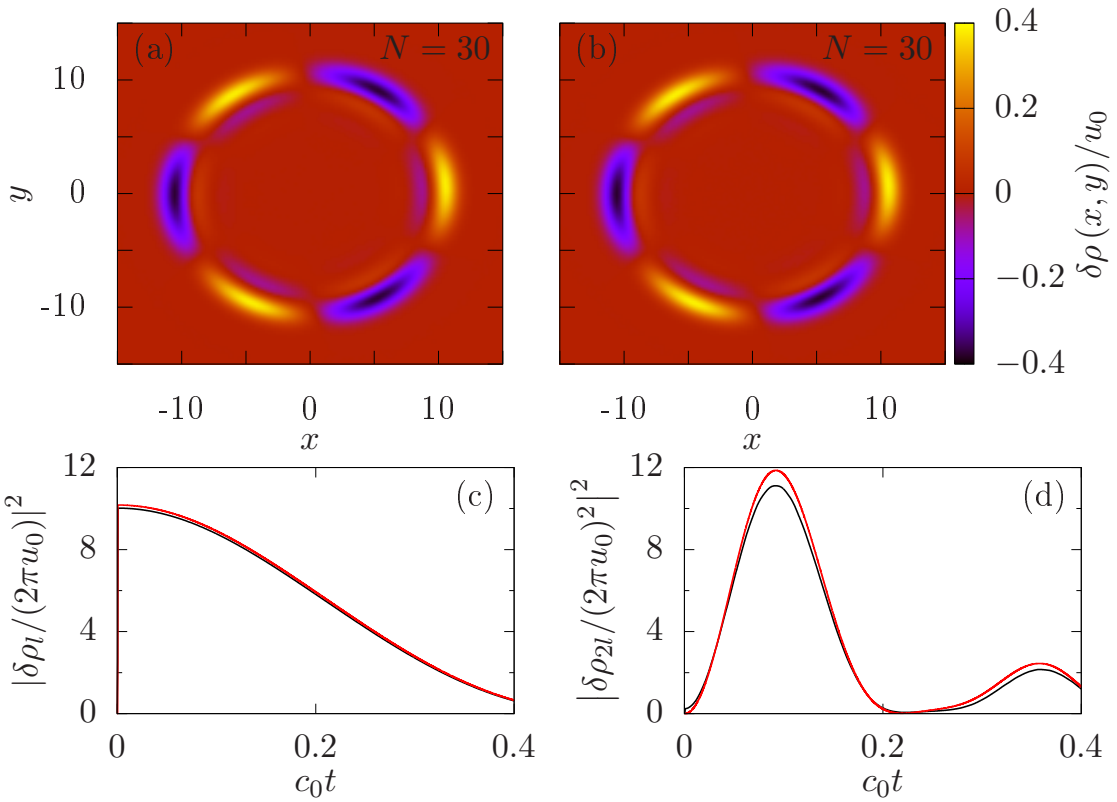

Figure B.1: Density variation $\delta\rho(x, y)$ at a time $c_0 t \simeq 0.1$ after the $\nu = 1/2$ cloud has been excited by means of (a) an excitation with a non-trivial radial profile described by Eq. (B.3) or (b) by a radially flat profile. (c,d) Time-evolution of the fundamental and second harmonic spatial Fourier components of the edge density variations in the same two cases (black and red). The confinement is quartic, $V_{\rm conf} \propto r^4$ and the system comprises $N = 25$ bosons at bulk filling $\nu = 1/2$.

To validate this physical picture, we compare the calculations presented in Chapter 5 for a radially uniform excitation potential U with a non-uniform one, by performing analogous numerical calculations but perturbing the droplet with an excitation of the form

$$U(r, \theta; t) = U_l(t)\ (r/R_{\rm cl})^l\ e^{il\,\theta} + \text{c.c.} \tag{B.3}$$

for which the radial variation of the excitation potential over the edge-mode shape may be not negligible. As shown in Fig.B.1, good qualitative agreement with the results for a flat $U(\theta; t) = U(R_{\rm cl}, \theta; t)$ is found: the density variations $\delta\rho(x, y)$ are in fact practically indistinguishable. Note that the excitation considered here was strong enough to trigger visible non-linear effects.

The comparison has been made more quantitative by looking at the time-evolution

of the spatial Fourier transforms of the edge density (bottom panels). The fundamental mode in the two cases can hardly be told apart. Slight quantitative differences appear in the second spatial harmonic, even though the qualitative shape remains the same. This confirms that the approximation made in Eq. (B.2) is a good one, especially at small l, so the simpler form Eq. (B.2) is an accurate effective description also for the more general coupling Eq. (B.1).

APPENDIX C

LINEAR RESPONSE ANALYSIS

In this Appendix we discuss the perturbative analysis of the linear response theory of a fractional quantum Hall cloud to a weak time-dependent external excitation.

C.1 Linear response

The key observable we consider is the edge density variation, which we define as

$$\delta\hat{\rho}(\theta) = \int_0^\infty \left(\hat{\psi}^\dagger(\mathbf{r})\hat{\psi}(\mathbf{r}) - \langle\hat{\psi}^\dagger(\mathbf{r})\hat{\psi}(\mathbf{r})\rangle\right) r\, dr \tag{C.1}$$

where the bra-kets denote the expectation value on the ground state and $\psi^\dagger(\mathbf{r})$ is the particle-creation operator at position $\mathbf{r}$.

Within linear response theory, the edge density variation induced by the external perturbing potential which couples to the edge-density (see Eq. (B.2))

$$\hat{V}(t) = \int U(\theta;t)\,\delta\hat{\rho}(\theta)\,d\theta \tag{C.2}$$

reads

$$\langle\delta\tilde{\rho}(\theta,t)\rangle = -i\left\langle\left[\delta\tilde{\rho}(\theta,t), \int_{-\infty}^{t}\tilde{V}(t')dt'\right]\right\rangle \tag{C.3}$$

where the system is assumed to be initially in its ground state at $t\to-\infty$, higher order terms $\mathcal{O}(U^2)$ have been neglected and the tilde indicate interaction picture with respect to the unperturbed $U=0$ Hamiltonian.

With straightforward algebra, the above formula can be rewritten as

$$\langle \delta\hat{\rho}(\theta,t)\rangle = 2\,\Im \int_{-\infty}^{t} dt' \int d\theta'\; U(\theta',t') \left\langle \delta\hat{\rho}(\theta)\, e^{-i(\hat{H}-E_0)(t-t')}\, \delta\hat{\rho}(\theta') \right\rangle . \tag{C.4}$$

Introducing the Fourier transforms

$$\begin{cases} \delta\hat{\rho}(\theta) = \frac{1}{2\pi}\sum_{l\neq 0} e^{il\theta}\delta\hat{\rho}_l \\ U(\theta,t) = \frac{1}{2\pi}\sum_{l\neq 0} e^{il\theta} U_l(t) \end{cases} \tag{C.5}$$

this can be reformulated as

$$\langle \delta\hat{\rho}(\theta,t)\rangle = 2\,\Im \int_{-\infty}^{t} dt' \frac{1}{(2\pi)^2} \sum_{l\neq 0} e^{il\theta}\, U_l(t')\, \mathcal{C}_l(t-t') \tag{C.6}$$

where the rotational invariance of the ground state has been used to remove a summation so that $\mathcal{C}_{ll'} = \mathcal{C}_l\,\delta_{ll'}$ and

$$\mathcal{C}_l(t) = \left\langle \delta\hat{\rho}_l\, e^{-i(\hat{H}-E_0)t}\, \delta\hat{\rho}_{-l} \right\rangle . \tag{C.7}$$

If we are interested in the late time dynamics of the system once the perturbation pulse has gone ($U_l(t) \to 0$ for late times), we can replace the upper boundary of the time integral with $t \to \infty$, use the convolution theorem and write

$$\langle \delta\hat{\rho}(\theta,t)\rangle = \frac{1}{\pi}\Im \left[\sum_l e^{il\theta} \int \widetilde{U}_l(\omega)\, S_l(\omega)\, e^{-i\omega t}\, d\omega \right] \tag{C.8}$$

where we defined the Fourier transforms

$$\widetilde{U}_l(\omega) = \int \frac{dt}{2\pi}\, e^{i\omega t}\, U_l(t) \tag{C.9}$$

$$S_l(\omega) = \int \frac{dt}{2\pi}\, e^{i\omega t}\, \mathcal{C}_l(t). \tag{C.10}$$

Combining Eq. (C.10) with Eq. (C.7) allows to recover the edge dynamic structure factor. As long as the confinement and excitation potentials are weak enough not to excite states above the many-body gap, we can introduce a projector onto these states only and rewrite

$$S_l(\omega) = \sum_n \delta\left(\omega - \omega_{l,n}\right) \left|\langle 0|\, \delta\hat{\rho}_l\, |l,n\rangle\right|^2 \tag{C.11}$$

where $|0\rangle$ is the Laughlin ground state and $\omega_{l,n} = E_{l,n} - E_0$ the excitation energy of

state $|l,n\rangle$ with respect to the ground state.

Integrating over the frequencies in Eq. (C.11) (restriction to energies below the many-body gap is automatically enforced by the projector onto the low-energy subspace) one obtains the edge static structure factor

$$S_l = \sum_n |\langle 0|\, \delta\hat{\rho}_l\, |l,n\rangle|^2 \tag{C.12}$$

which importantly is invariant under a deformation of the many-body Hamiltonian as long as the gap is not closed. Indeed, under this condition a unitary transformation between the "new" eigenstates $|l,n\rangle'$ and the "old" ones $|l,n\rangle$ is well defined. Hence, in the long wavelength/low energy limit the edge static structure factor maintains its chiral Luttinger liquid value regardless of the specific form of the confining potential. Namely, $S_l = \nu l$ when $l \geq 0$ (as shown in Fig. 5.4(c)) and 0 otherwise, reflecting the chirality of the system.

Assuming a narrowly peaked dynamic structure factor at $\omega \simeq \omega_l$ and including the chiral Luttinger liquid form of S_l, we can approximate Eq. (C.8) as

$$\langle \delta\hat{\rho}(\theta,t)\rangle = -\frac{\nu}{\pi}\frac{\partial}{\partial\theta}\sum_{l>0} \Re\left[e^{il(\theta-\omega_l t)}\widetilde{U}_l(\omega_l)\right], \tag{C.13}$$

which explicitly displays the proportionality of the edge response to the bulk filling factor of the fractional quantum Hall droplet, and is the key of our proposed measurement scheme of the transverse conductivity. Of course, this formula is only valid up to not-too-large times, namely as long as the dynamic structure factor broadening is not resolved, $\Delta E_l t \ll 1$.

Notice finally that the solution of the semiclassical equation introduced in Chapter 5 (Eq. (5.22)) perfectly matches this result as long as the nonlinear velocity term can be neglected.

APPENDIX D

DYNAMIC STRUCTURE FACTOR BROADENING IN A QUARTIC TRAP

In this Appendix we present a more detailed analysis of the second moment of the edge dynamic structure factor

$$\omega_2(l) = \frac{\int(\omega - \omega_1(l))^2\, S_l(\omega)\, d\omega}{\int\, S_l(\omega)\, d\omega} \tag{D.1}$$

in the case of a weak quartic $V_{\rm conf} = \lambda r^4$ potential confining the Laughlin droplet, and we compare the result to the simple prediction Eq. (5.42). This case is particularly simple: in the quartic trap, the angular velocity gradient is in fact constant and position independent,

$$c = \left.(r^{-1}\partial_r)^2\, V_{\rm conf}\right|_{r=R_{cl}} = 8\lambda \tag{D.2}$$

so we have

$$\omega_2(l) = \frac{16\lambda^2}{3\nu}\, l^2(l^2-1)\ : \tag{D.3}$$

when the product $\nu \times \omega_2(l)$ is plotted, data from different filling factors ν are then expected to collapse on the same curve.

In order to better highlight the long-wavelength limit, data for different values of the particle number N and filling factor ν are plotted in Fig. D.1(a) in terms of $q^2(q^2 - R_{cl}^{-2})$, where $q = l/R_{cl}$ is the edge excitation wavevector: it is apparent how all points accurately fall on the expected straight line Eq. (D.3). The difference $\Delta(q)$ from this line is shown in the bottom panel: the difference is always small and tends to zero in the long-wavelength limit.

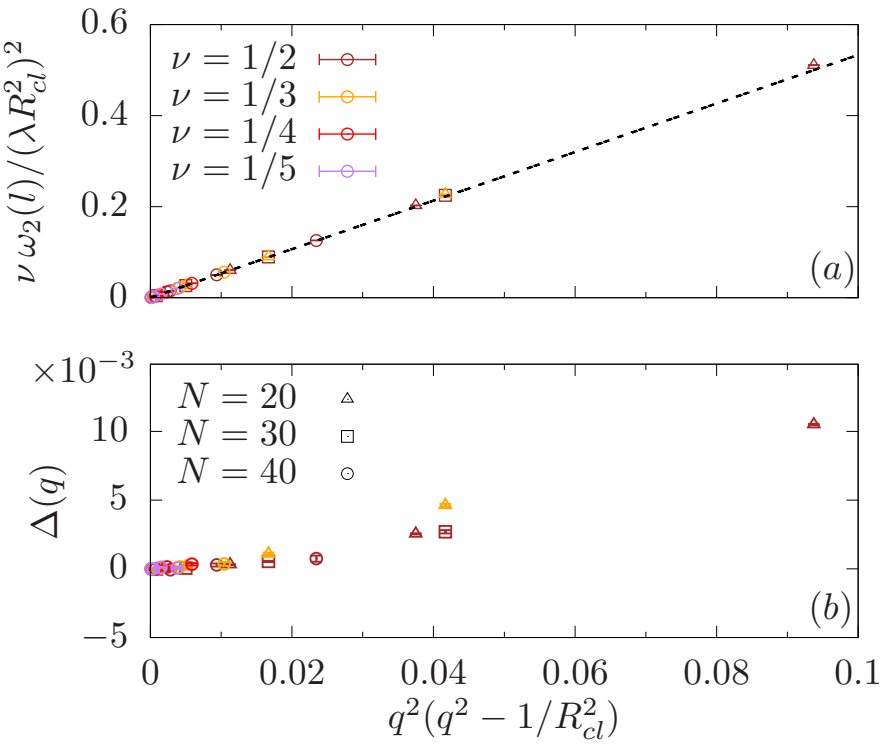

Figure D.1: (a) Numerically computed (and properly normalized) dynamic structure factor second moment $\omega_2(l)$ for the case of a quartic $\delta = 4$ trap, for different system sizes N and filling fractions ν; we plot it as a function of $q^2(q^2 - 1/R_{cl}^2)$ rather than $l^2(l^2 - 1)$, q being the momentum $q = l/R_{cl}$ carried by the edge excitation, in order to highlight the long-wavelength limiting behaviour. We compare it with Eq. (5.42) (black-dashed line), and show the distance from this line in panel (b); it can be seen that as $q \to 0$, the points systematically approach Eq. (5.42). The difference has been magnified by a factor 10^3.

APPENDIX E

OVERLAPS WITH JACK POLYNOMIALS

In this Appendix, we show how the 2D system eigenmodes at filling $\nu = 1/2$ in the quartic trap have large overlaps with a single Jack polynomial labelled by some root configuration η. We also show that, within the refermionized nonlinear edge theory, the corresponding eigenstate has a large overlap with a particle-hole state labelled by the same partition η.

E.1 Overlaps with Jacks

We now are going to show numerically that the eigenmodes at filling $\nu = 1/2$ in the quartic trap have large overlaps with a single Jack polynomial [285, 251, 252] of parameter $\alpha = -2/(r-1)$ with $r = 1/\nu = 2$ and labelled by a $(1, r)$-admissible root-configuration Ω'.

We expand $\Omega' = \Omega + \eta$, where Ω is the Laughlin state root partition [253] and η is the *edge-partition*, labelling a basis of edge excitations at angular momentum l. As described in [285], analogously to Eq. (3.16), one can write $J^{\alpha}_{\Omega+\eta} = J^{\beta}_{\eta} J^{\alpha}_{\Omega}$ where $\beta = 2/(r+1)$ and J^{α}_{Ω} is the Laughlin state. We consider it to be at filling $1/r = 1/2$.

Since the Laughlin state factors out, the overlaps between the eigenstates $|l, n\rangle$ and the edge-Jacks $J^{\alpha}_{\Omega'}$ are easily computed by means of a generalization of the Monte Carlo sampling we described in Appendix A. We start by expanding the eigenstates at angular momentum l as in Eq. (A.1) $|l, n\rangle = \sum_{\alpha_l} C^{[l,n]}_{\alpha_l} \frac{|\alpha_l, l\rangle}{\sqrt{\langle \alpha_l, l | \alpha_l, l\rangle}}$, so that we can

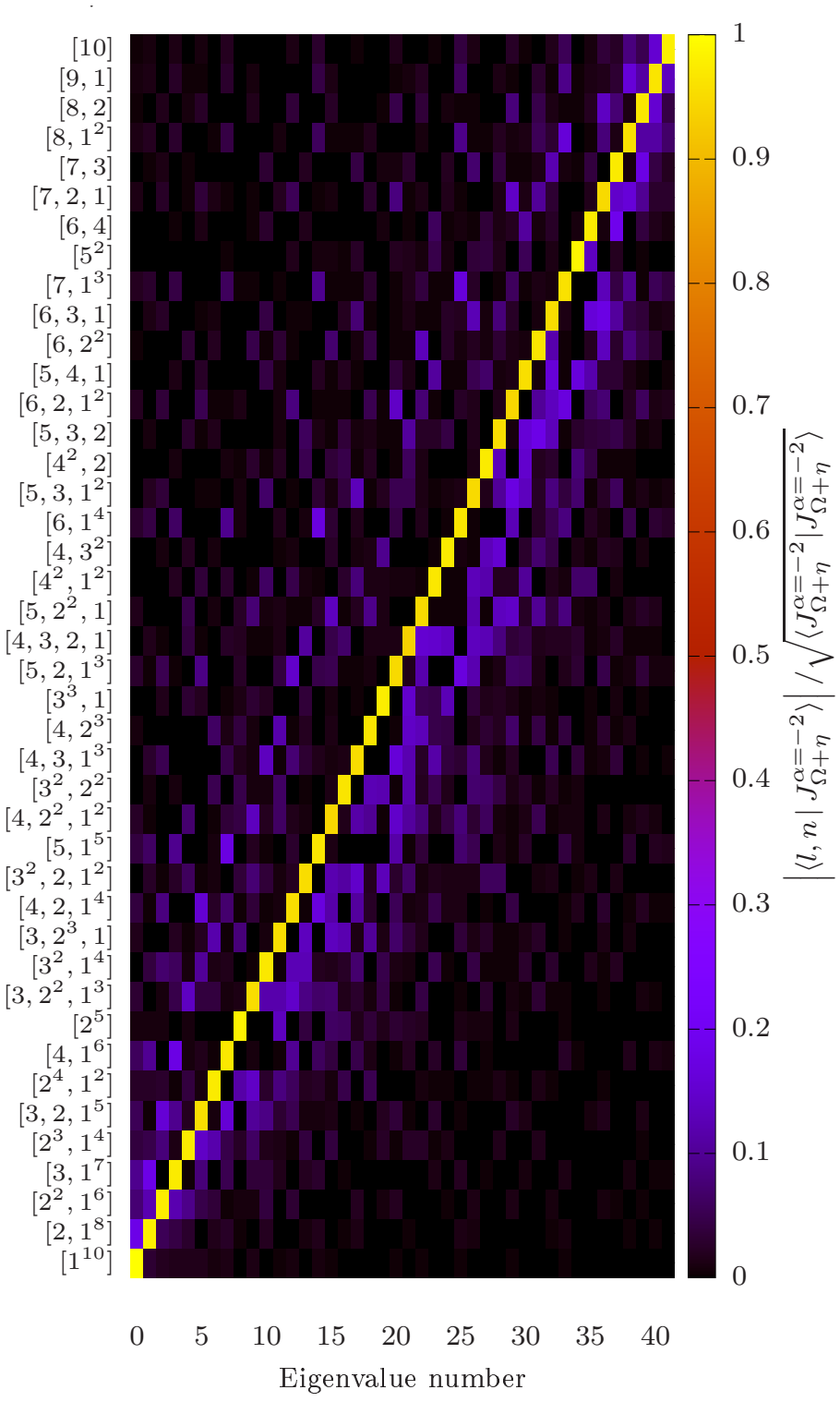

Figure E.1: Overlap matrix between the numerically obtained eigenstates $|l, n\rangle$ for a fractional quantum Hall cloud at $\nu = 1/2$ in a quartic trap $V_{\text{conf}} = \lambda r^4$ and the (normalized) Jack polynomials $J^{\alpha}_{\Omega+\eta}$ with $\alpha = -2/(r-1)$ and $r = 1/\nu$. On the x axis, the system's eigenvectors $|l, n\rangle$ are ordered by increasing eigenvalue number n. On the y axis we report the Jack edge-partitions η with which the overlap has been computed. The edge-partitions η, on the y-axis, have been ordered in such a way that the the largest overlap (close to 1) lies on the diagonal.

express the properly-normalized matrix elements of interest as

$$\frac{\langle l,n|J^{-2}_{\Omega'}\rangle}{\sqrt{\langle J^{-2}_{\Omega'}|J^{-2}_{\Omega'}\rangle}} = \sum_{\alpha_l} C^{[l,n]*}_{\alpha_l} \underbrace{\frac{\langle \alpha_l,l|J^{-2}_{\Omega'}\rangle}{\sqrt{\langle \alpha_l,l|\alpha_l,l\rangle\,\langle J^{-2}_{\Omega'}|J^{-2}_{\Omega'}\rangle}}}_{O_{\alpha_l;\eta}} . \tag{E.1}$$

Introducing the normalized probability density function

$$\mathcal{P}_{\alpha_l}(z) = \frac{|P_{\alpha_l}(z)\Psi_L(z)|^2}{\int |P_{\alpha_l}(z)\Psi_L(z)|^2 \mathcal{D}z} \tag{E.2}$$

where z is a shorthand for $z_1,\dots,z_N$, $\mathcal{D}z = d^2z_1\dots d^2z_N$ and $\langle z|\alpha_l,l\rangle = P_{\alpha_l}(z)\Psi_L(z)$, the normalized overlaps $O_{\alpha_l;\eta}$ appearing on the right-hand side of Eq. (E.1) read

$$O_{\alpha_l;\eta} = \frac{\int \mathcal{P}_{\alpha_l}(z)\frac{J^\beta_\eta(z)}{P_{\alpha_l}(z)}\mathcal{D}z}{\sqrt{\int \mathcal{P}_{\alpha_l}(z)\left|\frac{J^\beta_\eta(z)}{P_{\alpha_l}(z)}\right|^2 \mathcal{D}z}} . \tag{E.3}$$

These can be computed through Monte-Carlo sampling: once again, since the states $J^\alpha_{\Omega+\eta}$ and $P_{\alpha_l}\Psi_L$ are polynomials of not-too-large degree with a Laughlin wavefunction [Eq. (5.2)] as common factor, they share most of their zeros and the sampling procedure is highly efficient. Finally, the Jack polynomials J^β_η are computed by expanding them in the basis of power-sum symmetric polynomials seen above, $J^\beta_\eta(z) = \sum_{\alpha_l} j^{[\alpha_l]}_\eta P_{\alpha_l}(z)$.

The results for the overlaps matrix are shown in Fig. E.1. On the x axis, the system's eigenvectors $|l,n\rangle$ are ordered by increasing eigenvalue number n (which is, by increasing energy eigenvalue). On the y axis we show the edge-partition η labelling a specific Jack; we ordered the partitions along the y-axis so that the largest overlap lies on the diagonal. It is apparent how the eigenstates of our system have a large overlap ($\gtrsim 0.95$) with a single Jack polynomial, while the largest off-diagonal component remains $\lesssim 0.2$.

E.2 Comparison with particle-hole excitations within the refermionized nonlinear χLL

Finally, we want to compare the partitions η labelling the Jacks with those labelling particle-hole excitations in the refermionized model [Eq. (5.33)]. In order to do so, in Fig. E.2 we show the overlaps between the eigenstates $|l,n\rangle_F$ of the fermionic model

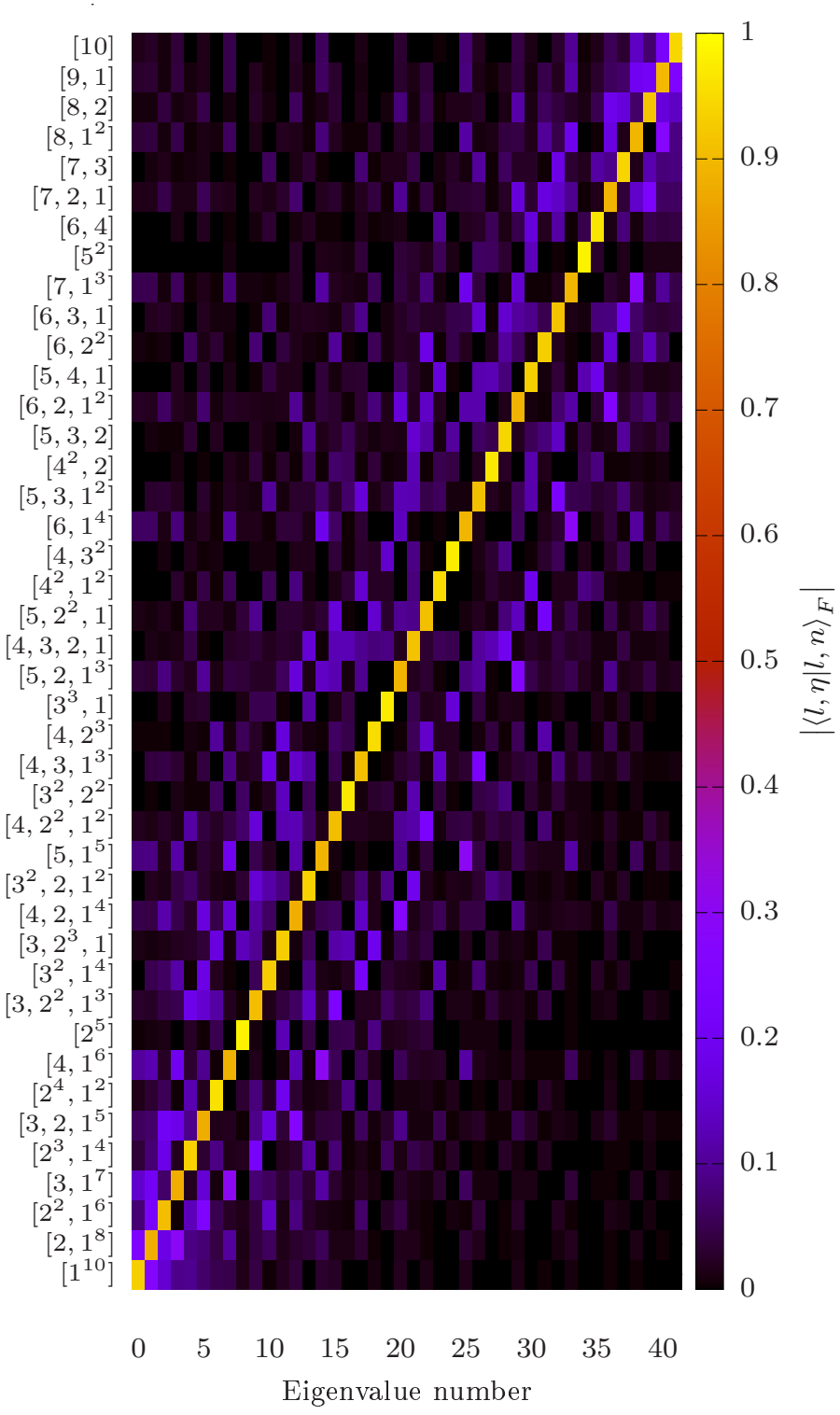

Figure E.2: Overlap matrix between the numerically obtained eigenstates $|l, n\rangle_F$ of the fermionic model [Eq. (5.33)] and the non-interacting particle-hole states labelled by the partition η shown on the y axis. On the x axis, the states are ordered by increasing n. The partitions η on the y axis have been ordered in the same way as in Fig.E.1. Note how this choice leads to the largest overlap being on the main diagonal.

with the non-interacting particle-hole excitations labelled by a partition η and carrying the same angular momentum l, $|l, \eta\rangle$. On the x axis, the system's eigenvectors $|l, n\rangle_F$ are ordered by increasing eigenvalue number n (which is, by increasing energy eigenvalue). On the y axis we show the partitions η labelling the particle-hole states; the same ordering is adopted as in Fig. E.1. It is apparent from Fig. E.2 how each eigenstate of the refermionized model has a dominant ($\gtrsim 90\%$) overlap with a single non-interacting particle-hole state. Remarkably, the fact that the weight is concentrated on the main diagonal of the overlap matrix, together with the energies of the nonlinear χLL being in good agreement with those of the full 2D fractional quantum Hall, shows that the partition η labelling the fermionic state through a non-interacting particle-hole state which satisfies the Pauli exclusion principle is the same as the one labelling the full 2D fractional quantum Hall eigenstates through a Jack polynomial satisfying a generalized exclusion principle [253].

APPENDIX F

ANGULAR VELOCITY AND CURVATURE PARAMETERS

In this Appendix we further discuss the angular velocity Ω and curvature c parameters introduced by heuristic thinking in Chapter 5. In this Appendix we take a more general approach, even though still relying on numerical results. We begin by identifying the edge mode angular velocity Ω with the dispersion of the dipole ($l = 1$) mode of the fractional quantum Hall cloud, and discuss small finite-size corrections to the extrapolations presented in Chapter 5. Then we introduce the curvature parameter c by analysing the quadrupole mode splitting in the thermodynamic limit. In this way the two parameters are defined as "angular momentum derivatives" of the lowest Landau level projected confinement instead of its gradients at the edge position. The relation between the two definitions is discussed in the last section.

F.1 Edge mode velocity

We start by discussing the confinement-induced velocity of edge modes; we can define it as

$$\Omega = E_{EE} - E_{GS} = \sum_l V_{\text{conf}}(l) \left(\langle a_l^\dagger a_l \rangle_{EE} - \langle a_l^\dagger a_l \rangle_{GS} \right) \tag{F.1}$$

where E_{EE} is the energy of the only edge-mode (the dipole mode) at angular momentum $L_{GS}+1$, $\psi_{EE} \propto \sum_i z_i \Psi_L$, and $V_{\text{conf}}(l) = \int |\Phi_l(z)|^2 V_{\text{conf}}(|z|) d^2z$ the confinement projected onto the lowest Landau level. The Lowest Landau level occupation num-

ber variation

$$\delta n_l = \langle a_l^\dagger a_l \rangle_{EE} - \langle a_l^\dagger a_l \rangle_{GS} \tag{F.2}$$

will in general differ from zero only near the boundary of the system, since ψ_{EE} is an excitation of the system's edge. In the case of an integer quantum Hall state of non-interacting fermions for example $\delta n_l = 1$ if $l = N$, $\delta n_l = -1$ if $l = N - 1$ and it vanishes otherwise. The strongly-correlated $\nu = 1/2$ case is shown in Fig. F.1(a). Since δn_l is localized at angular momenta l close to the last occupied angular momentum state at $(N-1)/\nu$, we expand the discrete U_l close to an effective Fermi point $l \sim l_F$, which at this point is arbitrary. Using Newton's series for finite differences

$$U_l = U_{l_F} + \Delta U_{l_F}(l - l_F) + \frac{1}{2}\Delta^2 U_{l_F}(l - l_F)(l - l_F - 1) + \dots \tag{F.3}$$

where $\Delta U_l = U_{l+1} - U_l$. Inserting this expansion in Eq. (F.1) and using the fact that conservation of the number of particles requires $\sum_l \delta n_l = 0$, together with the states having well defined angular momentum, requiring $\sum_l l\delta n_l = 1$, we obtain

$$\Omega = \Delta U_{l_F} + \frac{1}{2}\Delta^2 U_{l_F}\left(\sum_l l^2 \delta n_l - (2l_F + 1)\right) + \dots \tag{F.4}$$

We compute $\sum_l l^2 \delta n_l$ numerically, using the fact that $l^2 = \langle r^4/4 - 3r^2/2 + 1\rangle$ within the lowest Landau level. Therefore we can write

$$\left\langle \sum_l l^2 a_l^\dagger a_l \right\rangle = \left\langle \frac{1}{4}r^4 - \frac{3}{2}r^2 + 1 \right\rangle. \tag{F.5}$$

Using Eq. (F.2) and the previous Eq. (F.5), we can access $\frac{1}{2}\sum_l l^2 \delta n_l$. Based on the insight the $\nu = 1$ case provides, we find that the numerical data are perfectly captured by the following relation (see Fig. F.1(b))

$$\frac{1}{2}\sum_l l^2 \delta n_l = \frac{N-1}{\nu} + \frac{1}{2}, \tag{F.6}$$

and therefore the second order error in the expansion Eq. F.4 can be minimized by choosing

$$l_F = \frac{N-1}{\nu} \tag{F.7}$$

as one would have heuristically expected. In this way, we obtain

$$\Omega = \Delta U_{l_F} + \mathcal{O}(\Delta^3 U_{l_F}). \tag{F.8}$$

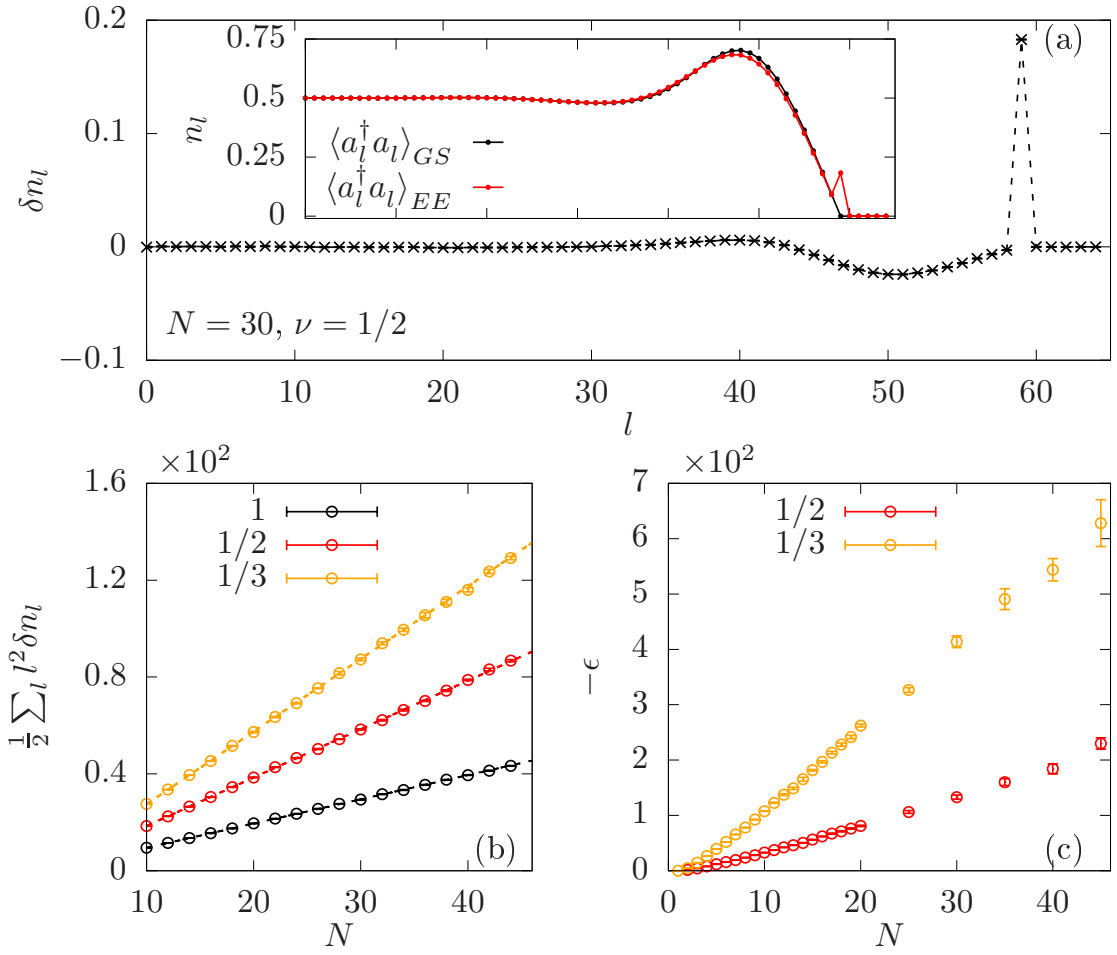

Figure F.1: (a) The occupation number variation δn_l of Eq. (F.2) (black crosses) between the first excited state and the Laughlin state, for a strongly-correlated system of $N = 30$ bosons at half filling; the inset shows the two contributions separately: the Laughlin state occupation numbers $\langle a_l^\dagger a_l \rangle_{GS}$ (black circles) and the excited state ones $\langle a_l^\dagger a_l \rangle_{EE}$ (red circles). (b) Difference between the moments $\frac{1}{2}\sum_l l^2 \delta n_l$ of the first edge state at $l = 1$ and the Laughlin state as a function of the number of particles N of the state, for different filling fractions ν (differently coloured circles). For each filling, the dashed line shows $(N-1)/\nu + 1/2$, which is found to be in excellent agreement with the numerics. (c) Error term ϵ of Eq. (F.9) for various filling fractions ν as a function of the number of particles N of the state (The $\nu = 1$ curve is not shown, for it vanishes identically).

The error term is seen to be $\propto \Delta^3 U_{l_F}$, which vanishes for $U \propto r^4$ potential and is negligible with respect to the leading order term for not-too-steep power-law confinements. More quantitatively, the coefficient multiplying $\Delta^3 U_{l_F}$ in Eq. (F.8) can be written as

$$\epsilon = \frac{1}{6}\left(\sum_l l^3 \delta n_l - (3l_F^2 + 3l_F + 1)\right). \tag{F.9}$$

We compute the quantity within the large parentheses numerically (see Fig. F.1(c)) at fillings $\nu = 1/2$ and $\nu = 1/3$ (for $\nu = 1$ it vanishes identically); at large N, it grows $\lesssim -N$ so, in order for the velocity of the edge modes to be given by ΔU_l, one needs $\Delta^3 U_{l_F}$ to decrease faster than $1/N$; for the hard-wall case of Sec. 5.5 this condition is not met though, so in practice the angular velocity parameter $\Omega = \Delta U_{l_F}$ is (slightly) renormalized by the higher order corrections.

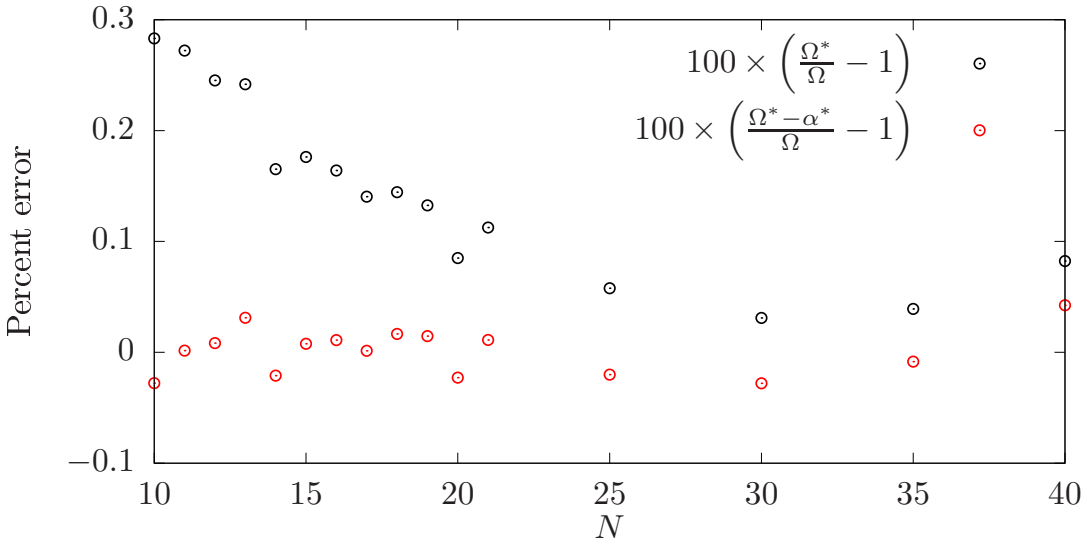

Figure F.2: Deviation (percent) of the fit parameters (black points) Ω^* and (red points) $\Omega^* - \alpha^*$ with respect to the expectation $\Omega = \Delta U_{l_F}$ of Eq. (F.8). It can be seen that the latter compares systematically better to ΔU_{l_F} than the foremost.

F.2 Finite size correction to the dispersion of linear waves

In Chapter 5, we extrapolated the parameters Ω^* and α^* appearing in Eq. (5.17) by a polynomial fit of the numerically computed dynamic structure factor first weighted moment, defined in Eq. (5.16). Here, as compared to Chapter 5, we introduced asterisks as a way of reminding that these two parameters are actually empirical. By comparing ω_l at $l = 1$ with the results of the previous section (see Eq. (F.8)), we obtain $\omega_1 = \Omega^* - \alpha^*$ rather than $\omega_1 = \Omega = \Delta U_{l_F}$. Therefore we see that the fit parameter $\Omega^* = \Omega + \alpha^*$ picks a finite size correction α^* with respect to the simple potential gradient ΔU_{l_F}. In other words, the dispersion of linear waves at cubic

order Eq. (5.18) can be rewritten as

$$\omega_l = \Omega l - \alpha^* l(l^2 - 1) \tag{F.10}$$

where now the coefficient of the linear term is related to the first angular momentum derivative of the lowest Landau level projected potential at the effective Fermi point, $\Omega = \Delta U_{l_F}$.

In Fig. F.2, we show that indeed $\Omega^* - \alpha^*$ compares to ΔU better than Ω^* alone, showing that the "correct" dispersion of linear waves is Eq. (F.10) rather than Eq. (5.18), where the angular velocity parameter Ω picks up a (small) finite size correction.

F.3 Curvature

By analysing the energetic splitting of the two quadrupole modes $|\psi_1\rangle$ and $|\psi_2\rangle$ (the states in the $l = 2$ angular momentum sector) and making use of some reasonable approximations, we now are going to relate the curvature parameter to the second angular momentum derivative of the lowest Landau level projected confinement potential at the effective Fermi point, $\Delta^2 U_{l_F}$.

Using of the expansion Eq. (F.3) we write

$$E_2 - E_1 = \frac{1}{2}\Delta^2 U_{l_F} \sum_l l^2 \delta n_l. \tag{F.11}$$

Making use of Eq. (F.5) and noticing that only the $\propto r^4$ term contributes to the variation (the two state have the same angular momentum), we obtain

$$E_2 - E_1 = \frac{1}{2}\Delta^2 U_{l_F} \left(\left\langle \frac{r^4}{4} \right\rangle_2 - \left\langle \frac{r^4}{4} \right\rangle_1 \right). \tag{F.12}$$

Provided the confinement is not too strong (so that one does not couple to states above the many-body energy gap), $|\psi_1\rangle$ and $|\psi_2\rangle$ are related by a unitary transformation to the analogous eigenstates in a quartic $U \propto r^4$ trap, $|\phi_1\rangle$ and $|\phi_2\rangle$. However, we expect the mixing to be small since, as discussed in Appendix E, the eigenstates in the quartic trap have large overlaps with Jack polynomials and such an overlap is expected to increase for steeper confinements [256, 251, 252]. In this way, we expect $|\psi_{1(2)}\rangle$ to be mostly $|\phi_{1(2)}\rangle$, and we therefore approximate

$$\langle \psi_2 | \, r^4 \, | \psi_2 \rangle - \langle \psi_1 | \, r^4 \, | \psi_1 \rangle \approx \langle \phi_2 | \, r^4 \, | \phi_2 \rangle - \langle \phi_1 | \, r^4 \, | \phi_1 \rangle = E_2^{[4]} - E_1^{[4]}, \tag{F.13}$$

where $E_1^{[4]}$ and $E_2^{[4]}$ are the energies of the r^4 trap eigenstates, $|\phi_1\rangle$ and $|\phi_2\rangle$, respectively.
In the case of the quartic trap, in Appendix D we showed that Eq. (D.3) gives the correct long-wavelength limit of the dynamic structure factor weighted second moment; therefore, at $l = 2$, we can write

$$\omega_2^{[4]}(2) = \frac{64}{\nu}. \tag{F.14}$$

The left-hand side of the equality, $\omega_2^{[4]}(2)$, is however easy to evaluate from its definition Eq. (5.41). Indeed in the thermodynamic limit the dynamic structure factor weights are equal $|\langle\phi_1|\,\delta\hat{\rho}_2\,|0\rangle|^2 = |\langle\phi_2|\,\delta\hat{\rho}_2\,|0\rangle|^2 = \nu$. It follows that

$$\omega_2^{[4]}(2) = \frac{E_1^{[4]} + E_2^{[4]}}{2} - \left(\frac{E_1^{[4]} + E_2^{[4]}}{2}\right)^2 = \frac{1}{4}\left(E_2^{[4]} - E_1^{[4]}\right)^2. \tag{F.15}$$

From Eq. (F.14) and Eq. (F.15) we then get $E_2^{[4]} - E_1^{[4]} = \frac{16}{\sqrt{\nu}}$ and thus, together with Eq. (F.13) the energy splitting Eq. (F.12) in a generic trap becomes

$$E_2 - E_1 \approx 2\,\frac{\Delta^2 U_{l_F}}{\sqrt{\nu}}. \tag{F.16}$$

This expression agrees with Eq. (5.39) obtained from the simple model Eq. (5.25) provided we identify

$$c = \Delta^2 U_{l_F} + \mathcal{O}(\Delta^3 U_{l_F}). \tag{F.17}$$

Again, the approximation works reasonably good in the case of power law confinement, but higher order terms slightly renormalize the result in the hard-wall case.

F.4 Relation to radial gradients of the confinement

We end this Appendix by noting that the relevant parameters

$$\Omega = \Delta U_{l_F} \tag{F.18}$$

$$c = \Delta^2 U_{l_F}, \tag{F.19}$$

properly defined in terms of angular momentum derivatives, reduce to those we heuristically introduced Chapter 5 in terms of radial gradients of the confinement

potential. Indeed, the single particle wavefunctions $|\Phi_l(z)|^2$ [Eq. (3.5)] are peaked at $r = \sqrt{2l}$. Therefore, if we assume that the confinement potential $V_{\rm conf}(r)$ varies slowly over the lengthscale set by the magnetic-length, the trap potential matrix elements U_l are simply related to the real-space one by

$$U_l \simeq U(\sqrt{2l}). \tag{F.20}$$

When the system is made larger and larger,

$$\Omega = \Delta U|_{l_F} \approx \left(r^{-1}\,\partial_r\right) U(r)|_{R_{cl}} \tag{F.21}$$

and analogously

$$c = \Delta^2 U|_{l_F} \approx \left(r^{-1}\,\partial_r\right)^2 U(r)|_{R_{cl}} \tag{F.22}$$

which indeed coincide with the heuristic expressions Eq. (5.12) and Eq. (5.14) we introduced.

APPENDIX G

THE SPIN OF THE QUASIELECTRON

In this Appendix we give some details on how the results for the spins

$$J_{qp}(R) = 2\pi \int_0^R r\, dr \, \left(\frac{r^2}{2} - 1 \right) (\rho_{qp}(r) - \rho(r)) \tag{G.1}$$

of the quasiparticles, which we presented in Chapter 6, have been obtained. In the previous expression, $\rho_{qp}(r)$ is the density of a fractional quantum Hall cloud with a quasiparticle placed at the origin, and $\rho(r)$ the background density of the fractional quantum Hall state hosting the fractionalized excitation. When $1 \ll r \ll R_{cl}$ (in units of the magnetic length l_B), $J_{qp}(R)$ has a plateau at the spin value.

The knowledge of the analytical form of model wavefunctions allows us to compute the spin by Monte Carlo sampling [236, 237, 238] the associated integral Eq. (G.1). This stochastic method allows at the same time to extract information on the charge and density profile of the quasiparticle excitation.

In the following sections some information on the numerics is given. The results for the spin [Eq. (G.1)] are shown in Fig. 6.2 in Chapter 6; here, in Fig. G.1, we complement by showing the density and the excess charge with respect to the bulk Laughlin liquid of the quasielectron states that will be discussed in the following sections.

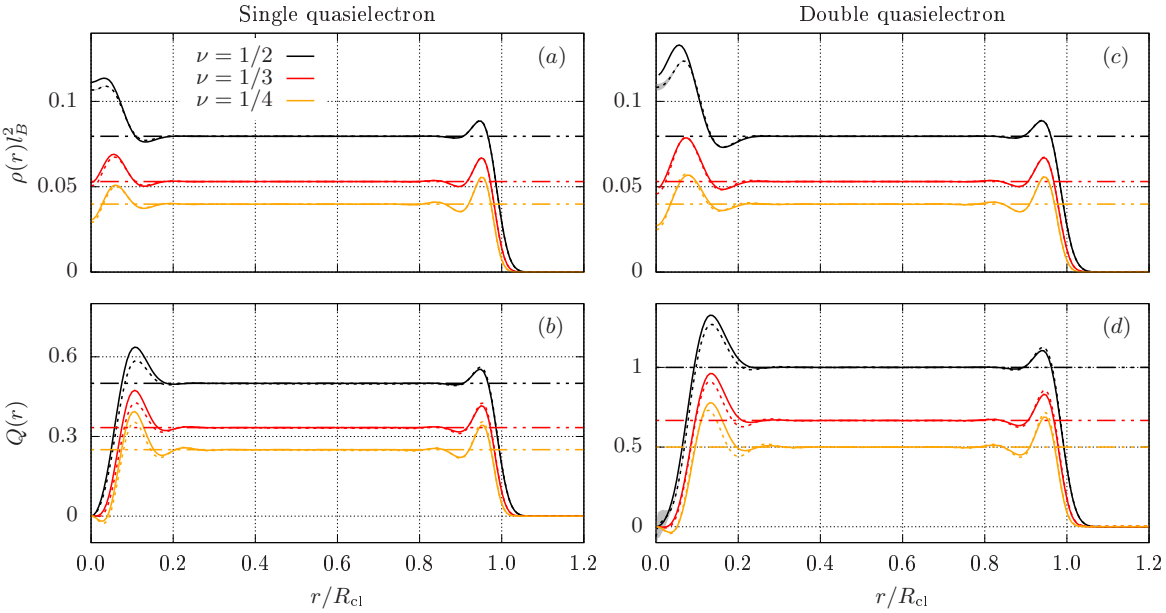

Figure G.1: Comparison of Jain's and Laughlin's quasielectron densities $\rho_{qp}(r)$ and charges $Q(r) = \int_0^r (\rho_{qp}(r') - \rho_L(r'))\, r' dr'$, where $\rho_{qp}(r)$ is the quasielectron density and $\rho_L(r)$ the background Laughlin density. The charge Q of the quasielectron coincides with the plateau appearing when r is far from the center and the boundary; $R_{\rm cl} = \sqrt{2N/\nu}$ is the classical radius of the droplet. Panel $(a)(/(c))$: comparison between the densities $\rho_{qp}(r)$ of single(/double) Jain's (full lines) and Laughlin's (dashed lines) quasielectrons, for $\nu = 1/2$, $1/3$ and $1/4$. Horizontal dashed-dotted lines represent the bulk Laughlin state density $\rho_b = \nu/2\pi l_B^2$. Panel $(b)(/(d))$: comparison between the charges $Q(r)$ of single(/double) Jain's (full lines) and Laughlin's (dashed lines) quasielectrons. Horizontal dashed-dotted lines represent the charge of Laughlin's quasiparticles, $Q = \nu$.

G.1 Single Jain's quasielectron

Jain's composite fermion approach to the fractional quantum Hall states suggests [168, 10]

$$\Psi_{JQE} = \hat{P}_{\rm LLL} \begin{vmatrix} z_0^* & z_1^* & z_2^* & \dots \\ 1 & 1 & 1 & \dots \\ z_0 & z_1 & z_2 & \dots \\ \vdots & \vdots & \vdots & \ddots \end{vmatrix} \prod_{i<j} (z_i - z_j)^{m-1} \tag{G.2}$$

as the simplest candidate wavefunction for the quasielectron on top of a Laughlin state at filling $\nu = \frac{1}{m}$. Here and in the following, Gaussian factors will be left implicit. Carrying out standard projection onto the lowest Landau level [196] gives

(apart for constant proportionality factors)

$$\Psi_{JQE} = \sum_i \left(\frac{1}{\prod_{l\neq i} z_l - z_i} \sum_{j\neq i} \frac{1}{z_i - z_j} \right) \prod_{i<j} (z_i - z_j)^m \tag{G.3}$$

which has already been shown to carry the correct fractional charge [198] and having the correct exchange statistics [276, 280].

G.2 Double Jain's quasielectron

Jain's composite fermion approach suggests the following wavefunction for a doubly charged quasielectron at the centre of a circularly symmetric droplet

$$\Psi_{J2QE} = \hat{P}_{\mathrm{LLL}} \begin{vmatrix} z_0^{*2} & z_1^{*2} & z_2^{*2} & \dots \\ z_0^{*} & z_1^{*} & z_2^{*} & \dots \\ 1 & 1 & 1 & \dots \\ z_0 & z_1 & z_2 & \dots \\ \vdots & \vdots & \vdots & \ddots \end{vmatrix} \prod_{i<j} (z_i - z_j)^{m-1}. \tag{G.4}$$

Notice that this wavefunction is not the most energetically-favourable double quasielectron state [200], which is realized by promoting two composite fermions to their first Landau level, nor it has the correct angular momentum for a double quasielectron state. We study this particular wavefunction because it has the same angular momentum as the Laughlin's double quasielectron state, allowing therefore for a more direct comparison [278]. The spin of a "true" quasielectron however differs only by integers from the one of Eq. (G.4).

We use standard lowest Landau level projection, although different inequivalent projection methods [281, 286, 10] have been proposed. After some tedious algebra (and again dropping constant proportionality factors) we find

$$\Psi_{J2QE} = \sum_{i\neq j} \left(\frac{(z_i - z_j)\Gamma_{ij}}{\prod_{k\neq i}(z_k - z_i) \prod_{k\neq j}(z_k - z_j)} \right) \prod_{i<j} (z_i - z_j)^m \tag{G.5}$$

where

$$\Gamma_{ij} = (m-1)^2 A_i^2 A_j - (m-1) B_i A_j + \frac{2(m-1)A_i}{(z_i - z_j)^2} - \frac{2}{(z_i - z_j)^3} \tag{G.6}$$

and

$$\begin{cases} A_i = \sum_{j\neq i} \frac{1}{z_i - z_j} \\ B_i = \sum_{j\neq i} \frac{1}{(z_i - z_j)^2}. \end{cases} \tag{G.7}$$

G.3 Single Laughlin's quasielectron

Laughlin proposed a quasielectron wavefunction by generalizing his successful quasihole wavefunction [23], based on the idea of adiabatic flux-insertion

$$\psi_{LQE} = \left(\prod_i 2\frac{\partial}{\partial z_i} \right) \prod_{i<j} (z_i - z_j)^m, \tag{G.8}$$

which however - unlike the quasihole counterpart - is not easy to deal with from the computational point of view, due to the N-th order derivative term. We are interested in computing expectation values of local, single-particle observables $\hat{O} = \sum_i \hat{o}_i$

$$\langle \hat{O} \rangle = \int \mathcal{D}z \, \psi^*_{LQE} O(z, z^*) \psi_{LQE} \tag{G.9}$$

where $\mathcal{D}z = \prod_i d^2 z_i$ and z is a shorthand for all the particles' coordinates. To simplify the expressions we assume $O(z, z^*) = O(|z|^2)$. By performing integration by parts $2N$ times we then get

$$\langle \hat{O} \rangle = \frac{1}{Z} \int \mathcal{D}z \left| \prod_{i<j} (z_i - z_j)^m \right|^2 \prod_i (|z_i|^2 - 2) \sum_i A_i(|z_i|^2) \tag{G.10}$$

where A_i is related to the observable o_i through

$$A(r^2) = o(r^2) - 4\frac{r^2 - 1}{r^2 - 2}\frac{\partial o(r^2)}{\partial r^2} + 4\frac{r^2}{r^2 - 2}\frac{\partial^2 o(r^2)}{\partial (r^2)^2} \tag{G.11}$$

but crucially involves its derivatives. The normalization factor Z can be found by looking at $\hat{O} = \mathbf{1}$.

As an example, we expand here the expressions for the observable $\hat{O}$ being the charge up to radius R

$$o(r^2) = \Theta(R^2 - r^2). \tag{G.12}$$

Here Θ is the step function. The case of the spin Eq. (G.1) is perfectly analogous but the expressions are more lengthy because of the $r^2/2 - 1$ factor multiplying the step function. The integrals involve derivatives of the δ function. It is convenient

to take these out of the integrals and rearrange Eq. (G.10) in the following form

$$Q(R) = I_0(R^2) + 4I_1(R^2) + 4\frac{\partial I_2(R^2)}{\partial R^2} \tag{G.13}$$

where

$$I_0(R^2) = \frac{1}{Z}\int \mathcal{D}z \left|\prod_{i<j}(z_i - z_j)^m\right|^2 \prod_i (|z_i|^2 - 2) \sum_i \theta(R^2 - r_i^2) \tag{G.14}$$

$$I_1(R^2) = \frac{1}{Z}\int \mathcal{D}z \left|\prod_{i<j}(z_i - z_j)^m\right|^2 \prod_i (|z_i|^2 - 2) \sum_i \delta(R^2 - r_i^2)\frac{r_i^2 - 1}{r_i^2 - 2} \tag{G.15}$$

$$I_2(R^2) = \frac{1}{Z}\int \mathcal{D}z \left|\prod_{i<j}(z_i - z_j)^m\right|^2 \prod_i (|z_i|^2 - 2) \sum_i \delta(R^2 - r_i^2)\frac{r_i^2}{r_i^2 - 2}. \tag{G.16}$$

Taking derivatives [Eq. (G.13)] of the noisy Monte-Carlo sampled observables [Eqs. (G.14)-(G.16)] is tricky; to circumvent the problem we Fourier transform the relevant quantities

$$\tilde{I}(k) = \int_0^\infty I(R) J_0(kR) R\, dR \tag{G.17}$$

where J_0 is the order 0 Bessel function of the first kind. We then filter out the "high-wavevector" noise superimposed to the "low-wavevector" signal $\tilde{I}_c(k) = c(k)\tilde{I}(k)$, with some suitably chosen cut-off function $c(k)$, and invert the transform

$$\frac{\partial^n I_c(R)}{\partial (R^2)^n} = \int_0^\infty \tilde{I}_c(k) \frac{\partial^n J_0(kR)}{\partial (R^2)^n} k\, dk. \tag{G.18}$$

Derivatives of J_0 can be expressed in closed compact form in terms of the ${}_0F_1$ hypergeometric function, thus avoiding the computation of finite differences.

G.4 Double Laughlin's quasielectron

A doubly charged Laughlin's quasielectron can be placed at the origin as [200]

$$\psi_{L2QE} = \left(\prod_i 2\frac{\partial}{\partial z_i}\right)^2 \prod_{i<j}(z_i - z_j)^m. \tag{G.19}$$

Again, carrying out the derivatives explicitly seems not to be feasible, however it is simpler to look at local observables as Eq. (G.9). Repeated integration by parts

yields

$$\langle \hat{O} \rangle = \frac{1}{Z} \int \mathcal{D}z \left| \prod_{i<j} (z_i - z_j)^m \right|^2 \prod_i (8 - 8|z_i|^2 + |z_i|^4) \sum_i A_i(|z_i|^2) \tag{G.20}$$

with

$$\begin{aligned} A(r^2) = o(r^2) - 8\frac{4 - 6r^2 + r^4}{8 - 8r^2 + r^4}\frac{\partial o(r^2)}{\partial r^2} + 8\frac{4 - 12r^2 + 3r^4}{8 - 8r^2 + r^4}\frac{\partial^2 o(r^2)}{\partial (r^2)^2} - \\ - 32\frac{-2r^2 + r^4}{8 - 8r^2 + r^4}\frac{\partial^3 o(r^2)}{\partial (r^2)^3} + 16\frac{r^4}{8 - 8r^2 + r^4}\frac{\partial^4 o(r^2)}{\partial (r^2)^4}. \end{aligned} \tag{G.21}$$

Once again, the expressions for the observables involve derivatives of the observable itself; whenever dealing with derivatives of the delta function, we adopted the procedure outlined in the previous section.

BIBLIOGRAPHY

[1] K. v. Klitzing, G. Dorda, and M. Pepper. New method for high-accuracy determination of the fine-structure constant based on quantized hall resistance. *Phys. Rev. Lett.*, 45:494–497, Aug 1980.

[2] D. C. Tsui, H. L. Stormer, and A. C. Gossard. Two-dimensional magnetotransport in the extreme quantum limit. *Phys. Rev. Lett.*, 48:1559–1562, May 1982.

[3] D. J. Thouless, M. Kohmoto, M. P. Nightingale, and M. den Nijs. Quantized hall conductance in a two-dimensional periodic potential. *Phys. Rev. Lett.*, 49:405–408, Aug 1982.

[4] Qian Niu, D. J. Thouless, and Yong-Shi Wu. Quantized hall conductance as a topological invariant. *Phys. Rev. B*, 31:3372–3377, Mar 1985.

[5] M. Z. Hasan and C. L. Kane. Colloquium: Topological insulators. *Rev. Mod. Phys.*, 82:3045–3067, Nov 2010.

[6] Xiao-Gang Wen. Choreographed entanglement dances: Topological states of quantum matter. *Science*, 363(6429):eaal3099, 2019.

[7] Xiao-Gang Wen. Colloquium: Zoo of quantum-topological phases of matter. *Rev. Mod. Phys.*, 89:041004, Dec 2017.

[8] L. Landau. Diamagnetismus der Metalle. *Zeitschrift fur Physik*, 64(9-10):629–637, September 1930.

[9] David Tong. Lectures on the quantum hall effect. 2016.

[10] Jainendra K. Jain. *Composite Fermions*. Cambridge University Press, 2007.

[11] M. O. Goerbig. Quantum hall effects. 2009.

[12] Klaus von Klitzing. The quantized hall effect. *Rev. Mod. Phys.*, 58:519–531, Jul 1986.

[13] Klaus von Klitzing. Developments in the quantum hall effect. *Philosophical Transactions of the Royal Society A: Mathematical, Physical and Engineering Sciences*, 363(1834):2203–2219, 2005.

[14] J. Weis and K. von Klitzing. Metrology and microscopic picture of the integer quantum Hall effect. *Philosophical Transactions of the Royal Society of London Series A*, 369(1953):3954–3974, October 2011.

[15] R. B. Laughlin. Quantized hall conductivity in two dimensions. *Phys. Rev. B*, 23:5632–5633, May 1981.

[16] B. I. Halperin. Quantized hall conductance, current-carrying edge states, and the existence of extended states in a two-dimensional disordered potential. *Phys. Rev. B*, 25:2185–2190, Feb 1982.

[17] M. Büttiker. Absence of backscattering in the quantum hall effect in multiprobe conductors. *Phys. Rev. B*, 38:9375–9389, Nov 1988.

[18] Gabriele Giuliani and Giovanni Vignale. *Quantum Theory of the Electron Liquid*. Cambridge University Press, 2005.

[19] Felice Appugliese, Josefine Enkner, Gian Lorenzo Paravicini-Bagliani, Mattias Beck, Christian Reichl, Werner Wegscheider, Giacomo Scalari, Cristiano Ciuti, and Jérôme Faist. Breakdown of topological protection by cavity vacuum fields in the integer quantum hall effect. *Science*, 375(6584):1030–1034, 2022.

[20] Cristiano Ciuti. Cavity-mediated electron hopping in disordered quantum hall systems. *Phys. Rev. B*, 104:155307, Oct 2021.

[21] R. Willett, J. P. Eisenstein, H. L. Störmer, D. C. Tsui, A. C. Gossard, and J. H. English. Observation of an even-denominator quantum number in the fractional quantum hall effect. *Phys. Rev. Lett.*, 59:1776–1779, Oct 1987.

[22] H. L. Stormer, A. Chang, D. C. Tsui, J. C. M. Hwang, A. C. Gossard, and W. Wiegmann. Fractional quantization of the hall effect. *Phys. Rev. Lett.*, 50:1953–1956, Jun 1983.

[23] R. B. Laughlin. Anomalous quantum hall effect: An incompressible quantum fluid with fractionally charged excitations. *Phys. Rev. Lett.*, 50:1395–1398, May 1983.

[24] Xie Chen, Zheng-Cheng Gu, and Xiao-Gang Wen. Local unitary transformation, long-range quantum entanglement, wave function renormalization, and topological order. *Phys. Rev. B*, 82:155138, Oct 2010.

[25] Kerson Huang. *Statistical mechanics*. John Wiley & Sons, 2008.

[26] X. G. Wen. Chiral luttinger liquid and the edge excitations in the fractional quantum hall states. *Phys. Rev. B*, 41:12838–12844, Jun 1990.

[27] R. Tao and Yong-Shi Wu. Gauge invariance and fractional quantum hall effect. *Phys. Rev. B*, 30:1097–1098, Jul 1984.

[28] X. G. Wen. Electrodynamical properties of gapless edge excitations in the fractional quantum hall states. *Phys. Rev. Lett.*, 64:2206–2209, Apr 1990.

[29] X. G. Wen. Gapless boundary excitations in the quantum hall states and in the chiral spin states. *Phys. Rev. B*, 43:11025–11036, May 1991.

[30] Xiao-Gang Wen. Theory of the edge states in fractional quantum hall effects. *International Journal of Modern Physics B*, 06:1711–1762, 1992.

[31] Xiao-Gang Wen. Topological orders and edge excitations in fractional quantum Hall states. *Adv. Phys.*, 44(5):405–473, 1995.

[32] A. M. Chang. Chiral luttinger liquids at the fractional quantum hall edge. *Rev. Mod. Phys.*, 75:1449–1505, Nov 2003.

[33] Alexei Kitaev and John Preskill. Topological entanglement entropy. *Phys. Rev. Lett.*, 96:110404, Mar 2006.

[34] Michael Levin and Xiao-Gang Wen. Detecting topological order in a ground state wave function. *Phys. Rev. Lett.*, 96:110405, Mar 2006.

[35] Daniel Arovas, J. R. Schrieffer, and Frank Wilczek. Fractional statistics and the quantum hall effect. *Phys. Rev. Lett.*, 53:722–723, Aug 1984.

[36] Gregory Moore and Nicholas Read. Nonabelions in the fractional quantum hall effect. *Nuclear Physics B*, 360(2):362–396, 1991.

[37] N. Read and E. Rezayi. Beyond paired quantum hall states: Parafermions and incompressible states in the first excited landau level. *Phys. Rev. B*, 59:8084–8092, Mar 1999.

[38] A.Yu. Kitaev. Fault-tolerant quantum computation by anyons. *Annals of Physics*, 303(1):2–30, 2003.

[39] Chetan Nayak, Steven H. Simon, Ady Stern, Michael Freedman, and Sankar Das Sarma. Non-abelian anyons and topological quantum computation. *Rev. Mod. Phys.*, 80:1083–1159, Sep 2008.

[40] Mitali Banerjee, Moty Heiblum, Amir Rosenblatt, Yuval Oreg, Dima E. Feldman, Ady Stern, and Vladimir Umansky. Observed quantization of anyonic heat flow. *Nature*, 545(7652):75–79, apr 2017.

[41] Mitali Banerjee, Moty Heiblum, Vladimir Umansky, Dima E. Feldman, Yuval Oreg, and Ady Stern. Observation of half-integer thermal Hall conductance. *Nature*, 559(7713):205–210, June 2018.

[42] J. Nakamura, S. Liang, G. C. Gardner, and M. J. Manfra. Direct observation of anyonic braiding statistics. *Nature Physics*, 16(9):931–936, September 2020.

[43] H. Bartolomei, M. Kumar, R. Bisognin, A. Marguerite, J. M. Berroir, E. Bocquillon, B. Plaçais, A. Cavanna, Q. Dong, U. Gennser, Y. Jin, and G. Fève. Fractional statistics in anyon collisions. *Science*, 368(6487):173–177, April 2020.

[44] M. Ruelle, E. Frigerio, J.-M. Berroir, B. Plaçais, J. Rech, A. Cavanna, U. Gennser, Y. Jin, and G. Fève. Comparing fractional quantum hall laughlin and jain topological orders with the anyon collider. *Phys. Rev. X*, 13:011031, Mar 2023.

[45] P. Glidic, O. Maillet, A. Aassime, C. Piquard, A. Cavanna, U. Gennser, Y. Jin, A. Anthore, and F. Pierre. Cross-Correlation Investigation of Anyon Statistics in the ν=1/3 and 2/5 Fractional Quantum Hall States. *Phys. Rev. X*, 13:011030, Mar 2023.

[46] Akinori Kamiyama, Masahiro Matsuura, John N. Moore, Takaaki Mano, Naokazu Shibata, and Go Yusa. Real-time and space visualization of excitations of the ν =1/3 fractional quantum Hall edge. *Physical Review Research*, 4(1):L012040, March 2022.

[47] L. Pitaevskii and S. Stringari. *Bose-Einstein Condensation and Superfluidity*. International series of monographs on physics. Oxford University Press, 2018.

[48] Immanuel Bloch, Jean Dalibard, and Wilhelm Zwerger. Many-body physics with ultracold gases. *Rev. Mod. Phys.*, 80:885–964, Jul 2008.

[49] Iacopo Carusotto and Cristiano Ciuti. Quantum fluids of light. *Rev. Mod. Phys.*, 85:299–366, Feb 2013.

[50] Tomoki Ozawa, Hannah M. Price, Alberto Amo, Nathan Goldman, Mohammad Hafezi, Ling Lu, Mikael C. Rechtsman, David Schuster, Jonathan Simon, Oded Zilberberg, and Iacopo Carusotto. Topological photonics. *Rev. Mod. Phys.*, 91:015006, Mar 2019.

[51] Iacopo Carusotto, Andrew A. Houck, Alicia J. Kollár, Pedram Roushan, David I. Schuster, and Jonathan Simon. Photonic materials in circuit quantum electrodynamics. *Nature Physics*, 16(3):268–279, March 2020.

[52] Tomoki Ozawa and Hannah M. Price. Topological quantum matter in synthetic dimensions. *Nature Reviews Physics*, 1(5):349–357, April 2019.

[53] I. M. Georgescu, S. Ashhab, and Franco Nori. Quantum simulation. *Rev. Mod. Phys.*, 86:153–185, Mar 2014.

[54] Nathan Goldman, Jérôme Beugnon, and Fabrice Gerbier. Detecting chiral edge states in the hofstadter optical lattice. *Phys. Rev. Lett.*, 108:255303, Jun 2012.

[55] Nathan Goldman, Jérôme Beugnon, and Fabrice Gerbier. Identifying topological edge states in 2D optical lattices using light scattering. *European Physical Journal Special Topics*, 217:135–152, February 2013.

[56] Nathan Goldman, Jean Dalibard, Alexandre Dauphin, Fabrice Gerbier, Maciej Lewenstein, Peter Zoller, and Ian B. Spielman. Direct imaging of topological edge states in cold-atom systems. *Proceedings of the National Academy of Sciences*, 110(17):6736–6741, 2013.

[57] M. A. Cazalilla, N. Barberán, and N. R. Cooper. Edge excitations and topological order in a rotating bose gas. *Phys. Rev. B*, 71:121303, Mar 2005.

[58] M. A. Cazalilla. Surface modes of ultracold atomic clouds with a very large number of vortices. *Phys. Rev. A*, 67:063613, Jun 2003.

[59] Matthew Killi and Arun Paramekanti. Use of quantum quenches to probe the equilibrium current patterns of ultracold atoms in an optical lattice. *Phys. Rev. A*, 85:061606, Jun 2012.

[60] V. W. Scarola and S. Das Sarma. Edge transport in 2d cold atom optical lattices. *Phys. Rev. Lett.*, 98:210403, May 2007.

[61] M. Hafezi, A. S. Sørensen, E. Demler, and M. D. Lukin. Fractional quantum hall effect in optical lattices. *Phys. Rev. A*, 76:023613, Aug 2007.

[62] Nigel R. Cooper and Steven H. Simon. Signatures of fractional exclusion statistics in the spectroscopy of quantum hall droplets. *Phys. Rev. Lett.*, 114:106802, Mar 2015.

[63] Duc Thanh Tran, Alexandre Dauphin, Adolfo G. Grushin, Peter Zoller, and Nathan Goldman. Probing topology by “heating”: Quantized circular dichroism in ultracold atoms. *Science Advances*, 3(8):e1701207, 2017.

[64] D. T. Tran, N. R. Cooper, and N. Goldman. Quantized rabi oscillations and circular dichroism in quantum hall systems. *Phys. Rev. A*, 97:061602, Jun 2018.

[65] C. Repellin and N. Goldman. Detecting fractional chern insulators through circular dichroism. *Phys. Rev. Lett.*, 122:166801, Apr 2019.

[66] C. Repellin, J. Léonard, and N. Goldman. Fractional chern insulators of few bosons in a box: Hall plateaus from center-of-mass drifts and density profiles. *Phys. Rev. A*, 102:063316, Dec 2020.

[67] Alexandre Dauphin and Nathan Goldman. Extracting the chern number from the dynamics of a fermi gas: Implementing a quantum hall bar for cold atoms. *Phys. Rev. Lett.*, 111:135302, Sep 2013.

[68] N. Read and N. R. Cooper. Free expansion of lowest-landau-level states of trapped atoms: A wave-function microscope. *Phys. Rev. A*, 68:035601, Sep 2003.

[69] N. R. Cooper, F. J. M. van Lankvelt, J. W. Reijnders, and K. Schoutens. Quantum hall states of atomic bose gases: Density profiles in single-layer and multilayer geometries. *Phys. Rev. A*, 72:063622, Dec 2005.

[70] R. O. Umucal ılar, Hui Zhai, and M. Ö. Oktel. Trapped fermi gases in rotating optical lattices: Realization and detection of the topological hofstadter insulator. *Phys. Rev. Lett.*, 100:070402, Feb 2008.

[71] L. B. Shao, Shi-Liang Zhu, L. Sheng, D. Y. Xing, and Z. D. Wang. Realizing and detecting the quantum hall effect without landau levels by using ultracold atoms. *Phys. Rev. Lett.*, 101:246810, Dec 2008.

[72] H. M. Price and N. R. Cooper. Mapping the berry curvature from semiclassical dynamics in optical lattices. *Phys. Rev. A*, 85:033620, Mar 2012.

[73] B. Paredes, P. Fedichev, J. I. Cirac, and P. Zoller. $\frac{1}{2}$-anyons in small atomic bose-einstein condensates. *Phys. Rev. Lett.*, 87:010402, Jun 2001.

[74] R. O. Umucal ılar, E. Macaluso, T. Comparin, and I. Carusotto. Time-of-flight measurements as a possible method to observe anyonic statistics. *Phys. Rev. Lett.*, 120:230403, Jun 2018.

[75] E. Macaluso, T. Comparin, L. Mazza, and I. Carusotto. Fusion channels of non-abelian anyons from angular-momentum and density-profile measurements. *Phys. Rev. Lett.*, 123:266801, Dec 2019.

[76] Yuhe Zhang, G. J. Sreejith, N. D. Gemelke, and J. K. Jain. Fractional angular momentum in cold-atom systems. *Phys. Rev. Lett.*, 113:160404, Oct 2014.

[77] Douglas Lundholm and Nicolas Rougerie. Emergence of fractional statistics for tracer particles in a laughlin liquid. *Phys. Rev. Lett.*, 116:170401, Apr 2016.

[78] Tobias Graß, Bruno Juliá-Díaz, Niccolò Baldelli, Utso Bhattacharya, and Maciej Lewenstein. Fractional angular momentum and anyon statistics of impurities in laughlin liquids. *Phys. Rev. Lett.*, 125:136801, Sep 2020.

[79] A. Muñoz de las Heras, E. Macaluso, and I. Carusotto. Anyonic molecules in atomic fractional quantum hall liquids: A quantitative probe of fractional charge and anyonic statistics. *Phys. Rev. X*, 10:041058, Dec 2020.

[80] Cheng Chin, Rudolf Grimm, Paul Julienne, and Eite Tiesinga. Feshbach resonances in ultracold gases. *Rev. Mod. Phys.*, 82:1225–1286, Apr 2010.

[81] N.R. Cooper. Rapidly rotating atomic gases. *Advances in Physics*, 57(6):539–616, 2008.

[82] Alexander L. Fetter. Rotating trapped bose-einstein condensates. *Rev. Mod. Phys.*, 81:647–691, May 2009.

[83] Jean Dalibard, Fabrice Gerbier, Gediminas Juzeliūnas, and Patrik Öhberg. Colloquium: Artificial gauge potentials for neutral atoms. *Rev. Mod. Phys.*, 83:1523–1543, Nov 2011.

[84] N Goldman, G Juzeliūnas, P Öhberg, and I B Spielman. Light-induced gauge fields for ultracold atoms. *Reports on Progress in Physics*, 77(12):126401, nov 2014.

[85] N. R. Cooper, J. Dalibard, and I. B. Spielman. Topological bands for ultracold atoms. *Rev. Mod. Phys.*, 91:015005, Mar 2019.

[86] K. W. Madison, F. Chevy, W. Wohlleben, and J. Dalibard. Vortex formation in a stirred bose-einstein condensate. *Phys. Rev. Lett.*, 84:806–809, Jan 2000.

[87] J. R. Abo-Shaeer, C. Raman, J. M. Vogels, and W. Ketterle. Observation of Vortex Lattices in Bose-Einstein Condensates. *Science*, 292(5516):476–479, April 2001.

[88] V. Schweikhard, I. Coddington, P. Engels, V. P. Mogendorff, and E. A. Cornell. Rapidly rotating bose-einstein condensates in and near the lowest landau level. *Phys. Rev. Lett.*, 92:040404, Jan 2004.

[89] Vincent Bretin, Sabine Stock, Yannick Seurin, and Jean Dalibard. Fast rotation of a bose-einstein condensate. *Phys. Rev. Lett.*, 92:050403, Feb 2004.

[90] Richard J. Fletcher, Airlia Shaffer, Cedric C. Wilson, Parth B. Patel, Zhenjie Yan, Valentin Cré pel, Biswaroop Mukherjee, and Martin W. Zwierlein. Geometric squeezing into the lowest landau level. *Science*, 372(6548):1318–1322, jun 2021.

[91] Biswaroop Mukherjee, Airlia Shaffer, Parth B. Patel, Zhenjie Yan, Cedric C. Wilson, Valentin Crépel, Richard J. Fletcher, and Martin Zwierlein. Crystallization of bosonic quantum hall states in a rotating quantum gas. *Nature*, 601(7891):58–62, jan 2022.

[92] Jairo Sinova, C. B. Hanna, and A. H. MacDonald. Quantum melting and absence of bose-einstein condensation in two-dimensional vortex matter. *Phys. Rev. Lett.*, 89:030403, Jun 2002.

[93] N. K. Wilkin, J. M. F. Gunn, and R. A. Smith. Do attractive bosons condense? *Phys. Rev. Lett.*, 80:2265–2268, Mar 1998.

[94] N. R. Cooper, N. K. Wilkin, and J. M. F. Gunn. Quantum phases of vortices in rotating bose-einstein condensates. *Phys. Rev. Lett.*, 87:120405, Aug 2001.

[95] N. K. Wilkin and J. M. F. Gunn. Condensation of "composite bosons" in a rotating bec. *Phys. Rev. Lett.*, 84:6–9, Jan 2000.

[96] N. Regnault and Th. Jolicoeur. Quantum hall fractions in rotating bose-einstein condensates. *Phys. Rev. Lett.*, 91:030402, Jul 2003.

[97] N. Regnault and Th. Jolicoeur. Quantum hall fractions for spinless bosons. *Phys. Rev. B*, 69:235309, Jun 2004.

[98] E. H. Rezayi, N. Read, and N. R. Cooper. Incompressible liquid state of rapidly rotating bosons at filling factor 3/2. *Phys. Rev. Lett.*, 95:160404, Oct 2005.

[99] N. Regnault and Th. Jolicoeur. Parafermionic states in rotating bose-einstein condensates. *Phys. Rev. B*, 76:235324, Dec 2007.

[100] Nathan Gemelke, Edina Sarajlic, and Steven Chu. Rotating few-body atomic systems in the fractional quantum hall regime. 2010.

[101] M. Popp, B. Paredes, and J. I. Cirac. Adiabatic path to fractional quantum hall states of a few bosonic atoms. *Phys. Rev. A*, 70:053612, Nov 2004.

[102] Alexis G. Morris and David L. Feder. Gaussian potentials facilitate access to quantum hall states in rotating bose gases. *Phys. Rev. Lett.*, 99:240401, Dec 2007.

[103] M. Roncaglia, M. Rizzi, and J. Dalibard. From rotating atomic rings to quantum hall states. *Scientific Reports*, 1(1), jul 2011.

[104] Bárbara Andrade, Valentin Kasper, Maciej Lewenstein, Christof Weitenberg, and Tobias Graß. Preparation of the 1/2 laughlin state with atoms in a rotating trap. *Phys. Rev. A*, 103:063325, Jun 2021.

[105] Y.-J. Lin, R. L. Compton, K. Jiménez-García, J. V. Porto, and I. B. Spielman. Synthetic magnetic fields for ultracold neutral atoms. *Nature*, 462(7273):628–632, dec 2009.

[106] Lindsay J. LeBlanc, Karina Jimé nez-García, Ross A. Williams, Matthew C. Beeler, Abigail R. Perry, William D. Phillips, and Ian B. Spielman. Observation of a superfluid hall effect. *Proceedings of the National Academy of Sciences*, 109(27):10811–10814, jun 2012.

[107] M. C. Beeler, R. A. Williams, K. Jiménez-García, L. J. LeBlanc, A. R. Perry, and I. B. Spielman. The spin hall effect in a quantum gas. *Nature*, 498(7453):201–204, jun 2013.

[108] N. R. Cooper. Optical flux lattices for ultracold atomic gases. *Phys. Rev. Lett.*, 106:175301, Apr 2011.

[109] N. R. Cooper and R. Moessner. Designing topological bands in reciprocal space. *Phys. Rev. Lett.*, 109:215302, Nov 2012.

[110] Nigel R. Cooper and Jean Dalibard. Reaching fractional quantum hall states with optical flux lattices. *Phys. Rev. Lett.*, 110:185301, Apr 2013.

[111] Douglas R. Hofstadter. Energy levels and wave functions of bloch electrons in rational and irrational magnetic fields. *Phys. Rev. B*, 14:2239–2249, Sep 1976.

[112] D. Jaksch and P. Zoller. The cold atom hubbard toolbox. *Annals of Physics*, 315(1):52–79, 2005. Special Issue.

[113] N. Goldman, J. C. Budich, and P. Zoller. Topological quantum matter with ultracold gases in optical lattices. *Nature Physics*, 12(7):639–645, jun 2016.

[114] N. R. Cooper, J. Dalibard, and I. B. Spielman. Topological bands for ultracold atoms. *Rev. Mod. Phys.*, 91:015005, Mar 2019.

[115] M. V. Berry. Quantal Phase Factors Accompanying Adiabatic Changes. *Proceedings of the Royal Society of London Series A*, 392(1802):45–57, March 1984.

[116] Y. Aharonov and D. Bohm. Significance of electromagnetic potentials in the quantum theory. *Phys. Rev.*, 115:485–491, Aug 1959.

[117] D Jaksch and P Zoller. Creation of effective magnetic fields in optical lattices: the hofstadter butterfly for cold neutral atoms. *New Journal of Physics*, 5(1):56, may 2003.

[118] M. Aidelsburger, M. Atala, S. Nascimbène, S. Trotzky, Y.-A. Chen, and I. Bloch. Experimental realization of strong effective magnetic fields in an optical lattice. *Phys. Rev. Lett.*, 107:255301, Dec 2011.

[119] M. Aidelsburger, M. Atala, M. Lohse, J. T. Barreiro, B. Paredes, and I. Bloch. Realization of the hofstadter hamiltonian with ultracold atoms in optical lattices. *Phys. Rev. Lett.*, 111:185301, Oct 2013.

[120] M. Aidelsburger, M. Lohse, C. Schweizer, M. Atala, J. T. Barreiro, S. Nascimbène, N. R. Cooper, I. Bloch, and N. Goldman. Measuring the chern number of hofstadter bands with ultracold bosonic atoms. *Nature Physics*, 11(2):162–166, dec 2014.

[121] J. Struck, C. Ölschläger, M. Weinberg, P. Hauke, J. Simonet, A. Eckardt, M. Lewenstein, K. Sengstock, and P. Windpassinger. Tunable gauge potential for neutral and spinless particles in driven optical lattices. *Phys. Rev. Lett.*, 108:225304, May 2012.

[122] Anders S. Sørensen, Eugene Demler, and Mikhail D. Lukin. Fractional quantum hall states of atoms in optical lattices. *Phys. Rev. Lett.*, 94:086803, Mar 2005.

[123] S. Tung, V. Schweikhard, and E. A. Cornell. Observation of vortex pinning in bose-einstein condensates. *Phys. Rev. Lett.*, 97:240402, Dec 2006.

[124] R. A. Williams, S. Al-Assam, and C. J. Foot. Observation of vortex nucleation in a rotating two-dimensional lattice of bose-einstein condensates. *Phys. Rev. Lett.*, 104:050404, Feb 2010.

[125] Rajiv Bhat, M. Krämer, J. Cooper, and M. J. Holland. Hall effects in bose-einstein condensates in a rotating optical lattice. *Phys. Rev. A*, 76:043601, Oct 2007.

[126] Hirokazu Miyake, Georgios A. Siviloglou, Colin J. Kennedy, William Cody Burton, and Wolfgang Ketterle. Realizing the harper hamiltonian with laser-assisted tunneling in optical lattices. *Phys. Rev. Lett.*, 111:185302, Oct 2013.

[127] R. N. Palmer and D. Jaksch. High-field fractional quantum hall effect in optical lattices. *Phys. Rev. Lett.*, 96:180407, May 2006.

[128] Rebecca N. Palmer, Alexander Klein, and Dieter Jaksch. Optical lattice quantum hall effect. *Phys. Rev. A*, 78:013609, Jul 2008.

[129] R. O. Umucal ılar and Erich J. Mueller. Fractional quantum hall states in the vicinity of mott plateaus. *Phys. Rev. A*, 81:053628, May 2010.

[130] Fabian Grusdt, Fabian Letscher, Mohammad Hafezi, and Michael Fleischhauer. Topological growing of laughlin states in synthetic gauge fields. *Phys. Rev. Lett.*, 113:155301, Oct 2014.

[131] Yin-Chen He, Fabian Grusdt, Adam Kaufman, Markus Greiner, and Ashvin Vishwanath. Realizing and adiabatically preparing bosonic integer and fractional quantum hall states in optical lattices. *Phys. Rev. B*, 96:201103, Nov 2017.

[132] M. Barkeshli, N. Y. Yao, and C. R. Laumann. Continuous preparation of a fractional chern insulator. *Phys. Rev. Lett.*, 115:026802, Jul 2015.

[133] Johannes Motruk and Frank Pollmann. Phase transitions and adiabatic preparation of a fractional chern insulator in a boson cold-atom model. *Phys. Rev. B*, 96:165107, Oct 2017.

[134] M. Eric Tai, Alexander Lukin, Matthew Rispoli, Robert Schittko, Tim Menke, Dan Borgnia, Philipp M. Preiss, Fabian Grusdt, Adam M. Kaufman, and Markus Greiner. Microscopy of the interacting Harper-Hofstadter model in the two-body limit. *Nature*, 546(7659):519–523, June 2017.

[135] Julian Léonard, Sooshin Kim, Joyce Kwan, Perrin Segura, Fabian Grusdt, Cécile Repellin, Nathan Goldman, and Markus Greiner. Realization of a fractional quantum hall state with ultracold atoms. 2022.

[136] T. W. Zhou, G. Cappellini, D. Tusi, L. Franchi, J. Parravicini, C. Repellin, S. Greschner, M. Inguscio, T. Giamarchi, M. Filippone, J. Catani, and L. Fallani. Observation of universal hall response in strongly interacting fermions. 2022.

[137] F. D. M. Haldane. Model for a quantum hall effect without landau levels: Condensed-matter realization of the "parity anomaly". *Phys. Rev. Lett.*, 61:2015–2018, Oct 1988.

[138] Gregor Jotzu, Michael Messer, Rémi Desbuquois, Martin Lebrat, Thomas Uehlinger, Daniel Greif, and Tilman Esslinger. Experimental realization of the topological haldane model with ultracold fermions. *Nature*, 515(7526):237–240, nov 2014.

[139] Titus Neupert, Luiz Santos, Claudio Chamon, and Christopher Mudry. Fractional quantum hall states at zero magnetic field. *Phys. Rev. Lett.*, 106:236804, Jun 2011.

[140] Evelyn Tang, Jia-Wei Mei, and Xiao-Gang Wen. High-temperature fractional quantum hall states. *Phys. Rev. Lett.*, 106:236802, Jun 2011.

[141] Kai Sun, Zhengcheng Gu, Hosho Katsura, and S. Das Sarma. Nearly flatbands with nontrivial topology. *Phys. Rev. Lett.*, 106:236803, Jun 2011.

[142] Yi-Fei Wang, Zheng-Cheng Gu, Chang-De Gong, and D. N. Sheng. Fractional quantum hall effect of hard-core bosons in topological flat bands. *Phys. Rev. Lett.*, 107:146803, Sep 2011.

[143] Eliot Kapit and Erich Mueller. Exact parent hamiltonian for the quantum hall states in a lattice. *Phys. Rev. Lett.*, 105:215303, Nov 2010.

[144] N. Regnault and B. Andrei Bernevig. Fractional chern insulator. *Phys. Rev. X*, 1:021014, Dec 2011.

[145] F. D. M. Haldane and S. Raghu. Possible realization of directional optical waveguides in photonic crystals with broken time-reversal symmetry. *Phys. Rev. Lett.*, 100:013904, Jan 2008.

[146] S. Raghu and F. D. M. Haldane. Analogs of quantum-hall-effect edge states in photonic crystals. *Phys. Rev. A*, 78:033834, Sep 2008.

[147] Zheng Wang, Yidong Chong, J. D. Joannopoulos, and Marin Soljačić. Observation of unidirectional backscattering-immune topological electromagnetic states. *Nature*, 461(7265):772–775, October 2009.

[148] Mikael C. Rechtsman, Julia M. Zeuner, Yonatan Plotnik, Yaakov Lumer, Daniel Podolsky, Felix Dreisow, Stefan Nolte, Mordechai Segev, and Alexander Szameit. Photonic floquet topological insulators. *Nature*, 496(7444):196–200, apr 2013.

[149] Jens Koch, Andrew A. Houck, Karyn Le Hur, and S. M. Girvin. Time-reversal-symmetry breaking in circuit-QED-based photon lattices. *Physical Review A*, 82(4), oct 2010.

[150] Jaeyoon Cho, Dimitris G. Angelakis, and Sougato Bose. Fractional quantum hall state in coupled cavities. *Phys. Rev. Lett.*, 101:246809, Dec 2008.

[151] R.O. Umucalılar and I. Carusotto. Many-body braiding phases in a rotating strongly correlated photon gas. *Physics Letters A*, 377(34):2074–2078, 2013.

[152] R. O. Umucal ılar, M. Wouters, and I. Carusotto. Probing few-particle laughlin states of photons via correlation measurements. *Phys. Rev. A*, 89:023803, Feb 2014.

[153] Nathan Schine, Albert Ryou, Andrey Gromov, Ariel Sommer, and Jonathan Simon. Synthetic Landau levels for photons. *Nature*, 534(7609):671–675, June 2016.

[154] Andrew D. Greentree, Charles Tahan, Jared H. Cole, and Lloyd C. L. Hollenberg. Quantum phase transitions of light. *Nature Physics*, 2(12):856–861, nov 2006.

[155] Michael J. Hartmann, Fernando G. S. L. Brandão, and Martin B. Plenio. Strongly interacting polaritons in coupled arrays of cavities. *Nature Physics*, 2(12):849–855, nov 2006.

[156] I. Carusotto, D. Gerace, H. E. Tureci, S. De Liberato, C. Ciuti, and A. Imamoğlu. Fermionized photons in an array of driven dissipative nonlinear cavities. *Phys. Rev. Lett.*, 103:033601, Jul 2009.

[157] R. O. Umucal ılar and I. Carusotto. Fractional quantum hall states of photons in an array of dissipative coupled cavities. *Phys. Rev. Lett.*, 108:206809, May 2012.

[158] Eliot Kapit, Mohammad Hafezi, and Steven H. Simon. Induced self-stabilization in fractional quantum hall states of light. *Phys. Rev. X*, 4:031039, Sep 2014.

[159] R. O. Umucal ılar and I. Carusotto. Generation and spectroscopic signatures of a fractional quantum hall liquid of photons in an incoherently pumped optical cavity. *Phys. Rev. A*, 96:053808, Nov 2017.

[160] Shovan Dutta and Erich J. Mueller. Coherent generation of photonic fractional quantum hall states in a cavity and the search for anyonic quasiparticles. *Phys. Rev. A*, 97:033825, Mar 2018.

[161] R. O. Umucal ılar, J. Simon, and I. Carusotto. Autonomous stabilization of photonic laughlin states through angular momentum potentials. *Phys. Rev. A*, 104:023704, Aug 2021.

[162] Pavel Kurilovich, Vladislav D. Kurilovich, José Lebreuilly, and Steven Girvin. Stabilizing the laughlin state of light: Dynamics of hole fractionalization. *SciPost Physics*, 13(5), nov 2022.

[163] Ningyuan Jia, Nathan Schine, Alexandros Georgakopoulos, Albert Ryou, Logan W. Clark, Ariel Sommer, and Jonathan Simon. A strongly interacting polaritonic quantum dot. *Nature Physics*, 14(6):550–554, mar 2018.

[164] Logan W. Clark, Nathan Schine, Claire Baum, Ningyuan Jia, and Jonathan Simon. Observation of Laughlin states made of light. *Nature*, 582(7810):41–45, June 2020.

[165] P. Roushan, C. Neill, A. Megrant, Y. Chen, R. Babbush, R. Barends, B. Campbell, Z. Chen, B. Chiaro, A. Dunsworth, A. Fowler, E. Jeffrey, J. Kelly,

E. Lucero, J. Mutus, P. J. J. O'Malley, M. Neeley, C. Quintana, D. Sank, A. Vainsencher, J. Wenner, T. White, E. Kapit, H. Neven, and J. Martinis. Chiral ground-state currents of interacting photons in a synthetic magnetic field. *Nature Physics*, 13(2):146–151, February 2017.

[166] Ruichao Ma, Brendan Saxberg, Clai Owens, Nelson Leung, Yao Lu, Jonathan Simon, and David I. Schuster. A dissipatively stabilized mott insulator of photons. *Nature*, 566(7742):51–57, feb 2019.

[167] B. I. Halperin. Theory of the quantized Hall conductance. *Helv. Phys. Acta*, 56:75–102, 1983.

[168] J. K. Jain. Composite-fermion approach for the fractional quantum hall effect. *Phys. Rev. Lett.*, 63:199–202, Jul 1989.

[169] D.J. Thouless. Theory of the quantized hall effect. *Surface Science*, 142(1):147–154, 1984.

[170] F. D. M. Haldane and E. H. Rezayi. Periodic laughlin-jastrow wave functions for the fractional quantized hall effect. *Phys. Rev. B*, 31:2529–2531, Feb 1985.

[171] F. D. M. Haldane. Fractional quantization of the hall effect: A hierarchy of incompressible quantum fluid states. *Phys. Rev. Lett.*, 51:605–608, Aug 1983.

[172] Ana Lopez and Eduardo Fradkin. Universal properties of the wave functions of fractional quantum hall systems. *Phys. Rev. Lett.*, 69:2126–2129, Oct 1992.

[173] S. A. Trugman and S. Kivelson. Exact results for the fractional quantum hall effect with general interactions. *Phys. Rev. B*, 31:5280–5284, Apr 1985.

[174] Steven H. Simon, E. H. Rezayi, and Nigel R. Cooper. Generalized quantum hall projection hamiltonians. *Phys. Rev. B*, 75:075318, Feb 2007.

[175] Steven H. Simon, E. H. Rezayi, and Nigel R. Cooper. Pseudopotentials for multiparticle interactions in the quantum hall regime. *Phys. Rev. B*, 75:195306, May 2007.

[176] Bertrand I Halperin and Jainendra K Jain. *Fractional Quantum Hall Effects*. WORLD SCIENTIFIC, jan 2020.

[177] J. M. Caillol, Dominique Lévesque, J. J. Weis, and Jean Pierre Hansen. A monte carlo study of the classical two-dimensional one-component plasma. *Journal of Statistical Physics*, 28:325–349, 1982.

[178] S. M. Girvin and A. H. MacDonald. *Multicomponent Quantum Hall Systems: The Sum of Their Parts and More*, chapter 5, pages 161–224. John Wiley & Sons, Ltd, 1996.

[179] Parsa Bonderson, Victor Gurarie, and Chetan Nayak. Plasma analogy and non-abelian statistics for ising-type quantum hall states. *Physical Review B*, 83(7), feb 2011.

[180] Xiao-Gang Wen. Edge transport properties of the fractional quantum hall states and weak-impurity scattering of a one-dimensional charge-density wave. *Phys. Rev. B*, 44:5708–5719, Sep 1991.

[181] C. L. Kane and Matthew P. A. Fisher. Impurity scattering and transport of fractional quantum hall edge states. *Phys. Rev. B*, 51:13449–13466, May 1995.

[182] C. L. Kane and Matthew P. A. Fisher. Quantized thermal transport in the fractional quantum hall effect. *Phys. Rev. B*, 55:15832–15837, Jun 1997.

[183] Michael Stone. Schur functions, chiral bosons, and the quantum-hall-effect edge states. *Phys. Rev. B*, 42:8399–8404, Nov 1990.

[184] S. M. Girvin, A. H. MacDonald, and P. M. Platzman. Magneto-roton theory of collective excitations in the fractional quantum hall effect. *Phys. Rev. B*, 33:2481–2494, Feb 1986.

[185] Bo Yang, Zi-Xiang Hu, Z. Papić, and F. D. M. Haldane. Model wave functions for the collective modes and the magnetoroton theory of the fractional quantum hall effect. *Phys. Rev. Lett.*, 108:256807, Jun 2012.

[186] Shiuan-Fan Liou, F. D. M. Haldane, Kun Yang, and E. H. Rezayi. Chiral gravitons in fractional quantum hall liquids. *Phys. Rev. Lett.*, 123:146801, Sep 2019.

[187] F. D. M. Haldane. Geometrical description of the fractional quantum hall effect. *Phys. Rev. Lett.*, 107:116801, Sep 2011.

[188] Kun Yang. Acoustic wave absorption as a probe of dynamical geometrical response of fractional quantum hall liquids. *Phys. Rev. B*, 93:161302, Apr 2016.

[189] Zhao Liu, Andrey Gromov, and Zlatko Papić. Geometric quench and nonequilibrium dynamics of fractional quantum hall states. *Phys. Rev. B*, 98:155140, Oct 2018.

[190] Zhao Liu, Ajit C. Balram, Zlatko Papić, and Andrey Gromov. Quench dynamics of collective modes in fractional quantum hall bilayers. *Phys. Rev. Lett.*, 126:076604, Feb 2021.

[191] R. de-Picciotto, M. Reznikov, M. Heiblum, V. Umansky, G. Bunin, and D. Mahalu. Direct observation of a fractional charge. *Nature*, 389(6647):162–164, September 1997.

[192] B. I. Halperin. Statistics of quasiparticles and the hierarchy of fractional quantized hall states. *Phys. Rev. Lett.*, 52:1583–1586, Apr 1984.

[193] J. M. Leinaas and J. Myrheim. On the theory of identical particles. *Nuovo Cimento B Serie*, 37(1):1–23, January 1977.

[194] Frank Wilczek. Magnetic flux, angular momentum, and statistics. *Phys. Rev. Lett.*, 48:1144–1146, Apr 1982.

[195] F. Wilczek. Quantum mechanics of fractional-spin particles. *Phys. Rev. Lett.*, 49:957–959, Oct 1982.

[196] S. M. Girvin and Terrence Jach. Formalism for the quantum hall effect: Hilbert space of analytic functions. *Phys. Rev. B*, 29:5617–5625, May 1984.

[197] Heidi Kjønsberg and Jan Myrheim. Numerical Study of Charge and Statistics of Laughlin Quasiparticles. *International Journal of Modern Physics A*, 14(04):537–557, feb 1999.

[198] H. Kjønsberg and J.M. Leinaas. Charge and statistics of quantum hall quasiparticles — a numerical study of mean values and fluctuations. *Nuclear Physics B*, 559(3):705–742, oct 1999.

[199] Gautam Dev and J. K. Jain. Jastrow-slater trial wave functions for the fractional quantum hall effect: Results for few-particle systems. *Phys. Rev. B*, 45:1223–1230, Jan 1992.

[200] Gun Sang Jeon and Jainendra K. Jain. Nature of quasiparticle excitations in the fractional quantum hall effect. *Phys. Rev. B*, 68:165346, Oct 2003.

[201] Arkadiusz Bochniak, Zohar Nussinov, Alexander Seidel, and Gerardo Ortiz. Mechanism for particle fractionalization and universal edge physics in quantum hall fluids. *Communications Physics*, 5(1), jul 2022.

[202] F D M Haldane. 'luttinger liquid theory' of one-dimensional quantum fluids. i. properties of the luttinger model and their extension to the general 1d interacting spinless fermi gas. *Journal of Physics C: Solid State Physics*, 14(19):2585, jul 1981.

[203] Daniel C. Mattis and Elliott H. Lieb. Exact solution of a many-fermion system and its associated boson field. *Journal of Mathematical Physics*, 6(2):304–312, 1965.

[204] Mats Horsdal and Jon Magne Leinaas. Explicit mapping between a two-dimensional quantum hall system and a one-dimensional luttinger liquid. i. luttinger parameters. *Phys. Rev. B*, 76:195321, Nov 2007.

[205] Mats Horsdal and Jon Magne Leinaas. Explicit mapping between a two-dimensional quantum hall system and a one-dimensional luttinger liquid. ii. correlation functions. *Phys. Rev. B*, 76:195322, Nov 2007.

[206] T. Giamarchi and Oxford University Press. *Quantum Physics in One Dimension*. International Series of Monographs on Physics. Clarendon Press, 2004.

[207] J Voit. One-dimensional fermi liquids. *Reports on Progress in Physics*, 58(9):977, sep 1995.

[208] H. J. Schulz, G. Cuniberti, and P. Pieri. Fermi liquids and luttinger liquids, 1998.

[209] T. H. Hansson, M. Hermanns, S. H. Simon, and S. F. Viefers. Quantum hall physics: Hierarchies and conformal field theory techniques. *Rev. Mod. Phys.*, 89:025005, May 2017.

[210] A. Luther and I. Peschel. Single-particle states, kohn anomaly, and pairing fluctuations in one dimension. *Phys. Rev. B*, 9:2911–2919, Apr 1974.

[211] A. M. Chang, L. N. Pfeiffer, and K. W. West. Observation of chiral luttinger behavior in electron tunneling into fractional quantum hall edges. *Phys. Rev. Lett.*, 77:2538–2541, Sep 1996.

[212] A. M. Chang, M. K. Wu, C. C. Chi, L. N. Pfeiffer, and K. W. West. Plateau behavior in the chiral luttinger liquid exponent. *Phys. Rev. Lett.*, 86:143–146, Jan 2001.

[213] C. de C. Chamon and X. G. Wen. Sharp and smooth boundaries of quantum hall liquids. *Phys. Rev. B*, 49:8227–8241, Mar 1994.

[214] Xin Wan, Kun Yang, and E. H. Rezayi. Reconstruction of fractional quantum hall edges. *Phys. Rev. Lett.*, 88:056802, Jan 2002.

[215] V. J. Goldman and E. V. Tsiper. Dependence of the fractional quantum hall edge critical exponent on the range of interaction. *Phys. Rev. Lett.*, 86:5841–5841, Jun 2001.

[216] Sudhansu S. Mandal and J.K. Jain. How universal is the fractional-quantum-hall edge luttinger liquid? *Solid State Communications*, 118(10):503–507, jun 2001.

[217] Sudhansu S. Mandal and Jainendra K. Jain. Relevance of inter-composite-fermion interaction to the edge tomonaga-luttinger liquid. *Phys. Rev. Lett.*, 89:096801, Aug 2002.

[218] Shivakumar Jolad, Diptiman Sen, and Jainendra K. Jain. Fractional quantum hall edge: Effect of nonlinear dispersion and edge roton. *Phys. Rev. B*, 82:075315, Aug 2010.

[219] Adilet Imambekov, Thomas L. Schmidt, and Leonid I. Glazman. One-dimensional quantum liquids: Beyond the luttinger liquid paradigm. *Rev. Mod. Phys.*, 84:1253–1306, Sep 2012.

[220] Andrea Cappelli, Carlo A. Trugenberger, and Guillermo R. Zemba. $w_{1+\infty}$ dynamics of edge excitations in the quantum hall effect. *Annals of Physics*, 246(1):86–120, 1996.

[221] Michael Stone, H. W. Wyld, and R. L. Schult. Edge waves in the quantum hall effect and quantum dots. *Phys. Rev. B*, 45:14156–14161, Jun 1992.

[222] S. Giovanazzi, L. Pitaevskii, and S. Stringari. Dispersion law of edge waves in the quantum hall effect. *Phys. Rev. Lett.*, 72:3230–3233, May 1994.

[223] Tom Price and Austen Lamacraft. Fine structure of the phonon in one dimension from quantum hydrodynamics. *Phys. Rev. B*, 90:241415, Dec 2014.

[224] Tom Price and Austen Lamacraft. Quantum hydrodynamics in one dimension beyond the luttinger liquid, 2015.

[225] Alexander G. Abanov and Paul B. Wiegmann. Quantum hydrodynamics, the quantum benjamin-ono equation, and the calogero model. *Phys. Rev. Lett.*, 95:076402, Aug 2005.

[226] E. Bettelheim, Alexander G. Abanov, and P. Wiegmann. Nonlinear quantum shock waves in fractional quantum hall edge states. *Phys. Rev. Lett.*, 97:246401, Dec 2006.

[227] P. Wiegmann. Nonlinear hydrodynamics and fractionally quantized solitons at the fractional quantum hall edge. *Phys. Rev. Lett.*, 108:206810, May 2012.

[228] R. Fern, R. Bondesan, and S. H. Simon. Effective edge state dynamics in the fractional quantum hall effect. *Phys. Rev. B*, 98:155321, Oct 2018.

[229] Alberto Nardin and Iacopo Carusotto. Non-linear edge dynamics of an integer quantum hall fluid. *Europhysics Letters*, 132(1):10002, nov 2020.

[230] Alberto Nardin and Iacopo Carusotto. Linear and nonlinear edge dynamics of trapped fractional quantum hall droplets. *Phys. Rev. A*, 107:033320, Mar 2023.

[231] Alberto Nardin and Iacopo Carusotto. Refermionized theory of the edge modes of a fractional quantum hall cloud. 2023.

[232] Xin Wan, E. H. Rezayi, and Kun Yang. Edge reconstruction in the fractional quantum hall regime. *Phys. Rev. B*, 68:125307, Sep 2003.

[233] Kun Yang. Field theoretical description of quantum hall edge reconstruction. *Phys. Rev. Lett.*, 91:036802, Jul 2003.

[234] Shivakumar Jolad and Jainendra K. Jain. Testing the topological nature of the fractional quantum hall edge. *Phys. Rev. Lett.*, 102:116801, Mar 2009.

[235] Shivakumar Jolad, Chia-Chen Chang, and Jainendra K. Jain. "electron operator at the edge of the 1/3 fractional quantum hall liquid". *Phys. Rev. B*, 75:165306, Apr 2007.

[236] Nicholas Metropolis and S. Ulam. The monte carlo method. *Journal of the American Statistical Association*, 44(247):335–341, 1949. PMID: 18139350.

[237] Nicholas Metropolis, Arianna W. Rosenbluth, Marshall N. Rosenbluth, Augusta H. Teller, and Edward Teller. Equation of state calculations by fast computing machines. *The Journal of Chemical Physics*, 21(6):1087–1092, 1953.

[238] W. K. Hastings. Monte carlo sampling methods using markov chains and their applications. *Biometrika*, 57(1):97–109, 1970.

[239] Adilet Imambekov and Leonid I. Glazman. Universal theory of nonlinear luttinger liquids. *Science*, 323(5911):228–231, jan 2009.

[240] M. Pustilnik, M. Khodas, A. Kamenev, and L. I. Glazman. Dynamic response of one-dimensional interacting fermions. *Phys. Rev. Lett.*, 96:196405, May 2006.

[241] J. E. Avron, R. Seiler, and P. G. Zograf. Viscosity of quantum hall fluids. *Phys. Rev. Lett.*, 75:697–700, Jul 1995.

[242] YeJe Park and F. D. M. Haldane. Guiding-center hall viscosity and intrinsic dipole moment along edges of incompressible fractional quantum hall fluids. *Phys. Rev. B*, 90:045123, Jul 2014.

[243] S. M. Girvin, A. H. MacDonald, and P. M. Platzman. Magneto-roton theory of collective excitations in the fractional quantum hall effect. *Phys. Rev. B*, 33:2481–2494, Feb 1986.

[244] Takuya Ito and Naokazu Shibata. Density matrix renormalization group study of the ν=1/3 edge states in fractional quantum Hall systems. *Phys. Rev. B*, 103:115107, Mar 2021.

[245] P.G. Drazin, R.S. Johnson, and D.G. Crighton. *Solitons: An Introduction*. Cambridge Texts in Applied Mathematics. Cambridge University Press, 1989.

[246] N. J. Zabusky and M. D. Kruskal. Interaction of "solitons" in a collisionless plasma and the recurrence of initial states. *Phys. Rev. Lett.*, 15:240–243, Aug 1965.

[247] Xin Wan, Zi-Xiang Hu, E. H. Rezayi, and Kun Yang. Fractional quantum Hall effect at ν =5/2: Ground states, non-Abelian quasiholes, and edge modes in a microscopic model. *Phys. Rev. B*, 77:165316, Apr 2008.

[248] F D M Haldane. 'luttinger liquid theory' of one-dimensional quantum fluids. i. properties of the luttinger model and their extension to the general 1d interacting spinless fermi gas. *Journal of Physics C: Solid State Physics*, 14(19):2585, jul 1981.

[249] N. Fabbri, M. Panfil, D. Clément, L. Fallani, M. Inguscio, C. Fort, and J.-S. Caux. Dynamical structure factor of one-dimensional bose gases: Experimental signatures of beyond-luttinger-liquid physics. *Phys. Rev. A*, 91:043617, Apr 2015.

[250] M. Khodas, M. Pustilnik, A. Kamenev, and L. I. Glazman. Fermi-luttinger liquid: Spectral function of interacting one-dimensional fermions. *Phys. Rev. B*, 76:155402, Oct 2007.

[251] E. Macaluso and I. Carusotto. Hard-wall confinement of a fractional quantum hall liquid. *Phys. Rev. A*, 96:043607, Oct 2017.

[252] E. Macaluso and I. Carusotto. Ring-shaped fractional quantum hall liquids with hard-wall potentials. *Phys. Rev. A*, 98:013605, Jul 2018.

[253] B. Andrei Bernevig and F. D. M. Haldane. Model fractional quantum hall states and jack polynomials. *Phys. Rev. Lett.*, 100:246802, Jun 2008.

[254] J. J. Palacios and A. H. MacDonald. Numerical tests of the chiral luttinger liquid theory for fractional hall edges. *Phys. Rev. Lett.*, 76:118–121, Jan 1996.

[255] F. D. M. Haldane. "fractional statistics" in arbitrary dimensions: A generalization of the pauli principle. *Phys. Rev. Lett.*, 67:937–940, Aug 1991.

[256] Richard Fern and Steven H. Simon. Quantum hall edges with hard confinement: Exact solution beyond luttinger liquid. *Phys. Rev. B*, 95:201108, May 2017.

[257] Alexander L. Gaunt, Tobias F. Schmidutz, Igor Gotlibovych, Robert P. Smith, and Zoran Hadzibabic. Bose-einstein condensation of atoms in a uniform potential. *Phys. Rev. Lett.*, 110:200406, May 2013.

[258] F. Chevy, K. W. Madison, and J. Dalibard. Measurement of the angular momentum of a rotating bose-einstein condensate. *Phys. Rev. Lett.*, 85:2223–2227, Sep 2000.

[259] W. Pauli. The connection between spin and statistics. *Phys. Rev.*, 58:716–722, Oct 1940.

[260] J. M. Leinaas and J. Myrheim. On the theory of identical particles. *Nuovo Cimento B*, 37(1):1–23, January 1977.

[261] A. Lerda. *Anyons: Quantum Mechanics of Particles with Fractional Statistics*. Lecture Notes in Physics Monographs ;. Springer, Berlin, Heidelberg, 1992.

[262] A. Khare. *Fractional Statistics and Quantum Theory*. World Scientific, 2nd edition, 2005.

[263] J. Preskill. *Lecture notes Lecture Notes for Physics 219: Quantum Computation*. June 2004.

[264] D. E. Feldman and B. I. Halperin. Fractional charge and fractional statistics in the quantum hall effects. *Rep. Prog. Phys.*, 84(7):076501, jun 2021.

[265] D. Li. The spin of the quasi-particle in the fractional quantum hall effect. *Phys. Lett. A*, 169(1):82–86, 1992.

[266] D. Li. Intrinsic quasiparticle's spin and fractional quantum hall effect on riemann surfaces. *Mod. Phys. Lett. B*, 07(16):1103–1110, 1993.

[267] T. Einarsson, S. L. Sondhi, S. M. Girvin, and D. P. Arovas. Fractional spin for quantum hall effect quasiparticles. *Nucl. Phys. B*, 441(3):515–529, 1995.

[268] N. Read. Quasiparticle spin from adiabatic transport in quantum hall trial wavefunctions, 2008.

[269] Andrey Gromov. Geometric defects in quantum hall states. *Phys. Rev. B*, 94:085116, Aug 2016.

[270] Ha Quang Trung, Yuzhu Wang, and Bo Yang. Spin-statistics relation and robustness of braiding phase for anyons in fractional quantum hall effect, 2022.

[271] S. L. Sondhi and S. A. Kivelson. Long-range interactions and the quantum hall effect. *Phys. Rev. B*, 46:13319–13325, Nov 1992.

[272] Jon Magne Leinaas. Spin and statistics for quantum hall quasi-particles. 1999.

[273] Tommaso Comparin, Alvin Opler, Elia Macaluso, Alberto Biella, Alexios P. Polychronakos, and Leonardo Mazza. Measurable fractional spin for quantum hall quasiparticles on the disk. *Phys. Rev. B*, 105:085125, Feb 2022.

[274] Alberto Nardin, Eddy Ardonne, and Leonardo Mazza. Spin-statistics relation for abelian quantum hall states. 2022.

[275] F. D. M. Haldane and E. H. Rezayi. Finite-size studies of the incompressible state of the fractionally quantized hall effect and its excitations. *Phys. Rev. Lett.*, 54:237–240, Jan 1985.

[276] Gun Sang Jeon, Kenneth L. Graham, and Jainendra K. Jain. Fractional statistics in the fractional quantum hall effect. *Phys. Rev. Lett.*, 91:036801, Jul 2003.

[277] Gun Sang Jeon, Kenneth L. Graham, and Jainendra K. Jain. Berry phases for composite fermions: Effective magnetic field and fractional statistics. *Phys. Rev. B*, 70:125316, Sep 2004.

[278] Gun Sang Jeon, A. D. Güçlü, C. J. Umrigar, and J. K. Jain. Composite-fermion antiparticle description of the hole excitation in a maximum-density droplet with a small number of electrons. *Phys. Rev. B*, 72:245312, Dec 2005.

[279] Gun Sang Jeon and J. K. Jain. Thermodynamic behavior of braiding statistics for certain fractional quantum hall quasiparticles. *Phys. Rev. B*, 81:035319, Jan 2010.

[280] J. Kjäll, E. Ardonne, V. Dwivedi, M. Hermanns, and T. H. Hansson. Matrix product state representation of quasielectron wave functions. *J. Stat. Mech.: Theory Exp.*, 2018(5):053101, May 2018.

[281] J. K. Jain and R. K. Kamilla. Quantitative study of large composite-fermion systems. *Phys. Rev. B*, 55:R4895–R4898, Feb 1997.

[282] Chetan Nayak and Frank Wilczek. 2n-quasihole states realize 2n-1-dimensional spinor braiding statistics in paired quantum hall states. *Nuclear Physics B*, 479(3):529–553, nov 1996.

[283] Alexei Kitaev. Anyons in an exactly solved model and beyond. *Annals of Physics*, 321(1):2–111, 2006. January Special Issue.

[284] W.R. Gilks, S. Richardson, and D. Spiegelhalter. *Markov Chain Monte Carlo in Practice*. Chapman & Hall/CRC Interdisciplinary Statistics. Taylor & Francis, 1995.

[285] Ki Hoon Lee, Zi-Xiang Hu, and Xin Wan. Construction of edge states in fractional quantum hall systems by jack polynomials. *Phys. Rev. B*, 89:165124, Apr 2014.

[286] J. K. Jain and R. K. Kamilla. Composite fermions in the hilbert space of the lowest electronic landau level. *International Journal of Modern Physics B*, 11(22):2621–2660, 1997.